

# Laser hardening of internal gearing for a Formula Student car

**Bart TYSKENS**  
**Ward LENAERTS**

Promotor(en): Prof. dr. ir. Bert Lauwers

Co-promotor(en): Ing. Jef Loenders,  
Ing. Jurgen Adriaensen & Ing. Benjamin Peeters

Masterproef ingediend tot het behalen van  
de graad van master of Science in de  
industriële wetenschappen: Elektromechanica  
Intelligent Mechanics

Academiejaar 2020 - 2021

©Copyright KU Leuven

Zonder voorafgaande schriftelijke toestemming van zowel de promotor(en) als de auteur(s) is overnemen, kopiëren, gebruiken of realiseren van deze uitgave of gedeelten ervan verboden. Voor aanvragen i.v.m. het overnemen en/of gebruik en/of realisatie van gedeelten uit deze publicatie, kan u zich richten tot KU Leuven Campus Groep T Leuven, Andreas Vesaliusstraat 13, B-3000 Leuven, +32 16 30 10 30 of via e-mail [iw.groept@kuleuven.be](mailto:iw.groept@kuleuven.be).

Voorafgaande schriftelijke toestemming van de promotor(en) is eveneens vereist voor het aanwenden van de in deze masterproef beschreven (originele) methoden, producten, schakelingen en programma's voor industrieel of commercieel nut en voor de inzending van deze publicatie ter deelname aan wetenschappelijke prijzen of wedstrijden.



# Voorwoord

Eerst en vooral willen we onze dank betuigen aan onze promotor Prof. dr. ir. Lauwers en onze co-promotoren, dhr. Ing. Adriaensen, dhr. Ing. Loenders en dhr. Ing. Peeters voor hun hulp en expertise zowel op technisch als op praktisch vlak tijdens het schrijven van onze masterproef.

Verder zouden wij ook graag alle mensen bij Absolem & OMC die ons hebben geholpen willen bedanken. Met name Siebe, Leo, Steven B., Kristof, Steven P. en Peter.

Naast Absolem en OMC zijn er nog veel andere partners die ons geholpen hebben op vlak van productie, materialen, software of metrologie. Zonder hen was het nooit mogelijk geweest om deze masterproef te realiseren. Bedankt aan volgende personen:

Dries Verschaete, Ventec NV, voor het cementeren van de ringwielen.

Prof. Van Rymentant & Oleksandr Kurtov, Campus De Nayer, voor het beschikbaar stellen van de nodige faciliteiten voor de microhardheidsmetingen en voor het verlenen van advies.

Frederiek Vanhoutte, Gearcraft Vanhoutte NV, voor de koolstofdifusie van de samples en ringwielen.

Alexandre Rogiers, Cadcamatic NV, voor het draadvonken van de ringwielen.

Dank aan Luc Pernot voor de hulp met en vervaardiging van de opstelling.

Anke Engelen & Geert van de Kerkhof, Van Hoof Groep. Dankzij hen hebben we elke stap van het proces kunnen valideren via uitgebreide metingen van de vertandingen.

Justin Sims & team, DANTE Solutions, for providing the necessary licenses and help during use of the software.

Stefaan Vanneste, Grimonprez Transmission Gears NV, voor het schenken van het staal.

Verder zouden wij graag onze families, vrienden, het Formula Electric Belgium team en in het bijzonder onze vriendinnen bedanken voor de steun doorheen het jaar.

# Samenvatting

In deze masterproef wordt het laserhardnen van een inwendige vertanding uit de meest recente wagen van Formula Electric Belgium onderzocht, gesimuleerd en gevalideerd. De motivatie achter dit onderzoek komt vanuit de probleemstelling dat de traditionele manier waarop deze vertanding gehard wordt - cementeren - voor vervormingen in de finale vertanding zorgt. Waar de uitwendige vertandingen in de tandwielkast worden geslepen na het cementeren, is dit niet mogelijk voor het inwendig vertandde ringwiel wegens de erg compacte afmetingen en moeilijke bereikbaarheid van de tanden.

Laserhardnen is een hardingstechniek waarbij er heel lokaal warmte toegevoegd kan worden. Daarom zou deze techniek mogelijk voor een vermindering van de vervormingen op het tandwiel zorgen en dus ook voor een hogere kwaliteit van de ringwielen. Omdat er een groot aantal parameters valt in te stellen bij het laseren en omdat testmateriaal duur en dus beperkt in hoeveelheid was, werd er gebruik gemaakt van simulatiesoftware. Door eerst te simuleren, kon het aantal testen drastisch beperkt worden. Voor de simulaties van het laserhardnen en het bepalen van het optimale concept, werden modellen in Ansys (eindige elementen software) en Dante (softwarepakket voor warmtebehandelingen op staal) opgesteld. Aan de hand van een uitgebreide literatuurstudie gecombineerd met berekeningen in KISSsoft (software voor het dimensioneren van tandwielkasten) zijn vervolgens de gewenste dimensies, hardheden en hardingsdiepten bepaald. Door deze gewenste waarden uit de literatuurstudie te combineren met de hardingsmodellen, werd het beste concept voor het laserhardnen gekozen. Voor dit concept zijn vervolgens de ideale procesparameters bepaald.

De simulaties van het hardnen zijn vervolgens gevalideerd door testen uit te voeren met een laser uit het OMC (Open Manufacturing Campus) te Turnhout op teststukken van het ringwiel. Op deze geharde teststukken werden er microhardheidsmetingen uitgevoerd om te bepalen of de gewenste hardheden behaald waren. Verder werden de teststukken opgemeten om de vervormingen na het laserhardnen te bepalen. Tot slot werden dezelfde metingen uitgevoerd op een klassiek gecementeerde inwendige vertanding om de twee verschillende technieken één op één te kunnen vergelijken.

# Abstract

In this masters thesis, the technology of laserhardening an internal gearing from the gearbox of a Formula Student car is researched, simulated and validated. The racecar of the Formula Student team Formula Electric Belgium (FEB) has 4 separate electric motors, one motor in each wheel. To each one of these motors, a 2 stage planetary gearbox is attached for torque multiplication to the wheels. The planetary system consists of a sun gear, 3 two stage planet gears and a ring gear. The external gears in the gearbox are turned, hobbled, case-hardened, grinded and finally shotpeened. The ring gear is manufactured by wire EDM and then it is case-hardened. Due to its compact size and complex geometry, it is not possible to grind the ring gear. The grinding step is necessary to compensate for any deformations that occurred during or after case hardening the gears. This means that the ring gear is deformed after hardening and that these deformations are retained on the final geometry of the gear, drastically reducing the quality of the gear. If one of the gears in the system has a lower accuracy grade than the others, the effects can be detrimental for the entire gearing system. A lower quality gear in the system is not only more prone to failure, it also accelerates the wear of all other gears, thus reducing the performance, efficiency and service life of the gearing system.

Laser hardening is a hardening technique where heat can be added to a component very locally. Because of this local heating —and therefore local hardening —when using laser hardening technology, deformations on the gear could be reduced. This means the quality of the internal gearing could be increased, therefore increasing the performance of the entire gearing system without the need for grinding the gear.

When laser hardening, there is quite a large number of parameters to set up. On top of that, because the parts needed for hardness tests are expensive to manufacture and therefore limited in numbers, simulation software is used to determine most of the required parameters beforehand. By simulating before testing, the number of tests could be drastically reduced, this way no test samples are 'wasted'.

On the basis of an extensive literature study combined with calculations in KISSsoft (software for dimensioning gearing systems), the desired dimensions, surface hardness and effective hardening depth of the ring gear were determined. The gear material used in the gearbox of FEB is a case-hardening steel, 16MnCr5, selected for its high ductility in combination with its high (case-)hardenability at the surface. Because of the low carbon content in 16MnCr5, the ring gears first had to be carburized, omitting the quenching step, in order to get a higher carbon concentration

at the surface of the gear teeth. After carbon diffusion, the gears are essentially ready to be laser hardened.

In order to simulate the laser hardening process and to determine the optimal laser track, a model in Ansys (finite element software) and Dante (a software extension for simulating heat treatments on steel) is developed. From the simulations in Ansys, thermal data was obtained. The results of the simulations in DANTE are hardness values and steel composition. By combining the desired hardening parameters with the simulation model, the best concept for laser hardening the ring gear was determined. Next, the simulations of hardening the internal gearing were validated by performing tests on the ring gears with a laser from the Open Manufacturing Campus (OMC) at Turnhout. On these hardened test samples, microhardness measurements were performed in order to determine the samples' effective hardening depth, surface hardness and the geometry of the hardened layer. Thereafter, the test samples were measured on a gear measuring bench in order to quantify the deformations after laser hardening. Finally, in order to compare the laser hardened results to the carburized results, the exact same measurements were performed on the original, conventionally carburized ring gears.

# Contents

<b>Voorwoord</b>	<b>iii</b>
<b>Samenvatting</b>	<b>iv</b>
<b>Abstract</b>	<b>vi</b>
<b>Inhoud</b>	<b>x</b>
<b>Figurenlijst</b>	<b>xiv</b>
<b>Tabellenlijst</b>	<b>xv</b>
<b>Symbolenlijst</b>	<b>xvi</b>
<b>Lijst met afkortingen</b>	<b>xviii</b>
<b>1 Introduction</b>	<b>1</b>
1.1 Formula Electric Belgium . . . . .	1
1.2 Gearbox Aurora Mk II . . . . .	2
1.3 Objective of the thesis . . . . .	4
1.4 Accuracy grade of the gear . . . . .	4
1.5 Dimensioning Gears in KISSsoft . . . . .	5
1.5.1 Basic Data . . . . .	5
1.5.2 Gear Loading . . . . .	7
1.5.3 Determining Dynamic Factor and Load Factor . . . . .	8
1.5.4 Calculation Results . . . . .	13
<b>2 Hardening steel</b>	<b>14</b>
2.1 Introduction . . . . .	14
2.2 Mechanism of hardening steel . . . . .	14
2.3 Properties of hardened steels . . . . .	16

2.4	Case hardening . . . . .	17
2.4.1	Carburizing . . . . .	17
2.4.2	Laser hardening case hardening steel . . . . .	19
2.4.3	System service life in relation to steel type . . . . .	21
<b>3</b>	<b>Mechanical properties hardened gears</b>	<b>23</b>
3.1	Introduction . . . . .	23
3.2	Failure mechanisms of gears . . . . .	23
3.2.1	Macropitting . . . . .	23
3.2.2	Tooth root bending fatigue . . . . .	25
3.2.3	Abrasive wear . . . . .	26
3.2.4	Tooth flank fracture . . . . .	27
3.3	Residual stresses . . . . .	28
3.4	Optimisation of the case hardening depth . . . . .	30
3.4.1	Macropitting . . . . .	30
3.4.2	Tooth root bending fatigue . . . . .	35
3.4.3	Abrasive wear . . . . .	36
3.4.4	Conclusion . . . . .	37
<b>4</b>	<b>Laserhardening</b>	<b>38</b>
4.1	Introduction . . . . .	38
4.2	The laser . . . . .	38
4.2.1	Lasers . . . . .	38
4.2.2	Trumpf TruDisk 5001 . . . . .	40
4.2.3	BPP and $M^2$ . . . . .	41
4.2.4	Defocusing laser spot . . . . .	42
4.3	Absorption . . . . .	43
4.3.1	Laser light absorption . . . . .	43
4.3.2	Absorptance tests . . . . .	45
4.4	Types of laser hardening . . . . .	47
4.4.1	Scanning laser hardening . . . . .	48
4.4.2	Single track hardening . . . . .	53
<b>5</b>	<b>Cooling</b>	<b>57</b>
5.1	Introduction . . . . .	57
5.2	Tempering . . . . .	57

---

5.3	Simulation without Cooling . . . . .	58
5.4	Simulation with cooling . . . . .	60
5.4.1	Thermal Contact Conductance . . . . .	60
5.4.2	Simulation results . . . . .	62
<b>6</b>	<b>Setup</b>	<b>65</b>
6.1	Introduction . . . . .	65
6.2	Design . . . . .	65
6.3	Improvement of setup . . . . .	68
<b>7</b>	<b>Simulations</b>	<b>69</b>
7.1	Introduction . . . . .	69
7.2	Approximate models . . . . .	69
7.3	Heat equation . . . . .	74
7.4	Simulations in Ansys & DANTE . . . . .	74
7.4.1	Used software packages . . . . .	74
7.4.2	Carbon diffusion . . . . .	75
7.4.3	Carburization . . . . .	76
7.4.4	Laser hardening . . . . .	77
7.5	Influence of the geometry . . . . .	78
<b>8</b>	<b>Results</b>	<b>82</b>
8.1	Introduction . . . . .	82
8.2	Carbon Diffusion . . . . .	82
8.3	Carburizing . . . . .	83
8.4	Laser hardening . . . . .	84
8.4.1	Quench cracks . . . . .	87
<b>9</b>	<b>Distortions</b>	<b>90</b>
9.1	Introduction . . . . .	90
9.2	Causes of distortions in case hardening . . . . .	91
9.3	Influence on efficiency and lifespan . . . . .	92
9.4	Measurements . . . . .	93
9.4.1	Wire EDM . . . . .	94
9.4.2	Carburized ring gear . . . . .	94
9.4.3	Laser hardened gear . . . . .	95
9.5	Validation of residual stress . . . . .	96

---

9.6 Conclusion . . . . .	97
<b>10 Conclusion</b>	<b>99</b>
<b>A Technical drawing ring gear</b>	<b>107</b>
<b>B Datasheet 16MnCr5</b>	<b>109</b>
<b>C KISSsoft calculation report 16MnCr5</b>	<b>111</b>
<b>D KISSsoft calculation report 42CrMo4</b>	<b>116</b>
<b>E KISSsoft calculation report: Planet 16MnCr5, Ring 42CrMo4</b>	<b>121</b>
<b>F KISSsoft calculation report 42CrMo4 Equivalent Lifespan</b>	<b>126</b>
<b>G Technical Information Sheet Trudisk</b>	<b>131</b>
<b>H Technical Drawings Laser Hardening Setup</b>	<b>134</b>
<b>I Calculation of the required tilt angle (<math>\theta</math>)</b>	<b>141</b>
<b>J Matlab script : Model concept 1 (see subsection 4.4.2)</b>	<b>142</b>
<b>K Measurement report ring gear wire EDM</b>	<b>147</b>
<b>L Measurement report carburized ring gear</b>	<b>151</b>
<b>M Measurement report laser hardened ring gear</b>	<b>155</b>
<b>N Roundness measurement laser hardened ring gear</b>	<b>159</b>



## List of Figures

1.1	Aurora Mk II	2
1.2	Exploded view of the inwheel of Aurora Mk II	2
1.3	Geometry of the two-stage planetary gearbox	3
1.4	Gear measurements	5
1.5	Profile shift & Tip and root relief	6
1.6	Crowning	7
1.7	Nominal circumferential force ( $F_t$ ) as defined by ISO 6336	9
1.8	Resonance ratio $N$ in function of specific loading $X = (F_t \cdot K_A) : b$	11
1.9	Effect of a non-uniform tooth load with multiple meshing teeth	13
2.1	Phase diagram of carbon steel	15
2.2	Three different crystal lattices: FCC, BCC & BCT	15
2.3	Wear resistance and fatigue limit	16
2.4	Influence of carbon content on martensite	17
2.5	Jominy test results for 16MnCr5, appendix B	17
2.6	Result of carburizing before case hardening in a crankshaft	18
2.7	Carbon diffusion speed and depths	19
2.8	Comparison of temperatures in laser hardening and conventional hardening	20
2.9	Optimum hardening depth related to gear module	20
2.10	Dimension of tooth top	21
2.11	Increased hardness in top and middle of the gear tooth	21
3.1	Pitting on a spur gear	24
3.2	Tooth root bending	25
3.3	Abrasive wear	26
3.4	Rolling of tooth surfaces	27
3.5	Shear stresses in tooth flank & tooth flank fracture	28
3.6	Generation of residual stresses during laser hardening	28

3.7	Influence of residual stress on fatigue . . . . .	30
3.8	Meshing of teeth . . . . .	31
3.9	Effective & ideal normal forces on gear tooth . . . . .	31
3.10	Calculation equivalent radius planet gear . . . . .	32
3.11	Hertzian stresses ring gear . . . . .	33
3.12	Shear stresses caused by Hertzian stresses at the contact patch . . . . .	34
3.13	Stress components tooth root bending . . . . .	35
3.14	Abrasive wear & specific sliding . . . . .	37
4.1	Absorption of laserlight for different materials and wavelengths . . . . .	39
4.2	Schematic representation of a thin disk laser . . . . .	40
4.3	Laser setup at FOKUS lab . . . . .	41
4.4	BPP and Beam Quality Factor (RP Photonics Encyclopedia, 2018) . . . . .	42
4.5	Beam diameter or $1/e^2$ width . . . . .	42
4.6	Effect of increasing defocus on laser beam distribution and quality . . . . .	43
4.7	Absorption, reflection and transmission of electromagnetic waves . . . . .	44
4.8	Absorption of laser light on a rough surface . . . . .	45
4.12	Different intensity profiles . . . . .	48
4.13	Scanning laser hardening . . . . .	49
4.14	High frequency zigzag . . . . .	50
4.15	Thermal markings for different laser settings . . . . .	51
4.16	Laser path from top to foot . . . . .	51
4.17	Laser path from foot to top . . . . .	51
4.18	Laser path from side to side . . . . .	51
4.19	Tilt angle of ring gear . . . . .	53
4.20	Back tempering effect . . . . .	53
4.21	250W, 30ms, 20mm defocus . . . . .	54
4.22	Different concepts of single track hardening for different Gaussian beam diameters . . . . .	55
4.23	Clarification equation 4.7 . . . . .	56
5.1	Working principle of tempering . . . . .	58
5.2	Simulated surface temperatures . . . . .	59
5.3	Simulated temperatures at 0.3mm depth . . . . .	59
5.4	Thermal contact conductance . . . . .	60
5.5	Surface temperature at the middle (5.5a) and the top (5.5b) of the tooth flank with cooling . . . . .	62

5.6	Surface temperature at the middle (5.6a) and the top (5.6b) of the tooth flank with cooling . . . . .	62
5.7	Influence of tempering time on the hardness of a medium carbon steel . . . . .	63
5.8	Influence of alloying elements in softening retardation at 260 °C (5.8a) and at 540 °C (5.8b) . . . . .	63
5.9	Tempering effect with cooling on the adjacent tooth flank (left) after hardening the next flank (right). Hardness values in HRC. . . . .	64
6.1	Pilot laser & workbench . . . . .	66
6.2	Concept of the setup . . . . .	67
6.3	Clamping system used for cooling . . . . .	67
7.1	Modification of model to work with curved surfaces . . . . .	70
7.2	Reflection & coordinate system . . . . .	70
7.3	Diffuse reflection in tooth flank . . . . .	71
7.4	Clarification of the important parameters that influence the model . . . . .	72
7.5	3D representation of model used for concept 1 . . . . .	73
7.6	Quenching oil & used samples . . . . .	75
7.7	Simulation data for carbon diffusion . . . . .	76
7.8	Simulation data of carburization simulation . . . . .	76
7.9	Optimised hardness profile . . . . .	78
7.10	Retained austenite & maximum temperatures . . . . .	78
7.11	Temperatures at the side of the ring gear . . . . .	79
7.12	Temperature compensation principle . . . . .	80
7.13	Temperature validation . . . . .	80
7.14	Laser hardened tooth with temperature compensation (Hardness in HRC) . . . . .	81
8.1	Phases of the steel in different positions . . . . .	83
8.2	Measurements carburization (1) . . . . .	84
8.3	Measurements carburization (2) . . . . .	84
8.4	Validation laser hardening with tempering . . . . .	85
8.5	Validation laser hardening optimal setting . . . . .	86
8.6	Validation laser hardening intermediate cooling pressure . . . . .	86
8.7	Hardness measurements optimal laser settings . . . . .	87
8.8	Observed crack in the tooth root for transverse velocity of 25mm/s . . . . .	88
9.1	Residual stresses wire EDM . . . . .	91

---

9.2	Tolerances on gears . . . . .	93
9.3	Helix & profile deviation ring gear after wire EDM . . . . .	94
9.4	Helix & profile deviation ring gear after carburizing . . . . .	95
9.5	Roundness (mm) carbon diffused ring gear, without laser hardening . . . . .	95
9.6	Helix & profile deviation ring gear after laser hardening . . . . .	96
9.7	Simulation of residual stresses . . . . .	97
9.8	Oversized ring gear dimensions . . . . .	98
9.9	Laser hardened ring gear . . . . .	98

## List of Tables

1.1	Ring gear geometry . . . . .	4
1.2	Ring gear load cycles . . . . .	8
1.3	Application factors for differing machine behaviour . . . . .	8
2.1	Comparison of system service life for different gear materials in KISSsoft . . . . .	22
3.1	Optimal case hardening depth (550HV) for the different failure mechanisms . . . . .	37

## List of symbols

$a_1, a_2, a_3$	Constants used for influence of temperature on absorption	[/]
$b$	Width of the gear	[ <i>mm</i> ]
$c_{y\alpha}$	Mean value of mesh stiffness	[ <i>N/m<sup>2</sup></i> ]
$h_c$	Heat transfer coefficient of contact	[ <i>W/m<sup>2</sup>K</i> ]
$h_{gap}$	Heat transfer coefficient of gap	[ <i>W/m<sup>2</sup>K</i> ]
$h_j$	Heat transfer coefficient of joint	[ <i>W/m<sup>2</sup>K</i> ]
$k$	Thermal conductivity	[ <i>W/(m · K)</i> ]
$n_{E1}$	Resonance running speed	[/min]
$q$	Heat flux	[ <i>W/m<sup>2</sup></i> ]
$q_{contact}$	Heat through contact points	[ <i>W/m<sup>2</sup></i> ]
$q_{gap}$	Conduction heat across surface gaps	[ <i>W/m<sup>2</sup></i> ]
$q_j$	Heat through joint of two objects	[ <i>W/m<sup>2</sup></i> ]
$q_{rad}$	Radiation heat	[ <i>W/m<sup>2</sup></i> ]
$t$	Thickness of tooth	[ <i>mm</i> ]
$w_0$	Beam waist radius	[ <i>mm</i> ]
$x$	Horizontal offset	[ <i>mm</i> ]
$A$	Absorptance	[/]
$A_1, A_2, A_3$	constants in intensity distribution	[/]
$A_{70^\circ}$	Absorptance at angle of incidence equal to 70°	[/]
$A_{surf}$	Surface area	[ <i>mm<sup>2</sup></i> ]
$B_p, B_f, B_k$	non-dimensional parameter for tooth deviations	[/]
$C1, C2$	constants in temperature control	[/]
$CHD_{opt}$	Optimal case hardening depth	[ <i>mm</i> ]
$C_p$	Specific heat for constant pressure	[ <i>J/(Kg · K)</i> ]
$C_{v1}$	Factor for pitch deviation	[/]
$C_{v2}$	Factor for tooth profile deviation	[/min]
$C_{v3}$	Factor for cyclic variation in mesh stiffness	[/]
$E_{eq}$	Equivalent Young's modulus	[ <i>GPa</i> ]
$F$	Force perpendicular to tooth surface	[ <i>N</i> ]
$F_1, F_2, n$	constants in intensity distribution	[/]
$F_t$	Tangential load on tooth flank	[ <i>N</i> ]
$G$	Standard deviation of the input laser	[/]

$H$	Hardness factor	[N]
$I$	Intensity	[W/m <sup>2</sup> ]
$I_0$	Input intensity	[W/m <sup>2</sup> ]
$I_{WithRamp}$	Intensity distribution with amplitude control	[W/m <sup>2</sup> ]
$K$	Wear rate factor	[m <sup>3</sup> /m]
$K_A$	Application factor	[/]
$K_{F\alpha}$	Transverse load factor for tooth root stress	[/]
$K_{F\beta}$	Face load factor for tooth root stress	[/]
$K_{H\alpha}$	Transverse load factor for surface stress	[/]
$K_{H\beta}$	Face load factor	[/]
$KV$	Dynamic factor	[/]
$L$	Sliding distance	[m]
$M_{red}$	Reduced mass of a gear pair	[Kg/m]
$M_F$	Martensite finish temperature	[°C]
$M_S$	Martensite start temperature	[°C]
$M^2$	Beam quality factor	[/]
$N$	Resonance ratio	[/]
$N_S$	Lower limit of resonance ratio	[/]
$Q$	Removed material by wear	[m <sup>3</sup> ]
$R_{top}$	Top circle radius of ring gear	[mm]
$T_0$	Initial temperature of the to be lasered object	[°C]
$V_Y$	Transverse velocity	[mm/s]
$W$	Normal load	[N]
$W_t$	Tangential force	[N]
$X$	X-position	[mm]
$Y$	Y-position	[mm]
$Z_i$	Amount of teeth	[/]
$\alpha$	Angle of incidence	[Rad]
$\epsilon_\gamma$	Contact ratio	[/]
$\lambda$	Wavelength	[nm]
$\lambda_0$	Vacuum wavelength	[nm]
$\nu$	Poisson coefficient	[/]
$\rho_{eq}$	Equivalent radius of curvature	[1/m]
$\rho_{mat}$	Density	[Kg/m <sup>3</sup> ]
$\rho_{planet}$	Equivalent radius of planet gear	[1/m]
$\rho_{ring}$	Equivalent radius of ring gear	[1/m]
$\sigma_b$	Bending stress	[MPa]
$\sigma_{b,lim}$	Limit bending stress	[MPa]
$\sigma_{hertz}$	Hertzian stress	[MPa]
$\theta$	Inclination angle	[rad]
$\theta_0$	Divergence half angle	[μrad]

## List of abbreviations

<b>2D</b>	Two dimensional
<b>BCC</b>	Body centered cubic
<b>BCT</b>	Body centered tetragonal
<b>BPP</b>	Beam parameter product
<b>CCT</b>	Continuous cooling transformation
<b>CHD</b>	Case hardening depth
<b>CNC</b>	Computer numerical control
<b>EDM</b>	Electrical discharge machining
<b>FCC</b>	Face centered cubic
<b>FEB</b>	Formula Electric Belgium
<b>FSAE</b>	Formula Society of Automotive Engineers
<b>HAZ</b>	Heat affected zone
<b>ISO</b>	International Organization for Standardization
<b>LLK</b>	Laser light cable
<b>PMSM</b>	Permanent magnet synchronous motor
<b>RA</b>	Retained austenite
<b>SPP</b>	Spiral phase plate
<b>TTT</b>	time-temperature-transformation
<b>YAG</b>	Yttrium aluminum garnet
<b>Yb-YAG</b>	Ytterbium-doped yttrium aluminum garnet



# 1

## Introduction

### 1.1 Formula Electric Belgium

Formula Electric Belgium (FEB) is a team of 28 engineering students from KU Leuven and students automotive technologies from Thomas More. Every year, FEB builds an entirely new electric race-car in order to participate in the Formula Student competition, the largest engineering competition in the world. During these competitions, the team is put on trial on one hand by measuring the performance of the car on different dynamic events. On the other hand, the team is also scored on the basis of non-technical test, such as pitching a business plan, giving design presentations and performing a full cost analysis of the car. A year for the FEB team starts together with the academic year. The first semester is used for designing the new car. At the beginning of December all designs must be final and all technical drawings are sent out to the millers. The period from January to April is predominantly used for building and assembling every part of the car. In the month of May, testing begins. Finally, for the entire summer the team partakes in several Formula Student events. For the design and financing of the car, the team can count on a broad network of partner companies. Working together with these partners, the team members of FEB do not only work on their technical skills, they also work on their communication and soft skills. This is why FEB is a very attractive project for graduating engineers, because it is a very educational experience on more than just a technical level.



Figure 1.1: Aurora Mk II

## 1.2 Gearbox Aurora Mk II

The 2021 car, Aurora Mk II, uses four separate electrical motors for propulsion. There is one of these four motors in each wheel. In order to keep the design as compact as possible, a small three phase PMSM machine is used, connected to a planetary gearbox, as depicted in figure 1.2.



Figure 1.2: Exploded view of the inwheel of Aurora Mk II

The power of the motor is transmitted from the sun gear (1. in figure 1.3) to three different two-stage planetary gears (2. in figure 1.3). These planetary gears spin in a fixed ring gear (3. in figure 1.3). The axles around which the planetary gears spin, are connected to the hub, which in turn is connected the wheel. A detailed view of the gears is shown in figure 1.3 below.

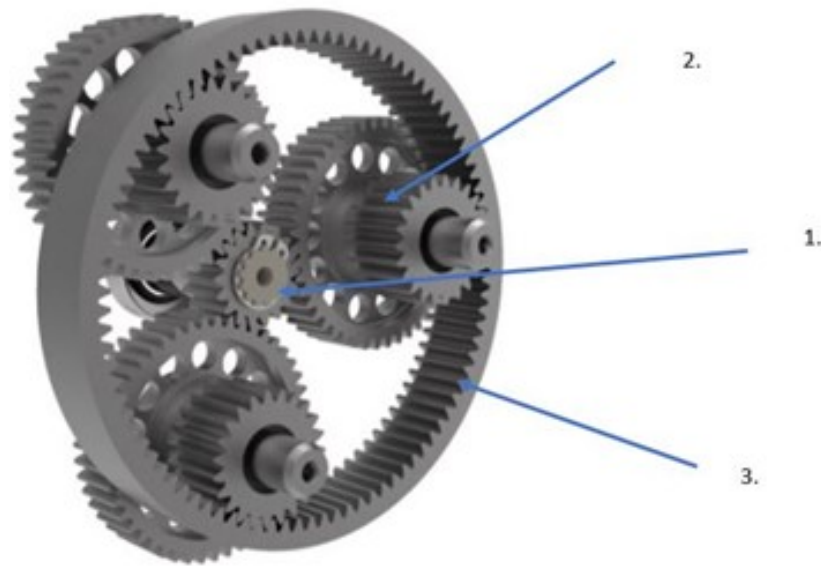


Figure 1.3: Geometry of the two-stage planetary gearbox

All gears —except for the ring gear —are produced in the following steps:

1. Turning of steel cylinder
2. Gear hobbing of tooth profile
3. Milling of weightsaving holes and slots
4. Case hardening of teeth
5. Grinding of teeth
6. Shot peening
7. Milling and wire EDM of splines

By grinding the tooth profiles after hardening, any deformations that might have occurred during or after hardening can be eliminated and the gears can be produced to a high quality. The ring gear has a different manufacturing process:

1. Turning of steel cylinder
2. Surface grinding of cylinder in order to get desired tolerance on flatness
3. Wire EDM of teeth and outside diameter of the gear. (This is done in multiple steps in order to obtain the desired roughness of the gear teeth)
4. Case hardening

Ring gear data	
Material	16MnCr5
Module	1mm
Number of teeth	90
Outer diameter	99.8mm
Width	14.8mm
Accuracy grade (ISO 1328:1995)	6
Pressure angle	20°

Table 1.1 Ring gear geometry

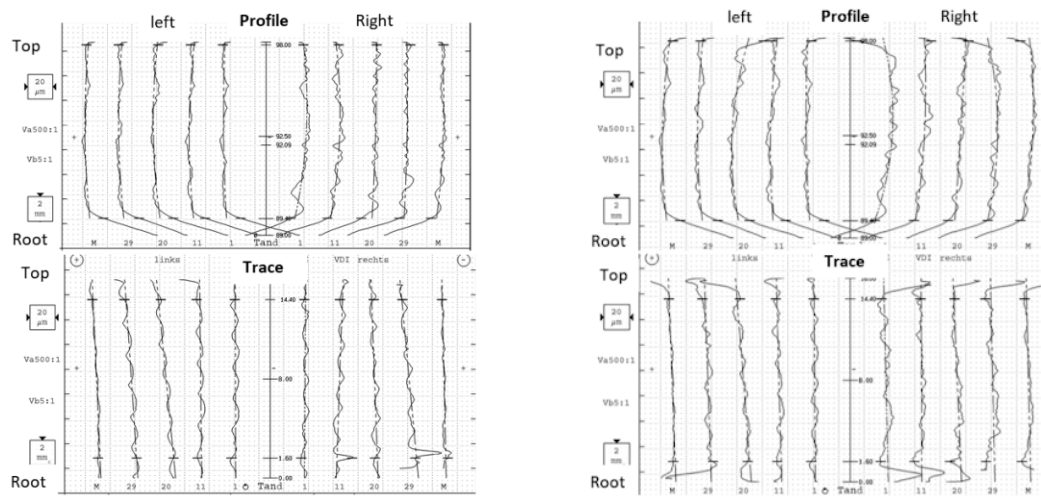
In table 1.1, the most important parameters of the ring gear geometry are provided. (For further information about the ring gear, see appendix A). Due to the rather small diameter of the ring gear and since the gearing is internal, it is nearly impossible to grind the teeth of this gear. Any deformations that occur during or after case hardening of the gear cannot be eliminated. These deformations may decrease the life expectancy of the entire gearing system. If these deformations can be sufficiently reduced, grinding of the teeth after hardening may become obsolete.

### 1.3 Objective of the thesis

The aim of this thesis is the development of the production of a laser hardened ring gear. In the past, the ring gears were hardened by case hardening, more specifically carburizing. Usually, a gear has to be grinded after carburizing because hardening causes the dimensions of the gear to be distorted. Due to the complex geometry (small pitch circle diameter & internal gearing) the ring gear used in the gearboxes of the FEB racecars cannot be grinded, thus the distortions are not eliminated. This eventually causes the entire gearbox to be underperforming. By laser hardening, it is attempted to reach the same surface hardness and hardening depth as with conventional carburizing while keeping the distortions at a minimum. Doing so, the quality of the gear can be improved, thereby increasing the performance of the entire gearbox.

### 1.4 Accuracy grade of the gear

As mentioned in table 1.1, the accuracy grade of the ring gear is quite high. Therefore it is important to check if the desired accuracy grade is attainable for a laser hardened gear. The gear measurements in figure 1.4b were taken from Bouquet (2016), where it is clear that neither the profile, nor the trace measurements exceeded  $8 \mu\text{m}$  (excluding a few peaks at the edges of the gear teeth). Since the gear studied in the research of Bouquet (2016) had much larger dimensions, it was assumed that accuracy grade 6 (according to ISO 1328:1995) should be attainable for laser hardening the ring gear. This is of course a part of the objective of this research.



(a) Gear measurements before laser hardening

(b) Gear measurements after laser hardening

Figure 1.4: Gear measurements

Source: Bouquet (2016)

## 1.5 Dimensioning Gears in KISSsoft

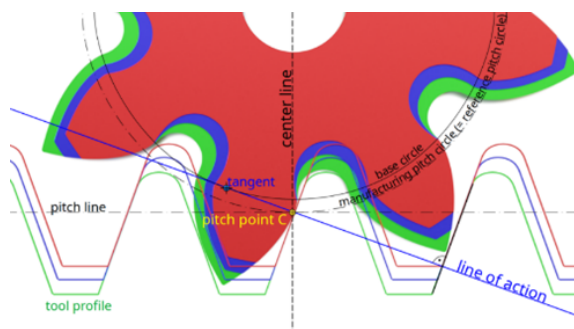
For calculating and dimensioning all different parts of the gearbox, several software packages are used. For the hub and carrier, structural simulations in Siemens NX are performed. For the upright, Siemens NX as well as Ansys is used. For the bearings, a software package from Schaeffler called BearinX is used and of course plenty of manual calculations are performed. In order to dimension the gears, a software package called KISSsoft is used. KISSsoft calculates different dimensioning parameters for a given load and basic geometry, by calculating all relevant strains and stresses (explained in chapter 3) and relating them to SN-curves of the selected materials. First of all, the basic geometry of the gear is calculated according to ISO 21771. For actual strength calculations and in order to obtain a detailed geometry for an optimal service life, ISO 6336 is used by checking for common defects (tooth root fracture, pitting, scuffing, micropitting). This standard is one of the most inclusive and detailed calculation methods currently available (KISSsoft, 2020). An overview of the used parameters in order to calculate gear geometry based on the KISSsoft 2020 Manual is provided below. (KISSsoft, 2020)

### 1.5.1 Basic Data

The basic data contains all parameters related to the geometry of the gear pair.

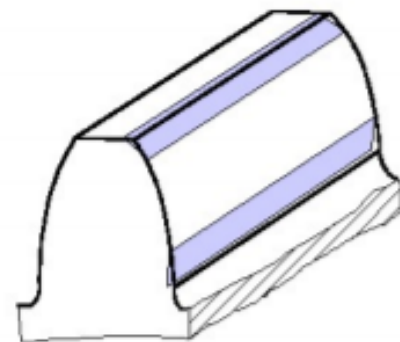
- **Normal module:** The normal module defines teeth sizing. Standard module values can be used from DIN 780 or ISO 54.

- **Pressure angle at normal section:** Usually, an angle  $\alpha$  of 20° is used. Smaller angles provide higher contact ratios (more teeth in mesh at any given moment), but decrease tooth strength. Larger angles increase tooth strength, but decrease the contact ratio and result in higher radial forces.
- **Helix angle:** This angle is set to zero in this application as noise is not an issue and the addition of high axial forces would only increase gearbox complexity and decrease gear and bearing service life.
- **Center distance:** The center distance is simply calculated from the diameters of the gear pair. However, if a profile shift is applied on one or both of the gears, this can also be taken into account from either a suggested value as defined in DIN 3992 or from an automatic tip alteration as defined in DIN 3960. The user can also define a preferred profile shift as own input instead.
- **Number of teeth:** The number of teeth is by default a whole number. Internally toothed gears have a negative value for the number of teeth as defined in ISO 221771. An undercut and the tip tooth thickness limit the minimum number of teeth.
- **Facewidth:** The facewidth is very important for the service life of a gear. A facewidth that is too small, will result in high contact pressures. A facewidth that is too large will deteriorate the contact pattern. In our application, a large facewidth is also not ideal as it makes the gear heavier. The facewidth of the pinion should always be larger than that of the gear.



(a) Profile shift

Source: tec science (2018)



(b) Tip and root relief

Source: KISSsoft (2020)

Figure 1.5: Profile shift &amp; Tip and root relief

- **Profile shift coefficient:** This coefficient is defined as the distance between the production pitch circle and the tool reference line, as demonstrated in figure 1.5a. Depending on whether

a positive or negative profile shift is performed, a thicker root with a narrower tip or a thinner tooth may be obtained. These alterations to the profile may be performed in order to obtain a stronger tooth root, a lower sliding velocity, etc. A suggested coefficient is based on DIN 3992 recommendations for well-balanced toothing. Later on, other tooth profile modifications such as tip/root relief (figure 1.5b) or crowning (figure 1.6) may be added as well depending on several load factors to be explained further in a coming section.

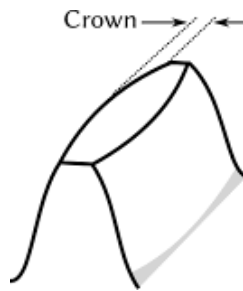


Figure 1.6: Crowning

Source: Schultz (2004)

- **Quality:** The quality of the gears takes into account that actual gear geometry differs from the theoretically desired geometry that is calculated. The higher the quality of the gears, the more narrow its tolerances will be. Increased quality also comes with increased production complexity and therefore a higher cost. However, gear quality is very important as reduced quality gears will result in the gears failing earlier, as discussed in the chapter gear failure mechanisms later on. Gear accuracy grade is according to ISO 1328.
- Furthermore there are some final details to fully define all basic data, such as the gear material, we use case-hardened 16MnCr5 as explained later in section 2.4, whether or not the gear is webbed and/or shotpeened and finally which lubrication is used (in our case 75W140 oil).

### 1.5.2 Gear Loading

A load can be entered in the calculation in order to calculate the system service life. In the past, the desired service life was set to 250 hours (Van Den Bergh and Van Assche, 2018). However, since this year's car will also be used to test the driverless system being developed at FEB, the gears have to last significantly longer so plenty of tests can be performed on the driverless system. It is important that during these tests, the gearbox and any other mechanical components are not a limiting factor in testing time. Therefore, the desired lifetime for the gearbox of Aurora Mk II is estimated at 1000 hours. Evidently, the load on the gearbox is not a constant load. The car has to perform on different dynamic events (acceleration, skidpad or figure eights, endurance,...) and has to endure many testing hours before heading to competition. This means that over its lifetime, the gearbox is loaded very dynamically. That is why the load on the gears is entered in KISSsoft

Load case	Frequency [%]	Torque factor	Speed factor
1	45	0.59	0.60
2	18	0.54	0.85
3	28	1.00	0.45
4	9	-0.70	0.60

Table 1.2 Ring gear load cycles

as a number of load cycles. For each type of load, the frequency of this load occurring is entered. Next, the average gear speed and torque (and therefore also average power) is entered for the type of load. Both speed and torque factor are entered as a percentage of the maximum speed and torque, respectively (with 1 being maximum speed/torque). The speed and torque values and their respective frequencies are based on track simulations (Aune, 2016) and team experience from the past. Values used for the load cycles can be found in table 1.2.

By combining these load cycles and their frequency with coefficients such as the dynamic factor ( $KV$ ), face load factor ( $KH\beta$ ) and transverse load factor ( $KH\alpha$ ), which will be explained in the next section, the gear lifetime can be calculated. Furthermore, an application factor  $K_A$  should be selected according to table 1.3 below. A value of 1.50 is selected.

Operational behavior of the driving machine	Operational behavior of the driven machine			
	uniform	moderate shocks	average shocks	heavy shocks
uniform	1.00	1.25	1.50	1.75
light shocks	1.10	1.35	1.60	1.85
moderate shocks	1.25	1.50	1.75	2.00
heavy shocks	1.50	1.75	2.00	2.25

Table 1.3 Application factors for differing machine behaviour

Source: KISSsoft (2020)

### 1.5.3 Determining Dynamic Factor and Load Factor

In this section the methods used for determining  $KV$ ,  $KH\beta$  and  $KH\alpha$  will be discussed, without going too much into detail as this falls beyond the scope of this thesis. The three listed coefficients all depend on a nominal tangential load, which, according to ISO 6336 (International Organization for Standardization, 2007), is the circumferential load acting on a tooth on the pitch circle and on the middle of the face width of the tooth, as depicted in figure 1.7 below, where  $F_t$  is the load in question. This load is used in as a calculation load for these factors as follows:

1. The dynamic factor  $KV$  uses the load  $F_t$  and application factor  $K_A$  as follows:  $F_t * K_A$
2. The face load factor  $KH\beta$  uses the load  $F_t$ , application factor  $K_A$  and the dynamic factor  $KV$  as follows:  $F_t * K_A * KV$



3. The transverse load factor  $KH\alpha$  uses the load  $F_t$ , application factor  $K_A$ , the dynamic factor  $KV$  and the face load factor  $KH\beta$  as follows:  $F_t * K_A * KV * KH\beta$

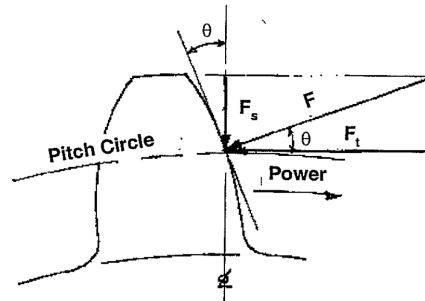


Figure 1.7: Nominal circumferential force ( $F_t$ ) as defined by ISO 6336

Source: Gopsill (nd)

### 1.5.3.1 Dynamic factor $KV$

The dynamic factor  $KV$  in this application should actually be defined as  $KV_B$ , since method B of ISO 6336 is used for determining this factor here.  $KV_B$  takes into account any dynamic loads or vibrations due to the relation between speed and load and the gear tooth accuracy. Factors to take into account are both related to manufacturing as well as design. The design of the gears determine the pitchline velocity, the tooth load and the inertia of the gears. Not only gear design, but the design of the entire gearbox is important, since the stiffness of the bearings, axles etc and the lubrication used can all cause different vibrations in the system. Due to limited accuracy in manufacturing of the gears, there might be deviations in the pitch, tooth flank or there might be runout on reference surfaces such as the tip or root circle. Besides that, balance of the gears as well as axles and bearings and fit of the bearings can all be taken into account.

When certain natural frequencies are present in the gearing system, it is to be avoided that any excitation frequencies (such as the frequency of meshing teeth) are the same or nearly the same as any of these natural frequencies. These natural frequencies depend on the design choices and manufacturing accuracy as mentioned above, since the dynamic response of the system is dependent of the mass as well as the stiffness of any gearbox components. It also depends on the damping in the system due to any friction in bearings and seals, but also on hysteresis (non-linearity in the stress-strain curve of the materials used) in shafts and on any viscous damping on lubricated sliding components. Ideally, the kinematics of a gear pair have a constant ratio between input and output rotations. Deviations in this ratio (the rotation of one gear not corresponding to the rotation of the other times the ratio) determine the vibration frequencies. These deviations can be due to:

1. A deviation in the pitch line velocity due to inaccuracies on the actual pitch circle of the gear.

2. Variation of the stiffness of the gear throughout the meshing cycle. This variation becomes less significant as the contact ratio rises. The ring and planet gear have a rather low contact ratio (about 1.7), so these variations have to be taken into account. Due to limitations in size of the gearbox, a module lower than 1 could be desirable, for example a module of 0.7. However, the gear manufacturer that FEB works with is not able to go any lower than module 1.
3. Variations in tooth loading will cause the gear to deflect further or back, which can also cause vibrations. It is possible to design gears in such a way, that for a certain load, the deflection is constant. However, since this application has a highly dynamic load, this is not possible in our application.
4. Finally, any unbalances in the gears or shafts, any contaminants in the lubrication system, any misalignment of the shafts and gear friction can all contribute to vibrations in the system.

In order to determine whether or not a pair of gears will cause vibrations due to resonance, the running speeds range should be compared to the resonance running speed. According to method B of ISO 6336-1 6, the resonance running speed is determined with formula 1.1:

$$n_{E1} = \frac{30000}{\pi z_i} \sqrt{\frac{C_{y\alpha}}{m_{red}}} \quad (1.1)$$

- With  $C_{y\alpha}$  being the mean value of mesh stiffness per unit face width (determined in ISO 6336-1 9) ( $N/m^2$ )
- With  $z_i$  being the amount of teeth
- $M_{red}$  being the reduced mass of a gear pair, for the calculation of this factor see International Organization for Standardization (2007) (Kg/m)

With  $n_{E1}$  now known, the resonance ratio  $N$  can be determined, which is the ratio of pinion speed to resonance speed, as follows:

$$N = \frac{n_1}{n_{E1}} \quad (1.2)$$

With  $n_1$  being the speed the gear is used at (/min).

Next, the range of speeds in which our gears work has to be determined. In order to do so, the lower limit of resonance ratio  $N_S$  has to be known. At loads where  $(F_t * K_A / b)$  is less than 100  $N/mm$ ,  $N_S$  can be determined as follows:

$$N_S = 0.5 + 0.35 \sqrt{\frac{F_t K_A}{100b}} \quad (1.3)$$

With  $b$  being equal to the width of the gear (mm)

If  $(F_t K_A / b)$  is equal to or greater than  $100 \text{ N/mm}$ , a value of 0.85 is chosen for  $N_S$ . (Note that since calculations are being made on the pinion,  $F_t$  should be divided by three as this is a planetary system!). From the resonance ratio and its lower limit, the range in which the set of gears is working can be known. There are four possible ranges, as shown in figure 1.8 below.

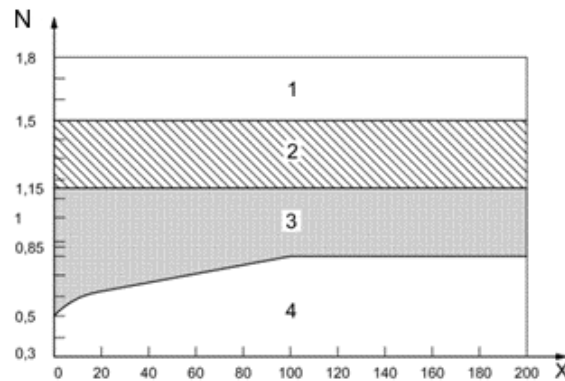


Figure 1.8: Resonance ratio  $N$  in function of specific loading  $X = (F_t \cdot K_A) : b$

Source: International Organization for Standardization (2007)

1. Supercritical range ( $N \geq 1.5$ ): this range is only for very accurate gears due to the very high speeds. Resonance peaks can occur at  $N = 2, 3, \dots$ , but the vibrations will often have small amplitudes.
2. Intermediate range ( $1.15 < N \leq 1.5$ ): this range requires a refined analysis by Method A, since it is close to the main resonance range, but might be fine in some applications.
3. Main resonance range ( $N_S < N \leq 1.15$ ): this zone should be avoided (especially with spur gears) since rather strong vibrations are very likely to occur. Only very high accuracy gears can be used, spur gears should have profile modifications accordingly.
4. Subcritical range ( $N \leq N_S$ ): in this range, resonances may occur at  $N = 1/2$  and  $N = 1/3$ . However, this can quite easily be solved with suitable profile modifications. Our application can also be situated in this range.

Since the used gear application is working in the subcritical range,  $KV$  can be determined as follows:

$$KV = (N \cdot K) + 1 \quad (1.4)$$

$$K = (C_{v1} \cdot B_p) + (C_{v2} \cdot B_f) + (C_{v3} \cdot B_k) \quad (1.5)$$

where

- $C_{v1}$  allows for pitch deviation effects and is assumed to be constant at  $C_{v1} = 0.32$

- $C_{v2}$  allows for tooth profile deviation effects. For a total contact ratio  $1 < \varepsilon_\gamma \leq 2$  a value of 0.34 is used. With  $1 < \varepsilon_\gamma \leq 2$  being equal to the contact ratio.
- $C_{v3}$  allows for the cyclic variation effect in mesh stiffness. For a total contact ratio  $1 < \varepsilon_\gamma \leq 2$  a value of 0.23 is used.
- $B_p, B_f$  and  $B_k$  are non-dimensional parameters to take into account the effect of tooth deviations and profile modifications on the dynamic load and will not be discussed any further.

### 1.5.3.2 Face load factors $K_{H\beta}$ and $K_{F\beta}$

The face load factors include the effects of an uneven load distribution over the gear face width into the calculations.  $K_{H\beta}$  is the face load factor for contact stress and takes into account the surface stress on the face width.  $K_{F\beta}$  is the face load factor for tooth root stress and takes the tooth root stress into account, which will also depend on the load distribution over the gear face width.

- $K_{H\beta}$  can be defined as

$$K_{H\beta} = \frac{\text{maximum load per unit face width}}{\text{average load per unit face width}} = \frac{(F/b)_{max}}{F_m/b} \quad (1.6)$$

- With  $F_m/b = (F \cdot K_A \cdot K_V)/b$
- $K_{F\beta}$  depends on the ratio  $b/h$  (face width/tooth depth) and on the determined value of  $(F/b)_{max}$ .

Some of the most important influential factors on the load distribution over the face width are the following:

1. Accuracy of both the gear tooth manufacturing and the alignment of the axes
2. Elastic deformations of gearbox elements
3. Thermal deformations
4. Running-in effects
5. Application factor  $K_A$  and dynamic factor  $K_V$
6. Centrifugal deflections due to operating speed
7. Gear geometry such as crowning

In the application, both face load factors are determined according to method B, which means that an iterative method is used with the help of computer aided calculations. Elastic deflections under load, static displacements and the stiffness of the entire system are to be accounted with. The effective stiffness used, largely depends on gear mesh, gear body and the stiffness of the shafts, shaft/hub connections, bearings, housing and foundation. Static displacements include thermal expansions, possible clearances and loose fits and manufacturing errors. The exact algorithm/method is not given in ISO 6336-1, but most of the relevant influential factors are given above.

### 1.5.3.3 Transverse load factors $K_{H\alpha}$ and $K_{F\alpha}$

The transverse load factors  $K_{H\alpha}$  and  $K_{F\alpha}$  (for surface stress and tooth root stress respectively) take into account the effect of a non-uniformly distributed tooth load when several gear teeth are in mesh simultaneously, as depicted by figure 1.9. The factors are defined as the maximum tooth load ratio between an actual gear pair and theoretically perfect gear pair near zero speed. These factors can be determined graphically and are mainly influenced by the following factors:

- Deflections under load.
- Profile modifications.
- Tooth manufacturing accuracy.
- Running-in effects.

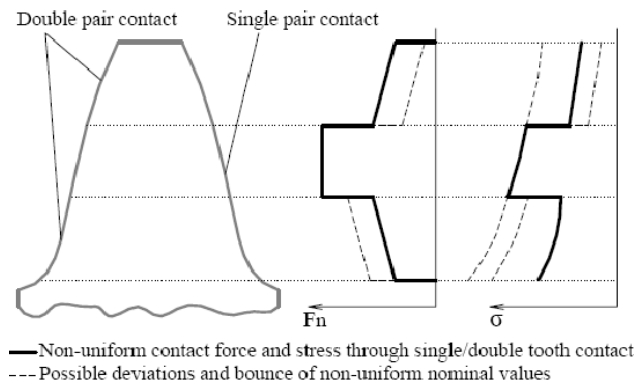


Figure 1.9: Effect of a non-uniform tooth load with multiple meshing teeth

Source: Milojevic (2013)

### 1.5.4 Calculation Results

A full KISSsoft calculation report can be found in appendix C. The next chapter will explain how gears are hardened. Later, in chapter 3, the relation between hardening and service life is elaborated upon.

# 2

## Hardening steel

### 2.1 Introduction

In this section the working principles of hardening steels are discussed shortly. The influence of hardening steel on strength, fatigue failure and other mechanical properties of the material are also be discussed in this chapter. Finally, the technique of case hardening and carbon diffusion in steels will be explained.

### 2.2 Mechanism of hardening steel

It is very common to perform heat treatments on steel in order to obtain desired material properties. Hardening is therefore also a very common practice in the industry. In order to transform a soft steel work piece into a hardened work piece (or to give the workpiece a hardened layer), first of all, the workpiece needs to be heated. It is important to heat the steel above the austenization temperature, as shown in figure 2.1 below, for a sufficient amount of time. This time is needed for the carbon atoms present in cementite to diffuse through the iron atoms once the austenitization temperature has been reached. The goal is to create uniform austenite, which has an FCC (Face Centered Cubic) lattice. In austenitic steel, the carbon and iron form what is called a solid solution: carbon atoms are 'dissolved' in the steel, as there is space for the carbon atom in the centre of the iron FCC elements as depicted in figure 2.2 below. The formation of austenitic steel is the first desired step in order to harden steel.

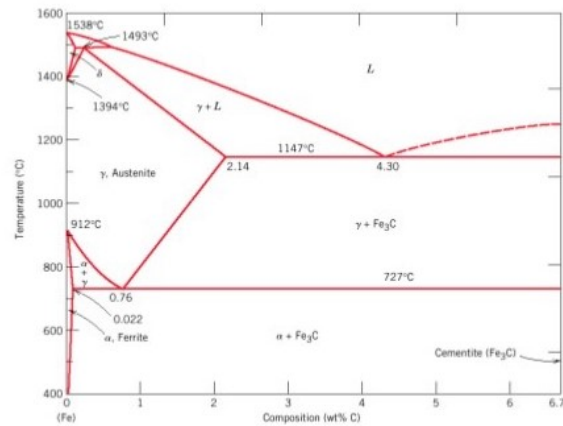


Figure 2.1: Phase diagram of carbon steel

Source: YenaEngineering (2019)

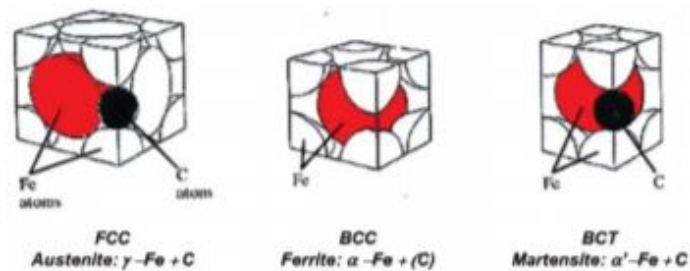


Figure 2.2: Three different crystal lattices: FCC, BCC &amp; BCT

Source: Brog et al. (2013)

Now, slow cooling of the steel corresponds to moving down on the phase diagram. As the steel cools down, different nuclei of ferrite will be formed. Ferrite has a BCC (Body Centered Cubic) lattice, therefore, solubility of carbon in interstitials of the lattice is very low. Because of its low solubility in ferrite, the carbon atoms diffuse away from the ferrite zones. As the steel cools down further, the carbon concentration around the ferrite zones becomes higher. Eventually, a point is reached where ferrite will no longer be formed, but cementite, an iron carbide, will start to develop. Cementite has a high carbon content of 6.67wt%. Once the part is cooled down entirely, a lamellar structure of cementite and ferrite, called pearlite, is formed. By cooling down slowly, the same structure (and therefore the same properties) as the original steel is obtained. This is true when the effect of grain growth or refinement during heating and cooling is neglected.

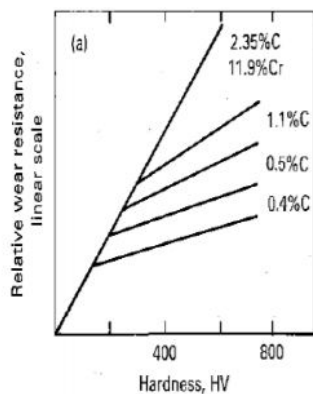
In order to harden the workpiece, a more radical approach needs to be used. By rapidly cooling—or quenching—the desired hardness can be achieved. When the steel is rapidly cooled, the carbon does not have enough time to diffuse away from the iron atoms to form ferrite. A different

structure, namely martensite, will be formed. Martensite has a BCT (Body Centered Tetragonal) lattice, which is very similar to a BCC structure, however in the BCT lattice there are carbon atoms dissolved in the lattice. The relatively high amount of carbon atoms in the structure cause many dislocations to form. These dislocations in the material are what makes martensite such a hard structure, however it is also the cause of the brittle behaviour of martensite.

### 2.3 Properties of hardened steels

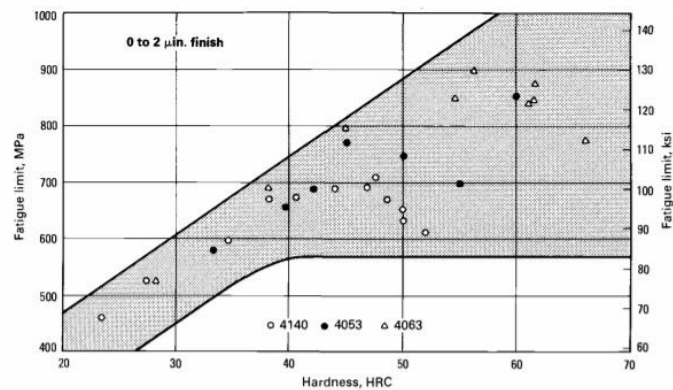
As mentioned above, martensite is a very hard material. The hardenability of martensite increases with increasing carbon content, as illustrated in figure 2.4b. This hardness is desirable for a number of reasons. First of all, a higher hardness provides greater wear resistance, as illustrated in figure 2.3a below. On top of that, an increased hardness also increases the fatigue limit of the material, as shown in figure 2.3b. A downside of the high hardness of martensite, is that it is very brittle and not very impact resistant.

There are methods to compensate these shortcomings. One of the most common methods is tempering. Tempering a hardened part means that it is heated again after hardening in order to transform some of the formed martensite to pearlite or bainite.



(a) Wear resistance in function of hardness for steel

Source: Klenam (2012)



(b) Fatigue limit in function of hardness for through hardened and tempered steels

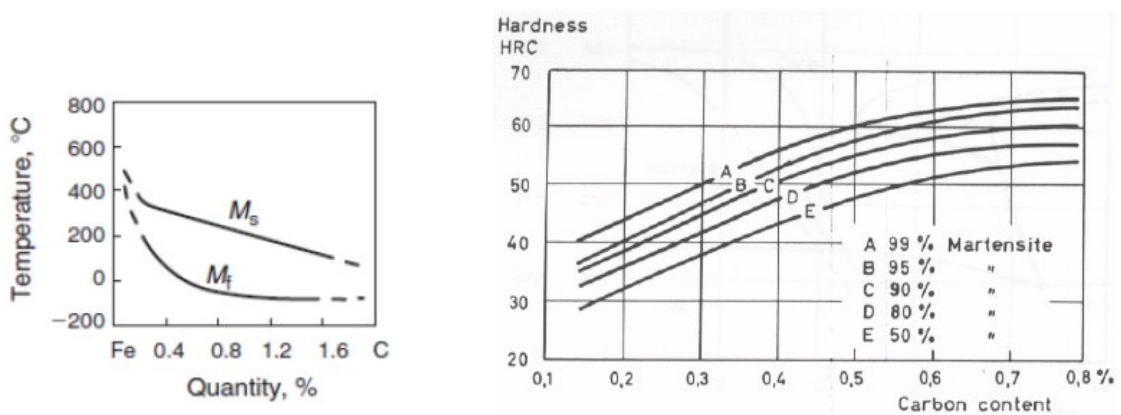
Source: Boardman (1990)

Figure 2.3: Wear resistance and fatigue limit

Another phenomenon that can alleviate the problem of brittle martensite, is retained austenite (RA). In steel alloys with a carbon content higher than 0.30wt%, the martensite finish temperature —the temperature that the steel needs to be cooled to in order to obtain 100% martensite —is below room temperature as illustrated by figure 2.4a (Herring, 2005). This means that the steel needs to be cooled below room temperature and often below 0 °C to get a structure consisting of 100% martensite. If the steel is not cooled sufficiently far, retained austenite is formed. Since austenite normally does not occur at temperatures below the austenitization temperature, retained austenite



is a metastable phase. In contrast to martensite, retained austenite is quite soft and ductile. At first sight, formation of retained austenite sounds problematic. Especially in applications where dimensional stability is of high importance and the maximum attainable hardness is desired, retained austenite can significantly reduce the performance of hardened steel parts. In the tool and die industry, RA is even recognised as a major cause for premature failure. However, in some applications, RA can be beneficial for performance of hardened parts. In gears for example, the ductility of RA can alleviate the problem of spalling (progressive macropitting). If the RA content is not too high and the RA grains are finely dispersed, crack initiation can be retarded and crack nucleation can be prevented by the fine, ductile RA grains. A more in depth explanation of gear failure mechanisms and its link to the material properties can be found in chapter 3.



(a) Martensite start and finish temperature related to carbon content

Source: Grum (2004b)

(b) Hardness of martensite as a function of carbon content

Source: Zhang et al. (2007)

Figure 2.4: Influence of carbon content on martensite

## 2.4 Case hardening

### 2.4.1 Carburizing

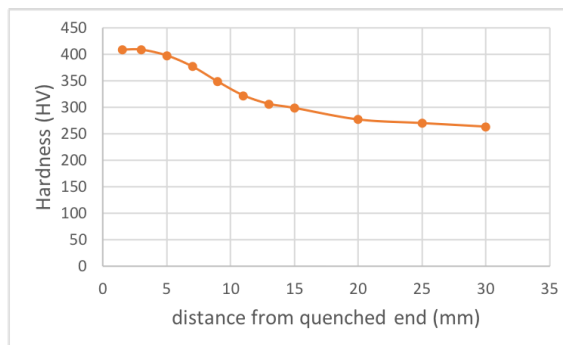


Figure 2.5: Jominy test results for 16MnCr5, appendix B

The ring gear in the gearbox of FEB is made from a low-carbon alloy, 16MnCr5, of which a datasheet —provided by FEB partner Grimonprez Transmission Gears —can be found in appendix B. 16MnCr5 is often used in high-stress mechanical applications such as gears and shafts and is selected due to its high ductility and toughness. Since it has a low carbon content (about 0.16 wt%), conventional hardening techniques do not deliver satisfying results, as the hardenability of low alloy steels is generally quite low. A standard test for measuring the hardenability of steels, is the Jominy test. Results for the jominytest are provided in figure 2.5. With a maximum hardness of about 400HV for standard 16MnCr5, it is quite clear that the desired hardness cannot be reached with the material if left as standard. For the hardening of these types of steel, case hardening is used. In the past, the ring gear has always been carburized and then quenched to achieve a high surface hardness, while retaining the original toughness in the core.

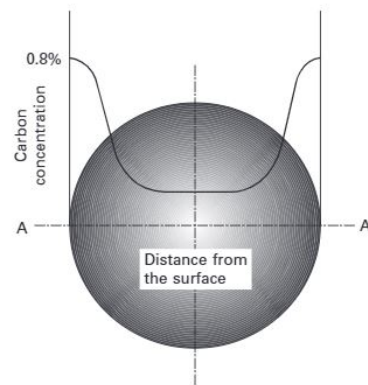
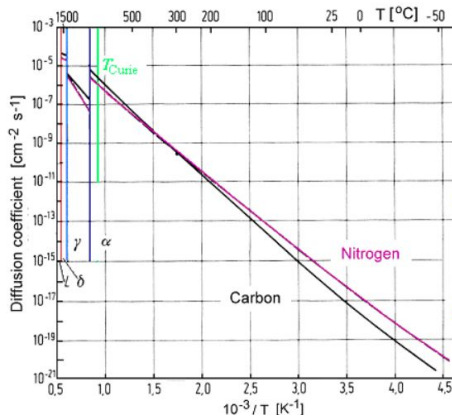


Figure 2.6: Result of carburizing before case hardening in a crankshaft

Source: Yamagata (2005)

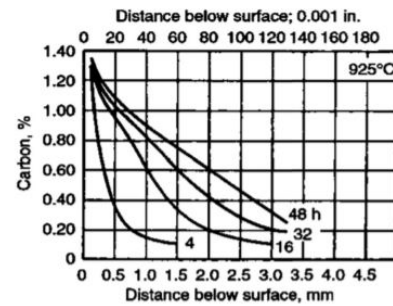
When carburizing a part, it is heated in a furnace and brought up to austenization temperature. In the furnace, the workpiece is surrounded by a high carbon atmosphere, this can be in either gaseous or solid form. Raising the temperature above the austenization temperature, not only forms austenite, but also accelerates the diffusion of carbon in steel, as we can see in figure 2.7a below. By increasing the carburizing time, carbon can diffuse further into the steel. Figure 2.7b shows the carburization depth in 16NiCr4 —also a case hardening steel —steel for a temperature of 925 °C in pack carburizing. It is clear that the longer the components is carburized, the deeper the carbon will have diffused. Carbon concentrations in the material always become higher moving closer to the edge of the material. In pack carburizing, the edge of the material will always contain a carbon concentration at the saturation limit of carbon in austenite (about 1.3 wt%). When gas carburizing, the carbon content in at the edge of the material can be kept lower by lowering the carbon concentration in the atmosphere of the furnace (Neelam, 2000). By quenching the workpiece after carburization, the carbon diffused in the outer layer (case) of the part will be 'trapped' in the austenite because of the high cooling rate close to the edges of the part. Martensite (and possibly retained austenite) will be formed at the edges of the part. The core of the workpiece will cool down

much slower, so there will no longer be martensite formation from a certain distance of the edges, depending on the cooling rate while quenching. That is why a tough, softer core with a hardened case can be obtained.



(a) Diffusion speed of carbon and nitrogen in steel in relation to temperature

Source: Föll (2019)



(b) Depth of carbon diffusion by pack carburizing in 16NiCr4 steel

Source: Hosseini and Zhuguo (2016)

Figure 2.7: Carbon diffusion speed and depths

## 2.4.2 Laser hardening case hardening steel

As explained in the first chapter, the goal of this thesis is to harden the ring gear using a laser. A benefit of laser hardening is that the heating time is very limited, since lasers can provide a lot of energy in a very short pulse. The benefit here is that the time the material that is to be hardened spends above the austenization temperature, is quite short, not allowing the austenite grains to grow large. Large austenite grains can lower the toughness of the hardened section of the gear and can promote brittle fracture (Li et al., 2014). However, because low alloy steel needs a carburizing step before hardening, this advantage is lost in the application of laser hardening the ring gear. It is not possible to place the laser in a carbon environment nor is it possible to harden with a laser in a high temperature environment as the principle of laserhardening relies on self-quenching (as explained later in chapter 4). In order to harden the ring gear with a laser, the carbon diffusion needs to be performed in a separate step, where austenite grains can grow larger. Usually, when carburizing, the furnace temperature is kept just above the austenization temperature, in an effort to keep austenite grain growth to a minimum. In industrial applications, reheating and quenching or even double reheating and quenching of the workpiece after it has been carburized and cooled down is used for die quenching for example (Canale et al., 2008). It is important to note that when laser hardening, the material needs to be heated to a higher temperature in comparison with classic carburizing/hardening, as illustrated by figure 2.8. When carburizing, the workpiece is kept above the austenization temperature for a sufficient amount of time to form homogeneous austenite. When laser hardening, the temperature of the surface is heated up for a very short time. However,

to obtain homogeneous austenite when heating from room temperature, the carbon needs time to diffuse from the cementite structure to the interstitials in the FCC austenite. As mentioned above, the diffusion speed of carbon in steel increases with increasing temperature, therefore we need to heat the layer we want to harden sufficiently higher than the austenization temperature ( $A_3$ ).

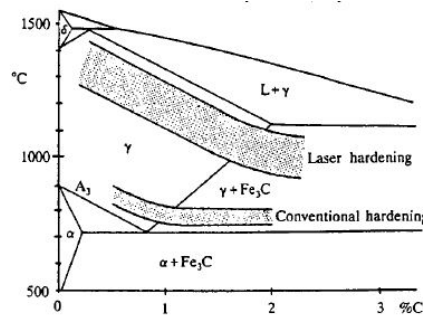


Figure 2.8: Comparison of temperatures in laser hardening and conventional hardening

Source: Meijer and Van Sprang (1991)

As mentioned earlier, carburization depth is dependent of time and temperature. Since hardenability of a material is mostly related to its carbon content, the effective hardening depth —the depth at which there is a hardness of 550 HV —is also strongly dependent of the carburization depth. From the calculations in KISSsoft, an optimum surface hardness of 60 HRC and a case hardening depth of 0.3mm is determined. If we compare this value to optimum values from ISO6336 in figure 2.9, it can be concluded that this is a reasonable depth. Therefore this value of 0.3mm effective hardening depth was passed on to the company that would perform the carbon diffusion on the ring gears in order to determine the furnace parameters. (Carburization was performed in a pack carburizing furnace). Because of the significant lead times on these parts, this value needed to be determined quite early in the year after limited research time. There are however some important sidenotes to make in relation to this hardening/diffusion depth.

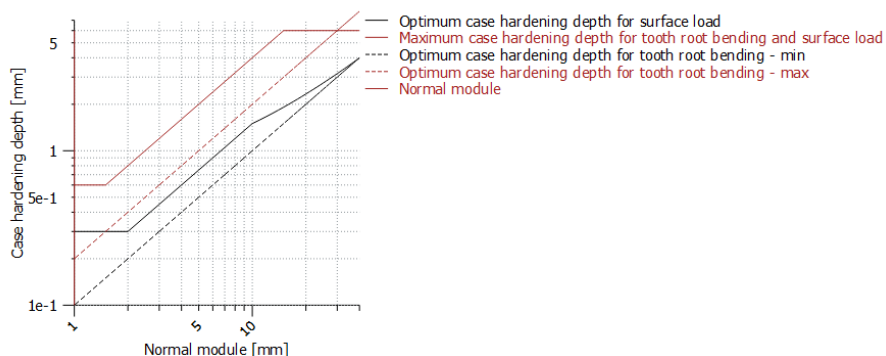


Figure 2.9: Optimum hardening depth related to gear module

Source: International Organization for Standardization (2007)

- Looking at the tip of the gear tooth, see figure 2.10, one can see that a hardening depth of 0.3mm would mean that almost the entire tip of the gear would be hardened, this is of course not ideal, so it is important to limit the heating in the tip of the tooth so the hardening depth is limited there. If too much heat were to be added, the entire tip of the gear would harden because the diffusion of carbon happens not only at the tooth flanks, but also at the tip.

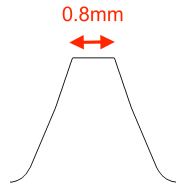


Figure 2.10: Dimension of tooth top

- Due to the small dimensions of the gear tooth the cooling rate after carburizing (even without quenching) can be quite high. Therefore, especially in the top and middle region of the teeth, a hardness increase might be observed. This increase is not only due to an increase in cementite because of the higher carbon content, but also because the pearlite grains might be quite fine compared to the original grain size before carburizing, which increases the hardness of the material.

The hardness increase in the top and middle of the teeth was observed during testing and is shown in figure 2.11b below. The influence of hardening depth and geometry are discussed in further detail in chapter 3.

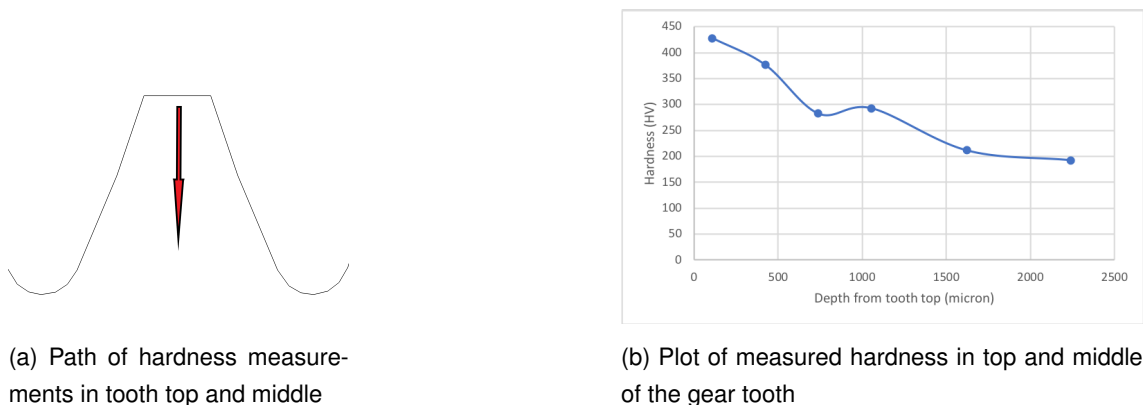


Figure 2.11: Increased hardness in top and middle of the gear tooth

### 2.4.3 System service life in relation to steel type

The hardening effects of carburizing before laserhardening can be quite significant. However, the toughness of case-hardened 16MnCr5 really is necessary in the application of a Formula Student gearbox. If a steel with a higher carbon content were to be used to make carburizing obsolete, the

System Service Life			
Material	Both 16MnCr5	Both 42CrMo4	Ring gear 42CrMo4, planet gear 16MnCr5
Tooth root service life (h)	1394	30	104
Tooth flank service life (h)	8.25e+04	407	1593
System service life (h)	1394	30	104

Table 2.1 Comparison of system service life for different gear materials in KISSsoft

increase in size and weight of the gears would be far from competitive compared to other Formula Student teams. In order to make a comparison, KISSsoft simulations for an alloy that is often used for laser hardening were conducted, 42CrMo4. The full calculation reports can be found in appendices C, D and E, a comparison of the system service lives can be found in table 2.1.

It is evident from the table that gears from 42CrMo4 would fail much too early if the same gear dimensions are used. Calculations with larger gear dimensions in order to obtain the required service life with 42CrMo4 gears were performed. The calculation report can be found in appendix F. The difference in mass between the 16MnCr5 gears and the 42CrMo4 gears calculated was over 20% higher in favour of 16MnCr5. This difference in mass is only due to the increase in gear size. Increases in size (and therefore weight) of axles, housing, bearings, etc. were not considered in the calculation. If these increases in mass would also be held into account, the mass difference would be even higher. Such a substantial increase in weight cannot be justified on a racecar where weight is one of the most important criteria for performance. From the service life and mass calculations, it can be concluded that the toughness of a carburizing alloy is needed for this compact application.

The next chapter will explain failing mechanisms in gears and their relation to the material properties of the alloy used. The relation between case hardening depth and prevention of mechanical failure is also elaborated upon.

# 3

## Mechanical properties hardened gears

### 3.1 Introduction

The purpose of a racecar is to complete a lap in the least amount of time. Because of this, the FEB team is always search for the best performing parts. Specifically for the gearbox the trade-off between weight and lifespan has to be made. In the upcoming section, this optimum and the reasoning behind it is explained.

### 3.2 Failure mechanisms of gears

Because of the complex geometry of a gear and the way its laoad are applied, gears have certain diverse failure mechanisms. The 4 most common are (Kren, 2007):

- Macropitting
- Tooth root bending fatigue
- Wear
- Tooth flank fracture

#### 3.2.1 Macropitting

The purpose of gears is to transmit torque. This is done by transmitting contact forces on the tooth flanks. These contact forces will introduce hertzian stresses on the surface and shear stresses

deeper in the material under the contact patch.

$$\sigma_{hertz} = \sqrt{\frac{F \cdot E_{eq}}{2 \cdot \pi \cdot (1 - \nu^2) \cdot b \cdot \rho_{eq}}} (MPa) \quad (3.1)$$

In which  $F$  is the force acting between the 2 surfaces,  $E_{eq}$  the equivalent Young's modulus of the 2 used materials,  $\nu$  the poisson coefficient,  $b$  the width of the contact and  $\rho_{eq}$  the equivalent radius of curvature at the contact (Wittel et al., 2016)

Due to the involute tooth geometry the equivalent radius of curvature depends on the angle of rotation of the gear itself. Because of this, the contact stresses will also differ, meaning that pitting is more likely to occur in particular regions of the tooth flank. Besides that, the contact stresses are also dependent of the meshing stiffness, contact ratio and tooth profile modifications of the gear pair. In an upcoming section (3.4.1), this is explained in more detail.

The material of the gear has a certain fatigue limit for Hertzian stresses. When the gear's tooth flank goes through too many cycles, fatigue will occur and thereafter small cracks will occur at the surface or right below it (Edge, 2021). When the crack occurs beneath the surface and the loads are applied continuously the crack will move to the surface, as can be seen in figure 3.1. At this point some of the material is lost resulting in vibrations of the meshing gears. These vibrations will only increase the loading on the gear which will result in failure of the gear. It can also occur that the tooth will fail due to tooth root bending after pitting has damaged the surface. Due to the pitting damage, the load on the tooth flank increases, which may overload the tooth root, causing it to fail. The occurring Hertzian stress is also highly dependent on the surface roughness of the tooth flanks, the oil film thickness and any debris in the oil. All of these can cause the force to be transmitted over a much smaller surface thus increasing the Hertzian stress.

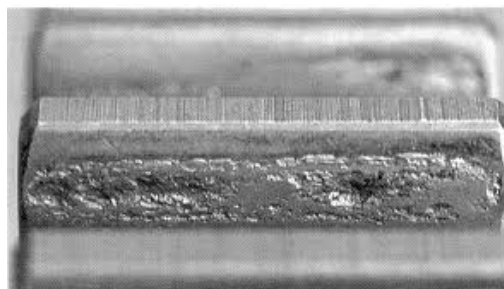


Figure 3.1: Pitting on a spur gear

Source: Corporation (2011)



### 3.2.2 Tooth root bending fatigue

The load coming from the meshing gears does not only induce a contact stress in the contact patch and its surroundings, it also generates a moment around the tooth root, which in turn results in a bending stress in the tooth root.

A good approximation of this stress can be made with simple strength theory.

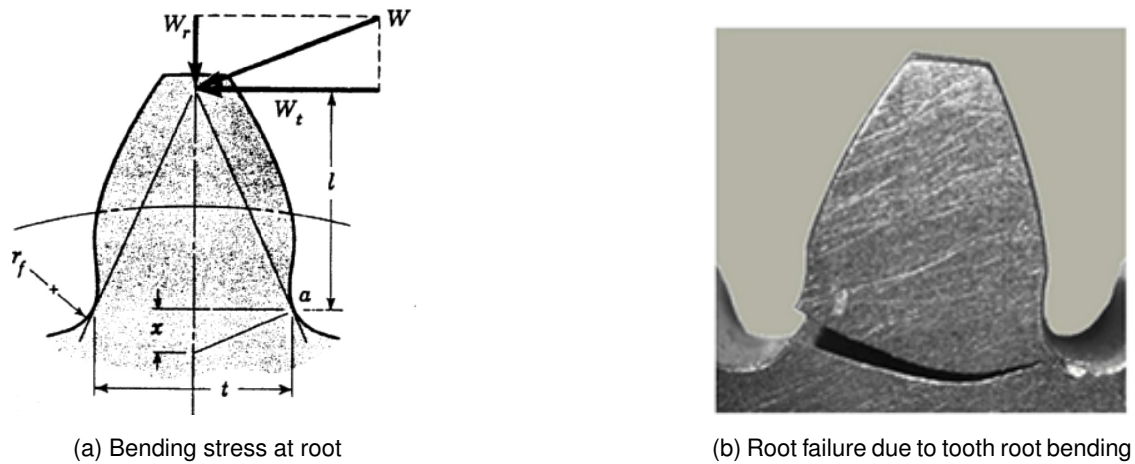


Figure 3.2: Tooth root bending

Source: Akpolat (2018)

$$\sigma_b = \frac{W_t \cdot l \cdot \frac{t}{2}}{\frac{b \cdot t^3}{12}} (MPa) \quad (3.2)$$

With  $b$  being the width of the gear. The rest of the parameters can be derived from figure 3.2a

The tooth root bending stress then has to be related to the fatigue bending stress at the root to determine how long the tooth root will last. When the fatigue strength is reached, cracks will begin to occur at the root. These cracks will propagate further down the depth of the material with every cycle, generating beach marks. When the crack has become too great in size, the rest of the root will break in a brittle manner.

Although the formula above can give a good first indication on the magnitude of the stress, this stress is also highly dependent on the way the load is applied and the gear geometry itself. For example, the contact ratio and meshing stiffness are very important factors to consider when determining the maximum bending stress in the root. The reason why these are so important will be explained in section 3.4. All these influences can be summarized in the so called K- and Y-factors.

$$\sigma_{b,lim} \geq (\sigma_b \cdot \sum K) \cdot \sum Y \quad (3.3)$$

If the above equation is satisfied, the tooth root will in theory not fail due to the bending for an infinite amount of cycles.

### 3.2.3 Abrasive wear

Like pitting, wear is a mechanism in a gear that takes place at the contact patch of the meshing teeth. Abrasive wear arises from the roughness of the mating teeth. The roughness peaks on one gear will scrape material from the second gear and vice versa.

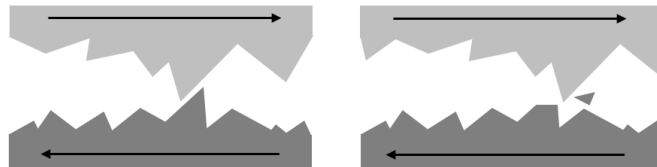


Figure 3.3: Abrasive wear

Source: FailureAtlas (2020)

The debris that ends up in the oil of the gearbox will in its turn also end up in the oil film between the meshing gears, resulting in even more wear. However, wear is normal when two gears are being meshed for the first time. This period is called the run-in period of a gearbox. During this period, the oil should be refreshed periodically. Wear can also occur after the run-in period depending on the finishing of the gear and other factors. The thickness of the oil film is very important here. In well operated gearboxes, there will always be a thick enough oil film between the meshing teeth such that there is no metallic contact between the two flanks, resulting in quasi none abrasive wear. The pitch line velocity and load on the tooth flanks of the gear pair have a great influence on the thickness of the oil film and therefore also on the amount of wear (Chitta, 2012).

The amount of wear can differ a lot depending on the location on the tooth flank. Based on figure 3.4 it is easy to see that the teeth have a relative speed at the contact patch. This relative speed is also called the sliding velocity. It is important to state here that the sliding velocity at contact on the pitch line is zero, the tooth flanks will only roll over each other in this point. Flodin (2000) proposed that when the sliding velocity is increased, the material will locally interact with more asperities compared to if the sliding velocity were lower. As a result of this, the tooth surface will wear the most where specific sliding is the greatest.

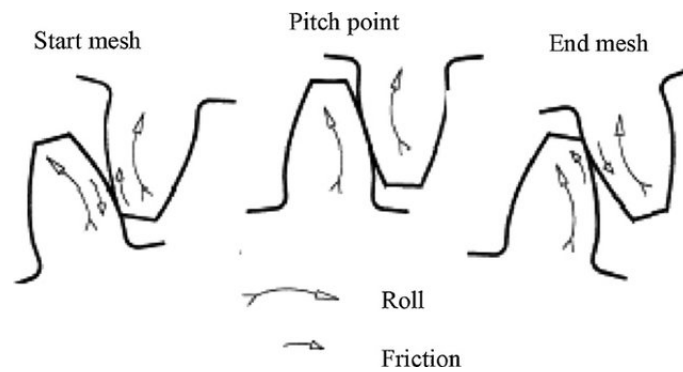


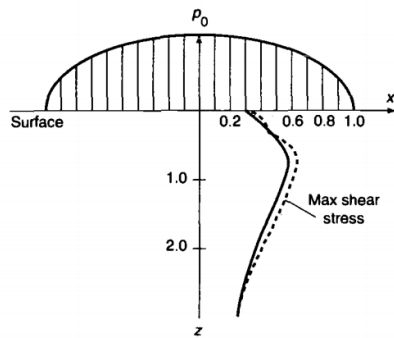
Figure 3.4: Rolling of tooth surfaces

Source: Mao, K. and Hooke, C. J. (2009)

### 3.2.4 Tooth flank fracture

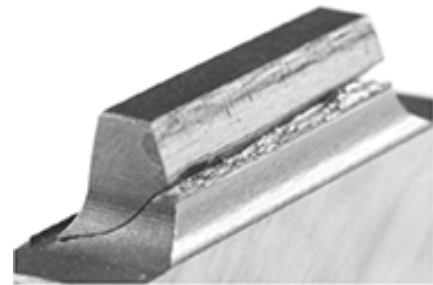
The purpose of gears is to transmit torque. They do this by transmitting contact forces on the tooth flanks. These contact forces will introduce contact stresses in the surface and shear stresses deeper in the material under the contact patch. When the shear stress induced in the material reaches a certain fatigue stress the stress will cause a crack to form. The maximum shear stress will be induced at a certain depth under the surface. This depth is correlated to the equivalent radius of curvature, the Hertzian stress acting at the contact & the equivalent Young's modulus. The maximum shear stress is induced at a depth because when we split the tooth up in planes at certain depths from the surface we see that a plane at a depth differing from zero has the greatest curvature in relation to its equilibrium state and thus the greatest shear stresses will occur here.

The causes of tooth flank fracture are very similar to those of macropitting. In addition, tooth flank fracture can also be caused by pitting. Depending on the gear geometry and load, a crack will show up at the surface or deeper in the material. The cracks typically develop at non-metallic inclusions, because these inclusions will have a different Young's modulus than the bulk material, so a stress concentration is formed there (Boiadjev et al., 2015). When the crack originates sub-surface and the loads are still being induced, the crack will grow towards the surface as well as toward the bulk of the material, since the crack itself acts as a stress riser for the surrounding material. Eventually the crack will reach the surface. After the crack has moved into a certain depth, the tooth can eventually fail with a brittle fracture when the remaining surface is overloaded (Stahl et al., 2018). Because tooth flank fracture is not a common failure mode of gears, this mode will not be discussed in detail.



(a) Shear stresses in contact patch

Source: Glaeser and Shaffer (1996)



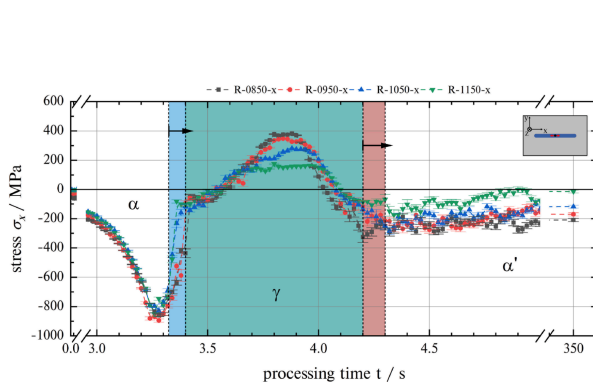
(b) Tooth flank fracture

Source: Boiadjiev et al. (2015)

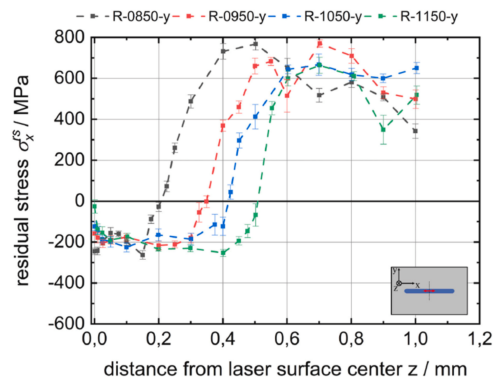
Figure 3.5: Shear stresses in tooth flank & tooth flank fracture

### 3.3 Residual stresses

In section 2 it was already explained how the mechanical properties of a part change when it is hardened. Because the part cools down to room temperature in a non-uniform manner when it is carburized, the part does not have a uniform microstructure. The thermal and transformational stresses will cause residual stresses to remain in the part. Residual stresses are very important to consider because they can enhance or deteriorate the mechanical properties even further. In this section it is explained how residual stresses are formed on the surface and in the depth of the material when a sample is laserhardened.



(a) Stress state of part during laser hardening



(b) Example of residual stresses for different beam sizes

Figure 3.6: Generation of residual stresses during laser hardening

Source: (Kiefer et al., 2021a)

Figure 3.6a illustrates the generation of the residual stresses. In the ' $\alpha$ ' region, the compressive stress rises. This happens because the laser spot approaches the coordinate for which the stress is monitored. The laser spot will cause this spot to heat and as a result the material will expand thermally, but the expansion is stopped by the cold material surrounding the spot. Since the spot is brought to a higher temperature, its yield strength will also drop because the atoms will oscillate with a larger amplitude so less energy should be added for dislocations to move to another equilibrium position.

Thereafter in the ' $\gamma$ ' region, the material is heated above the austenitization temperature. Because the FCC austenite has a larger atomic packing factor than the BCC ferrite, the density of austenite will be larger than the density of ferrite, thus the material will shrink and the compressive stresses will be lowered. From this point on the temperature of the spot is decreasing. Because austenite has a higher thermal expansion coefficient than ferrite, the material will locally want to shrink even further while the temperature is dropping, resulting in higher tensile stresses. Meanwhile the temperature is dropping further and at a certain point in time the material will reach the martensite transformation temperature, where martensite will be formed. At this moment, the material will expand because BCT martensite has a lower atomic packing factor than austenite, resulting in compressive stresses. Because the martensite start and end temperature are fairly low, the material will have lost a big part of its ductility so the compressive stresses cannot be compensated by a shrinkage of the material. Thus the compressive stresses are permanent (Kiefer et al., 2021b).

Because of the carbon concentration gradient on the surface explained in section 2, the material will have a different martensite start and end temperature depending on the depth from the surface. The martensite start temperature ( $M_S$ ) and end temperature ( $M_F$ ) will drop with higher carbon concentrations, see figure 2.4a. When the carbon concentration is high enough the martensite end temperature can even drop under room temperature, causing retained austenite to be created. Because of the atomic packing factor of retained austenite, the compressive stresses at the surface can be lowered or even converted to tensile stresses. Another factor that can contribute to the lowering of the residual compressive stresses is the reduced resistance to shrinkage of the material at the surface of the part.

Although the origin of residual stresses is understood, it is very difficult to describe their magnitude and how the stresses change as a function of the depth from the surface. The stress is dependent on a lot of factors: laser trajectory, spot size, intensity of the laser, carbon concentration gradient, etc. The residual stress is nonetheless very important to determine the optimal case hardening depth because the residual stresses change the fatigue limit of the material, see figure 3.7. Because there is no straightforward mathematical model to determine the residual stresses, these stresses are simulated using the heat treatment software, DANTE (explained in section 7).

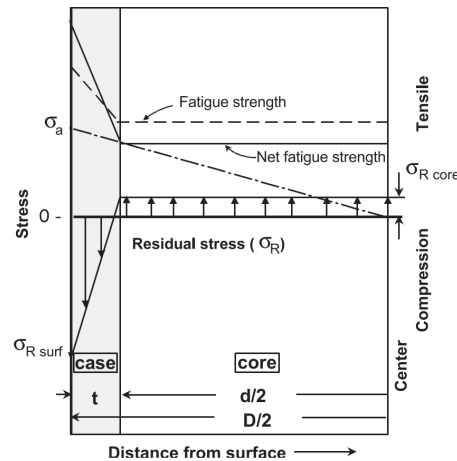


Figure 3.7: Influence of residual stress on fatigue

Source: (Genel, 2005)

### 3.4 Optimisation of the case hardening depth

In this subsection the optimal case hardening depth according to the previously explained failure mechanisms is determined. This case hardening depth is very important because it will be used as a goal during selection of all the different laser parameters.

#### 3.4.1 Macropitting

As stated, macropitting is directly related to the Hertzian stresses between two meshing tooth flanks. Despite the equation to find the Hertzian stress being relatively straightforward, a lot of attention should be paid when defining the force  $F$ . Supposing the torque on the input gear is constant, the force on the tooth flank will not be constant. This is due to several reasons.

First of all, the amount of gears in mesh changes with the rotation of the gears, this effect is expressed as the contact ratio of a gear set. The higher this ratio the better the load is distributed over a higher number of teeth. The contact ratio can be determined using simple trigonometry. In this case, the gear pair has a contact ratio value of around 1.7, which means that around 80% of the time 2 teeth are in mesh at the same time. From figure 3.8 it is concluded that the region of the tooth flank that solely transmits torque is the region around the middle of the height of the tooth flank. Here, an early assumption that macropitting is more likely to occur at the middle of the toothflank than around the dedendum or addendum circle can be made.

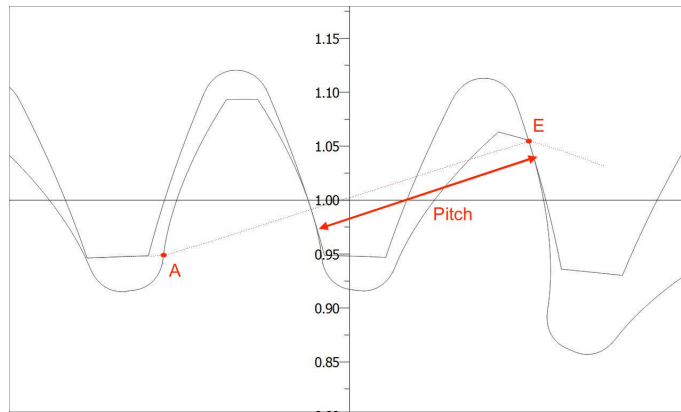
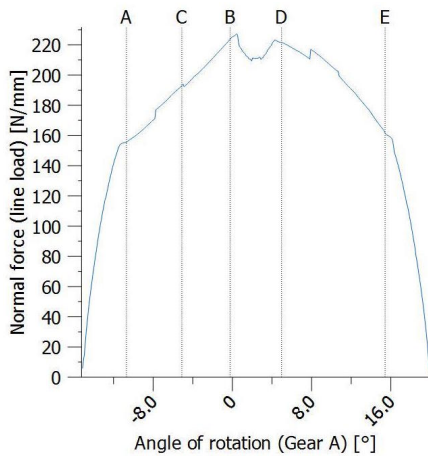
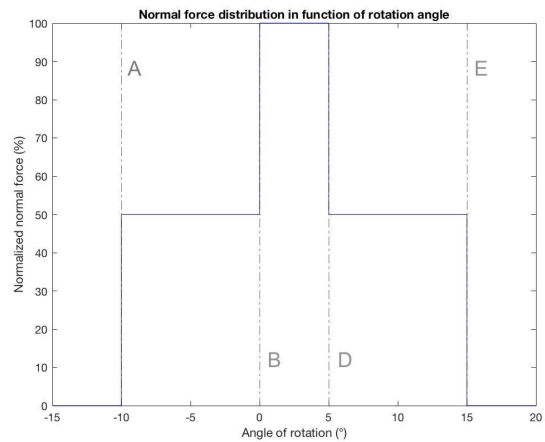


Figure 3.8: Meshing of teeth

Knowing the contact ratio, it is possible to determine how the loads will be distributed over the different teeth as a function of the gear angle. Supposing that the gears are infinitely stiff, the load distribution for a certain tooth can be found, figure 3.9b. In reality, the normal force distribution will look a lot different because the gear teeth will deform under load. The way the teeth deform, depends on the location of the normal force. This reasoning explains why the normal force rises between *A* and *B* and drops between *D* and *E* on figure 3.9a. Another reason why the real normal force distribution is more constant than in theory, is because of tip relief, the profile modification explained in section 1.5.1.



(a) Stress state of part during laser hardening



(b) Example of residual stresses for different beam sizes

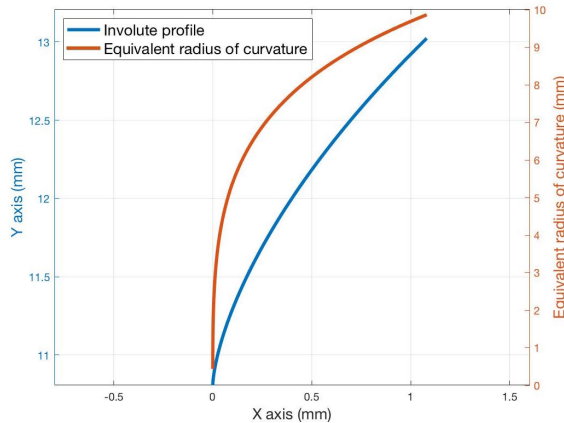
Figure 3.9: Effective & ideal normal forces on gear tooth

As stated earlier, the equivalent radius of curvature,  $\rho_{eq}$ , is of equal importance as the normal force

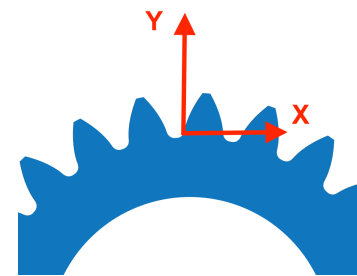
to calculate the Hertzian stresses. To get an insight in this effect, an approximate calculation of the radii of curvature is performed. When looking at figure 3.8, it can be assumed that the radius of curvature for the ring gear,  $\rho_{ring}$ , is constant, with a value of  $\pm 15mm$ . This value may be assumed as constant because of the amount of teeth the ring gear has in relation to the planet gear. The equivalent radius of curvature is calculated using following formula :

$$\rho_{eq} = \frac{2 \cdot \rho_{ring} \cdot \rho_{planet}}{\rho_{ring} + \rho_{planet}} \quad (3.4)$$

The radius of curvature for the planet gear,  $\rho_{planet}$ , for every point on the contact line is calculated by plotting the involute profile of the tooth and fitting the best possible circle to every section of the contact patch. It is important to point out that for this calculation the tooth profile is assumed to be a perfect involute. In reality this will not be the case because the roughness of the tooth flank also has an influence on the profile. Apart from this, the gears are also pit relieved which changes the radius of curvature in the region of the tooth top. The calculation is just to show to what extent the equivalent radius of curvature changes when travelling from tooth root to tooth top. Looking at figure 3.10a one can conclude that the radius of curvature for the planet gear is smallest near the tooth root which results in the highest Hertzian stresses in this area. Looking at the ring gear, it is concluded that the highest Hertzian stresses will occur near the tooth top since the tooth root of the planet gear will be in mesh with the tooth top of the ring gear and vice versa.



(a) Involute profile & equivalent radius of curvature for the planet gear



(b) Coordinate system for figure 3.10a

Figure 3.10: Calculation equivalent radius planet gear

The rolling and sliding of the tooth flanks explained in section 3.2.3 can also alter the shear stress state under the surface (Fernandes and McDulling, 1997). Negative sliding always occurs in the region between the pitch line and tooth root. When it occurs, the rolling will cause the material to be pushed in one direction and sliding causes it to be pushed in the other direction. This has as an effect that the maximum shear stress will be raised and will appear closer to the surface.



A last factor that will be discussed, is crowning of the tooth flank. In chapter 1 a short explanation can be found on why one would crown the tooth flanks of a gear. The result of this adjustment is that when the axis of both gears are perfectly perpendicular, most of the load will be transmitted through the center of the width of the tooth flank. KISSsoft can also provide a calculation result of the Hertzian stresses based on all these factors. In figure 3.11 a plot of the Hertzian stresses of the planet gear in relation to its rotation angle can be found. Although the Hertzian stresses for the planet gear are plotted, they will stay the same for the ring gear. The only difference is the angle of rotation. From these plots one can conclude that the largest Hertzian stress will appear at the tooth top of the ring gear at the center of the width of the tooth flank. After the tooth is meshed, the Hertzian stress will drop in a quasi-linear way with the angle of rotation.

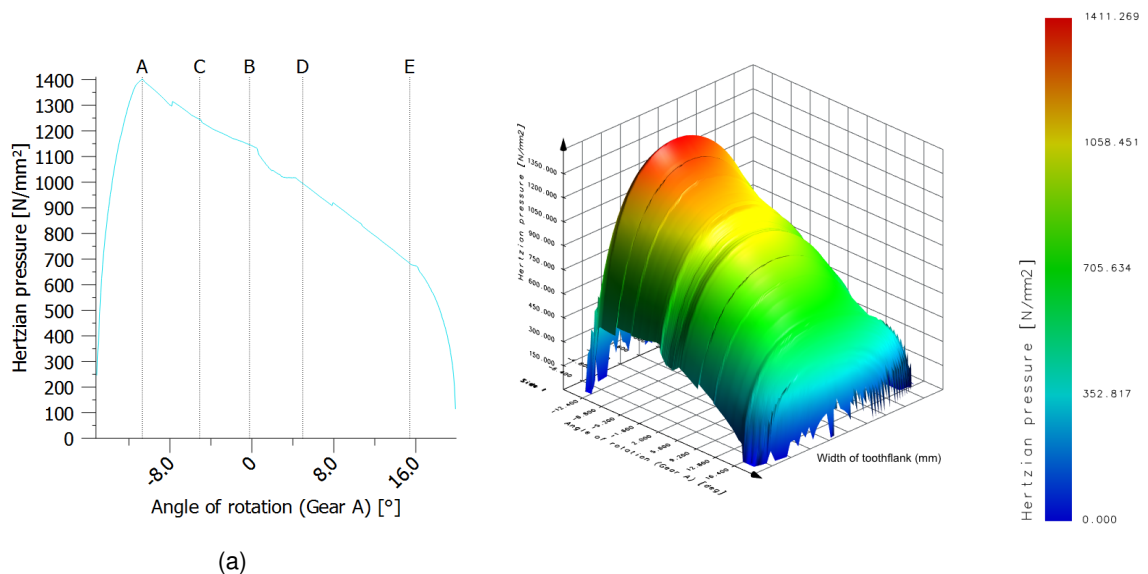


Figure 3.11: Hertzian stresses ring gear

As stated earlier in this chapter, the fatigue stress and tensile stress of steel will change in a quasi linear fashion with the hardness of the material (Stahl et al., 2018). That is why the desired surface hardness is as high as possible —having regard for the increased brittleness— so the surface will not deform plastically due to the contact stresses. For 16MnCr5 the maximum achievable hardness lies around 60 to 66 HRC (Steel, 2016). It is of great importance that the high surface hardness is assured around the region of highest Hertzian stresses, the tooth top. The tensile strength can be plotted as a function of the hardness (International Organization for Standardization, 2014) and the hertzian stresses at every point of contact on the tooth flank can be used to determine the required hardness, but eventually the tooth flanks have to be laser hardened. This would be a lot easier if a constant surface hardness over the tooth flank is assumed. Besides, a higher surface hardness in the tooth root area will not cause the tooth root to fail earlier than it would with a lower surface hardness, as will be discussed in section 3.4.2.

In order to determine the needed effective case hardening depth for the macropitting failure mode, it is necessary to have a look at the shear stresses under the surface induced by the Hertzian stresses and its influences discussed earlier. In subsection 3.2.4 it is explained why the shear stresses reach a maximum under the surface. The occurring shear stresses typically have a magnitude of 30% of the maximum hertzian stress (Shimizu, 2012). Although the shear stresses have a limited magnitude in comparison with the hertzian stresses, they become very important when looking at crack initiation. Looking at the hardness profile, it is necessary for the case hardening depth to be higher than the depth at which the maximum shear stress occurs. This way it is assured that the fatigue strength for a certain amount of cycles does not intersect with the peak of the shear stress at its depth, see figure 3.12a.

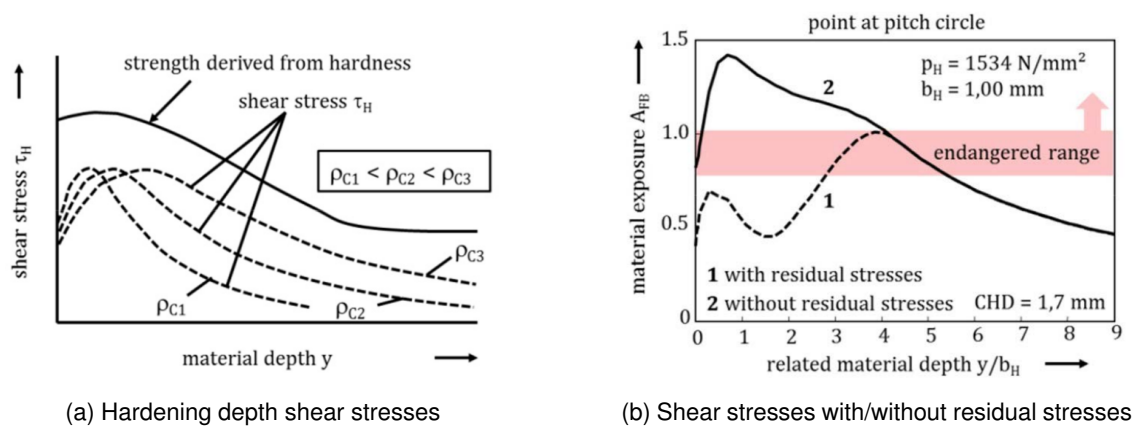


Figure 3.12: Shear stresses caused by Hertzian stresses at the contact patch

Source: (Tobie et al., 2018)

Considering how the optimal case hardening depth is determined, how the Hertzian stresses are induced and how they are related to the shear stresses, it is required to determine the depth of maximum shear stresses. This can be done by using KISSsoft which accounts for the influence of the contact ratio, meshing stiffness, etc. A maximum shear stress was found at a depth of  $0.044\text{mm}$ . It is advisable to choose a case hardening depth greater than this maximum shear stress depth, since no intersection between the material strength and the occurring shear stress may occur. DNV 41.2 (2015) states that the case hardening depth should be double of the maximum shear stress depth, being  $0.088\text{mm}$ . Residual stresses also influence where the maximum shear stress will occur, the residual compressive stresses at the surface will cause the maximum shear stress depth to become deeper in the material, but at a lower maximum shear stress, thus increasing the lifetime of the tooth flank, see figure 3.12b. Because the laserhardening proces —explained in chapter 4— has a lot of different parameters that will influence the residual stress distribution, it is very hard to predict how the case hardening depth should be changed accordingly. This should be revised once the residual stresses caused by laser hardening are more clear.

### 3.4.2 Tooth root bending fatigue

KISSsoft can provide a calculation of the tooth root bending stress concerning all the influencing factors considered in section 3.2.2. Just as with the pitting failure mode, it is desired for the surface hardness to be as high as possible such that the strength increases and the tooth root will not fail when a load is applied. When moving further into the depth of the material, the way the stress state changes with the depth needs to be examined in order to determine the optimal case hardening depth.

Looking at the theoretical formula for tooth root bending stress, it is easy to understand that the bending stress changes linearly with the depth. The bending stress will reach a maximum on the surface because there the distance from the neutral axis is the largest. When moving deeper in the material, the bending stress decreases until it reaches a zero value at the depth of the neutral axis. It is important to consider that the contact force on the tooth flank also has a radial component which compresses the tooth radially and lowers the maximum tensile bending stress, see 3.13.

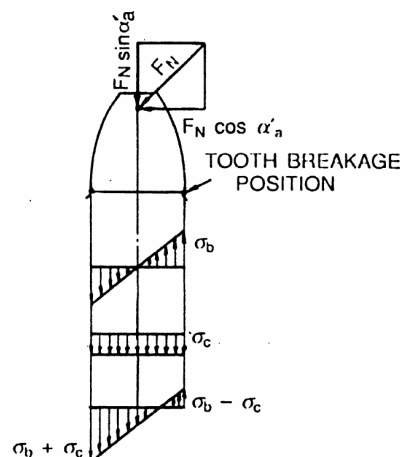


Figure 3.13: Stress components tooth root bending

Source: (Eritenel, 2019)

Knowing this, the ideal hardness profile would also be linear, considering the tensile strength changes linearly with the hardness. Unfortunately, stress concentrations will always occur, changing the stress distribution drastically, despite the tooth root having a fillet. Depending on the gear's geometry (size, root fillet, module,...) the stress concentration will dissipate more quickly/slowly in the depth of the material. Another factor that has a very big influence on what case hardening depth is optimal, are the residual stresses. Tobie et al. (2005) did research on the optimum case hardening depth for tooth root bending and they also considered the effect of the residual stresses caused by a carburizing process. They carried out fatigue tests on gears out of 16MnCr5 with several different modules and case hardening depths. They experimentally found a relation for the

optimal case hardening depth for tooth root bending. As mentioned, this is the optimal case hardening depth for carburized gears. The residual stresses profile will not be the same for carburizing or laser hardening, but this hardening depth will be used for now because the generation of residual stresses looks very much alike.

$$CHD_{opt} = 0.1 \cdot m \quad (3.5)$$

With  $CHD_{opt}$  the optimal case hardening depth,  $m$  the module of the gear set.

### 3.4.3 Abrasive wear

As stated in section 3.2.3 a lot of factors influence the amount of wear. Therefore it is not easy to come up with a comprehensive formula to determine the wear. Winter and Plewe (1982) have done research on how to calculate the wear rate factor depending on the oil film thickness and the type of oil used for case hardened gears. This wear rate factor can then be used to calculate the wear using Archard's wear equation.

$$Q = \frac{K \cdot W \cdot L}{H} \quad (3.6)$$

At which  $Q$  the volume of material removed by wear,  $K$  wear rate factor,  $W$  normal load,  $L$  sliding distance,  $H$  factor related to the hardness of the material

However, knowledge about the way the roughness of the flanks influences the wear rate is very limited. For this reason, the wear rate factor calculated by their methods should be multiplied with a value ranging from 0.01 to 1. In this case, the wear rate factor is multiplied by 1, since this accounts for the most material being removed and thus for the worst case. The wear calculation based on the factors above is built in in KISSsoft and can be done iteratively because of the changing loads when the tooth flank surface wears down. KISSsoft supposes a surface hardness of 60HRC.

From figure 3.14a it can be observed that the cumulative wear has a maximum value of  $0.068\mu m$  on the ring gear tooth flank. One can conclude that the wear does not really influence the selected case hardening depth any further, because the other criteria —pitting and tooth root bending fatigue—are more constraining. Though it is important to emphasize that the surface hardness of  $\pm 60HRC$  has to be reached for the calculated wear to have any significance.

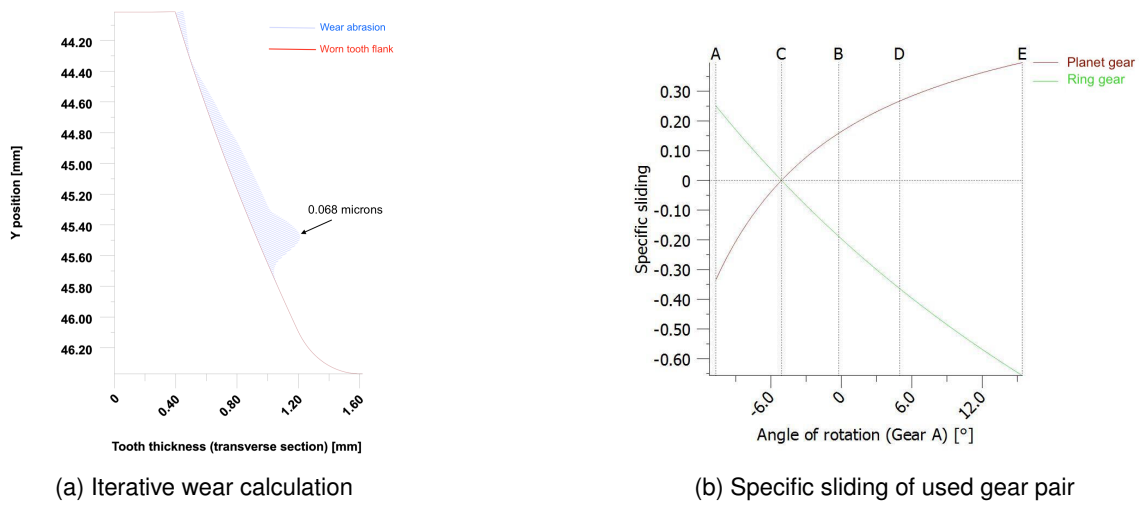


Figure 3.14: Abrasive wear & specific sliding

### 3.4.4 Conclusion

All the optimal case hardening depths for the different failure mechanisms are summarized in table 3.1. The case hardening depth for abrasive wear is no constraint for determining the optimal laser parameters because the constraint by pitting will always be greater. It is also important to mention that these case hardening depths should effectively be validated by fatigue tests for tooth root bending & pitting. However, this is not within the scope of this masters thesis. For this reason the optimum case hardening depth at the tooth flanks is set to  $\pm 200\mu m$ , in this thesis no fatigue tests will be conducted and thus there is a certain risk that the above determined case hardening depths are too minimal and the gear would fail after a short period. Therefore the mean between the above determined optimum case hardening depth ( $\pm 100\mu m$ ) and the optimum case hardening depth determined by International Organization for Standardization (2007) being  $\pm 300\mu m$  is chosen.

Optimal Case Hardening Depth	
Pitting	$\geq 88\mu m$
Bending	$\geq 100\mu m$
Abrasive wear	/

Table 3.1 Optimal case hardening depth (550HV) for the different failure mechanisms

# 4

## Laserhardening

### 4.1 Introduction

In this chapter it is explained how to use lasers to reach the predetermined hardness requirements. The concept choice and simulation models will also be emphasized in this section.

### 4.2 The laser

#### 4.2.1 Lasers

There are many different types of lasers, but the two most common types of lasers used in for hardening are CO<sub>2</sub> lasers and YAG lasers, where YAG stands for yttrium aluminum garnet). These two types of lasers have quite a different wavelength, in fact the wavelength of YAG lasers is exactly 10 times smaller than the wavelength of a CO<sub>2</sub> laser (EpilogLaser, 2014). In figure 4.1, an overview of different laser wavelengths is provided, as well as the absorption coefficients for laserlight of these wavelengths.

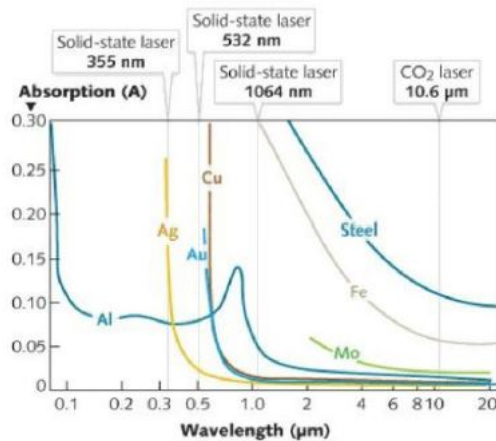


Figure 4.1: Absorption of laserlight for different materials and wavelengths

Source: Totten (2006)

As is evident from the figure, the absorption (more on that subject in section 4.3) of laserlight in steels is much higher for YAG lasers than for CO<sub>2</sub> lasers. The laser used in this research is a Yb-YAG laser (Ytterbium-YAG), meaning that the YAG-crystals are ytterbium-doped. YAG lasers are a type of thin-disk laser. Without going too much into detail, the working principle of thin-disk lasers is as follows: a small diodelaser generates a small laserbeam, called the pump beam. This laserbeam is projected onto a parabolic mirror, which directs the laserbeam onto the crystal (in this case the Yb-YAG crystal). In the crystal, several electrons are excited by the laserbeam. When the energy level of these electrons drops again, they emit a photon. This process is called stimulated emission. The enhanced laserbeam is directed back at the parabolic mirror again. Due to part of this mirror being only partially silvered (partially reflecting), part of the laserbeam is directed into the fibre which transports the output laserbeam to the laser target. The other part of the laserbeam is directed back at the crystal and again creates stimulated emission. This process is repeated continuously, creating a powerful output beam (Physics and Radio-Electronics, 2015).

### THE DISK LASER TECHNOLOGY

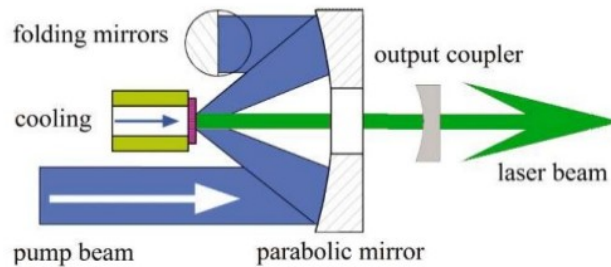


Figure 4.2: Schematic representation of a thin disk laser

Source: Pandey (2015)

#### 4.2.2 Trumpf TruDisk 5001

The laser used in this thesis as mentioned above is an Yb-YAG laser, namely the Trumpf TruDisk 5001. Some of the most important attributes of this laser are listed below, a Trumpf datasheet can be found in appendix G.

- Minimum power = 100W
- Maximum power = 5kW
- Active power regulation accurate to 1%
- Wavelength  $\lambda = 1030\text{nm}$  (infrared light)
- BPP= 4 mm mrad
- $M^2$ -factor=12.2
- Brightline Weld function (explained further in section 4.4)
- Laser optics can move in X-, Y- and Z- direction.

The last item is especially important. Not only is it possible to make the laser follow a certain track in a 2D plane, it is also possible to adjust defokus of the laser (physically by adjusting the height of the suspended bar of the system, as well as in the software, albeit that the software has a more limited range). This means that it is possible to enlarge the spotsize projected onto the part. The



setup of the laser is shown in figure 4.3 below. The following items can be distinguished on the picture:

1. Laser source
2. Guide rails for height adjustment laser
3. LLK (Laser Light Cable)
4. Laser optics
5. Workbench laser



Figure 4.3: Laser setup at FOKUS lab

### 4.2.3 BPP and $M^2$

The BPP or Beam Parameter Product is the product of the radius of the laserbeam and the beam divergence half-angle, with the radius of the beam being measured at the beam waist (RP Photonics Encyclopedia, 2018). Figure 4.4a illustrates how the BPP is determined. The BPP is a measure for the beam quality, a lower BPP signifying a higher beam quality. The Beam Quality Factor  $M^2$  is another measure for the beam quality, relating the BPP to the wavelength of the laserlight as in equation 4.2. The  $M^2$  compares the actual shape of the laser beam to an ideal Gaussian beam. Looking at figure 4.4b, it is clear that the laser used, produces quite a qualitative laserbeam compared to other types of lasers.

$$BPP = w_0 \theta_0 \quad (4.1)$$

With  $w_0$  being the beam waist radius (mm).  $\theta_0$  the divergence half angle ( $\mu rad$ )

$$M^2 = \frac{BPP\pi}{\lambda} \quad (4.2)$$

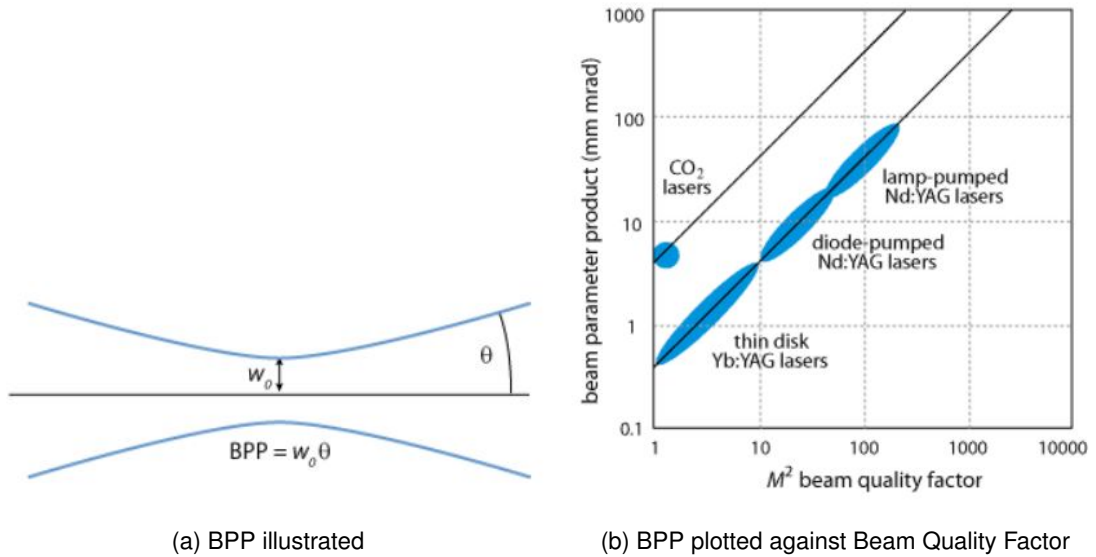


Figure 4.4: BPP and Beam Quality Factor (RP Photonics Encyclopedia, 2018)

### 4.2.4 Defocusing laser spot

An ideal laser spot has a Gaussian distribution. The beam diameter of the laser is defined as the  $1/e^2$  width: the distance between two points on the distribution that have a value of  $0.135 (= 1/e^2)$  times the distribution maximum value, as depicted in figure 4.5. As mentioned in section 4.2.2, by adjusting the height of the laser optics relative to the workpiece, the laser spot on the workpiece can be made larger. It is clear that by bringing the point where the laser beam hits the object's surface further out of focus (moving to the left or right in figure 4.4a), the spot diameter increases. Most lasers spots in focus are quite small ( $180 \mu m$  for the TruDisk 5001), meaning that for a powerful laser there is a very high energy density at the centre of the beam. When defocusing, besides the spot size increasing, the Gaussian distribution is also 'flattened', providing a more uniform energy density over the entirety of the spot. This increased spot diameter can be useful in applications where a larger surface needs to be heated uniformly, as a small spot size heats the material very locally.

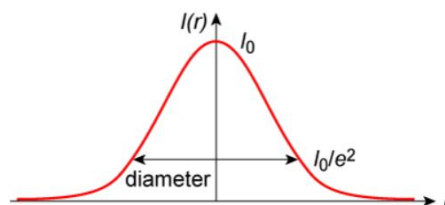


Figure 4.5: Beam diameter or  $1/e^2$  width

Source: Semrock (nd)

Defocusing a laser beam does come at a price, however. A larger spot size tends to heat the material less deep compared to a small spot size due to the reduced local intensity. On top of that, beam quality can reduce quite drastically, depending on certain laser parameters. Figure 4.6 illustrates this deterioration of beam quality with increasing defocusing distance. When defocusing from 0 to 3mm, the distribution mostly becomes more uniform (flattening of the Gaussian distribution), however, at 4mm defocus, the distribution of the spot becomes very uneven. The extent to which the beam quality deteriorates by defocusing, is strongly dependent of the type of laser used.

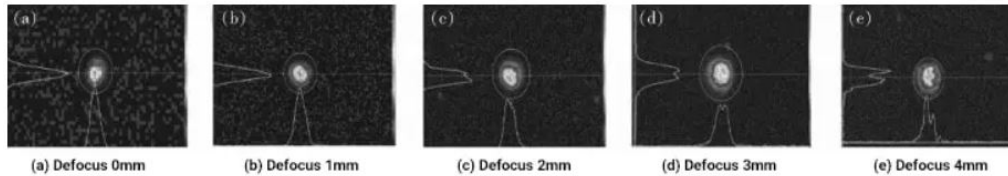


Figure 4.6: Effect of increasing defocus on laser beam distribution and quality

Source: MachineMFG (nd)

## 4.3 Absorption

### 4.3.1 Laser light absorption

Since lasers emit electromagnetic radiation, the mechanism of absorption of laser light is as with regular light. When electromagnetic radiation strikes a surface, 3 things can happen, as illustrated by figure 4.7:

1. The surface can absorb the laser light, transmitting its energy to the neighboring material.
2. The surface can reflect the light, either by diffuse and/or specular reflection.
3. The light can also be transmitted through the material.

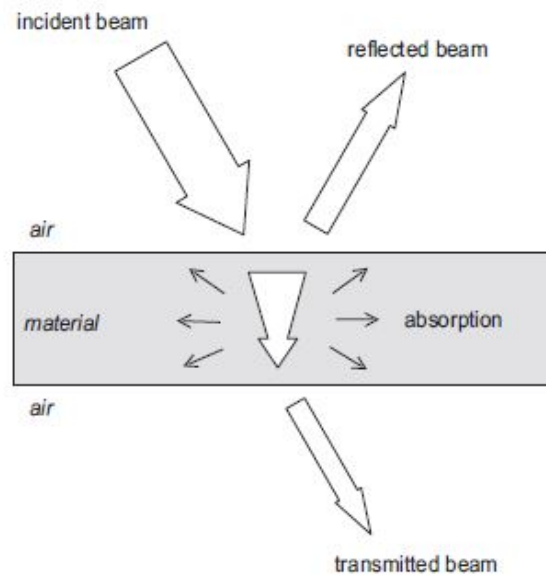


Figure 4.7: Absorption, reflection and transmission of electromagnetic waves

Source: Bergström (2008)

Usually, a combination of the three occurs, depending on several different factors. In the application of laser hardening, the most important phenomenon is absorption. Absorption can be seen as the decrease in intensity over distance of an electromagnetic wave passing through an absorbing medium. This decrease in intensity in relation to the absorption depth  $I_z$  can be defined according to Beer's Law <sup>1</sup>:

$$I(z) = I_0 e^{-\alpha z} \text{ (W/m}^2\text{)} \quad (4.3)$$

where  $\alpha = \frac{4\pi nk}{\lambda_0}$  is the absorption coefficient and  $\lambda_0$  is the vacuum wavelength (nm).  $n$  and  $k$  are optical constants.  $I_0$  is the input intensity ( $\text{W/m}^2$ ). A quantity related to the absorption coefficient and perhaps easier to interpret and directly measure compared to the absorption coefficient, is the absorptance  $A$ .

$$A = \frac{\text{Absorbed laser power}}{\text{Total laser power incident on the surface}} \quad (4.4)$$

In order to get an idea of the laser power needed to heat the ring gear material to an appropriate temperature, it is important to have an estimation of the value of the absorption coefficient or the absorptance.

In laser light absorption, the following parameters play a vital role in the amount of energy that is absorbed (Bergström, 2008):

<sup>1</sup>This definition of absorption is only valid for homogeneous media, in heterogeneous media, the optical constants depend on position and/or direction of propagation. Here  $\alpha$  must be replaced by  $\alpha(z)$  (Bergström, 2008)

**Laser Beam:**

- Intensity
- Wavelength [ $\lambda$ ]
- Angle of Incidence [ $\alpha$ ] (see also figure 4.1)
- Polarization, p or s (parallel or perpendicular to the plane of incidence)

**Material:**

- Composition (eg. material type, alloy composition,... see also figure 4.1)
- Temperature (T)
- Surface roughness
- Surface and bulk defects and impurities (eg. cracks, dust particles,...)

From the literature, there is quite some data available for absorption tests on similar steels and lasers with equal wavelength as the ones used in this experiment. However, because laser light absorption is dependent on so many different variables, the best way to get an accurate estimation of the absorptance, is to perform an experiment in conditions equal to those when laser hardening the ring gear.

**4.3.2 Absorptance tests**

For the absorptance tests, first a number of tests was performed. Several 16MnCr5 steel blocks were milled with a fine surface finish in order to get a roughness value of  $Ra=0.8\mu m$ , similar to the roughness value of the ring gear teeth (see appendix A). The roughness of the surface has a significant impact on the absorptance, as rough surfaces will generally have a much higher absorptivity, as illustrated by figure 4.8. The higher the surface roughness, the higher the portion of laserlight that will be reflected back at the surface, causing more of the light to be absorbed.

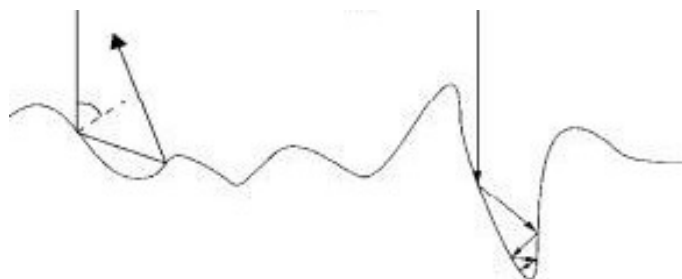
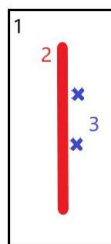


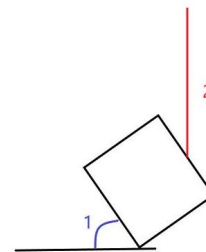
Figure 4.8: Absorption of laser light on a rough surface

Source: Bergström (2008)

Next, the steel blocks were sent to FEB partner Gearcraft Vanhoutte to perform the carburizing step required for hardening the low alloy steel. This is a very important step, since composition of the material has a large influence on the absorptivity of an object's surface. Besides the difference in composition, the steel block also gets a matte finish after carburizing, which influences the relative amount of absorbed laser light as well. After carburizing, two thermocouples were welded onto the blocks, a few millimeters from the were the laser will track as depicted in figure 4.9a. Once this has been done, the samples were ready for the lasering step. A 35mm long track in the middle of the block (see figure 4.9b) was made with the laser, close to the melting temperature.

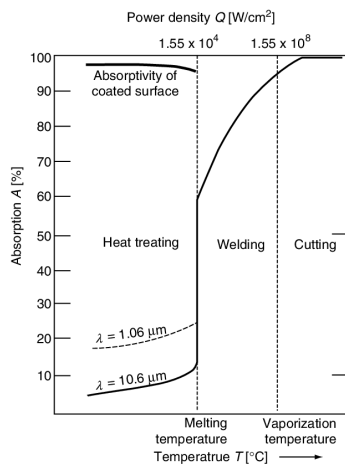


(a) 16MnCr5 block (1) with the 35mm long laser-track (2) and two thermocouple welds (3)



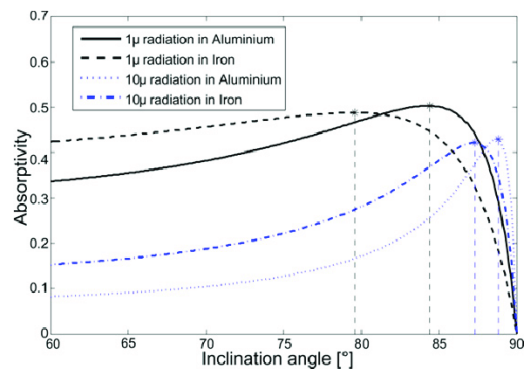
(b) Inclination angle (1) and incident laser beam (2) for the absorption test setup

This lasertrack was performed on a number of samples for a varying incident angle and for varying powers (first close to the melting point, gradually lowering power to achieve lower surface temperatures). These two variables were experimented with, since they can have quite a significant influence on the absorptivity (see figures 4.10a and 4.10b). After the lasering step, the samples were put under the microscope to measure the distance from the thermocouple welds to the middle of the laser track. This distance will become very important to determine the absorptivity.



(a) Influence of temperature on laser light absorptivity

Source: Grum (2004a)



(b) Influence of incidence angle on laser light absorptivity

Source: Costa Rodrigues et al. (2014)

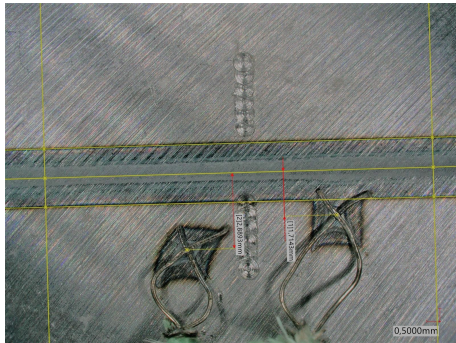
After testing, a simulation in Ansys (see chapter 7) was performed. The steel blocks were modeled and a Gaussian heat flux following a straight path of 35mm long was modeled to heat up the steel block. Next, a temperature probe was placed at a distance from the centre of the heat flux path equal to the measured distance between thermocouple weld and laser path. By adjusting the heat flux power until the simulated temperature corresponded with the measured temperature, an estimation of the absorbed power could be determined from the simulated value. The following formula was used to obtain an estimated value for the absorptance  $A$ :

$$A = \frac{\text{Heat flux power in the simulation}}{\text{Actual laser power}} \quad (4.5)$$

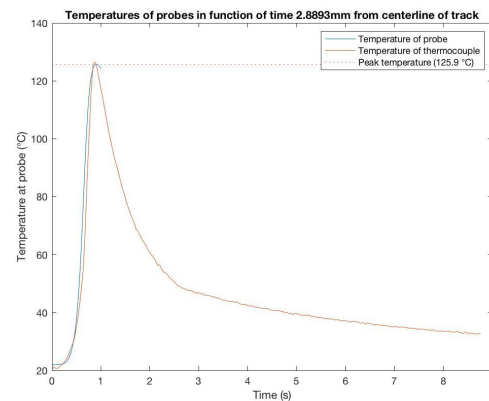
The hardening concept explained later in 4.4.1 uses a laser light incidence angle of about  $70^\circ$ . The average absorptance value at  $70^\circ$  inclination for the carburized 16MnCr5 was found to be:

$$A_{70^\circ} = 83.9\% \quad (4.6)$$

This absorptance value was used later in chapter 8 to obtain an indicative value to transition from simulation to physical experiment without losing much time and samples to determine the optimum laser power. In figure 4.11a, a picture from the absorptivity test is shown. A graph with the measured and the simulated value is also included in figure 4.11b.



(a) Laser track and thermocouple welds on steel block



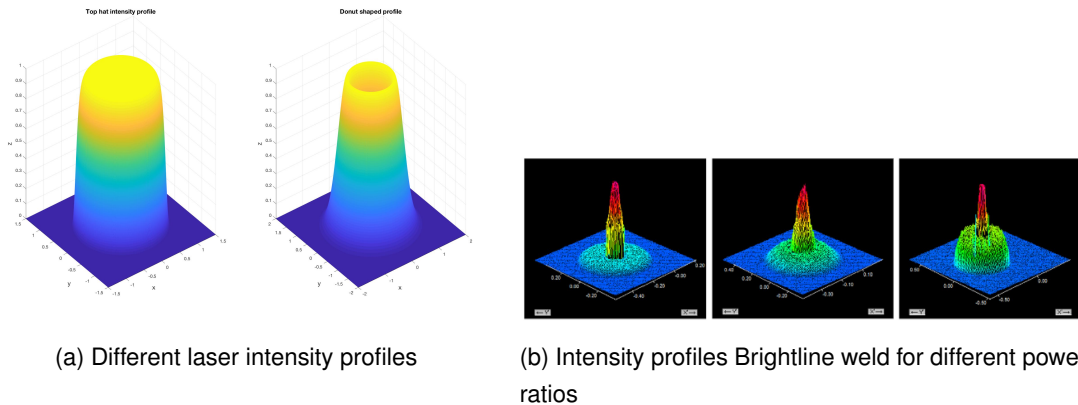
(b) Simulated and measured value for absorptivity tests

## 4.4 Types of laser hardening

As explained in previous sections the ability of a laser to heat the material is used to harden the ring gears. In comparison with conventional hardening techniques—such as carburizing or nitriding—heat can be applied very locally. Consequently the underlying material can be used as a heatsink to ensure sufficiently high cooling rates.

Lasers also have the advantageous property that their intensity profile can be chosen within certain

limits. Most lasers have a Gaussian intensity profile due to the cavity modes characteristic for the used cavity Paschotta (2017). As explained earlier in section 4.2.1, the beam diameter can be chosen freely, depending on how far from the focal point the laser enters the material. This property provides a lot of freedom because the entire surface of the gear is to be heat treated. Next to the Gaussian mode, the intensity profile can also be altered into other profiles such as top-hat, donut, etc. depending on the application, see figure 4.12a.



Source: Trumpf (2017)

Figure 4.12: Different intensity profiles

As stated earlier the laser used was equipped with the TRUMPF patented 2-in-1 laser light fibre technology called Brightline Weld. This technology enables the user to choose how much power is put in the inner and outer fibre, later referred to as the core and ring. The inner fibre generates a Gaussian intensity profile, the outer fibre generates a donut type intensity profile. The combination of the two gives the user a lot of freedom to optimize the process. The technique was originally created to reduce the amount of spatter while welding (Trumpf, 2017). For laser hardening this function can also be exploited because it enables the user to generate profiles that can uniformly heat the workpiece instead of heating very locally as one does when only using the core fibre. In section 4.4.1 the intensity profile of the laser will be elaborated upon.

Now the different methods of laser hardening will be discussed further, in following order :

- Scanning laser hardening
- Single track hardening

#### 4.4.1 Scanning laser hardening

In scanning laser hardening the laser spot moves in the feed direction at relatively low speed, meanwhile the spot oscillates with a certain amplitude perpendicular to the feed direction with a



far greater speed, see figure 4.13. Research done by Bouquet (2016) showed that oscillating in a zig-zag motion results in the most uniform hardness. Other scanning profiles have also been researched and can generate sufficient results (Martinez et al., 2011). A big advantage of this technique is that very large surfaces can be hardened with a limited power output of the laser. In addition, the effective case hardening depth can be kept very constant over the surface and can be chosen freely within certain limits. A disadvantage of this technique is that it is very difficult to regulate the power as function of the position of the laser spot. At the edges of the part there will be a heat build-up because in these regions the laser spot passes 2 times in a very short time. This effect should be countered by decreasing the power and/or increasing the oscillation speed. Mostly this power regulation is done by use of a feedback loop and measurements of the surface temperature using pyrometers (Bouquet, 2016), (Martinez et al., 2011).

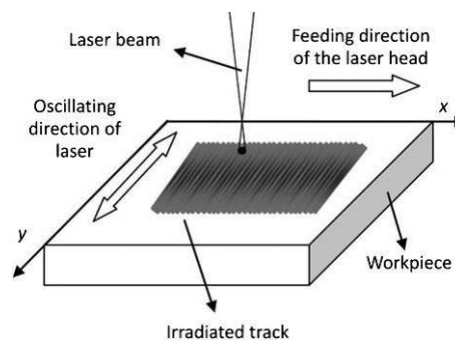


Figure 4.13: Scanning laser hardening

Source: Bouquet (2016)

Another disadvantage of this type of hardening is that the oscillation speed should be kept high, otherwise tempering of already hardened tracks will occur, resulting in an unusable gear. (tempering will be further discussed in chapter 5). A consequence of this is that the mirrors inside the laser also have to be able to oscillate at high frequencies. The mirrors itself will have a certain inertia which causes the zigzag pattern to be rounded of at the corners because the mirror cannot have an infinitely large angular acceleration due to a finite torque applied on the mirror (Bouquet, 2016). This effect will further enhance the temperature build-up at the corners causing the material to melt at these positions when the effect would not be counteracted. In figure 4.14 we can see melt at the edges of oscillation when the above explained effect is not counteracted.

Another factor that is really important to see if this approach is feasible, is the intensity distribution of the laser spot. The goal is for every section of material at the surface and at a depth from the surface to go through the same thermal history in order to obtain a constant surface hardness and an effective case hardening depth with minimal distortions. It is best to approach this target with a top-hat intensity profile, as this profile enables the user to heat up as much of the surface as possible up to a certain temperature without it melting, as would happen with a Gaussian profile.

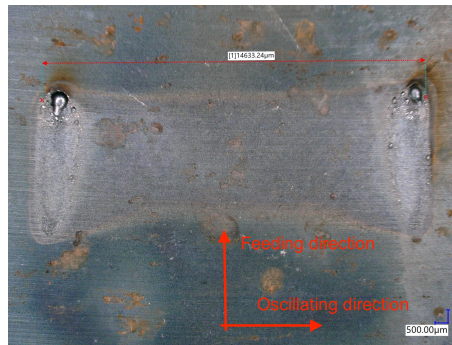


Figure 4.14: High frequency zigzag

For this reason the ability of the laser to create top-hat like intensity profiles is looked into. Because the 'Brightline Weld' technique is patented (and very little information on this function is available) it is unclear how the donut shaped profile is formed. In literature it is found that the donut profile can for example be achieved by the use of axicons to generate bessel beams (Colombier et al., 2017) or by spiral phase plates (SPP) and binary spiral phase holograms to convert the Gaussian profile into a donut profile (Steiger et al., 2013). Because it is unclear which of these techniques is used in the FOKUS laser, it is not possible to devise an equation for its intensity profile as a function of the defocus height relative to the focal plane. For this reason, the intensity profile is determined experimentally.

First, tests were conducted for in focus steel samples with all the power in the outer fibre and zero in the inner fibre. The power was then gradually increased until it was easy to demarcate a heat affected zone at the surface of the sample. These kind of tests should ideally be conducted by use of beam analyzers but because the lower power threshold of the laser is 100W, a suitable beam analyzer could not be found. This is why the less accurate visual method was used. The power was applied to the sample in a very short pulse to minimise the effect of heat diffusion within the material. The result of this test can be seen in figure 4.15a. From this figure and the tempering colors and temperatures of steel, (Hamza, 2020), it is clear that the intensity profile is most definitely donut shaped. The effect of defocusing the sample is shown in figure 4.15b. Thus, a top-hat intensity profile can be accomplished by defocusing the laser. It is important to emphasize that this method of determining the intensity is by no means ideal, but it can provide a good indication.

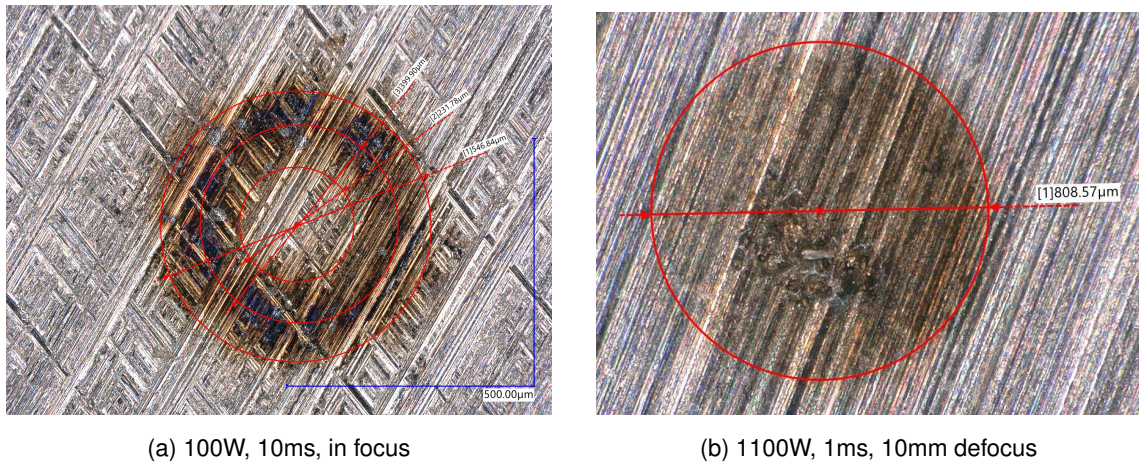


Figure 4.15: Thermal markings for different laser settings

Scanning laser hardening can be applied in different ways to the ring gear. One could feed from side to side, top to root of the teeth and vice versa, as seen in figure 4.16 to 4.18. The method depicted in 4.18 has the advantage that the same result can be achieved with lower velocities. This is because the height of the tooth is a factor  $\pm 7$  times smaller than the width of the gear. For the exact dimensions a technical drawing is attached in appendix A. Lower velocities are sufficient because the path length of one oscillation is much smaller than the oscillation length of the laser paths in 4.16 and 4.17. The speed in itself is not a big problem for the laser used in this thesis, as it can reach speeds up to 15000 mm/s which is sufficient considering the literature (Bouquet, 2016) (Martinez et al., 2011). However the accelerations can become a problem as stated earlier in this section.

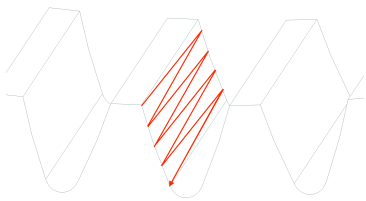


Figure 4.16: Laser path from top to foot

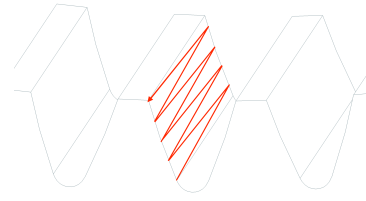


Figure 4.17: Laser path from foot to top

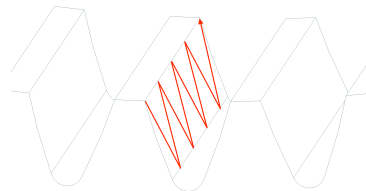


Figure 4.18: Laser path from side to side

A disadvantage of a feed direction from side to side is that the root also needs to be hardened because of the bending stresses acting there explained in section 3.4.2. When looking at the tangent angle of surface from top to root in figure 4.19a one can see that the angle changes a lot in the area of the root fillet. As explained in section 4.3 it is clear that the angle of incidence has an influence on the absorptivity. Because of this the absorptivity of the laser will change depending on the position where the laser beam hits the surface, which makes the power regulation extra difficult. When pyrometers and a feedback loop would be used this effect would not make the problem harder because it is self-resolving due to the loop. However, there was no pyrometer available, meaning the laser power and speed could not be changed once the laser has started. Therefore, all the laser parameters have to be determined experimentally or using simulations. The simulation aspect will be covered further in section 7.

Due to the complex geometry of the ring gear the number of ways to point the laser beam at the surface is limited. Ideally, the laser beam would point as perpendicular as possible to the surface such that errors due to misalignment are minimised. On the one hand the ring gear should be rotated around the Y-axis, figure 4.19b, when the laser beam would impinge vertically. This is because if the laser beam were to be pointed in the plane of the ring gear, the tooth surface would be out of reach because the gearing is internal, so the other side of the gear would block the laser path. This problem could be avoided by the use of a mirror at the center of the ring gear but this will enhance the errors due to misalignment. On the other hand it is impossible for the beam to hit the tooth perpendicular to the tooth surface in the YZ-surface because an adjacent tooth will block the path. In order to hit as perpendicularly as possible, the adjacent tooth face will be placed parallel with the laser beam. Taking these factors into account, the optimal gear alignment can be determined in figure 4.19c. Due to the angle between the tooth surface and the impinging laser beam in the YZ-plane not being equal to  $90^\circ$  whatever the intensity profile is, it will be stretched when it is projected onto the surface. This is the same effect as when looking at a penny from an angle, it will seem elliptical. This angle was found to be a maximum of  $\pm 40^\circ$ . Because the gear teeth only have a tooth height of  $\pm 2.4\text{mm}$  and the top hat beam diameter is  $\pm 0.8\text{mm}$ , it will become very difficult to harden the gears using scanning laser hardening because there is not much room to move. This will most likely cause a non-uniform hardness at the edges of the irradiated area. Based on these disadvantages there was opted to look into alternatives for this method which will be discussed in upcoming sections.

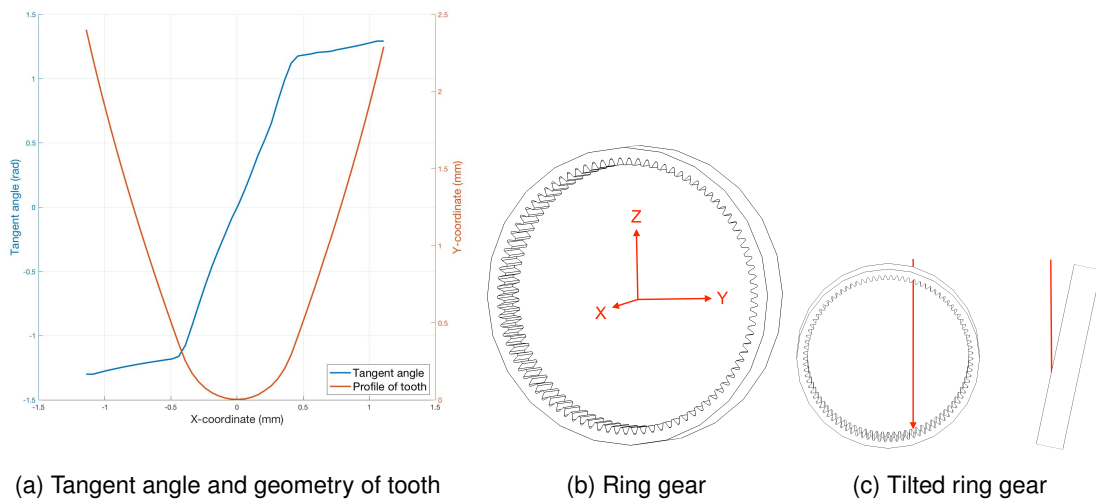


Figure 4.19: Tilt angle of ring gear

#### 4.4.2 Single track hardening

In single track hardening the laser beam translates over the surface with a low speed in comparison to the oscillation speed of scanning laser hardening. Sufficient areas can be hardened because this type of hardening is done with very large beam sizes. By translating slowly over the surface, enough energy can be added such that the steel changes to an austenitic microstructure. Once the laser has traveled far enough away from the previously heated point, the cool material underneath will ensure self quenching of the material such that a martensitic microstructure is achieved. Although large hardened surfaces can be achieved with this method, its dimensions are finite because the intensity profile of the beam has a finite width. As a consequence several tracks next to each other should be hardened after each other which causes tempering, see figure 4.20 (Giorleo and Semeraro, 2010) (Oosterlinck and Steenberghen, 2018). This effect can be minimized by choosing an appropriate beam distribution. A wide beam with very sharp edges would be ideal such that the overlap zone can be kept as small as possible so the tempering effect is minimized. However if there is an overlap zone, the ring gear will fail in this location because in gears the contact patches are very small, so this method is not an option for this application. Despite that, for applications in which the forces are distributed over great surfaces, moulds for example, this is an option.

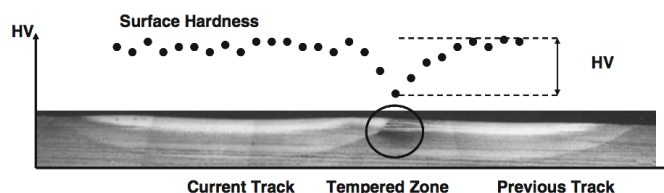


Figure 4.20: Back tempering effect

Source: (Giorleo and Semeraro, 2010)

In this case, the fact that the module is so small can be turned to an advantage. From appendix A one can see that the distance between two adjacent tooth tops is  $\pm 2.3\text{mm}$ . If the sample to be hardened were to be put out of focus, the diameter of the impinging beam would increase. However, it is impossible to use the outer fibre to get a top hat profile with the needed diameter, because the top hat profile will change in another distribution which is unknown. Tests were conducted on out of focus focal planes for the outer fibre, but the uncertainty on its distribution is too significant, see figure 4.21. This is why the Gaussian beam generated by the inner fibre was used, since the Gaussian distribution is maintained when the sample is put out of focus. The only thing that changes is its diameter. (The quality of the beam will also deteriorate a bit, but this effect will be neglected).

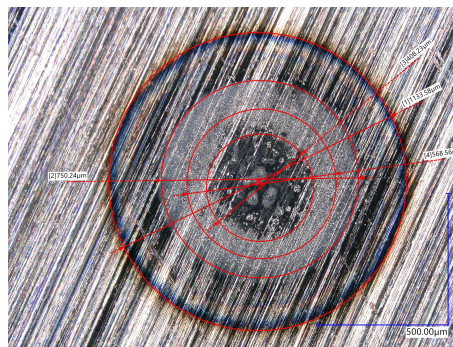


Figure 4.21: 250W, 30ms, 20mm defocus

There are 2 possible concepts using this technique. The first is to let the middle of the Gaussian beam travel along the middle of the tooth root, depicted in figure 4.22a. This way 2 tooth flanks are hardened in one laser movement. The second concept consists of only one tooth flank that is hardened at the same time, depicted in figure 4.22b. It is important to state here that the green lines on these figures represent the part of the beam used to heat the tooth flank, the red lines represent unused power that will be blocked off. As explained, the first concept can harden 2 teeth at the same time, but there is also the disadvantage that there are less parameters to adjust compared to the second concept. In concept 2 there is the possibility to choose where the maximum intensity of the Gaussian beam will impinge, in concept 1 the maximum intensity always hits at the middle of the root. Next to this, in concept 1 the incident angle of the beam can be chosen within certain limits ( $0^\circ$  to  $\pm 40^\circ$ ), this angle is limited because the laser may not impinge the adjacent tooth top as explained earlier. This can aid to reach the optimum case hardening depth because the absorptivity will change depending on the incidence angle, see section 4.3. A disadvantage of the second concept is that there will be an overlap zone between the hardened paths of the two adjacent teeth in which tempering will occur. But as observed in section 3.4.2, this should not be a big problem because the stresses at the middle of root are low compared to the maximum bending stresses in the root.



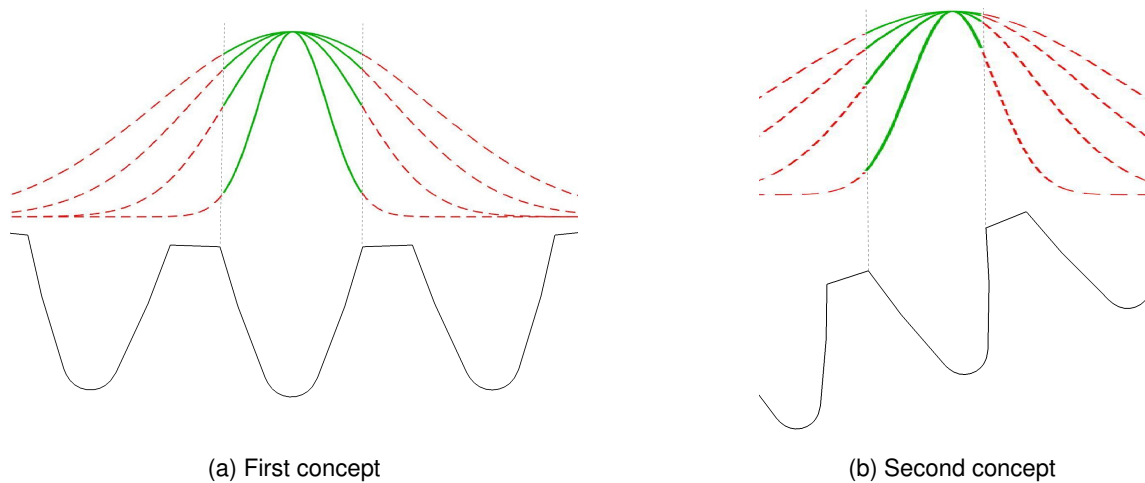


Figure 4.22: Different concepts of single track hardening for different Gaussian beam diameters

The setup to laser harden the ring gears using the above concepts is very similar to the setup for scanning laser hardening, discussed in section 4.4.1. The ring gear should again be tilted about the Y-axis according to figure 4.19b. The angles at which the ring gears should be inclined were determined for both concepts. This angle only provides a good indication of the optimal angle since in reality the beam diameter and the fact that this beam diameter changes with the distance from the focal plane has to be taken into account. This angle ( $\theta$ ), figure 4.23b, can be calculated using the following formula :

$$\theta = \arccos\left(\frac{\left(\frac{b}{2}\right)^2}{R_{top}^2 - x^2}\right) \quad (4.7)$$

With  $b$  the width of the ring gear, being 14.8mm.  $R_{top}$  the top circle radius, being 44.024mm (appendix A),  $x$  being the horizontal offset from a line passing vertically through the center of the ring gear, see figure 4.23a. The derivation of this equation can be found in appendix I.

Using the above equation it was determined that the ring gear in concept 1 should be inclined  $\pm 80^\circ$  because  $x$  will need to be equal to zero. For concept 2 theta can range from  $\pm 79^\circ$  to  $\pm 80^\circ$  depending on the desired angle of incidence. Because the angles differ so little, the setup was held at an angle of  $79^\circ$ . This angle will also have an influence on the projection of the beam on the tooth surface, one of the axes will get stretched. However, due to the small difference in angle compared to  $90^\circ$ , the axis will only get stretched by  $\pm 2\%$ . Thus, this influence will be neglected in further calculations. Next to the change in projected intensity profile, this angle will also cause one side of the gear tooth to be lower/higher than the other, causing the laser beam to be more in focus at one side. This effect can be compensated for by carefully implementing the geometry in the software that controls the laser (**TruTops PFO**). The laser itself can change the focal plane's height depending on the position where the laser impinges.

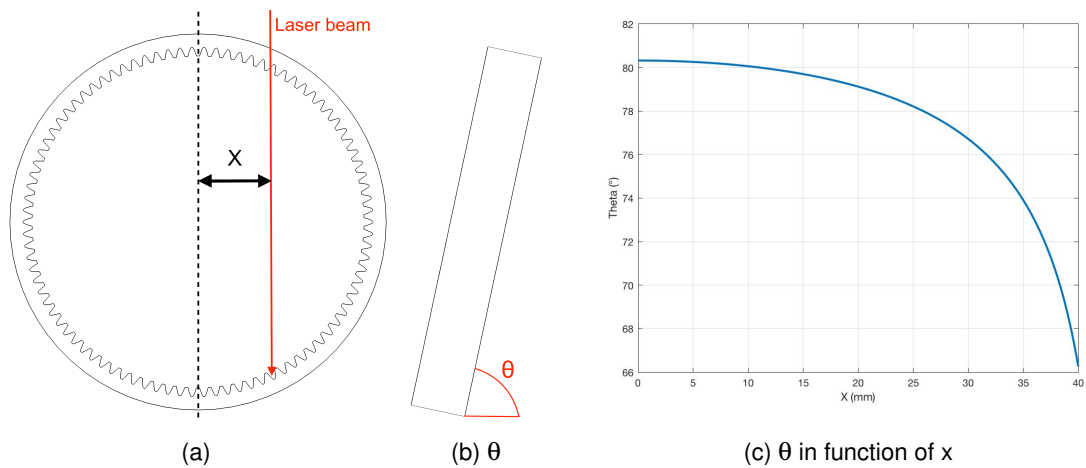


Figure 4.23: Clarification equation 4.7

In chapter 7 a model for the intensity profile for concept 1 will be developed. This model will be used in the hardening and residual stress simulations. In the upcoming chapter the setup to make the concepts achievable is featured in detail. In chapter 6 the setup to make the concepts achievable is elaborated upon.



# 5

## Cooling

### 5.1 Introduction

One of the first issues encountered while developing an appropriate setup and concept for hardening, was the issue of back tempering. Back tempering is the reduction of hardness by reheating the hardened material, allowing it to soften. In this chapter, the issue of back tempering and how to counter this issue is elaborated upon.

### 5.2 Tempering

Tempering is a heat treatment that can reduce the hardness of steel. The working principle of tempering is illustrated in figure 5.1 below. After hardening, the material is reheated again to a temperature below the lower critical temperature (to avoid losing the martensitic structures in the steel). Depending on the tempering temperature and time, a desired hardness lower than the original hardness can be achieved. This reduction in hardness is partly caused by relieving the compressive stress in the martensite layer and partly caused by diffusion of the carbon atoms out of the martensite lattice (again dependent of the tempering temperature and time) creating pearlite. When tempering, the retained austenite will also decompose. In practice, tempering is mostly used in applications where either the hardness after quenching is too high or where a higher toughness is desired. However, in our application, this softening effect when tempering is undesired. Due to the relatively small tooth size, by hardening two adjacent tooth flanks, the hardness of the previously hardened flank might be reduced drastically.

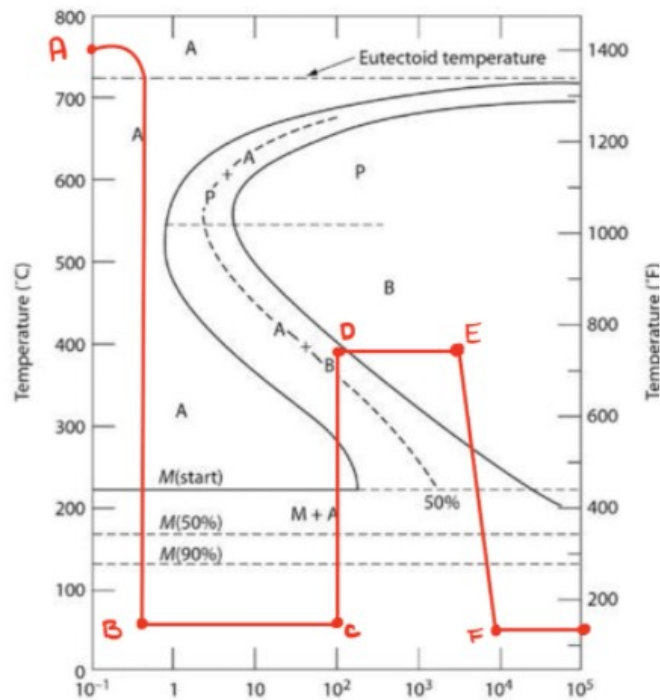


Figure 5.1: Working principle of tempering

Source: Schwab (2021)

### 5.3 Simulation without Cooling

In order to have an estimation of the backtempering effect, temperature and hardness simulations were performed, the model of which will be explained later in chapter 7. In figure 5.2 the results of these simulations are shown graphically. In figures 5.2a and 5.2b, two distinct peaks are visible. The first peak is the temperature peak of hardening the flank itself. The second temperature peak is caused by hardening the adjacent tooth flank with the second laser track. Temperatures are shown for both the middle of the tooth flank and the top of the tooth, as illustrated by 5.2c. Next, in figure 5.3, the same temperature spikes are shown for the same lasertracks, this time however 0.3mm below the surface.

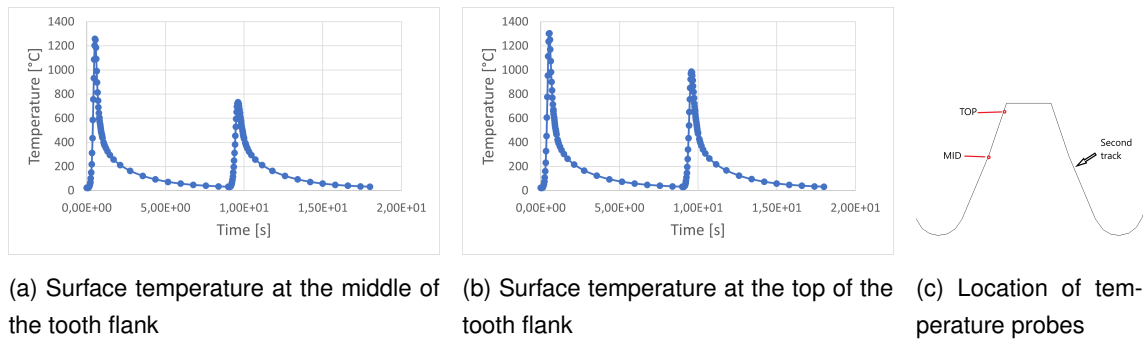


Figure 5.2: Simulated surface temperatures

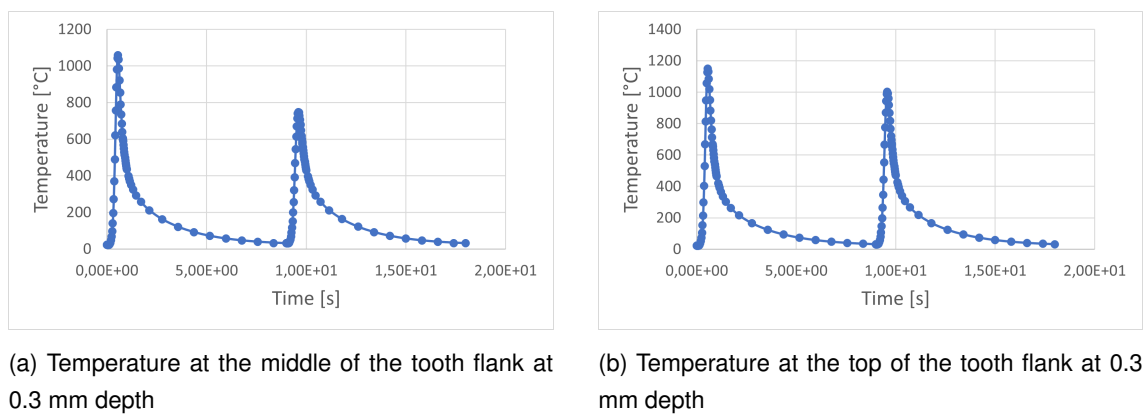


Figure 5.3: Simulated temperatures at 0.3mm depth

As is clear from the graphs, the temperature at 0.3 mm depth as well as at the surface far exceed reasonable temperatures to avoid tempering. At 0.3 mm depth at the top of the tooth flank, the temperature even exceeds the austenization temperature. This should of course be avoided at all cost.

In order to overcome the backtempering issue, the following solution was proposed: by pressing an aluminium block against the tooth flank that may not be tempered, the cooling rate at this flank will increase, causing the temperature at the tooth flank to drop. To find out whether or not this idea is valid, another simulation was performed. In this simulation, instead of convection with the air, a thermal contact conductance was determined, explained in the next section.

## 5.4 Simulation with cooling

### 5.4.1 Thermal Contact Conductance

Heat flow through homogeneous, isotropic materials has been understood for quite a long time and it can be expressed as:

$$q = -k * A_{surf} * \frac{dT}{dx} \quad (5.1)$$

where  $k$  is the thermal conductivity of the material. This coefficient is dependent on the material type, temperature, etc. With  $A_{surf}$  equal to the surface area. Thermal contact conductance is similar to conduction through homogeneous materials, however there are a few fundamental differences. Although surfaces with a low roughness might seem quite smooth to the naked eye, on microscopic level there will always be peaks and depressions visible at the surface. Due to these irregularities, the actual surface for heat conduction is quite a lot smaller than it seems at first sight. As is shown in figure 5.4a, heat conduction between two different objects will only occur between the contact points on both object's surfaces.

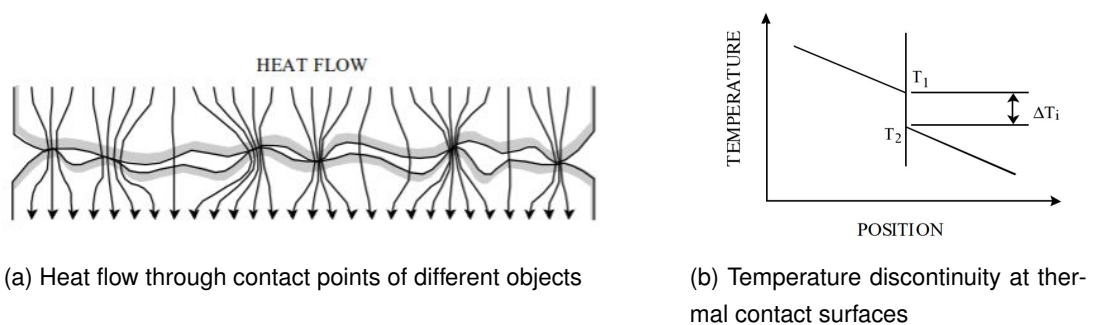


Figure 5.4: Thermal contact conductance

Source: Ayers (2003)

Due to these limited contact points, the temperature distribution close to the contact surface is quite complex. To approximate this temperature distribution, a temperature discontinuity as illustrated by figure 5.4b can be assumed at the contact surface. This temperature discontinuity is proportional to a constant called the thermal contact conductance  $h_c'$ . The meaning of this constant can be explained as follows (Ayers, 2003): A heat flux between two surfaces can occur in three different ways: conduction at the contact points, conduction across gaps between the surfaces or radiation through these gaps. (Convection in gaps that are filled with air can be neglected. Due to the size of the gaps, no bulk fluid motion will occur.) Therefore, the heat transfer rate between two surfaces can be expressed as:

$$q_j = q_{contact} + q_{gap} + q_{rad} \quad (5.2)$$

where

- $q_j$  is the heat transferred through the joint of the two objects
- $q_{contact}$  is the heat transferred by conduction through the contact points
- $q_{gap}$  is the heat transferred by conduction across the surface gaps
- $q_{rad}$  is the heat transferred by radiation

Due to the low emissivity of steel, aluminium and copper with fine surfaces (more on the use of copper later), the heat transfer caused by radiation can be neglected in this case, as the heat transfer through conduction will be much higher. Linking the heat transfer rate to the temperature difference, the following heat transfer coefficients can be defined :

$$h_j = \frac{q_j}{A_{app} \cdot \Delta T_j}, \quad h_c = \frac{q_{contact}}{A_{app} \cdot \Delta T_j}, \quad h_{gap} = \frac{q_{gap}}{A_{app} \cdot \Delta T_j} \quad (5.3)$$

Rewriting equation 5.2 using equation 5.3 gives:

$$Q_j = h_j A_{app} \Delta T_j = (h_c + h_{gap}) A_{app} \Delta T_j \quad (5.4)$$

It is clear from equation 5.4 that the heat transfer due to contact conductance is dependent of quite a few different parameters. Roughness, temperature gradient and thermal conductivity of both materials play a vital role in thermal contact conductance. However, also the softness and therefore the applied pressure on both materials is of high importance. A soft material might fill up the roughness gaps in its neighbouring material much better compared to a harder material, increasing the thermal contact conductance.

Several experiments for determining thermal contact conductance have been performed. For the combination steel-aluminium, conductance values of 50.000 to 59.000  $W/m^2K$  can be achieved. However, these values are for low roughness conditions (a maximum roughness value of 2.0  $\mu m$ ) under high pressure (up to 35 MPa). The roughness of the gear teeth is below this limit, but the infrastructure needed to achieve a pressure of 35 MPa can be quite difficult to implement into the compact setup used in this thesis for the laser hardening, which will be elaborated upon in chapter 6. Therefore, instead of using aluminium, copper was used in order to cool down the tooth flank. Copper has a higher thermal conductivity value than aluminium and is generally softer and more malleable, which should provide a higher thermal contact conductivity (for a similar surface roughness and pressure). Since no clear value was found for contact conductivity between steel and copper, in the simulation the maximum value for steel - aluminium contact was used. This way, adequate cooling could be achieved and by adjusting the pressure on the two surfaces when performing the experiments, the ideal cooling and pressure setup could be determined. The full results of the experiments are discussed in chapter 8.

### 5.4.2 Simulation results

After running a simulation with cooling (to be discussed further in chapter 7), a noticeable difference could be spotted in the temperature. Looking at a plot of the results in figures 5.5 and 5.6, a significant drop in temperature can be observed. In these plots, the temperature peak of the first track (the hardening track) is omitted and only the temperature change during the second track (where tempering might occur) is displayed.

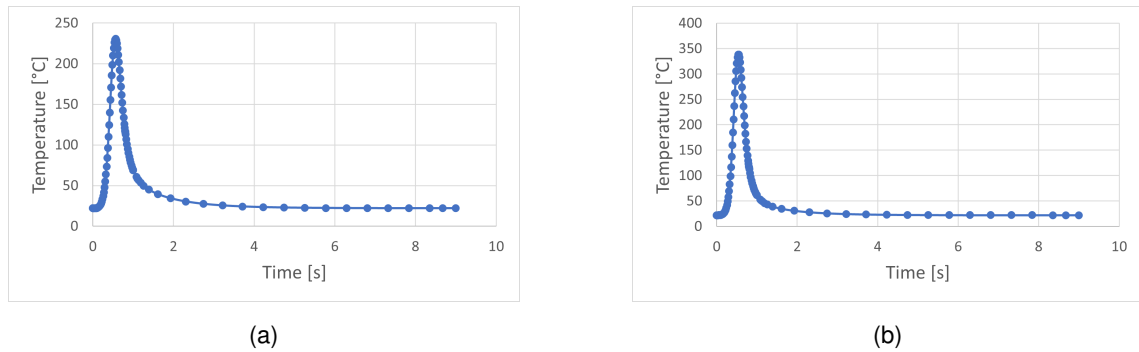


Figure 5.5: Surface temperature at the middle (5.5a) and the top (5.5b) of the tooth flank with cooling

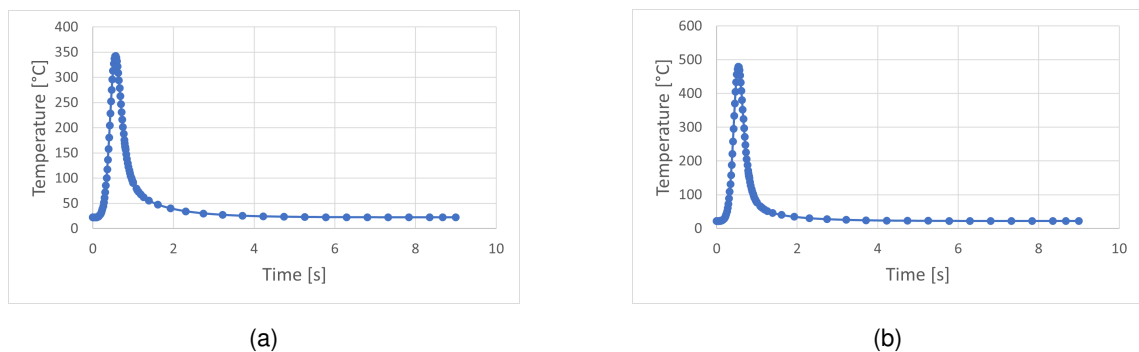


Figure 5.6: Surface temperature at the middle (5.6a) and the top (5.6b) of the tooth flank with cooling

When comparing the graphs with cooling to those without cooling from section 5.3, one can observe that the temperatures on the adjacent flank are halved or even further reduced, meaning that the block helps to cool down the tooth flank. However, in figure 5.6b a temperature of just below 500 °C still occurs at the tooth top 0.3mm beneath the surface. The following graph (figure 5.7) is from a study by Cvetkovski et al. (2012), where the influence of short heat pulses on martensite properties is investigated. The graph shows the diminishing of the hardness in relation to tempering time for a few different temperatures. One can observe that even at relatively low tempering temperatures—quite far below the austenization temperature—the hardness is reduced to below half of its original value after just 0.1s.

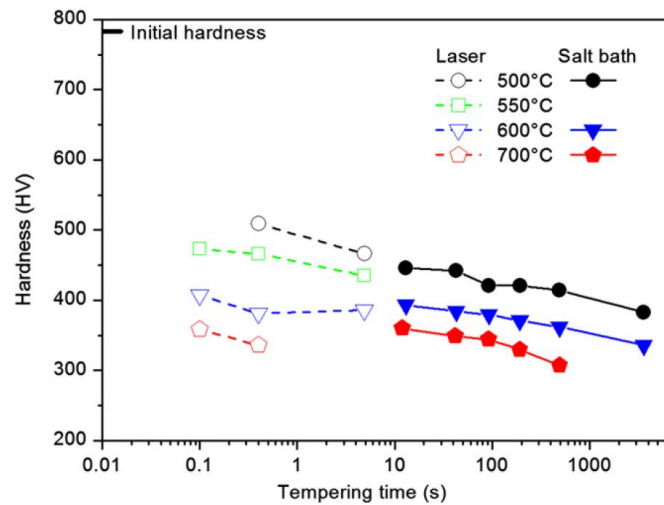


Figure 5.7: Influence of tempering time on the hardness of a medium carbon steel

Source: Cvetkovski et al. (2012)

For the simulated temperatures at the surface and at 0.3mm below the surface at the middle of the tooth flank, the maximum temperatures are quite low. Tempering —if any— should be very limited in these locations. The temperature peak at 0.3mm below the surface at the top of the tooth flank, is more of a concern regarding tempering. Looking at figure 5.7, 500 °C can reduce the hardness significantly, even for a very limited tempering time. Again, it should be considered that the tempering time is very short, but it would be reasonable to expect some tempering at this location. An advantage that 16MnCr5 has over the steel used in the article, is that it contains quite a high percentage of manganese and chromium, which aids in the retardation of softening while tempering, as illustrated by figure 5.8. This means that the hardened zone should retain its hardness much better than the medium carbon steel used in the research of Cvetkovski et al. (2012).

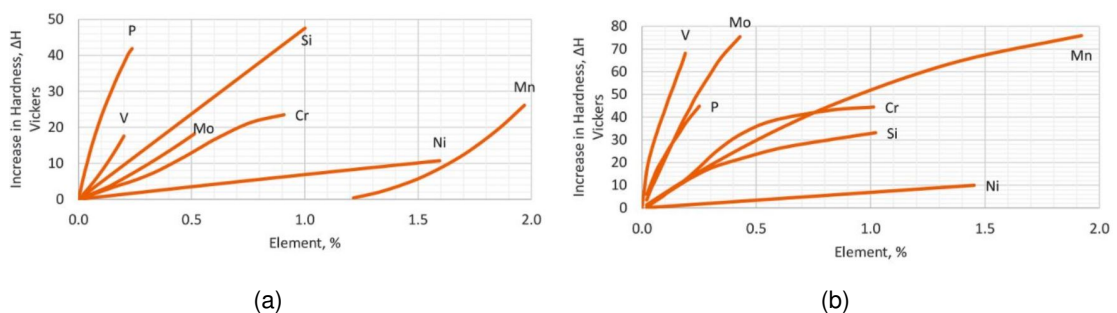


Figure 5.8: Influence of alloying elements in softening retardation at 260 °C (5.8a) and at 540 °C (5.8b)

Source: MacKenzie (2019)

Since tempering in these zones is dependent of so many different parameters, a simulation in Dante elaborated upon in chapter 7 was performed. Dante is an add-on in Ansys to simulate heat treatments on steel parts. The result of this simulation is shown in figure 5.9. A small tempering effect can be observed as the thickness of the hardest layer is slightly reduced.

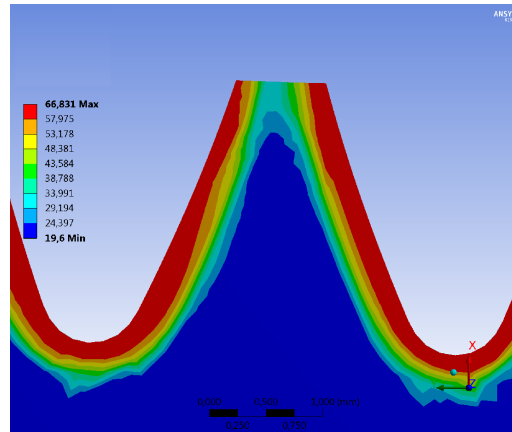


Figure 5.9: Tempering effect with cooling on the adjacent tooth flank (left) after hardening the next flank (right). Hardness values in HRC.

Although the simulations give a good indication of the tempering effect, the best way to know if tempering does indeed have a noticeable impact, is to perform experiments with the laser. If needed, the pressure on the copper cooling block can be increased or decreased depending on the test results, since the copper block should have significantly better cooling properties compared to the aluminium block first proposed as a solution. The test results are elaborately discussed in chapter 8.

In the next chapter, the setup for laser hardening the ring gear is explained. The implementation of the cooling blocks can also be found in the next chapter.



# 6

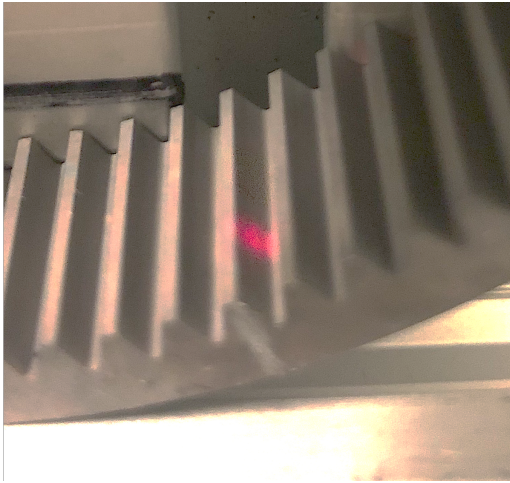
## Setup

### 6.1 Introduction

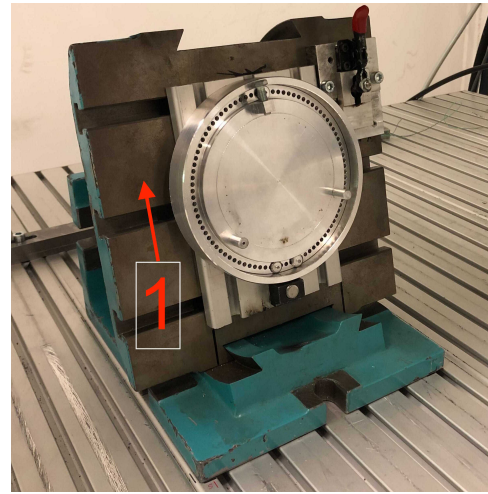
Because the ring gear has very small dimensions, see appendix A, the complexity of the research will not only lie in finding the optimal laserparameters. A great deal of thought must also be given to the design of the setup. On the one hand, the accuracy of the setup is considered and on the other hand the ease of use, after all there is a total of 180 tooth flanks to be hardened per ring gear.

### 6.2 Design

As told in chapter 4 the ring gear has to be tilted about the Y-axis, figure 4.19b. This will be taken care of by the workbench with adjustable angle depicted in figure 6.1b. Besides this angle, it is very important that the center of the laser beam is positioned exactly at the desired position depending on the selected concept. This alignment is rather difficult because the only way to know the absolute origin of the laser coordinate system is by use of a pilot laser, see figure 6.1a. This pilot laser enables the user to see where the laser beam would hit because it follows the same path as is programmed for the high power laser. Despite this being a useful tool, the system has a limited accuracy due to the diameter of the pilot laser ( $\pm 1mm$ ) and the fact that the ring gear has to be positioned by visual check.



(a) Pilot laser pointing at tooth flank

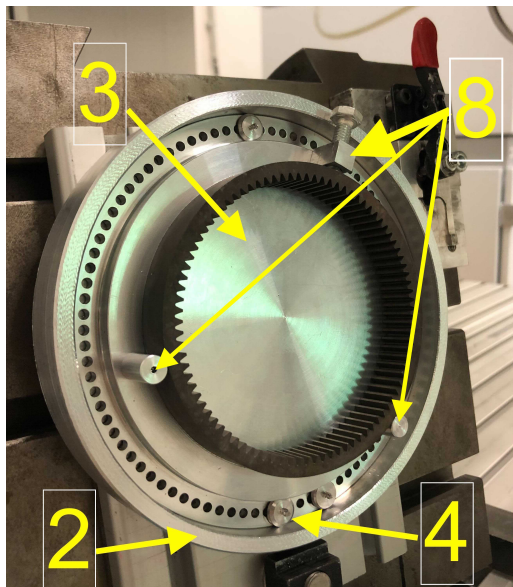


(b) Workbench used in setup (1)

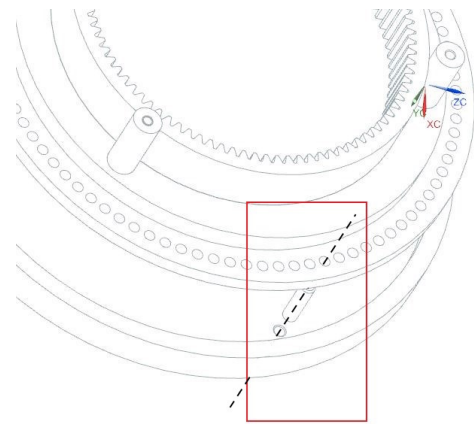
Figure 6.1: Pilot laser &amp; workbench

Once the ring gear is positioned as accurately as possible, it is important to note the fact that per ring gear 180 tooth flanks have to be hardened, thus the accuracy should be assured for every tooth. To achieve this, the setup visible in figure 6.2 was designed. The setup consists of several crucial components and is based around the baseplate. This baseplate is rigidly mounted on the adjustable workbench. Within the baseplate, a cylindrical hole is provided in which the turntable can spin freely. Between the baseplate and turntable a clearance fit is used such that the centers of both parts align correctly and the accuracy of the system is ensured. There are 90 holes in the turntable (equal to the amount of teeth per ring gear) as shown in figure 6.2b. This way, every tooth gets hardened in the same manner. The ring gear itself is locked relative to the turntable by use of a 3-point clamping system, also visible in figure 6.2. The most important components of the setup can be seen on figure 6.1b, 6.2a and 6.3a. These are :

- |               |                   |
|---------------|-------------------|
| 1. Workbench  | 5. Clamping block |
| 2. Baseplate  | 6. Copper insert  |
| 3. Turntable  | 7. Clamping bolt  |
| 4. Dowel pins | 8. Gear clamp     |



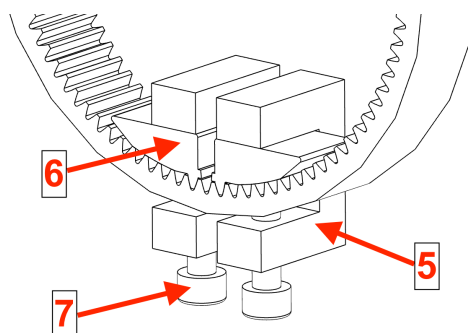
(a)



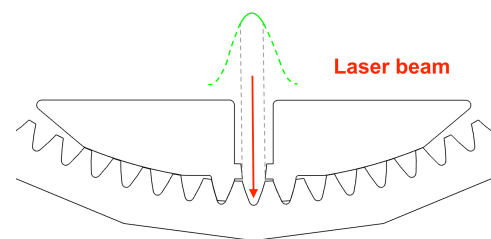
(b) Alignment holes in baseplate and turntable for dowel pin

Figure 6.2: Concept of the setup

As explained in the previous chapter, two copper inserts will be used for the cooling. These inserts are produced by wire EDM, which enables the contour of the insert to be quasi the same as the tooth profile. This is very important to ensure the required cooling. After wire EDM, the inserts will be polished at the contact surface in order to reduce the surface roughness, further improving the cooling, as stated in section 5. To generate the desired pressure on the surface between the copper insert and the tooth flank, a type of clamping system is necessary. This system is depicted in figure 6.3a. The clamping block together with the clamping bolt are used to press the copper insert against the adjacent tooth flank. The copper insert also has the function of blocking off the input Gaussian beam from hitting the tooth top, as explained in section 7.2. This effect can be seen in figure 6.3b. Technical drawings of all the custom designed parts can be found in appendix H.



(a) Clamping system of the copper inserts



(b) Blocking off incoming laserbeam

Figure 6.3: Clamping system used for cooling

### 6.3 Improvement of setup

When performing the tests described in chapters 4 and 8, a few features that could be improved for the future setup were noted. First of all, there were some issues with ring gear alignment. Using the pilot laser, a lot of attention had to be paid to aligning the ring gear. Instead of using the pilot laser, a more accurate solution for this could be to first position the ring gear using the pilot laser and afterwards, impinging certain parts of the ring gear with very small spots using the powerful laser. These spots should be chosen such that it is clear to see if the gear is positioned correctly or not, for example at straight edges. The advantage of this is that the spot size, and thus the marking, can be kept very small (0.18mm), increasing the accuracy. A drawback of this is that the alignment is still very dependent on observations by the user. In addition, the small markings can damage the material locally. However, due to the design of the setup, once the alignment is correct for one gear tooth, it is correct for all other teeth. On top of that, with a spot of 0.18mm, more than sufficient alignment can be achieved.

Another difficulty in the setup is that the Z-distance of the part to be lasered has to be set manually. The only way to know if the surface is positioned in the focal plane, is by a physical reference. It can be quite time-consuming to get this vertical positioning right. Therefore, if all ring gears would be lasered for use in the car, it might be interesting to manufacture a second reference object that corresponds to the height of a reference point on the ring gear measured from the laser workbench. This solution was not applicable for this thesis, as the turntable was used by many different people. This meant that the setup had to be deconstructed after every visit to the FOKUS lab.

In the next chapter, the simulations performed before testing are explained. In chapter 8, the actual results obtained with the setup described in this chapter are analyzed in detail.

# 7

## Simulations

### 7.1 Introduction

The goal of this chapter is to devise a model that represents the laser which can be used for thermal and hardening simulations. These simulations will be used to minimize the amount of experiments to perform. On the one hand many samples are required to do the experiments. These samples can be expensive and time consuming to produce. On the other hand, there is a lot of insight to be gained in the way the hardness at the surface is generated by devising a model instead of just changing all the laser parameters until a sufficient result is achieved.

### 7.2 Approximate models

As indicated in section 4.4.2, first a model will be devised for the intensity profile for single track hardening using concept 1. In the thermal simulation software, Ansys, the laser is mimicked as a heat source by using a heat flux at the tooth surface. The fact that the tangent angle of the tooth surface changes from top to root makes the generation of the model more complex. In Ansys a curved surface will be seen as a flat surface in which the length of the flat surface is equal to the circumference of the curved surface. For this reason using a Gaussian intensity profile as a heat flux will not generate the desired realistic result. This principle is further clarified in figure 7.1. Overall, the projected Gaussian has a lower amplitude than the original Gaussian. This is because the tangent angle at a position on the tooth flanks different from the middle of the tooth root differs from  $0^\circ$ , causing the same amount of heat flux having to be shared by a greater surface area. Of course the original Gaussian possesses the same amount of energy as the projected Gaussian,

that is why the intensity amplitude is proportional to the cosine of the tangent angle at that point measured in relation to the horizontal.

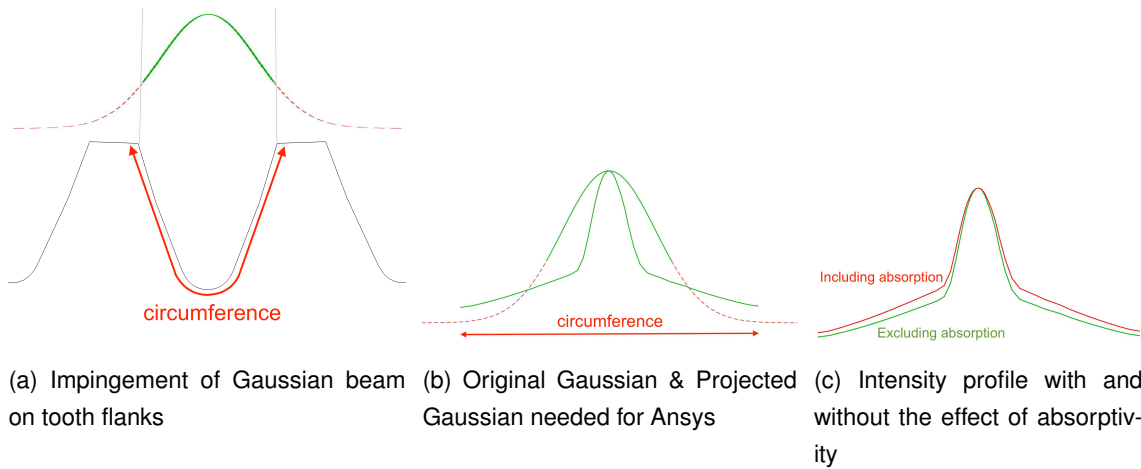


Figure 7.1: Modification of model to work with curved surfaces

As seen in chapter 4, the absorptivity of the laser beam changes with the incident angle. Although the absorptivity is dependent on a lot of parameters the Fresnel equations are used because they have been approved by the industry as well (Duflou et al., 2014). Ideally a relationship between the 2 quantities would be established experimentally, but since the used method of determining the absorptivity is adequate to determine a ball park figure, this did not seem very suitable for this application. Overall one can observe that the absorptivity is increased with the angle up until the brewster angle, which in most cases is larger than the maximum incident angle for our application. Therefore the absorbed intensity will increase at the tooth flanks. When implementing this effect into the model, an intensity profile like the one in figure 7.1c is obtained.

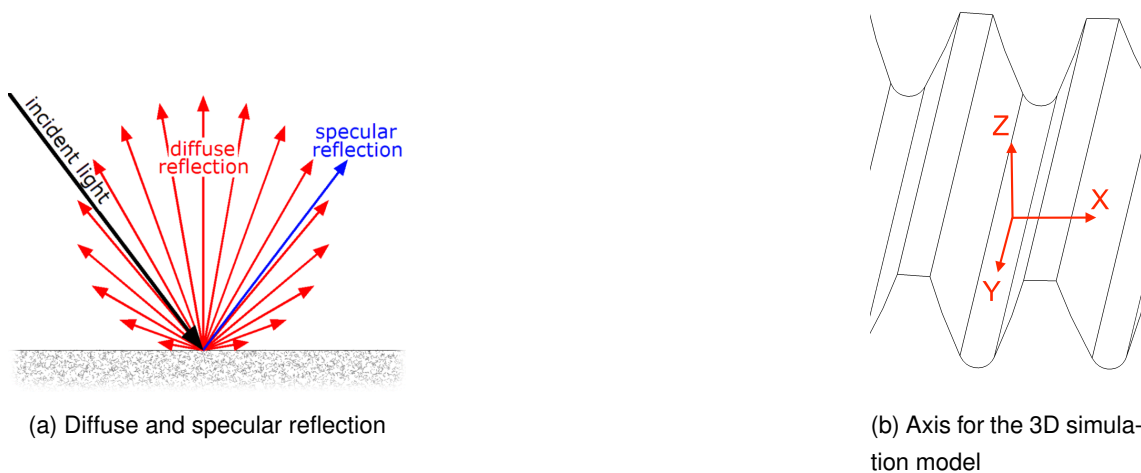
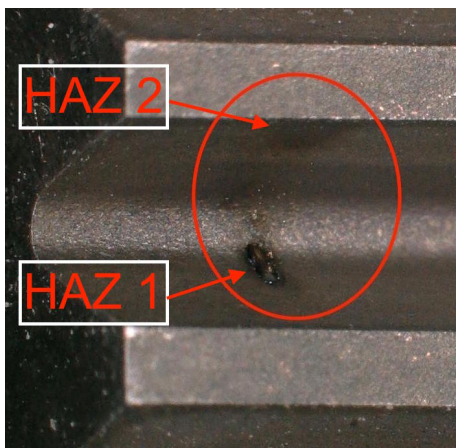
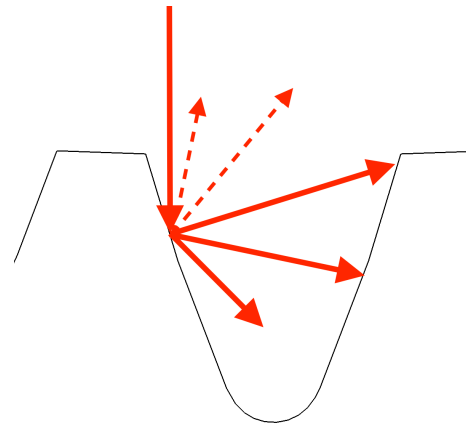


Figure 7.2: Reflection & coordinate system

Reflection from one tooth to the adjacent one can also have an influence on the intensity profile. The absorptivity of a laser beam will never be equal to 100%. The energy of the laser beam that is reflected can then be absorbed by an adjacent tooth surface. Two types of reflection can be distinguished: specular and diffuse reflection. Diffuse reflection is the most common for metal surfaces. For surfaces with a very low roughness, mirror-like, specular reflection is also possible. The roughness of the gear is relatively high and thus diffuse reflection will be more likely (Choudhury, 2014). Because reflection is very dependent of several variables, experiments were executed on this subject. In figure 7.3a it can be seen where most of the reflected power is pointed towards. During these tests the laser beam was impinged in the same way as in figure 7.1a, except here the beam diameter was kept way smaller and the center of the laser beam was positioned so it hit the bottom of the tooth flank (HAZ 1). One can observe that most of the reflected power hit the top of the adjacent tooth flank, which suggests the presence of diffuse reflection because the intensity of the reflected power is highest in the direction perpendicular to the surface from which the laser light is radiated.



(a) Reflection experiment



(b) Visualisation of diffuse reflection

Figure 7.3: Diffuse reflection in tooth flank

To incorporate this effect in the intensity profile model some assumptions have to be made. First of all, the reflected power is dependent on the absorptivity, which is a quantity that is difficult to determine. Besides that, it will be assumed that only diffuse reflection will occur, in reality some percentage of the reflection will be specular. Not all of the initially reflected power will be absorbed by the adjacent tooth because some of the reflected beams will pass above the adjacent tooth top or the reflected beams might impinge on parts of the ring gear relatively far away from the heated zone and as such they have little to no influence. Besides that, the other flank also has a certain absorptivity for the laser beam. For the mathematical derivation of how reflection will influence the intensity profile, see appendix J. Figure 7.4 shows a summary of all aspects that influence the final intensity profile. From this figure it is clear that the used Gaussian beam diameter has a very significant impact on the model and that it can easily be used to get a uniformly hardened surface layer. Next to this, due to the effect of the incident angle on the absorption coefficient and the effect

of reflectivity, the intensity will increase at the tooth flanks in comparison to the projected Gaussian model, 7.1b.

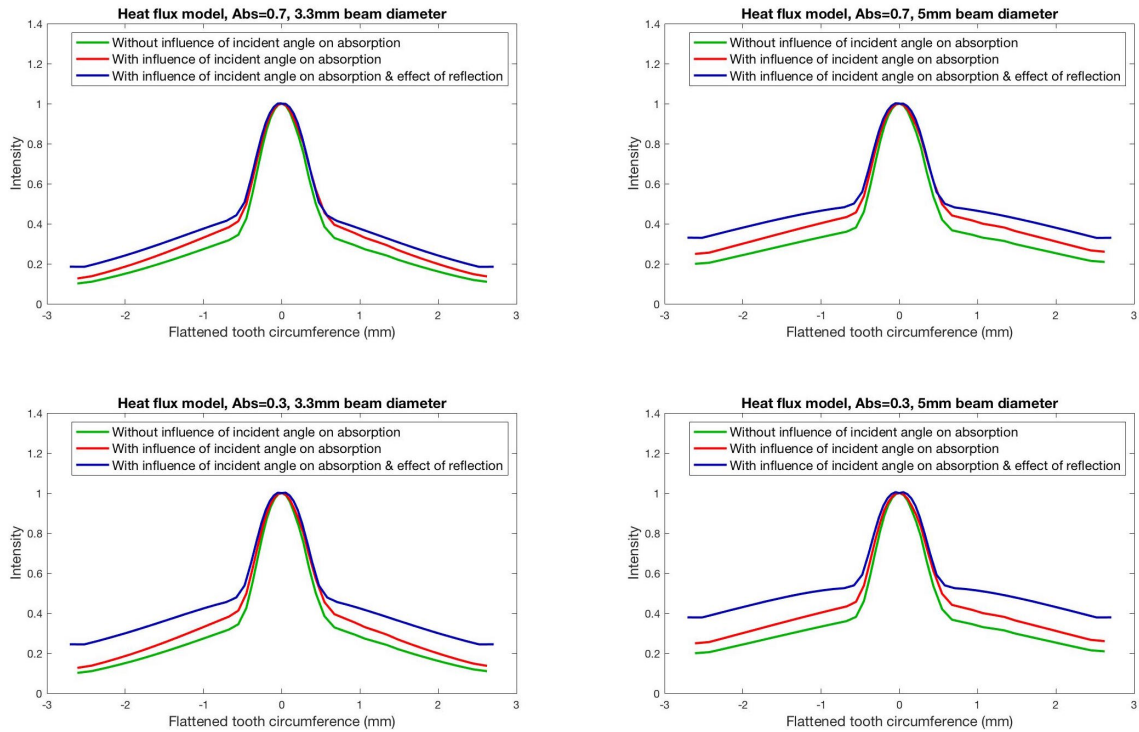


Figure 7.4: Clarification of the important parameters that influence the model

One last effect on the intensity profile is considered: the influence of the temperature on the absorption of a laser beam as explained in section 4.3.2. It is known that the absorption increases with the temperature of the surface that is being impinged. To explain why this has an influence on our situation, a thought experiment follows. When the laser impinges the surface for the first time the temperature of the surface will be directly correlated to the amplitude of the intensity profile at that point because not enough time is allowed for the heat to dissipate, so the fact that the tooth top has less quenching media underneath it in comparison with the tooth root is of no influence. One timestep later the laser beam sees that some parts of the surface are hotter than others and thus the absorptivity will change accordingly. To process this into the model, it is required to know how the absorptivity changes with temperature. As explained earlier, the absorptivity tests did not provide exact values. That is why values that are known from the literature were used (Grum, 2007). A quadratic relation between the absorptivity and temperature is supposed in the working temperature range (20 °C - ±1450 °C), see 7.1.

$$T_{influence} = (a_1 + a_2 \cdot (T - T_0)^2) / a_3 \quad (7.1)$$

With  $a_1$ ,  $a_2$  and  $a_3$  constants depending on the surrounding and melting temperature and absorptivities.  $T$  temperature.  $T_0$  the surrounding temperature.



In conclusion the model still has to be adjusted such that it consists of a 3D-model instead of a 2D-model. The change of the intensity profile due to the tooth profile had already been determined (the XZ-plane on figure 7.2b). To cope with the intensity profile in the YZ-plane one has to look at the axisymmetric Gaussian input beam. Due to the fact that the ring gear is symmetric through the XZ-plane, the intensity profile can be copied from the Gaussian input in this direction. Being :

$$I = e^{-(y/G)^2} \quad (7.2)$$

With  $I$  the intensity of the laser beam,  $G$  the standard deviation of the laser beam.

To program the derived model derived in Ansys, a comprehensive equation dependent on the X- and Y-position and time is required, here equation 7.3. A 3D representation of this model is shown in figure 7.5

$$I = (A_1 + A_2 \cdot e^{-(X/F_1)^2} - A_3 \cdot X^2) \cdot T_{influence} \cdot e^{-(X/F_2)^n} \cdot e^{-((Y-V_Y \cdot t)/G)^2} \quad (7.3)$$

With  $A_1$ ,  $A_2$ ,  $A_3$  and  $n$  constants which are also dependent on the desired input power.  $F_1$  and  $F_2$  are standard deviations.  $G$  is the standard deviation in the Y-direction depending on the Gaussian beam diameter.  $V_Y$  is the velocity in the Y-direction because the beam will translate across the tooth root.

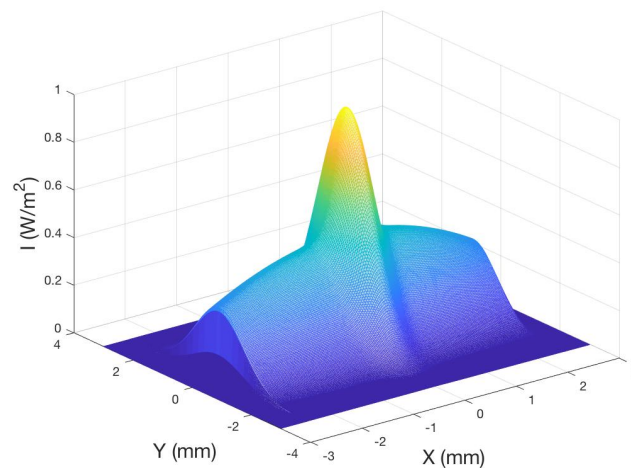


Figure 7.5: 3D representation of model used for concept 1

From figure 7.5 it is observed that the sides in the X-direction are cut off. This was necessary in the model since this position represents the highest point of the tooth top. Of course the Gaussian input beam will not stop at this point but it is blocked off using a copper cover, see section 6.

Next up, all the variables that can be changed during the simulations to get the uniform hardness at the proposed case hardening depth discussed in section 3.4. First of all, the input beam diameter

—which offers many different possibilities to get an ideal hardening profile —has to be determined. Up next are the translation speed in the Y-direction and the used power. These two variables go hand in hand and should be selected with caution. They can have a very large influence in the reached case hardening depth.

### 7.3 Heat equation

To know how the above model will influence the temperature of the gear, the heat equation (7.4) will have to be incorporated in some way. The heat equation is a partial differential equation which makes it rather difficult to solve (Kruth et al., 2007). These equations will be solved using FEA software, Ansys in this case.

$$\frac{\partial^2 T}{\partial X^2} + \frac{\partial^2 T}{\partial Y^2} + \frac{\partial^2 T}{\partial Z^2} + \frac{\dot{q}}{k} = \frac{\rho_{mat} C_p}{k} \frac{\partial T}{\partial t} \quad (7.4)$$

In the past, models have been developed to solve the heat equation in laser processing for Gaussian and other intensity profiles (Xia and Majumdar, 2007) (Komanduri and Hou, 2001). These models do have a big drawback, namely that they can only be used when the material is thick enough for the heat generated by the laser to be dissipated. A good rule of thumb is that the depth of the material is at least five times bigger than the desired case hardening depth such that self quenching is guaranteed (Altergott and Patel, 1982). The geometry of the ring gear does not comply with this, see appendix A, which is why FEA is required to get an insight into the process. In the coming section, the results of the simulations in Ansys will be discussed. These results will then be coupled to the results from the DANTE simulations, the heat treatment software to simulate the hardening proces.

## 7.4 Simulations in Ansys & DANTE

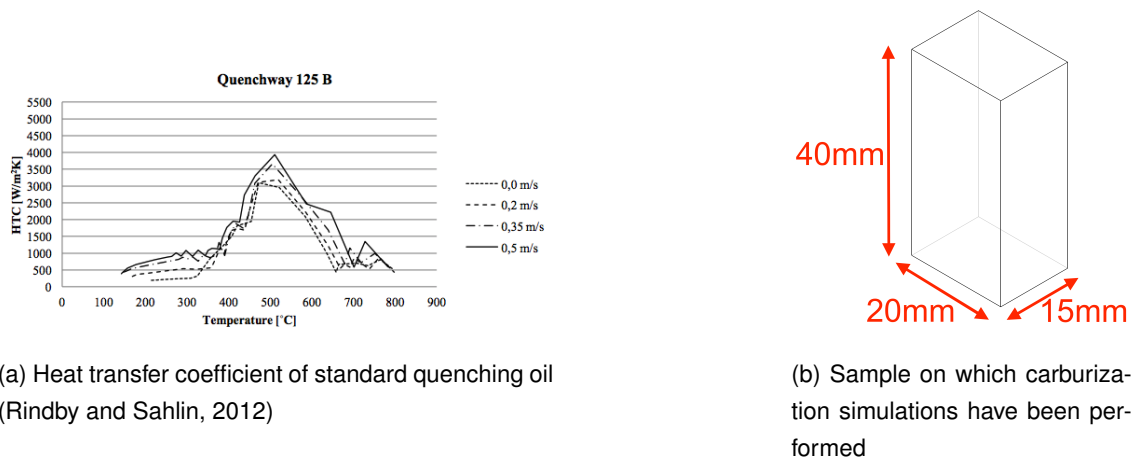
### 7.4.1 Used software packages

As stated earlier Ansys and DANTE will be used for the simulations. Ansys is a very well known FEA software package which is capable of very advanced transient thermal simulations while remaining user friendly. An excellent feature of Ansys is that heat fluxes can be added to all sorts of surfaces by implementing multivariable equations in the APDL commands. Using the thermal histories gained from the model in Ansys, it was possible to derive the fraction of martensite —and therefore the hardness —at every point in the material using TTT/CCT diagramma. However, it is also interesting to know how the residual stresses at the surface and beneath are formed. For this, analytical phase transformation models are required, since the strain due to the phase transformations and thermal gradients has to be known at every moment in time. This is where the heat treatment software, DANTE, comes in handy. Dante includes the analytical models to derive all the phases during and at the end of a thermal process. Besides that, DANTE also has shown

compliance with the stress and distortion states of workpieces during and at the end of thermal processing. DANTE has also put a great deal of focus on the carbon diffusion process which enables the user to model carburizing processes.

### 7.4.2 Carbon diffusion

After wire EDM of the gear profile, the first step in getting the ring gear hardened is carbon diffusion. FEB partner, Gearcraft Vanhoutte NV, provided the information that in general, for workpieces to reach a case hardening depth of 0.3mm during a traditional carburizing process (with quenching), these parts have to remain in the furnace for  $\pm 20$  minutes at  $920^\circ\text{C}$ . However, the carbon concentration gradient that will occur in the depth of the material is still unknown, because the rate at which carbon will be absorbed, is unknown. For this reason, several carburizing simulations were performed on a large sample, seen in figure 7.6b, to know what film coefficient should be applied in the model to obtain carburized ring gears with a case hardening depth of 0.3mm. The difficulty in this is that type and quality of quenching oil the partner would use in a traditional process is also unknown. That is why heat transfer coefficients found in literature for standard quenching oils were used, see figure 7.6a.



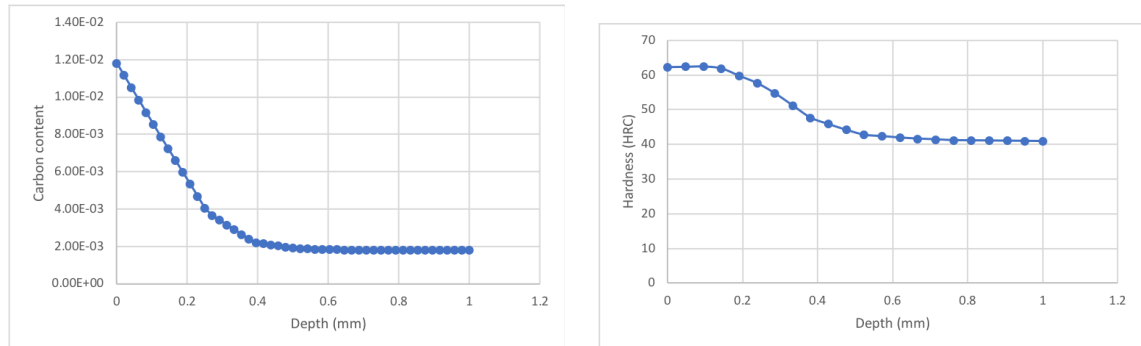
(a) Heat transfer coefficient of standard quenching oil (Rindby and Sahlin, 2012)

(b) Sample on which carburization simulations have been performed

Figure 7.6: Quenching oil & used samples

After iterating the simulation for different values of the film coefficient, a film coefficient of  $0.0129\text{W/mm}^2$  was found to give the best result. Results can be seen on 7.7. This carbon distribution will be used in the further simulations for laser hardening. On figure 7.7b a relatively high hardness can also be observed deeper in the material. This occurs because even deeper in the material, the cooling rate can be quite high because of the compact dimensions of the sample. Even though 16MnCr5 contains a low amount of carbon, martensite can still be formed if the cooling rate is sufficiently high. Due to the reduced carbon content, the martensite that is formed will have a considerably lower hardness compared to the martensite at the outer edges of the material. It can also be observed that the carbon content stagnates at a depth of  $\pm 0.4\text{mm}$  with a carbon content of  $\pm 0.18\text{ wt}\%$ ,

which is the untreated carbon content of the material used, see appendix B. This carbon gradient is used in further simulations of carburizing and laser hardening the ring gear.

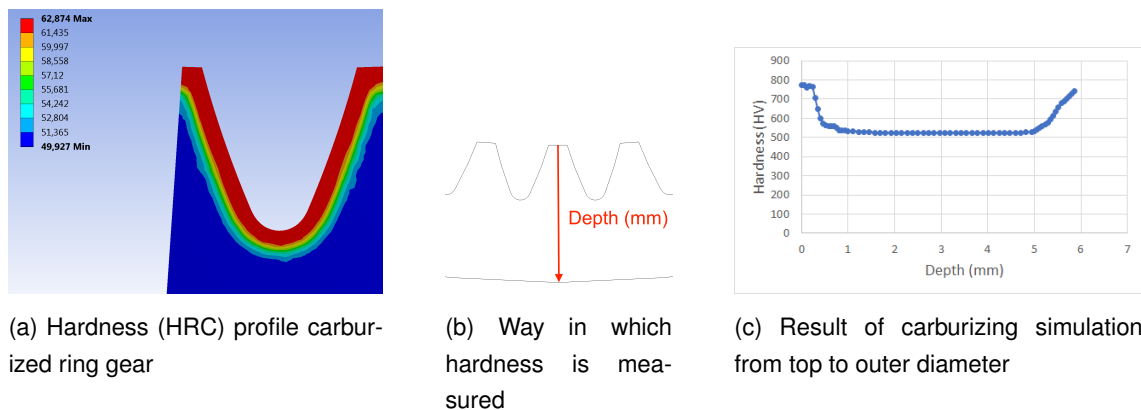


(a) Optimised carbon content for carburization of large sample in Dante (b) Optimised hardness profile for carburization of large sample in Dante

Figure 7.7: Simulation data for carbon diffusion

### 7.4.3 Carburization

To have a general idea about the microstructure and hardness of the traditionally carburized gear, carburizing simulations were performed on the ring gear. In order to do this, the above carbon distribution was determined. The same oil quenching data as in section 7.4.2 was used. The results of this simulation can be seen in figure 7.8. It is clear from figure 7.8c that the hardness at the bulk of the ring gear is very high, especially for a ring gear that is intended to be case hardened. This effect has the same reason as explained in section 7.4.2. In the next chapter these simulations will be validated.



(a) Hardness (HRC) profile carburized ring gear (b) Way in which hardness is measured (c) Result of carburizing simulation from top to outer diameter

Figure 7.8: Simulation data of carburization simulation

#### 7.4.4 Laser hardening

As seen earlier in chapter 2, to generate a hard surface layer, this layer of material has to go through a certain thermal history. To reach this result in the simulations, a study was performed on the influences of all the parameters which are free to choose in the concept. After some time, it became clear that external cooling was needed on top of the cooling that was already present due to the self quenching property of the gear because the desired case hardening depth is relatively large in comparison with the thickness of the tooth. From the simulations it was abundantly clear that without cooling on the adjacent tooth surfaces, back tempering would occur as explained in chapter 5. After implementing the cooling in the transient thermal model, the free variables of the model had to be changed again until the desired hardness values were reached. The cooling gave a new free variable as the pressure with which the copper block is pressed against the tooth surface could be chosen freely. After several iterations between the free variables, the optimal theoretical parameters were found to be :

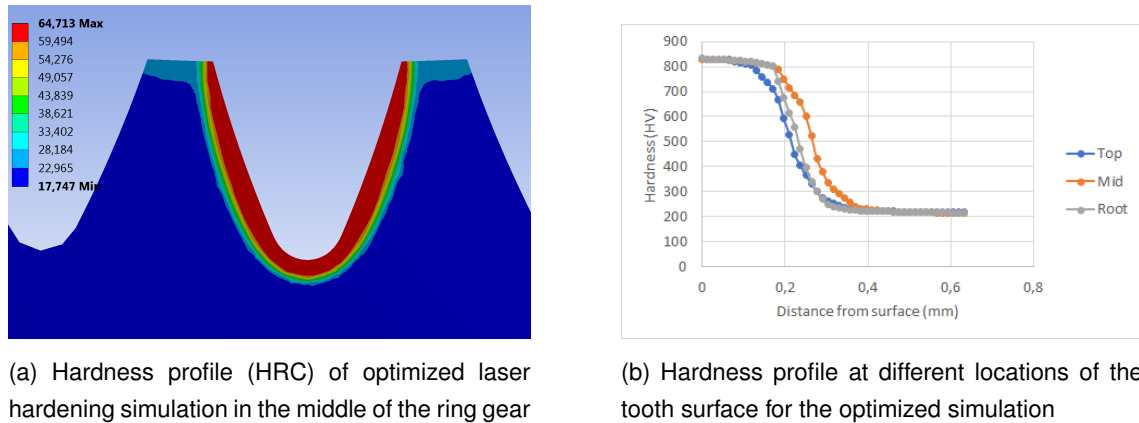
- A transverse velocity about the Y-axis (7.2b) of 15mm/s
- A Gaussian input beam diameter of 5mm
- 600W absorbed power

As for the intensity amplitude of the input Gaussian beam: this variable should be derived experimentally, since the exact absorptivity to the laserlight is unknown. Although an adequate absorptivity value to work with was found, iterations should still be made to find the optimum intensity amplitude. As seen earlier, section 2.4, the maximum temperature over the surface should be as high as possible without melting. However, temperatures close to the melting temperature can also have a great influence on the absorptivity as seen in section 4.3 and thus making the model more complex.

In figure 7.9 the hardness values in the tooth flank and root of the optimised simulation can be found. From this figure one can see that a very nice hardness profile is obtained as the hardening depth is quasi constant over the tooth surface. Because of the large amount of cooling mass at the root of the gear teeth, the effect of the high power density at the gear root is not as noticeable as expected. The case hardening depth of this simulation is greater than the optimum case hardening depth determined in section 3.4. It will be explained why a case hardening depth greater than the optimum is not that much of a problem in section 8. It is also important to state here that in the simulation, carbon diffusion has only been applied to the surface that has been laser hardened later. This is why the adjacent tooth flank has the same hardness as the bulk material. In reality, the higher carbon content at the surface of the teeth will cause the hardness to be higher even when the teeth are not yet hardened.

As explained in section 2.2, it is also clear from figure 7.10a that there will still be a certain amount of retained austenite after hardening. On figure 7.10b the maximum temperature distribution at this point of the ring gear can be seen. As explained earlier the maximum temperature is desired

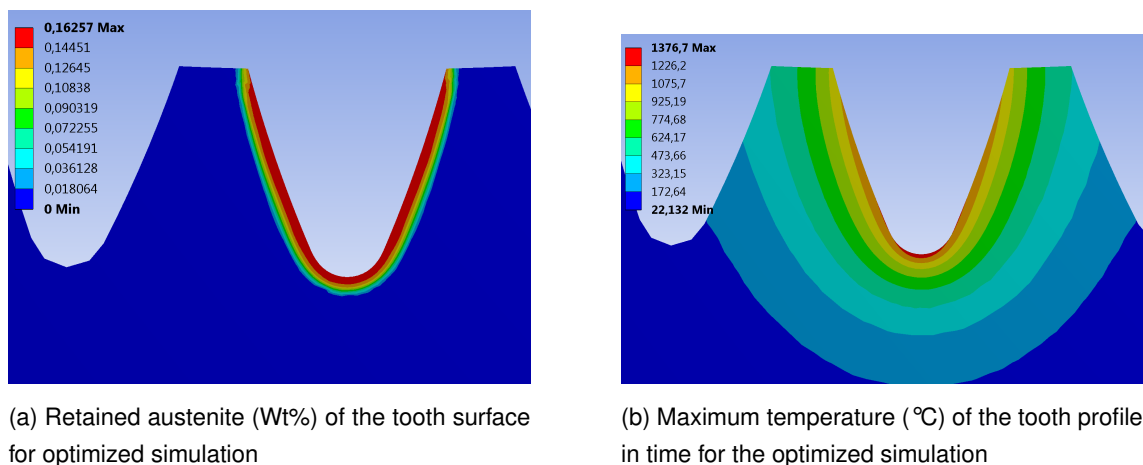
to be as high as possible but still lower than the melting temperature, which is why this maximum temperature ( $\pm 1377^\circ\text{C}$ ) was selected.



(a) Hardness profile (HRC) of optimized laser hardening simulation in the middle of the ring gear

(b) Hardness profile at different locations of the tooth surface for the optimized simulation

Figure 7.9: Optimised hardness profile



(a) Retained austenite (Wt%) of the tooth surface for optimized simulation

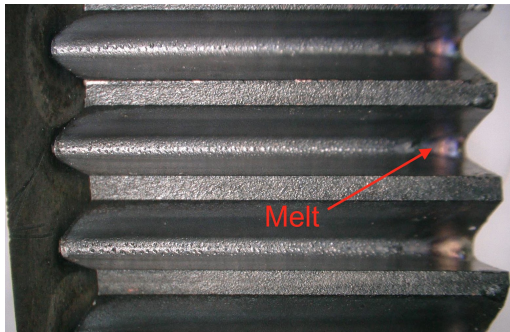
(b) Maximum temperature ( $^\circ\text{C}$ ) of the tooth profile in time for the optimized simulation

Figure 7.10: Retained austenite & maximum temperatures

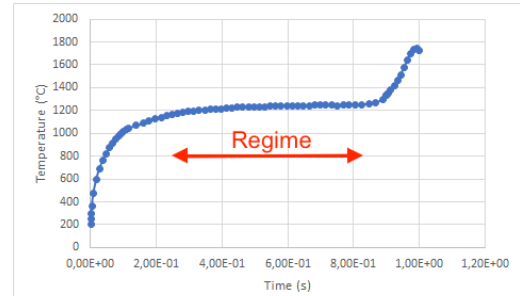
## 7.5 Influence of the geometry

The previously shown hardness profiles, figure 7.9b, were the hardness values measured at the middle plane of the ring gear, figure 7.12a. Around the middle plane of the ring gear the thermal history of all the points of the material will be in regime, meaning that maximum temperature of all the points of the material will not increase or decrease in time. This effect can be seen in figure 7.11b. The points at the sides of the ring gear need to have the same maximum temperature over time, but at the beginning of the laser track some time is needed to get into the regime, thus a less deep hardening depth will be achieved. At the end of the laser track there will be a lot of heat build-up because there is less material for the heat to dissipate to and thus a greater hardening

depth or even melt, see figure 7.11a. If this effect is not compensated, the ring gear would become unusable.



(a) Optimal laser settings without compensation at the sides



(b) Regime of maximum temperature without intensity compensation at edges

Figure 7.11: Temperatures at the side of the ring gear

To fix this problem, the intensity of the laser had to change depending on the distance from the middle plane where the laser was impinging. A function is built into the Trumpf laser which is called 'ramp-up' or 'ramp-down'. This function enables us to change the intensity in a linear way up until or from a certain percentage ( $I_{ramp}$ ) of the intensity for a certain distance ( $Y$ ), both  $I_{ramp}$  and  $Y$  can be chosen freely. A clarification of this effect can be seen in figure 7.12b. Another way to solve this problem may be to let the input laser beam not start/end at the edge of the ring gear but at some distance from the side. This way there will be less heat build up because there is enough material that is still at a relatively low temperature such that the heat can dissipate easily. The first possible solution was implemented into the model used in Ansys and DANTE such that the optimal  $I_{ramp}$  and  $Y$ -values in the start and end of the laser track could be determined. Specifically, this aspect was implemented by adding an extra term to equation 7.3, as can be seen in equation 7.5. With this intensity profile a total of 3 different equations is required, which will be implemented one after another in 3 different timesteps. One for the ramp up/down at the start, one for the constant intensity when the temperatures are in regime and one with a ramp down at the end of the laser track.

$$I_{WithRamp} = I \cdot (C1 + C2 \cdot Y) \quad (7.5)$$

With  $I_{WithRamp}$  the intensity equation for concept 1 with the implementation of the start and end ramp.  $C1$  and  $C2$  are constants depending on where the ramp starts and how steep the ramp is.

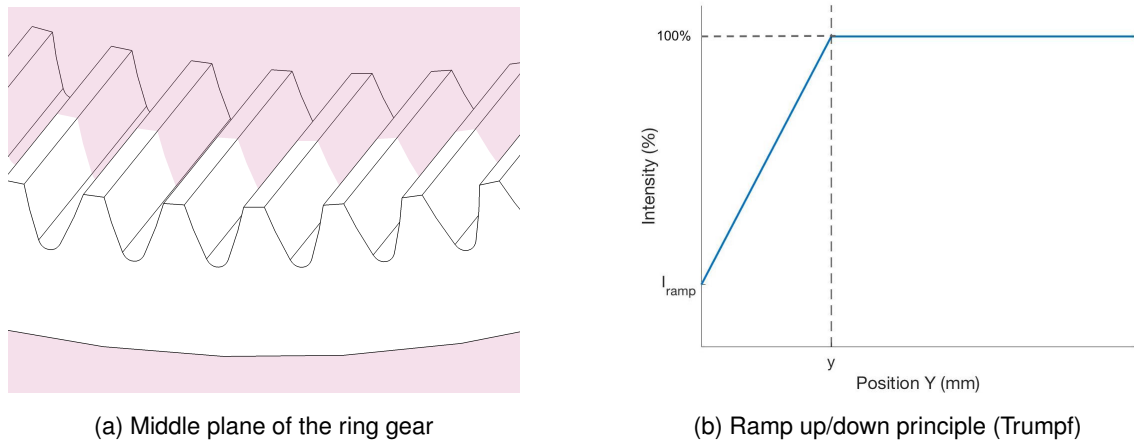


Figure 7.12: Temperature compensation principle

After iterating the above variables it was found that a ramp-down in the beginning and end would be needed for the temperature profile over time to get a quasi constant maximum value. Results of this can be seen in figure 7.13. Due to the optimisation there is a very clear difference noticeable between the temperature profiles, figure 7.11b and figure 7.12b. The maximum temperature (and thus the hardening depth) was kept relatively constant over time and there was certainly no melt at the end of the laser track. Of course, the quenching rate at the sides can also differ from the quenching rate in regime which causes more or less martensite to be formed, affecting the hardness. From the simulations a slight difference in case hardening depth was observable, which is acceptable. These simulations should still be validated, but during the initial hardness tests more ring gears were used than anticipated and thus no samples were left for validation of this principle. In the conclusion the entirely laser hardened ring gear will be discussed. On this ring gear the above ramp-down settings were used to ensure no melting at the sides would occur, since this ring gear was needed for the measurement of the distortions. However, a hardness simulation in DANTE has been conducted with the temperature compensation. Results can be seen on figure...

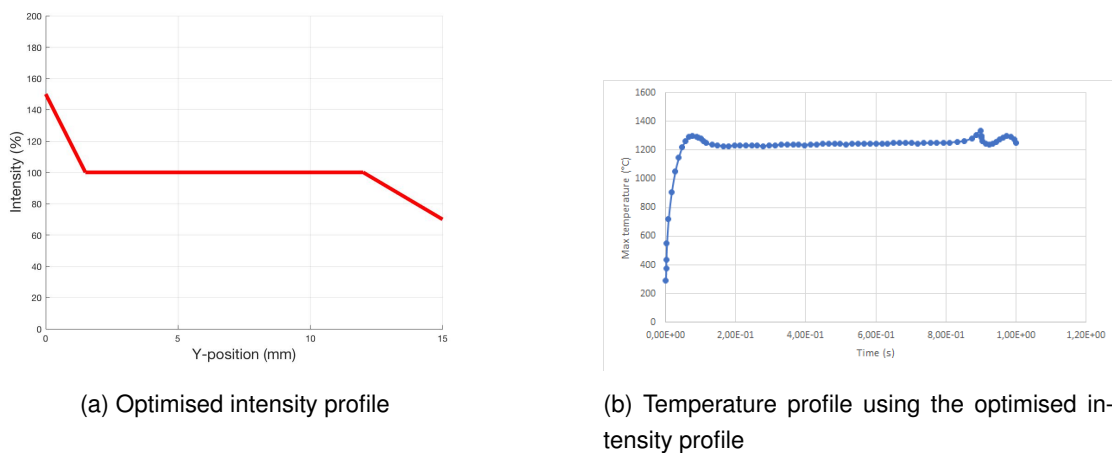


Figure 7.13: Temperature validation



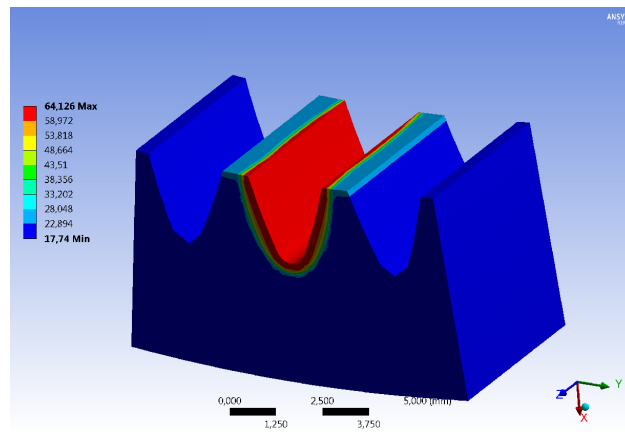


Figure 7.14: Laser hardened tooth with temperature compensation (Hardness in HRC)

# 8

## Results

### 8.1 Introduction

In this chapter the simulations from chapter 7 will be validated. The different phases of the carbon diffused steel are analyzed. Afterwards the hardness values of the carburized and laser hardened gear will be measured. While analyzing the results, the actual test data will be compared with data from the simulations.

### 8.2 Carbon Diffusion

To know how the simulations differ from the laser hardened gear, it is important to carefully monitor every step in the hardening process, the first of which is the carbon diffusion step.

It is rather difficult to know the exact carbon concentrations at the surface of the ring gear and beneath it. A simple approximate method of knowing how much carbon is present in the material is by visual inspection of the phases. On figure 8.1 the phase distribution of different depths in the material can be seen. In the bulk ferrite and pearlite can easily be distinguished, which proves that the steel is hypoeutectoid at this point. Close to the edge ( $\pm 210\mu m$ ) cementite and pearlite can be distinguished, meaning that the steel is hypereutectoid. It is important to keep the carbon content as low as possible in the zones which will not be hardened, since hypereutectoid steels are very brittle, especially when compared to hypoeutectoid steels. In addition, the tensile strength of the steel will drop if the carbon content is increased above the eutectoid composition. Because the optimal case hardening depth at the tooth flanks was determined to be around  $\pm 100\mu m$  (section 3.4), the depth of carbon diffusion most probably is a bit too deep. This is unfortunately the case

because the ideal hardening depth was determined after the test samples were produced and carburized. There was quite a lead time on these test samples, so the hardening depth was based on the one used on last year's ring gear.

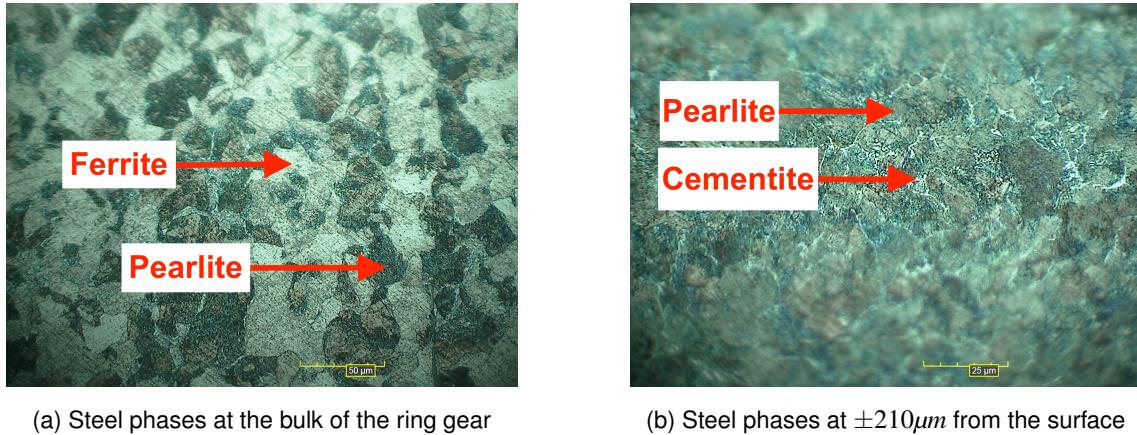


Figure 8.1: Phases of the steel in different positions

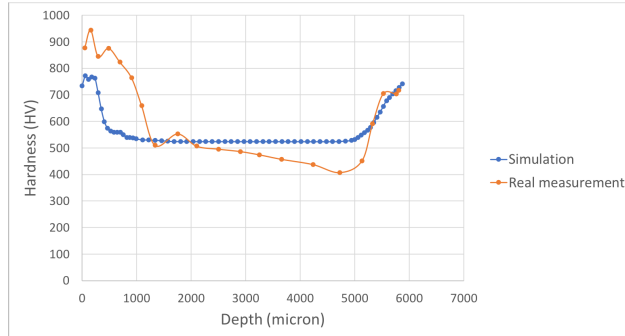
### 8.3 Carburizing

The objective of this thesis is to improve the operation of the gearbox by changing the production process of the ring gear. For this reason hardness measurements will be made on the traditionally carburized ring gears. The analyzed carburized gears are hardened in accordance with the technical drawing found in appendix A. In figure 8.2a the microhardness measurements of a carburized gear and the simulation (subsection 7.4.3) are shown, the measurements were made the same way as depicted in figure 7.8b. Figure 8.3 shows the results of the hardness measurements from the center of one tooth flank to the other.

On figure 8.2b can be seen that the case hardening depth of the simulation is much less deep than in the ring gear itself. The reason for this is that the desired case hardening depth provided in the technical drawing was between 0.3 and 0.6mm, these values were based on the values used in previous years for the design of the gearbox and thus before the case hardening optimization in section 3.4. The case hardening depth of the simulation was optimised for a depth of 0.3mm as mentioned earlier.

Next to this, the hardness of the ring gear never drops below 400HV independent of the point of measurement. This is due to the fact that the surface area of the ring gear is rather large compared to the volume, see appendix A. For this reason the entire ring gear is quenched at quite a high rate, causing martensite to be formed everywhere in the material. Because the carbon content in the bulk is lower than at the surface, the hardness of the martensite will be lower, section 2.3. The effect of an increased core hardness can be a advantage and a disadvantage of traditional

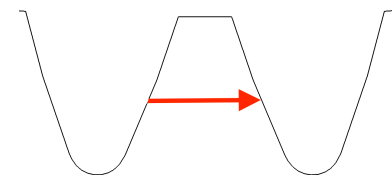
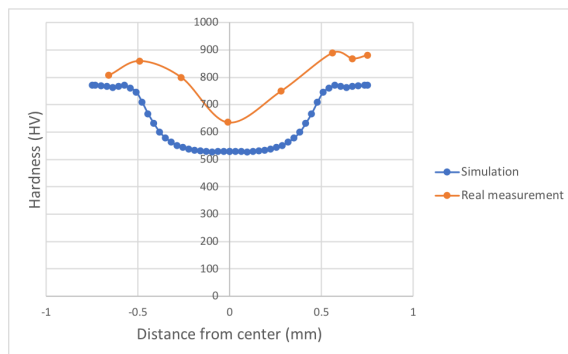
carburizing. On the one hand the higher hardness will increase the tensile strength of the material but at the same time there is a loss of ductility. To determine the impact of this effect fatigue tests should be conducted.



(a) Measurement and simulation results of carburized ring gear from tooth top to the outer diameter

(b) Carburized teeth of the ring gear

Figure 8.2: Measurements carburization (1)



(a) Hardness measurements middle of tooth flank

(b) Measuring direction figure 8.3a

Figure 8.3: Measurements carburization (2)

### 8.4 Laser hardening

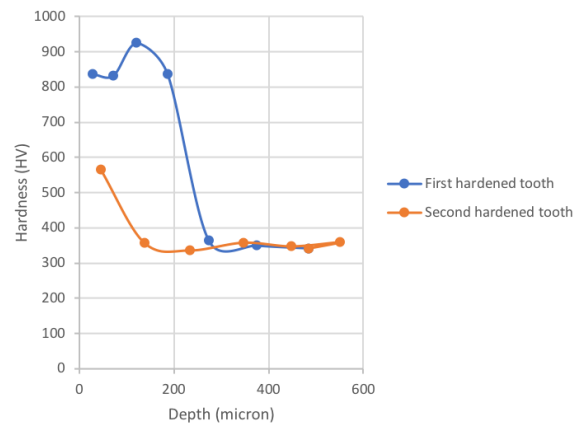
In this section the results of the simulations for laser hardening of the ring gear are compared with the experimental results for the optimal setting.

As can be seen in figure 8.4 the back tempering effect is very distinct at the left tooth flank. This was expected, because no cooling was applied (the right flank was hardened after the left flank). When approaching the root of the tempered tooth surface, it can be seen that the fraction of martensite rises again. This effect occurs because at the root, there is enough cooling mass for the heat to be dissipated such that tempering does not occur. On top of that, at the root, the gear flank is further away from the heated surface of the adjacent tooth. This way, the maximum temperature over time at the root will be lower than the maximum temperature over time at the top and thus less

tempering. As discussed earlier this effect is detrimental for the performance of the ring gear and should therefore be solved.



(a) Laser hardened tooth without cooling and visible tempering



(b) Measured hardness values for two adjacent tooth flanks without cooling, measured around the tooth top

Figure 8.4: Validation laser hardening with tempering

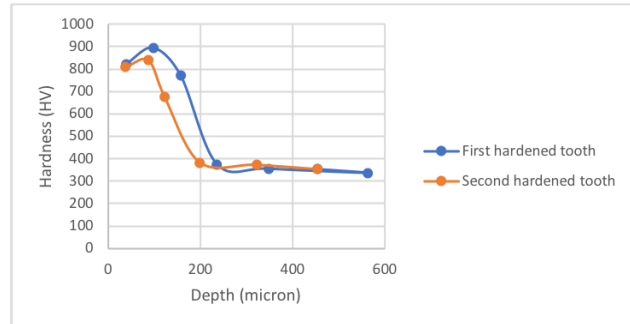
In figure 8.5 and figure 8.6 the microhardness measurements for the ring gear teeth with the copper inserts functioning as cooling are shown. Because it is very difficult to determine the thermal contact resistance between the copper and the tooth flank, as explained in section 5, this experiment was iterated for different pressures between the two surfaces. Figure 8.6 shows the microhardness measurements and phases of a sample for which an intermediate pressure between the copper inserts and the tooth flanks was used. There still is some tempering, but a lot less than without the cooling inserts. Because this setting was not optimal, the pressure was increased further, shown in figure 8.5. In this figure it is visible that almost no tempering occurs because the two hardness curves follow each other very well. The second hardened tooth hardening depth is slightly less than the first hardened tooth but still within limits because the effective case hardening depth (550HV) is still at a sufficient depth according to section 3.4.

In the optimized simulation (figure 7.9b) it was clear that the core of the tooth root was still very soft. This occurred because the carbon profile, figure 7.7a, reached its original value (0.018 Wt% C) at a depth (0.4mm) not much greater than the envisioned case hardening depth (0.3mm). Because of this, the microstructure of the steel that arises at greater depths than 0.4mm is the same as the bulk material and thus has a low hardness. For the test samples, figure 8.5b and 8.7b, one can see that the hardness at depths deeper than 0.4mm lies around 350HV ( $\pm 37$ HRC), in the ring gears that were not yet laser hardened but that had went through the carbon diffusion step, figure 2.11. This effect can partly be explained by the fact that the ring gear was air cooled after carbon diffusion. These cooling rates can still be high enough for fine pearlite to be formed and thus a higher hardness as explained in section 2.4. Next to this, the additional amount of cementite at the surface will further enhance this effect. The hardness at the depths where laser hardening

cannot heat the material above the austenitization temperature stays quasi the same. In theory grain growth due to annealing could occur due to the elevated temperatures but since the time at which these high temperatures occur is very short, it will have almost no effect on the hardness.

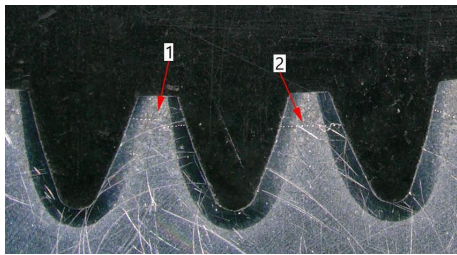


(a) Laser hardened tooth with cooling, high pressure

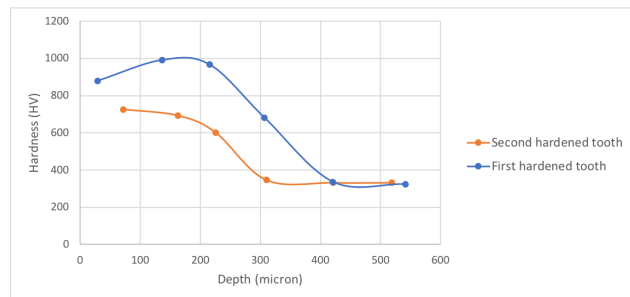


(b) Measured hardness values for two adjacent tooth flanks with cooling, high pressure, measured around the tooth top

Figure 8.5: Validation laser hardening optimal setting



(a) Laser hardened tooth with cooling, intermediate pressure



(b) Measured hardness values for two adjacent tooth flanks with cooling, intermediate pressure, measured around middle of tooth flank

Figure 8.6: Validation laser hardening intermediate cooling pressure

Currently only the hardness profile at the top of the teeth was discussed. Of course, the hardness lower on the tooth surface and in the root are very important too, but these are less sensitive to tempering as explained earlier. In figure 8.7a and 8.7b plots of the hardness measurements at the top, middle and root for two adjacent tooth surfaces are shown. From these plots it is concluded that there is quite a big difference in case hardening depth depending on the position on the tooth profile. This result is not quite the same as the hardness profile that was envisioned because it was desired for this profile to have a constant hardening depth for all the positions. This effect could be explained by the copper inserts, these could absorb too much heat such that layers of the material in the depth can not get hot enough so no austenite was formed—and therefore no martensite—. If the pressure on the copper block were to be lowered a little, this effect could possibly be canceled out, but then the amount tempering on the adjacent tooth will increase. Despite the fact that the hardening depth is not completely constant, these are very good results since the optimum case

hardening depths determined in section 3.4 are lower limits. The reason case hardening depths are kept just above the lower limit (optimum), is mostly because of the economical factor, higher case hardening depths mean that the part has to stay in the furnace for longer, thus reducing profit. Of course it is undesirable to through harden the tooth top because then the entire gear would become too brittle, lowering the lifetime of the gear. In the optimization of the case hardening depth from ISO 6336 (International Organization for Standardization, 2007), figure 2.9, it is clear that there is a very wide range of possible case hardening depths. The optimum case hardening depth is very dependent on the gear and the gear loads. In the conclusion, 10, a future approach is discussed.

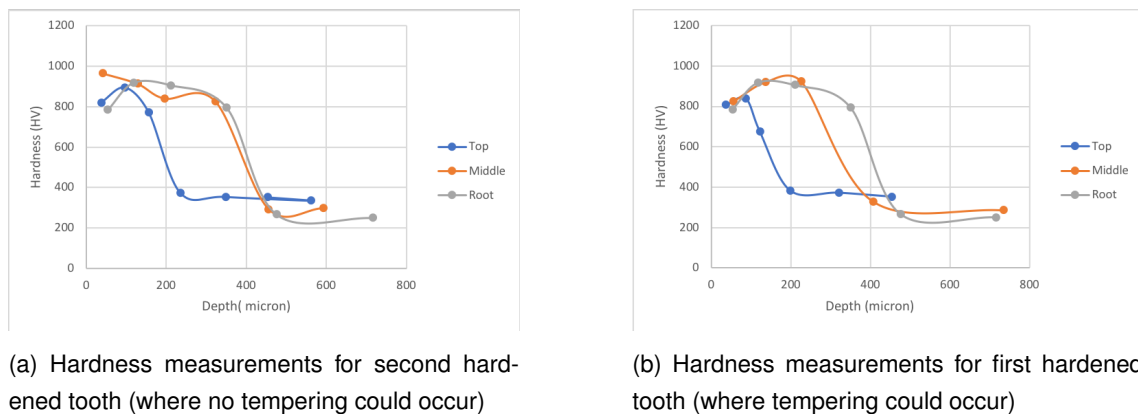


Figure 8.7: Hardness measurements optimal laser settings

The above results were made for ring gears hardened with the optimal laser hardening parameters stated in section 7.4.4. However, experiments were also conducted with smaller or larger spot sizes and different feed rates. Smaller spot sizes resulted in a hardened tooth root but no martensitic transformation at the tooth flanks itself, larger spotsizes gave the opposite of this. By changing the feed rate, different case hardening depths can be achieved. This relation is however not linear, because a lot depends on how the warm front is pushed forward in the teeth itself during laser hardening. By using a velocity that is too low, the gear will just keep heating and a regime for the maximum temperature of the surface in time will never be reached, resulting in large differences in case hardening depth.

### 8.4.1 Quench cracks

During the laser hardening tests, in certain spots cracks would appear at the tooth root that start at the surface and grow outward radially. An example of this can be seen in figure 8.8. Obviously, once there is a crack on one tooth, the gear becomes unusable, so this effect is something that must be closely monitored.

It is very difficult to explain this phenomenon because a lot of factors can have an influence. During the thermal cycle of laser hardening, a portion of the ring gear is first heated into the austenitic region causing a volume decrease which results in a tensile stress. This tensile stress is gener-



ated because the underlying material and material in front of the warm zone still has the same microstructure as the base material (section 3.3). These tensile stresses could potentially cause cracks. Next to this the effect could also be explained due to cracks during the martensitic transformation, also known as quench cracks. From the region of the material that is heated above the austenitization temperature, the material closest to the bulk will transform into martensite first. This change in martensite causes a volume increase at that point. However, at the material closer to the surface that is still austenitic (higher density), a tensile stress will occur because of the balance of forces between the sections of the material. The above failure modes are due to phase transformations of the steel, volumetric changes due to temperature gradients will also induce stresses which makes it even more difficult to determine the root cause of the problem.

Due to the carbon diffusion by carbon pellets (pack carburizing) a very steep carbon gradient is obtained at the surface with a carbon content up to 1.3% at the surface, section 2.4. The higher carbon content causes a higher probability of quench cracks due to the greater volume expansion caused by the extra interstitial carbon compared to lower carbon steels. Next to this, the martensite start & finish temperature ( $M_s$  &  $M_f$ ) of higher carbon steels are lower compared to lower carbon steels. For this reason martensite is formed at lower temperatures and thus a lower ductility of the steel, causing a higher probability of cracks (Totten et al., 2002).

The reason why the cracks occur at the tooth root, can be explained by comparing the maximum temperatures in the root compared to those at the tooth flanks, the cooling rate in the root and the shape factor. On figure 7.10b one can easily see that the maximum temperature is reached at the tooth root thus the highest thermal stresses will occur in the tooth root due to the largest thermal gradient. Next to this, the highest cooling rate will occur in the tooth root because of the large amount of quenching mass underneath it, this high cooling rate causes extra strain and thus thermal stresses (Herring, 2012). The fact that the tooth is curved in the tooth root area can further enhance the probability of quench cracks because this curve acts as a stress riser.



Figure 8.8: Observed crack in the tooth root for transverse velocity of 25mm/s

During the experiments quench cracks were only observed in the samples for which a transverse speed of 25mm/s was used, which is higher than the optimum value (15mm/s) discussed in sub-section 7.4.4. This phenomenon could be explained because of the higher thermal gradients using



the higher transverse velocity and thus higher thermal stresses.

It is important to emphasize here that because no quench cracks occurred using the transverse velocity of 15mm/s does not mean that the ring gear is completely fine. Thermal gradients will still occur which will have an influence on the residual stresses inside the ring gear and thus the lifespan of the ring gear. This aspect will be further discussed in the next chapter.

# 9

## Distortions

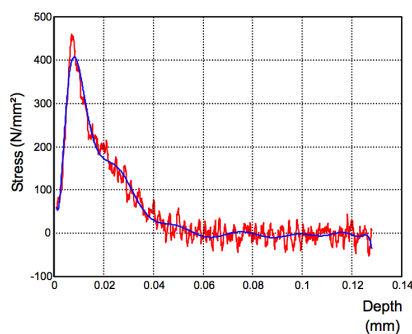
### 9.1 Introduction

As explained in the introduction, the goal of this thesis is on the one hand to produce a gear that has the desired case hardening depth. On the other hand, distortions of the gear are of equal importance. While optimizing the process it is important to take in mind both factors. A properly hardened gear with too much distortions is unusable and vice versa. The aspect of distortions is also the reason why for this application, research has been done in the laser hardening of gears. Within laser hardening heat is only applied to the regions which are desired to harden. In this chapter it is discussed why this is beneficial. There are also other methods of applying heat locally such as induction hardening or flame hardening. Laser hardening was preferred, because with induction hardening, heat is typically also applied deeper under the surface. For this reason extra quenching media are needed to ensure martensitic transformation which will increase distortions. Next to this, with induction hardening it is more difficult to access very small features of a workpiece and thus it is difficult or even impossible to generate constant hardening depths (IndustrialLaser-Solutions, 2010). Flame hardening is not discussed further, because this process is inaccurate in comparison with laser hardening or induction hardening. On top of that, it is almost impossible to incorporate flame hardening on a CNC milling machine which is one of the greatest advantages of laser hardening because this can further increase the quality of the gear and reduce lead times of components (Bouquet, 2016).

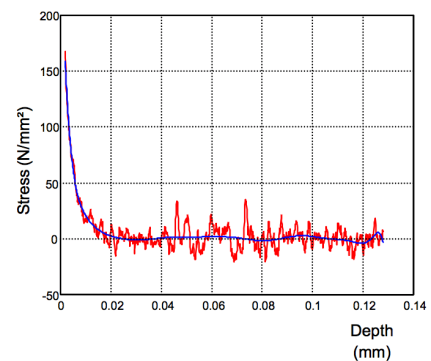
## 9.2 Causes of distortions in case hardening

A first possible cause of distortions due to case hardening lies in how the component was processed before the heat treatment and during the period in the austenitic region. As with all types of case hardening, the material has to be brought into the austenitic region for martensite to be formed. Because of the very high temperatures in the austenitic region, steel will lose most of its strength. When the part is then placed in the furnace, stresses occur in the workpiece and creep may occur which causes distortions of the part (Lindell, 2004). These stresses can be due to the way the part is placed in the oven, for example by weight of other parts or its own dead weight. Next to externally generated stresses on the workpiece, residual stresses can also occur in the part due to earlier processing of the part. When heated, these stresses want to dissipate themselves by causing distortions.

As mentioned in section 1.2, the ring gears will be produced by wire EDM. Research has been done by Kruth and Bleys (2000) on the amount of residual stress in components produced by wire EDM. They found that the residual stresses are very dependent on the amount of finishing steps as can be seen on figure 9.1. The residual stresses could be kept relatively low in comparison to turning or milling when the part is finished in several steps. For this application, a surface roughness of  $0.8 \mu\text{m}$  is required, which can only be reached with several finishing steps according to FEB partner, Cadcamatic. For this reason the distortions due to the residual stresses will be minimal for the ring gear, however there will still be distortions to some extent.



(a) Residual stresses rough wire EDM



(b) Residual stresses wire EDM with 4 finishing steps

Figure 9.1: Residual stresses wire EDM

Source: Kruth and Bleys (2000)

The most important factor that influences distortions during laser hardening are phase transformations. Phase transformations always involve volume changes because the crystal lattice changes. During the heating step the initial BCC  $\alpha$ -phase is converted into the FCC  $\gamma$ -phase. Because of this, a volume reduction will occur because of the difference in atomic packing factors. This volume

decrease causes tensile stresses to be generated in the surface layer. As known, a stress is always accompanied by a strain and thus also by a deformation relative to its initial state. During the martensitic transformation there will be a volume increase as explained in section 3.3. This effect will also increase the overall distortions.

However, in carburizing, the entire part is converted into the  $\alpha$ -phase and thereafter only a region of it will convert into martensite. At the same time there will be a lot of thermal gradients in the entirety of the component also causing strains. Because of this reason laser hardening should involve fewer distortions.

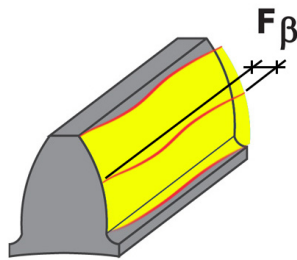
There still is a last factor that can cause minor distortions for case hardening steels. In case hardening steel, carbon is added to the surface layer. Consequently, the volume of the surface layer will increase. In pack carburizing, the carbon concentrations are typically higher than in vacuum carburized parts. In vacuum carburization, there are a lot more variables to shape the form of the carbon gradient such that the bare minimum amount of carbon is added to the material in order to reach the desired case hardening depths. Because of this, the volume increase due to carbon diffusion by pack carburizing is larger than with vacuum carburizing, which is not beneficial for the total distortions.

In a standard carburization process, carbon diffusion is combined with a quenching step at the end. In this case the hardening step is separate from the carbon diffusion step. For this reason, the ring gear will go through more phase transformations because it is heated 2 times into the  $\alpha$ -phase. It is important to state here that the heating and cooling rates during the carbon diffusion step (first part of pack carburizing) should be kept very low to minimise the amount of thermal gradients, minimizing the deformations. This effect could be minimised even further if parts of the ring gear that do not need to be hardened, would be shielded from the carbon atmosphere. When the cooling rates are kept low and the above discussed creep due to the setup in the oven is minimal to non-existent, the ring gear should not have deformed too much before laser hardening it. This way there should be enough of a buffer for any small additional distortions during laser hardening. Even in combination with the distortions due to the carbon diffusion, the distortions could be smaller compared to the distortions of a classically carburized ring gear. Carburizing in which the part is cooled down after the carbon diffusion step and then to be reheated and quenched is a known method of carburizing in the industry (Lindell, 2004).

### 9.3 Influence on efficiency and lifespan

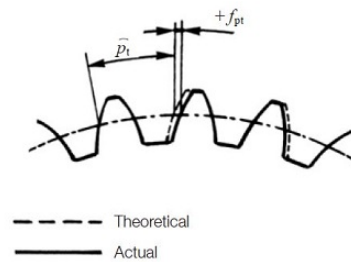
A lot of research has been conducted on how the different tolerances in gears influence the efficiency of a gearbox and the stress state of the tooth flank and root. There is no rule of thumb to determine how the lifespan of a gear is affected by the tolerance grade, because every gear is processed in a different way. A particular deviation from the ideal geometry might have more severe consequences than another deviation. In general, it is known that the higher the tolerance grade, the shorter the lifespan and the worse the efficiency. This can be explained due to the fact that

for an ideal, theoretical gear, the loads are distributed over a certain surface. When for example the helix deviation ( $F_{\beta}$ ) or total profile deviation ( $F_{\alpha}$ )<sup>1</sup> of the gear is distorted, this contact patch will become smaller and thus contact and bending stresses are increased. Therefore it follows that the lifespan will decrease. Next to a smaller contact patch, single pitch deviations ( $F_{pt}$ ) or runout errors ( $F_r$ )<sup>2</sup> can cause sudden backlash of the teeth and thus increasing shocks and stresses on the teeth, with a lower lifespan as a result (Wei et al., 2011).



(a) Helix deviation ( $F_{\beta}$ )

Source: AsTheGearTurns (2014)



(b) Single pitch deviation ( $F_{pt}$ )

Source: Kohara-Gear-Industry (nd)

Figure 9.2: Tolerances on gears

The efficiency of meshing gears will also lower with increasing deviations from the perfectly dimensioned gear. Efficiency is closely related to the amount of heat generated in meshing gears. This heat generation depends on the specific sliding of the gears and the normal force on the contact patch. As said, with certain deviations of a gear's dimensions, the area of the contact patch will decrease and thus the normal force, friction and the temperature will increase. A temperature increase of the gear will increase the amount of friction even further because of the thermal expansion of the gear. Due to this thermal expansion the normal forces on the tooth surfaces will be raised (Ghewade et al., 2016). In addition to the increase in friction, local loading of a tooth can also cause the bearings to be adversely loaded, which also creates more friction and thus reduces the overall efficiency of the gearbox.

## 9.4 Measurements

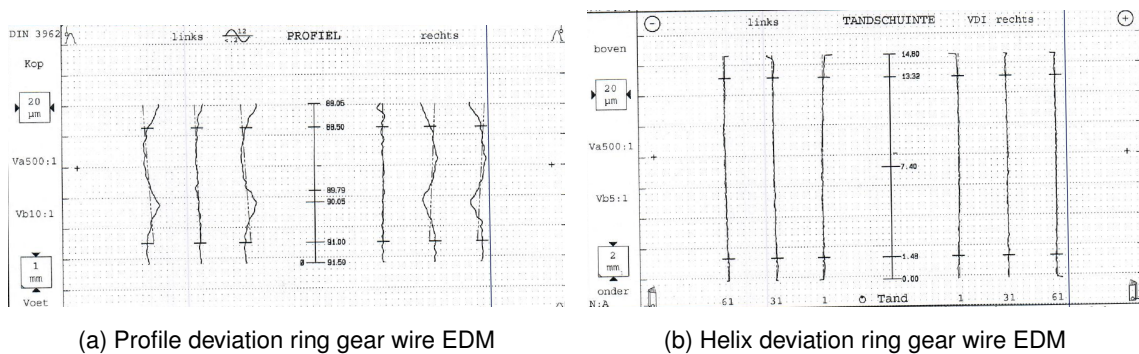
In this section measurements of the ring gear after wire EDM, carbon diffusion, laser hardening and carburizing will be discussed and compared with each other.

<sup>1</sup>  $F_{\alpha}$  is a measure for how much the actual tooth profile differs from the ideal involute profile.

<sup>2</sup>  $F_r$  is a measure for how much runout exists on the pitch diameter

### 9.4.1 Wire EDM

At first it is important to have an idea about the distortions on the ring gears after wire EDM in order to conclude how much each step of hardening contributes to the total distortions. In figure 9.3 the total profile deviations ( $F_\alpha$ ) and helix deviations ( $F_\beta$ ) for the ring gear after wire EDM are shown. For the entire report with the allowed & actual distortions, see appendix K. The conclusion of these measurements is that most of the teeth are already out of tolerance on the basis of profile deviation. This is far from ideal because these gears still have to be carburized or carbon diffused and laser hardened. The helix deviations however are within tolerance.



(a) Profile deviation ring gear wire EDM

(b) Helix deviation ring gear wire EDM

Figure 9.3: Helix & profile deviation ring gear after wire EDM

Next to involute profile the roundness of the top circle was also measured. This measurement was made to see how every hardening step affects warping of the ring gear. The roundness is  $20\mu m$  which is sufficient because the allowable roundness is  $30\mu m$ . For the measurements, see appendix K.

### 9.4.2 Carburized ring gear

Up next, the carburized gears were measured. From the measurement is concluded that the profile deviation increased, none of the gear teeth were in tolerance anymore. For the helix deviation almost no teeth were in tolerance. It is clear to see that this distortion will cause the lifespan of the gear to be reduced drastically due to the loads to be concentrated at a certain side of the tooth flanks. In conclusion, the carburized ring gears are not within the desired tolerance grade and thus not optimal for use in the gearbox. It is difficult to say if the ring gear would have been in tolerance if the deviations due to wire EDM would have been smaller.

The roundness of the carburized ring gear is also considered because this dimension is very difficult to preserve due to the geometry of the ring gear. The slightest pressure due to quenching will cause the ring gear to warp. This pressure can be caused by thermal gradients or phase transformations but maybe even more important is the way the part is quenched or how the ring gear is set up for carbon diffusion. The measured roundness has a value of  $102\mu m$  which is a lot greater than the allowed value,  $30\mu m$ . Due to this deformation, the carburized gear is certainly not optimal for

use. On the one hand a lot of pitch deviation will occur causing the loads on the tooth flanks to be increase. On the other hand, the outer diameter of the ring gear is a very important dimension because this dimension is used for a press fit into the gearbox housing. Of course the top circle diameter roundness cannot be directly related to the roundness of the outer diameter but it gives a very good indication. The entire measurement report of this gear can be found in appendix L.

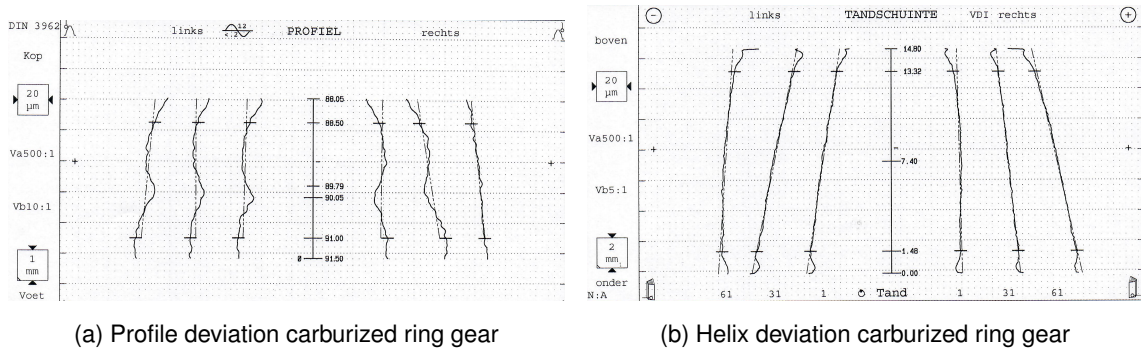


Figure 9.4: Helix & profile deviation ring gear after carburizing

### 9.4.3 Laser hardened gear

For analyzing the distortions of the laser hardened ring gear the carbon diffusion and laser hardening step have to be observed closely. Unfortunately generating a measurement report for a carbon diffused ring gear without the laser hardening step was not possible which makes it more difficult to draw conclusions. However, a roundness measurement of the outer diameter of the ring gear before and after laser hardening has been conducted. From this a good estimation can be made on how much distortions are caused by carbon diffusion or laser hardening.

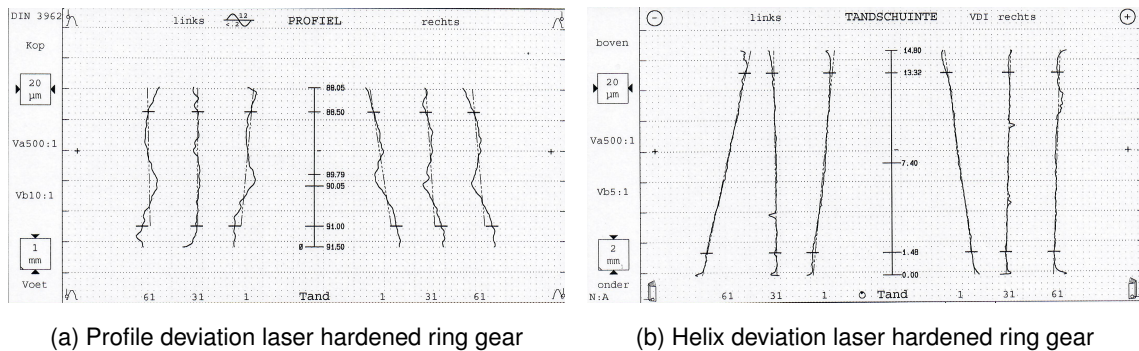
00007	Cirkel Gauss R99.8 (2)	X=	303.165	α=	90:00:00	φ=	99.802
		Y=	291.869	β=	90:00:00	d=	0.1276
		Z=	83.458	γ=	0:00:00	n=	16

Figure 9.5: Roundness (mm) carbon diffused ring gear, without laser hardening

In comparison with the ring gears after wire EDM a very large distortion on the roundness is observed. A value of  $\pm 128\mu\text{m}$  is observed which is much greater than the desired value and thus the ring gear is already out of tolerance before laser hardening. This effect can be explained due to the influences discussed in subsection 9.2. The fact that the ring gears are carbon diffused by use of carbon pellets used in the pack carburizing of parts can further explain this effect. Because of the carbon pellets it is very difficult to heat up the parts without an external stress being applied to them. First of all the weight of the ring gears itself will cause stresses, next to this it is very probable more ring gears were placed in the same container causing the ring gears at the bottom of the container to feel the weight of the ring gears above.

After this measurement the same gear was laser hardened using the optimal laser parameters explained in section 7.4.4. The total profile and helix deviation for the laser hardened gear can

be found in figure 9.6. Overall, it is seen that the profile deviation of the laser hardened ring gear resembles the profile deviation of the carburized ring gear. For the profile deviation measurements, see appendix M. Half of the measured tooth flanks were within helix deviation tolerance while in the carburized gear no tooth flanks were in tolerance for helix deviation. It is impossible to know what amount of deviation is caused by the carbon diffusion or the laser hardening step. It is however certain that due to the carbon diffusion the teeth will have been distorted.



(a) Profile deviation laser hardened ring gear

(b) Helix deviation laser hardened ring gear

Figure 9.6: Helix &amp; profile deviation ring gear after laser hardening

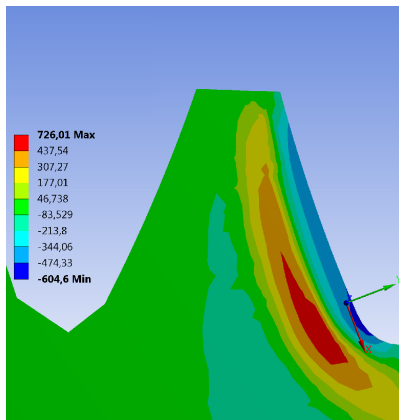
Possible warping of the laser hardened gear has also been investigated by an additional roundness measurement of the outer diameter of the ring gear, which can be seen in appendix N. The measured roundness was  $143\mu\text{m}$ . Compared with the roundness of the ring gear after the carbon diffusion step ( $128\mu\text{m}$ ) the difference is rather limited. There is no certainty that the ring gear would have been within tolerance if the roundness distortion due to carbon diffusion would have been much smaller. However, it is certain that the influence of laser hardening on roundness distortions is much smaller compared to the carbon diffusion step from these measurements.

## 9.5 Validation of residual stress

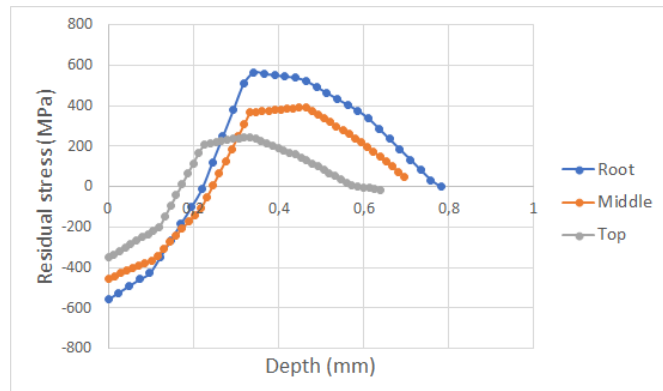
As said in section 3.3 the optimal case hardening depth is very dependent on the distribution of the residual stresses at the tooth flank. The only way of determining the residual stresses is by simulation. Methods exist for determining these stresses for real gears, such as X-ray diffraction, but these were not possible to conduct in this research. In figure 9.7 the residual stresses for the optimal simulation discussed earlier can be found. It is visible that the occurring compressive residual stresses at the surface are very high. However, there is a fairly large difference in the size of stresses depending on the tooth root or flanks. It is very difficult to state if this difference is beneficial or not because the loads on the gear will change with the angle of rotation. The disadvantage of compressive residual stresses is that they have to be counteracted deeper in the material causing tensile stresses in the core. Depending on how the bending stresses in the root and the shear stresses at the tooth flank evolve in the depth this tensile stress can dramatically lower the lifespan of the gear. A lot of factors have an influence on the depth and size of the residual stress. Ideally this should be investigated in further research to find the optimum setting



between the case hardening depth and residual stress to find the optimum lifespan.



(a) Simulation of normal stresses at tooth flank (MPa)



(b) Residual stresses at tooth root, flank & top

Figure 9.7: Simulation of residual stresses

## 9.6 Conclusion

From the previous measurements it is clear that the distortions of the laser hardened gear are not optimal. Somewhere along the production process—starting with wire EDM, then carbon diffusion and then laser hardening—the ring gears were deformed the most, causing them to be out of tolerance. It must however be emphasized that overall, the distortions of laser hardened gear profile are of the same or even better quality compared to the carburized ring gear profile. There is a large probability that by optimizing the carbon diffusion step, the laser hardened gears will have a higher accuracy grade than the carburized gears. The laser hardened gears might even be within the required accuracy grade if the diffusion step was optimized. A recommendation on how to reduce the distortions during carbon diffusion could be to use a different type of furnace. For example, using the carbon diffusion step during vacuum carburizing would increase the accuracy due to the way the ring gear could be placed in the oven in a quasi stress-free state.

Besides that, a more drastic approach to solving the distortion problem could be to conduct the carbon diffusion step on an oversized gear. After carbon diffusion, the final toothing profile could be cut out by wire EDM. Of course there is a loss of carbon potential to be hardened, but due to pack carburizing, a very high carbon concentration at the surface can be achieved. Because of this, the loss of carbon potential could easily be compensated by placing the ring gear in the furnace for a longer period of time. After wire EDM, a very accurate part already containing carbon at the edges is obtained. Then, the ring gear could be laser hardened, which would cause a much lower total distortion of the final part. This principle is clarified in figure 9.8 with [1] being the surface that is carburized without the quenching step, thus a carbon gradient is created. Surface [2] is the actual desired tooth geometry that could be achieved by a second wire EDM process.

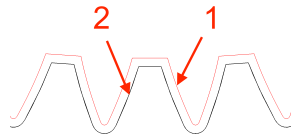


Figure 9.8: Oversized ring gear dimensions

On figure 9.9 the entirely laser hardened gear can be seen.

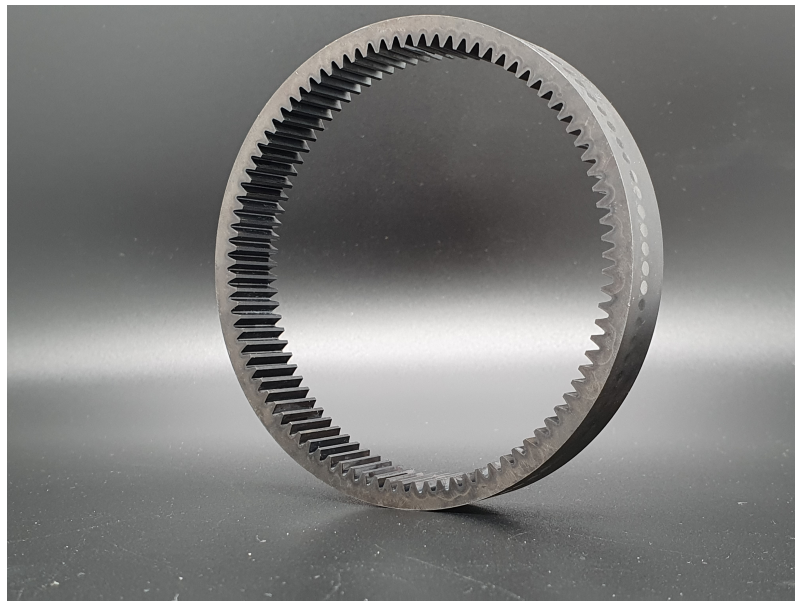


Figure 9.9: Laser hardened ring gear

# 10

## Conclusion

This thesis has as an objective to improve the hardening process of a ring gear of a Formula Student gearbox. The reason for conducting research on this subject are the limitations in the current method for hardening this ring gear. For the past few years, all the gears in the gearbox were made from a case hardening steel, 16MnCr5. Because of the complex geometry of the ring gear, it was produced by wire EDM followed by a hardening process : carburizing. This last step introduces distortions into the part which decrease the quality and therefore the lifespan of the gear. Since it is impossible to grind the ring gear the only way to increase the quality is by minimizing distortions. The technology of laser hardening might be the solution to this problem.

First, the optimal case hardening depth was determined for the ring gear by analyzing all the relevant common failure mechanisms in gears. By establishing this case hardening depth, the selective heating properties in laser hardening were used to full advantage. Out of a few different ideas, the optimal concept was selected. This concept consists of the simultaneous hardening of two adjacent tooth flanks. In order to realise the desired hardening depth, a model had to be developed. In this model the influence of the input laser beam, reflection and different absorption coefficients have been taken into account to make the model as realistic and useful as possible. The model was developed in Matlab and implemented in Ansys. Ansys was used for thermal simulations of the model. Afterwards DANTE, an Ansys extension to simulate heat treatments on steels, was used to simulate the phases, hardness and other relevant parameters.

After optimising the parameters necessary to reach the required hardening depth, these parameters were validated by using a TRUMPF TruDisk 5001 laser to provide the heat required to harden the gear. In addition a solution was devised to overcome the problem of back tempering the adjacent

tooth flank. By using the appropriate amount of external cooling and by fine tuning the hardening process the desired hardness profile was obtained. In order to harden the case hardening steel the gears were carburized without the quenching step such that a carbon gradient was created at the surface before laser hardening the gears.

After obtaining the required hardness profile, the associated distortions were measured and compared to distortions of a ring gear hardened using the conventional hardening technique. The carburized ring gears had a very deep hardening depth and a high core hardness value. Especially the high core hardness is not very desirable for this application due to the brittle behaviour of the material. Although there were significant distortions with both techniques, most of the distortions in the laser hardened gear were probably due to deforming during carbon diffusion. Possible solutions to avoid these distortions are provided in the last chapter. By applying one of these solutions it is strongly suspected that the desired accuracy grade in combination with the correct hardness could be obtained. Ideally fatigue tests would be conducted in the future in order to validate the method of laser hardening the ring gear in this application.

## Bibliography

- Akpolat, A. (2018). Effects of asymmetric cutter tip radii on gear tooth root bending stress. <https://gearsolutions.com/features/effects-of-asymmetric-cutter-tip-radii-on-gear-tooth-root-bending-stress/>.
- Altergott, W. and Patel, P. (1982). Spur gear laser surface hardening. *MM&T Program*, 81:1–120.
- AsTheGearTurns (2014). Helix deviation. <http://asthegearturns.com/2014/11/03/lead-variation-wobble/>.
- Aune, P. A. (2016). a four wheel drive system for a formula style electric racecar.
- Ayers, G. H. (2003). *Cylindrical Thermal Contact Conductance*. PhD thesis, Texas A&M University.
- Bergström, D. (2008). *The Absorption of Laser Light by Rough Metal Surfaces*. PhD thesis, Lule University of Technology.
- Boardman, B. (1990). Fatigue resistance of steels. *ASM Handbook: Properties and Selection, Irons, Steels and High-Performance Alloys*, 1:673–688.
- Boiadjiev, I., Witzig, J., Tobie, T., and Stahl, K. (2015). Tooth flank fracture - basic principles and calculation model for a sub-surface-initiated fatigue failure mode of case-hardened gears. [https://www.geartechnology.com/articles/0815/Tooth\\_Flank\\_Fracture\\_-\\_Basic\\_Principles\\_and\\_Calculation\\_Model\\_for\\_a\\_Sub-Surface-Initiated\\_Fatigue\\_Failure\\_Mode\\_of\\_Case-Hardened\\_Gears/](https://www.geartechnology.com/articles/0815/Tooth_Flank_Fracture_-_Basic_Principles_and_Calculation_Model_for_a_Sub-Surface-Initiated_Fatigue_Failure_Mode_of_Case-Hardened_Gears/).
- Bouquet, J. (2016). *Reducing lead time and increasing flexibility in high precision manufacturing*. PhD thesis, KU Leuven, Celestijnenlaan 300B box 2402, B-3001 Heverlee, Belgium.
- Brog, J. P., Chanez, C. L., Crochet, A., and Fromm, K. M. (2013). Polymorphism, what it is and how to identify it: a systematic review.
- Canale, L. C. F., Mesquita, R. A., and Totten, G. E. (2008). *Failure Analysis of Heat Treated Steel Components*. ASM International.
- Chitta, S. (2012). *Elastohydrodynamic lubrication in spur and helical gear contacts*. PhD thesis, KTH Industrial Engineering and Management Machine Design.
- Choudhury, A. K. R. (2014). *Principles of Colour and Appearance Measurement*. WP.

- Colombier, J., Bhuyan, M., Kumar, V., and Somayaji, M. (2017). *3D Nano-Fabrication using controlled Bessel-Glass interaction in ultra-fast modes*. PhD thesis, Université de Lyon, Université Jean Monnet, 10 Rue Trefilerie, 42100 Saint Etienne, France.
- Corporation, E. (2011). Understanding spur gear life, trsm0913. <http://www.consolidatedtruck.com/wp-content/uploads/2016/04/Transmission-Gear-Wear-Explained.pdf>.
- Costa Rodrigues, G., Vanhove, H., and Duflou, J. (2014). Direct diode lasers for industrial laser cutting: A performance comparison with conventional fiber and co2 technologies. *Physics Procedia*, 56:901–908.
- Cvetkovski, K., Ahlström, J., and Karlsson, B. (2012). Influence of short heat pulses on properties of martensite in medium carbon steels. *Materials Science & Engineering A*, 561:321–328.
- DNV 41.2 (2015). Calculation of Gear Rating for Marine Transmissions. Standard, Det Norske Veritas, Høvik.
- Duflou, J., Vanhove, H., and Rodrigues, G. C. (2014). Direct diode lasers for industrial cutting : A performance comparison with conventional fiber and co2 technologies. *Physics Procedia*, 56:901–908.
- Edge, E. (2021). Gear pitting and lubrication. [https://www.engineersedge.com/gears/gear\\_pitting\\_lubrication.htm](https://www.engineersedge.com/gears/gear_pitting_lubrication.htm).
- EpilogLaser (2014). Yag laser vs. co2 lasers. <http://support.epiloglaser.com/article/8205/42827/yag-vs-co2-lasers>.
- Eritenel, T. (2019). Gear tooth bending stress. <https://drivetrainhub.com/notebooks/gears/strength/Chapter%20-%20Root%20Stress.html>.
- FailureAtlas (2020). Abrasive wear - gear failures. <https://onyxinsight.com/wind-turbine-failures-encyclopedia/gear-failures/abrasive-wear/>.
- Fernandes, P. J. L. and McDulling, C. (1997). Surface contact fatigue failures in gears. *Engineering failure analysis*, 4(2).
- Flodin, A. (2000). *Wear of spur and helical gears*. PhD thesis, KTH Royal Institute of Technology.
- Föll, H. (2019). Diffusion in iron.
- Genel, K. (2005). Estimation method for the fatigue limit of case hardened steels. *Surface and Coatings Technology*, 194(1).
- Ghewade, D. V., Nagarale, S. S., and Pandav, A. N. (2016). *Heat Generation Analysis and its Reduction in Meshing Gears*. PhD thesis, Department of Mechanical, Maharashtra, India.

- Giorleo, L. and Semeraro, Q. (2010). Modelling of back tempering in laser hardening. *The International Journal of Advanced Manufacturing Technology*, 54:969–977.
- Glaeser, W. A. and Shaffer, S. J. (1996). *Contact Fatigue*. ASM, Battelle.
- Gopsill, J. A. (n.d.). Design & manufacture 2. <https://jamesgopsill.github.io/MechanismDesign/>.
- Grum, J. (2004a). 6 laser surface hardening.
- Grum, J. (2004b). *Handbook of metallurgical process design*. Marcel Dekker, New York.
- Grum, J. (2007). Comparison of different techniques of laser surface hardening. *Journal of achievements in Materials and Manufacturing engineering*, 24(1).
- Hamza, M. (2020). Tempering steel proces. <https://materials-today.com/tempering-steel-process/>.
- Herring, D. H. (2005). A discussion of retained austenite. *Industrial Heating Magazine*, pages 14–16.
- Herring, D. H. (2012). Quench cracking. <https://www.industrialheating.com/articles/90314-quench-cracking>.
- Hosseini, S. R. E. and Zhuguo, L. (2016). Pack carburizing: Characteristics, microstructure, and modeling. *Encyclopedia of Iron, Steel, and Their Alloys*, pages 1–24.
- IndustrialLaserSolutions (2010). Laser hardening heats up. <https://www.industrial-lasers.com/surface-treatment/article/16485093/laser-hardening-heats-up>.
- International Organization for Standardization (2007). Calculation of load capacity of spur and helical gears – part 1: Basic principles, introduction and general influence factors. Standard, International Organization for Standardization, Geneva, CH.
- International Organization for Standardization (2014). Metallische werkstoffe - umwertÄ¼ng von hÄ¼rtewerten. Standard, International Organization for Standardization, Geneva, CH.
- Kiefer, D., Simon, N., Beckmann, F., Wilde, F., and Gibmeier, J. (2021a). Real-time stress evolution during laser surface line hardening at varying maximum surface temperatures using synchrotron x-ray diffraction. *Optics and Laser Technology*, 140(1).
- Kiefer, D., Simon, N., Beckmann, F., Wilde, F., and Gibmeier, J. (2021b). Real-time stress evolution during laser surface line hardening at varying maximum surface temperatures using synchrotron x-ray diffraction. *Optics & Laser Technology*, 140(39).
- KISSsoft (2020). Kisssoft release 2020 user manual. <https://old.kisssoft.ag/Manual/en/index.htm>.

- Klenam, D. E. P. (2012). *Effect of temperature and carbonaceous environment on the fatigue behaviour of AISI 316L austenitic stainless steel*. PhD thesis, University of the Witwatersrand.
- Kohara-Gear-Industry (n.d.). Pitchlinedeviation. [https://khkgears.net/new/gear\\_knowledge/gear\\_technical\\_reference/accuracy\\_of\\_gears.html](https://khkgears.net/new/gear_knowledge/gear_technical_reference/accuracy_of_gears.html).
- Komanduri, R. and Hou, Z. B. (2001). Thermal analysis of the laser surface transformation hardening process. *International Journal of Heat and Mass Transfer*, 44:2845–2862.
- Kren, L. (2007). Recognizing gear failures. <https://www.machinedesign.com/news/article/21816731/recognizing-gear-failures>.
- Kruth, J. P. and Bleys, P. (2000). *Measuring residual stress caused by Wire EDM of tool steel*. PhD thesis, KU Leuven, Dept. of Mechanical Engineering.
- Kruth, J. P., Van Elsen, M., Baelmans, M., and Merckel, P. (2007). Solutions for modelling moving heat sources in a semi-infinite medium and applications to laser material processing. *International Journal of Heat and Mass Transfer*, 50:4872–4882.
- Li, X., Ma, X., Subramanian, S., Shang, C., and Misra, R. (2014). Influence of prior austenite grain size on martensite austenite constituent and toughness in the heat affected zone of 700mpa high strength linepipe steel. *Materials Science and Engineering: A*, 616:141–147.
- Lindell, G. D. (2004). Reducing distortion in heat-treated gears. <https://gearsolutions.com/features/reducing-distortion-in-heat-treated-gears/>.
- MachineMFG (n.d.). How does the laser defocus affect the beam quality and welding effect? <https://www.machinemfg.com/how-does-the-laser-defocus-affect-the-beam-quality-and-welding-effect/>.
- MacKenzie, D. S. (2019). Getting back to basics with tempering. *GEAR Solutions*.
- Mao, K. and Hooke, C. J. (2009). Friction and wear behaviour of acetyl and nylon gears.
- Martinez, S., Tabernero, L., Lamikiz, A., and Ulkar, E. (2011). Laser hardening process with 2d scanning optics. *Physics Procedia*, 39.
- Meijer, J. and Van Sprang, I. (1991). *Optimization of Laser Beam Transformation Hardening by One Single Parameter*. PhD thesis, University of Twente/Netherlands.
- Milojevic, M. (2013). Optimization of transverse load factor of helical and spur gears using genetic algorithm. *Applied Mathematics & Information Sciences*, 7:1323–1331.
- Neelam (2000). Pack carb 1500.
- Oosterlinck, M. and Steenberghen, C. (2018). *Optimal path planning and closed loop control for scanning laser hardening*. PhD thesis, KU Leuven, Andreas Vesaliusstraat 13, 3000 Leuven, Belgium.

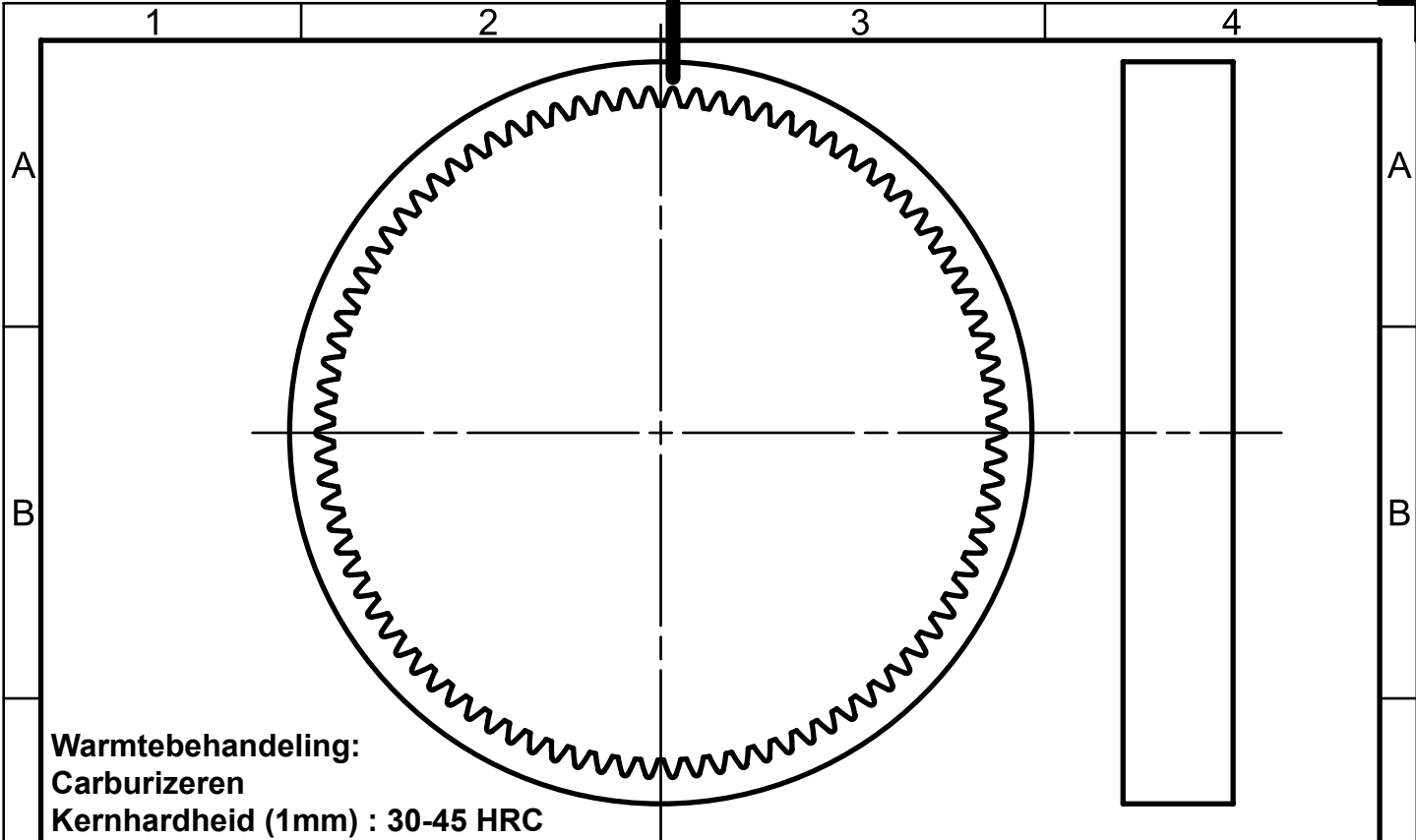


- Pandey, A. (2015). Disk laser. [https://pt.slideshare.net/ankit\\_pandey/disk-laser/5?smtNoRedir=1](https://pt.slideshare.net/ankit_pandey/disk-laser/5?smtNoRedir=1).
- Paschotta, R. (2017). Gaussian beams. [https://www.rp-photonics.com/gaussian\\_beams](https://www.rp-photonics.com/gaussian_beams).
- Physics and Radio-Electronics (2015). Nd:yag laser. <https://www.physics-and-radio-electronics.com/physics/laser/ndyaglaser.html>.
- Rindby, A. C. A. and Sahlin, A. (2012). *Compilation and Validation of Heat Transfer Coefficients of Quenching Oils*. PhD thesis, Chalmers University of Technology.
- RP Photonics Encyclopedia (2018). Beam parameter product. *RP Photonics Encyclopedia*.
- Schultz, C. D. (2004). Introduction to gear design. [http://bdtechconcepts.com/portfolio/gear\\_design/design-How-Should-They-Be-Made-.html](http://bdtechconcepts.com/portfolio/gear_design/design-How-Should-They-Be-Made-.html).
- Schwab, T. (2021). How the crystal structure of carbon-steel changes during tempering. <https://calfdm.com/2021/02/13/how-the-crystal-structure-of-carbon-steel-changes-during-tempering/>.
- Semrock (n.d.). Laser damage threshold. <https://www.semrock.com/laser-damage-threshold.aspx>.
- Shimizu, S. (2012). A new life theory for rolling bearings - by linkage between rolling contact fatigue and structural fatigue. *Tribology Transactions*, 55(5).
- Stahl, K., Hein, M., and Tobie, T. (2018). Calculation of tooth flank fracture load capacity. <https://gearsolutions.com/features/calculation-of-tooth-flank-fracture-load-capacity-2/>.
- Steel, O. S. (2016). 16mncr5 gear steel carburizing steel. <https://www.otaisteel.com/products/bearing-steel-and-gear-steel/16mncr5-steel-1-7131-carburizing-steelgearing-steel-round-bar-din-17210/>.
- Steiger, R., Ritsch-Marte, M., and Bernet, S. (2013). Mapping of phase singularities with spiral phase contrast microscopy. *Optics Express*, 21(14).
- tec science (2018). Profile shift of involute gears. Available at <https://www.tec-science.com/mechanical-power-transmission/involute-gear/profile-shift/>. visited: 2021/02/18.
- Tobie, T., Hein, M., and Stahl, K. (2018). Calculation of tooth flank fracture load capacity. <https://gearsolutions.com/features/calculation-of-tooth-flank-fracture-load-capacity-2/>.
- Tobie, T., Oster, P., and Höhn (2005). Systematic investigations on the influence of case depth on the pitting and bending strength of case carburized gears. <https://www.geartechnology.com/issues/0705x/hohn.pdf>.

- Totten, G. (2006). *Steel heat treatment: equipment and process design*. CRC press.
- Totten, G. E., Narazaki, M., Blackwood, R. R., and Jarvis, L. M. (2002). *Failures Related to Heat Treating Operations*. ASM.
- Trumpf (2017). Spatarm lassen met straalvormingstechnologie. [https://www.trumpf.com/nl\\_NL/oplossingen/toepassingen/laserstraallassen/spatarm-lassen-met-straalvormingstechnologie/](https://www.trumpf.com/nl_NL/oplossingen/toepassingen/laserstraallassen/spatarm-lassen-met-straalvormingstechnologie/).
- Van Den Bergh, D. and Van Assche, L. (2018). Design of a gearbox with focus on profile modifications for a 4wd formula student car.
- Wei, J., Sun, W., and Wang, L. (2011). Effects of flank deviation on load distributions for helical gear. *Journal of Mechanical Science and Technology*, pages 1781–1789.
- Winter, H. and Plewe, H. J. (1982). Calculation of slow speed wear of lubricated gears. *Forschungsstelle fur Zahnrad und getriebebau*, 1.
- Wittel, H., Muhs, D., Jannasch, D., and Voß iek, J. (2016). *Roloff-Matek machineonderdelen, theorieboek*. Academic Service.
- Xia, H. and Majumdar, P. (2007). A green's function model for the analysis of laser heating of materials. *Applied Mathematical Modelling*, 31:1186–1200.
- Yamagata, H. (2005). The crankshaft. In Yamagata, H., editor, *The Science and Technology of Materials in Automotive Engines*, pages 165–206. Woodhead Publishing.
- YenaEngineering (2019). Practical effects of different types of heat treatment on steel. <https://yenaengineering.nl/effects-different-type-heat-treatment-on-steel/>.
- Zhang, L., Rong, Y. M., Purushothaman, and Kang, J. (2007). Microstructure and property predictions by using a heat-treatment planning system, cht-q/t. *ASM Heat Treating Society Conference*, 24.



## Technical drawing ring gear

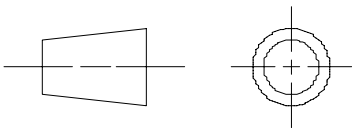


**Warmtebehandeling:**  
**Carburizeren**  
**Kernhardheid (1mm) : 30-45 HRC**  
**Oppervlaktehardheid : 60 HRC**  
**CHD (50 HRC) : 0.3-0.6mm**

**Ruwheid tandflanken :**  
**0.8um**

**Vertandingsgegevens**

Aantal tanden	z	90
Tandbreedte	b	14.8 mm
Normale modulus	m	1.0 mm
Tandhoek	$\beta$	0°
Normale drukhoek	a	20°
Referentieprofiel		1.25/0.38/1.0 ISO 53:1998 Profiel A
Nauwkeurigheidsgraad (ISO 1328:1995)		6
Profielverschuivingscoëfficiënt	x	-0.0238
Referentiecirkeldiameter	d	90.000 mm
Topcirkeldiameter	da	88.048 (+0.000/-0.035)mm
Voetcirkeldiameter	df	92.548 (-0.120/-0.1749) mm



**Ra 3,2**

FORMULA ELECTRIC BELGIUM		MAATTOLERANTIES VOLGENS ISO 2768-m		VORM- EN PLAATSTOLERANTIES VOLGENS ISO 2768-K	
DATUM	21/12/2020	Ringwiel_FormulaElectricBelgium			
GETEKEND DOOR	Bart Tyskens				
TELEFOONR.	0479 04 85 12				
EMAIL	bart.tyskens@formulaelectric.be	GROOTTE	297.0 x 210.0	REV.	A
MAATEENHEID	mm	Ringwiel_FormulaElectricBelgium		A	
MATERIAAL	16MnCr5	SCHAAL 1:1	AANTAL: 4	BLAD 1 VAN 1	

# B

Datasheet 16MnCr5

**INSPECTION CERTIFICATE**  
СВИДЕТЕЛЬСТВО ПРОИЗВОДИТЕЛЯ

<b>Producer:</b> CJSC Metallurgical Works Petrostal Russia, St.Petersburg, pr.Stachek, 47 Изготовитель ЗАО "Металлургический завод "ПЕТРОСТАЛЬ" Россия, Санкт-Петербург, пр.Стачек, 47	<b>Inspection Certificate No. 153510</b> Свидетельство производителя EN 10204-3.1
---	---

<b>Contract:</b> 056/08844200/16013 Контракт <b>Customer ref.:</b> 44779 Номер заказа <b>Works ref.:</b> 3501602 Заводской заказ	<b>Customer:</b> Заказчик <b>Stappert Intramet SA</b> <b>Route du parc industriel 5, Engis, 4480, Belgiu</b>
---	--


Steel grade Марка	Dimensions, mm Размеры, мм	Melt No. Номер плавки	No. of bundles Кол. пак.	Weight, mt Вес, т	No. of pieces Кол. штук
16MnCrS5select-2	Round 110	65255	4	9.160	20

Chemical Composition, % Химический состав	C	Si	Mn	S	P	Cr	Ni	Cu	Al	Mo	Ti	V	W
	0.180	0.270	1.120	0.027	0.009	1.010	0.190	0.200	0.040	0.020	0.015	0.007	0.010

<b>Mechanical tests:</b> Механические испытания	<b>Grain: 7</b>
--	-----------------

Re N/mm2	Rm N/mm2	A %	Z %	KV(-20C) J	HB
-	-	-	-	-	197.0

<b>Note:</b> Примечание	<p>Ultrasonic test: УЗК - EN 10308 class 3</p> <p>Экологические характеристики: Прутки произведены из незагрязненного ртутью и нерадиоактивного сырья.</p> <p>Ecologic characteristics: Bars are produced from mercury-free and non-radioactive raw materials.</p> <p>Antimixing control .</p> <p>Melting method: OH + LF.</p> <p>Non-metallic inclusions: A=2.50; B=2.50; C=1.00; D=2.00.</p> <p>Hardenability (Jominy), HRC/mm: 43.00/1.50; 43.00/3.00; 42.00/5.00; 40.00/7.00; 37.00/9.00; 34.00/11.00; 32.00/13.00; 31.00/15.00; 28.00/20.00; 27.00/25.00; 26.00/30.00.</p>
----------------------------	---

<p>Hereby we certify that the above mentioned products conform to the contracted requirements. Удостоверяем, что продукция соответствует условиям контракта. <b>056/08844200/16013</b></p> <p><b>Specification No. 2-079/01; "Tolerance according to DIN EN10060" "Chemical analysis of the steel grade is corresponds to EN 10084-2008"</b></p>	<p><b>Signature:</b> Подпись</p>  <p><b>Date: 01.11.2016</b> Дата</p>
--	--

Quality control department  
Eco-log inspector foreman  
Glazov A.

C

KISSsoft calculation report 16MnCr5

**Important hint: At least one warning has occurred during the calculation:**

1-> Calculation for load spectra:  
 The application factor should be set to 1,0!

2-> Load spectrum with negative torque:  
 In the transition from + to - torque the tooth is submitted to alternating bending stress.  
 This transition should be considered with an additional duty cycle element with an alternating bending factor (mean stress influence factor, Y<sub>M</sub>).  
 Consult the manual for more information.  
 (Element no. 4)

Load spectrum with negative load bins:  
 The working flank changes from right flank to left flank or vice versa.  
 These bins can be neglected when calculating the damage.  
 See the corresponding inputs in 'Details' of tab 'Rating'.

**Calculation of a spur-toothed cylindrical gear pair**

Drawing or article number:  
 Gear 1: 0,000,0  
 Gear 2: 0,000,0

**Load spectrum**

Own Input  
 Number of bins in the load spectrum: 4  
 Reference gear: Gear 1  
 Application factor, K<sub>A</sub>: 1,50

Bin No.	Frequency [%]	Power [kW]	Speed [1/min]	Torque [Nm]	Coefficients							
					K <sub>v</sub>	K <sub>α</sub>	K <sub>Fβ</sub>	K <sub>Hα</sub>	K <sub>y</sub>	Y <sub>M1</sub>	Y <sub>M2</sub>	
1	45,0000	7,1862	4183,8	16,4020	1,056	1,251	1,208	1,017	1,000	1,000	1,000	
2	18,0000	9,3176	5927,1	15,0120	1,084	1,271	1,224	1,030	1,000	1,000	1,000	
3	28,0000	9,1349	3137,8	27,8000	1,030	1,130	1,108	1,000	1,000	1,000	1,000	
4	9,0000	-8,5259	4183,8	-19,4600	1,050	1,204	1,170	1,000	1,000	1,000	1,000	

Numbers of load cycles			
Bin No.	Frequency	Load cycles, gear 1	Load cycles, gear 2
	[1]	[1]	[1]

[%]			
1	45,0000	112962600	28868220
2	18,0000	64012140	16358658
3	28,0000	52715880	13471836
4	9,0000	22592520	5773644
SUM	00,0000	252283140	64472358

Notice:  
 - Tooth flank with load spectrum: Consider all negative load spectrum bins as positive  
 - Tooth root with load spectrum: Consider all negative load spectrum bins as positive

S-N curve (Woehler line) in the long life domain according: according to standard

Notice:  
 Calculation-method according to:  
 - ISO 6336-6 / DIN3990-6  
 During the calculation all the load factors (ISO 6336/DIN 3990: Kv, KHβ, KFβ, AGMA 2001: Kv, Km, ...) for each load spectrum bin are calculated separately.

Notice:  
 Calculation with methods ISO 6336 and AGMA 2001 results in a reduction of resistance in the domain of fatigue resistance (from circa 10<sup>7</sup> to 10<sup>8</sup> cycles).  
 The lifetime calculation takes this into account (also with the S-N curve (Woehler Curve) of the Miner type).

**Results**

**Calculation for load spectra:**  
**The application factor should be set to 1,0!**

Safeties, calculated with load spectrum:  
 Root safety: 1,208 1,226  
 Flank safety: 1,030 1,148

Safeties against scuffing/micropitting/EHT/TFE are indicated for the most critical element of the load spectrum:  
 Safety against scuffing (integral temperature): 3,859  
 Safety against scuffing (flash temperature): 10,382

Analysis of critical elements in load spectrum: See section 10

**Only as information: Calculation with reference power**

Calculation method	ISO 6336:2006 (replaced)
Power (kW)	[P] 20,300
Speed (1/min)	[n] 6973,0 1782,0
Torque (Nm)	[T] 27,8 108,8
Application factor	[K <sub>A</sub> ] 1,50
Required service life (h)	[H] 1000,00
Gear driving (+) / driven (-)	+ -
Working flank gear 1:	Right flank

Gear 1 direction of rotation: Counterclockwise

**Tooth geometry and material**

Geometry calculation according to ISO 21771:2007		----- Gear 1 -----	Gear 2 --
Center distance (mm)	[a]	33,000	
Center distance tolerance	ISO 286:2010 Measure js7		
Normal module (mm)	[m]	1,0000	
Normal pressure angle (°)	[αn]	20,0000	
Helix angle at reference circle (°)	[β]	0,0000	
Number of teeth	[z]	23	-90
Facewidth (mm)	[b]	15,20	14,80
Hand of gear	Spur gear		
Accuracy grade	[Q-ISO 1328:1995]	6	6
Inner diameter (mm)	[d]	15,00	
External diameter (mm)	[d <sub>e</sub> ]		99,80
Inner diameter of gear rim (mm)	[d <sub>bi</sub> ]	0,00	
Outer diameter of gear rim (mm)	[d <sub>be</sub> ]		0,00

Material  
 Gear 1  
 16 MnCr 5 (1), Case-carburized steel, case-hardened  
 ISO 6336-5 Figure 9/10 (MQ), Core hardness >=25HRC Jominy J=12mm<HRC28

Gear 2  
 16 MnCr 5 (1), Case-carburized steel, case-hardened  
 ISO 6336-5 Figure 9/10 (MQ), Core hardness >=25HRC Jominy J=12mm<HRC28

Surface hardness		----- Gear 1 -----	Gear 2 --
Material treatment according to ISO 6336:2006 Normal, life factors ZNT and YNT >=0,85		HRC 59	HRC 59
Fatigue strength, tooth root stress (N/mm <sup>2</sup> )	[σ <sub>Flim</sub> ]	430,00	430,00
Fatigue strength for Hertzian pressure (N/mm <sup>2</sup> )	[σ <sub>Hlim</sub> ]	1500,00	1500,00
Tensile strength (N/mm <sup>2</sup> )	[σ <sub>B</sub> ]	1000,00	1000,00
Yield point (N/mm <sup>2</sup> )	[σ <sub>S</sub> ]	695,00	695,00
Young's modulus (N/mm <sup>2</sup> )	[E]	206000	206000
Poisson's ratio	[ν]	0,300	0,300
Roughness average value DS, flank (μm)	[RA <sub>H</sub> ]	0,60	0,60
Roughness average value DS, root (μm)	[RA <sub>F</sub> ]	3,00	3,00
Mean roughness height, Rz, flank (μm)	[RZ <sub>H</sub> ]	4,80	4,80
Mean roughness height, Rz, root (μm)	[RZ <sub>F</sub> ]	20,00	20,00

Gear reference profile 1:		1,25 / 0,38 / 1,0 ISO 53:1998 Profil A
Reference profile	[h <sub>FP</sub> ]	1,250
Dedendum coefficient	[p <sub>FP</sub> ]	0,380 (p <sub>FPmax</sub> = 0,472)
Root radius factor	[ha <sub>FP</sub> ]	1,000
Addendum coefficient	[pa <sub>FP</sub> ]	0,000
Tip radius factor	[hpr <sub>FP</sub> ]	0,000
Protuberance height coefficient	[αpr <sub>FP</sub> ]	0,000
Protuberance angle	[hFa <sub>FP</sub> ]	0,000
Tip form height coefficient	[αk <sub>FP</sub> ]	0,000
Ramp angle		not topping

Gear reference profile 2:		1,25 / 0,38 / 1,0 ISO 53:1998 Profil A
Reference profile	[h <sub>FP</sub> ]	1,250
Dedendum coefficient	[p <sub>FP</sub> ]	0,380 (p <sub>FPmax</sub> = 0,472)
Root radius factor	[ha <sub>FP</sub> ]	1,000
Addendum coefficient	[pa <sub>FP</sub> ]	0,000
Tip radius factor	[hpr <sub>FP</sub> ]	0,000
Protuberance height coefficient	[αpr <sub>FP</sub> ]	0,000
Protuberance angle	[hFa <sub>FP</sub> ]	0,000
Tip form height coefficient	[αk <sub>FP</sub> ]	0,000
Ramp angle		not topping

Information on final machining			
Dedendum reference profile	[h <sub>FP</sub> ]	1,250	1,250
Tooth root radius Refer. profile	[p <sub>FP</sub> ]	0,380	0,380
Addendum Reference profile	[ha <sub>FP</sub> ]	1,000	1,000
Protuberance height coefficient	[hpr <sub>FP</sub> ]	0,000	0,000
Protuberance angle (°)	[αpr <sub>FP</sub> ]	0,000	0,000
Tip form height coefficient	[hFa <sub>FP</sub> ]	0,000	0,000
Ramp angle (°)	[αk <sub>FP</sub> ]	0,000	0,000
Type of profile modification:		none (only running-in)	
Tip relief by running in (μm)	[Ca L/R]	2,0 / 2,0	2,0 / 2,0
Lubrication type		Oil bath lubrication	
Type of oil		ISO-VG 220	
Lubricant base		Mineral-oil base	
Oil nominal kinematic viscosity at 40°C (mm <sup>2</sup> /s)	[ν <sub>40</sub> ]		220,00
Oil nominal kinematic viscosity at 100°C (mm <sup>2</sup> /s)	[ν <sub>100</sub> ]		17,50
Specific density at 15°C (kg/dm <sup>3</sup> )	[ρ]		0,895
Oil temperature (°C)	[TS]		70,000

Gear pair			
Overall transmission ratio	[itot]		3,913
Gear ratio	[u]		-3,913
Transverse module (mm)	[m <sub>t</sub> ]		1,000
Transverse pressure angle (°)	[α <sub>t</sub> ]		20,000
Working pressure angle (°)	[α <sub>w</sub> ]		17,459
	[α <sub>w,t,e/l</sub> ]		17,390 / 17,528
Working pressure angle at normal section (°)	[α <sub>wn</sub> ]		17,459
Helix angle at operating pitch circle (°)	[β <sub>w</sub> ]		0,000
Base helix angle (°)	[β <sub>b</sub> ]		0,000
Reference center distance (mm)	[a <sub>d</sub> ]		33,500
Pitch on reference circle (mm)	[p <sub>t</sub> ]		3,142
Base pitch (mm)	[p <sub>bt</sub> ]		2,952
Transverse pitch on contact-path (mm)	[p <sub>et</sub> ]		2,952
Sum of profile shift coefficients	[Σx <sub>i</sub> ]		0,4702
Transverse contact ratio	[ε <sub>α</sub> ]		1,688
Transverse contact ratio with allowances	[ε <sub>α,e/m/v</sub> ]		1,703 / 1,675 / 1,647
Overlap ratio	[ε <sub>β</sub> ]		0,000



Total contact ratio	[ev]	1,668
Total contact ratio with allowances	[ev,e/m/l]	1,703 / 1,675 / 1,647
Length of path of contact (mm)	[ga, e/l]	4,924 / 5,029 / 4,863
Length T1-A (mm)	[T1A]	2,345 / 2,241 / 2,387
Length T1-B (mm)	[T1B]	4,317 / 4,317 / 4,298
Length T1-C (mm)	[T1C]	3,399 / 3,413 / 3,384
Length T1-D (mm)	[T1D]	5,298 / 5,193 / 5,339
Length T1-E (mm)	[T1E]	7,269 / 7,269 / 7,251
Length T2-A (mm)	[T2A]	12,246 / 12,183 / 12,246
Length T2-B (mm)	[T2B]	14,218 / 14,260 / 14,158
Length T2-C (mm)	[T2C]	13,300 / 13,356 / 13,244
Length T2-D (mm)	[T2D]	15,199 / 15,135 / 15,199
Length T2-E (mm)	[T2E]	17,170 / 17,212 / 17,110

Length T1-T2 (mm)	[T1T2]	9,901 / 9,943 / 9,859
Minimal length of contact line (mm)	[Lmin]	14,800

**Gear 1**

Profile shift coefficient	[x]	0,4940
Tooth thickness, arc, in module	[sn*]	1,9304
Tip alteration (mm)	[k*mm]	0,030
Reference diameter (mm)	[d]	23,000
Base diameter (mm)	[db]	21,613
Tip diameter (mm)	[da]	26,048
(mm)	[da,e/l]	26,048 / 26,027
Tip diameter allowances (mm)	[Ada,e/l]	0,000 / -0,021
Tip form diameter (mm)	[dFa]	26,048
(mm)	[dFa,e/l]	26,048 / 26,027
Root diameter (mm)	[df]	21,488
Generating Profile shift coefficient	[xE,e/l]	0,4198 / 0,3786
Generated root diameter with xE (mm)	[dF,e/l]	21,340 / 21,257
Root form diameter (mm)	[dFf]	22,163
(mm)	[dFf,e/l]	22,071 / 22,024

Internal toothing: Calculation dFf with pinion type cutter (z0= 25, x0=0,000)	[dFf,e/l]	22,071 / 22,024
Involute length (mm)	[l_dFa_l_dFf]	2,166
Addendum, m <sub>a</sub> (h <sub>a</sub> *+x*k) (mm)	[ha]	1,524
(mm)	[ha,e/l]	1,524 / 1,514
Dedendum (mm)	[hf=mn*(hF*-x)]	0,756
(mm)	[hf,e/l]	0,830 / 0,871
Tooth height (mm)	[h]	2,280
Virtual gear no. of teeth	[zn]	23,000
Normal tooth thickness at tip circle (mm)	[san]	0,477
(mm)	[san,e/l]	0,429 / 0,382
Normal tooth thickness at tip form circle (mm)	[sFan]	0,477
(mm)	[sFan,e/l]	0,429 / 0,382
Normal space width at root circle (mm)	[efn]	0,000
(mm)	[efn,e/l]	0,000 / 0,000

**Gear 2**

Profile shift coefficient	[x]	-0,0238
---------------------------	-----	---------

5/15

Tooth thickness, arc, in module	[sn*]	1,5535
Tip alteration (mm)	[k*mm]	0,000
Reference diameter (mm)	[d]	90,000
Base diameter (mm)	[db]	84,572
Tip diameter (mm)	[da]	88,048
(mm)	[da,e/l]	88,048 / 88,013
Tip diameter allowances (mm)	[Ada,e/l]	0,000 / -0,035
Tip form diameter (mm)	[dFa]	88,048
(mm)	[dFa,e/l]	88,048 / 88,013
Root diameter (mm)	[df]	92,548
Generating Profile shift coefficient	[xE,e/l]	-0,1200 / -0,1749
Generated root diameter with xE (mm)	[dF,e/l]	92,850 / 92,740
Root form diameter (mm)	[dFf]	91,910
(mm)	[dFf,e/l]	92,244 / 92,124
Internal toothing: Calculation dFf with pinion type cutter (z0= 29, x0=0,000)	[dFf,e/l]	92,244 / 92,124
Involute length (mm)	[l_dFa_l_dFf]	2,055
Addendum, m <sub>a</sub> (h <sub>a</sub> *+x*k) (mm)	[ha]	0,976
(mm)	[ha,e/l]	0,994 / 0,976
Dedendum (mm)	[hf=mn*(hF*-x)]	1,274
(mm)	[hf,e/l]	1,370 / 1,425
Tooth height (mm)	[h]	2,250
Virtual gear no. of teeth	[zn]	90,000
Normal tooth thickness at tip circle (mm)	[san]	0,887
(mm)	[san,e/l]	0,818 / 0,768
Normal tooth thickness at tip form circle (mm)	[sFan]	0,887
(mm)	[sFan,e/l]	0,818 / 0,768
Normal space width at root circle (mm)	[efn]	0,586
(mm)	[efn,e/l]	0,574 / 0,566

**Gear specific pair data Gear pair 1, Gear 1**

Operating pitch diameter (mm)	[dw]	22,657
(mm)	[dw,e/l]	22,648 / 22,665
Active tip diameter (mm)	[dNa]	26,048
(mm)	[dNa,e/l]	26,048 / 26,027
Theoretical tip clearance (mm)	[c]	0,250
Effective tip clearance (mm)	[c,e/l]	0,424 / 0,333
Active root diameter (mm)	[dNf]	22,116
(mm)	[dNf,e/l]	22,134 / 22,073
Reserve (dNf-dFf)/2 (mm)	[cF,e/l]	0,055 / 0,001
Max. sliding velocity at tip (m/s)	[vga]	2,104
Specific sliding at the tip	[ζa]	0,396
Specific sliding at the root	[ζf]	-0,334
Mean specific sliding	[ζm]	0,365
Sliding factor on tip	[Kga]	0,254
Sliding factor on root	[Kgf]	-0,069
Roll angle at dFa (°)	[ζdFa,e/l]	38,543 / 38,443
Roll angle to dNa (°)	[ζdNa,e/l]	38,543 / 38,443
Roll angle to dNf (°)	[ζdNf,e/l]	12,657 / 11,881
Roll angle at dFf (°)	[ζdFf,e/l]	11,861 / 11,222
Diameter of single contact point B (mm)	[d-B]	23,274 ( 23,274 / 23,260 )
Diameter of single contact point D (mm)	[d-D]	24,070 ( 23,979 / 24,107 )
Addendum contact ratio	[ε]	1,311 ( 1,306 / 1,310 )

6/15

**Gear specific pair data Gear pair 1, Gear 2**

Operating pitch diameter (mm)	[dw]	88,657
(mm)	[dw,e/l]	88,690 / 88,623
Active tip diameter (mm)	[dNa]	88,048
(mm)	[dNa,e/l]	88,048 / 88,013
Theoretical tip clearance (mm)	[c]	0,280
Effective tip clearance (mm)	[c,e/l]	0,408 / 0,324
Active root diameter (mm)	[dNf]	91,279
(mm)	[dNf,e/l]	91,310 / 91,233
Reserve (dNf-dFf)/2 (mm)	[cF,e/l]	0,505 / 0,407
Max. sliding velocity at tip (m/s)	[vga]	0,573
Specific sliding at the tip	[ζa]	0,251
Specific sliding at the root	[ζf]	-0,657
Mean specific sliding	[ζm]	0,365
Sliding factor on tip	[Kga]	0,069
Sliding factor on root	[Kgf]	-0,254
Roll angle at dFa (°)	[ζdFa,e/l]	16,508 / 16,593
Roll angle to dNa (°)	[ζdNa,e/l]	16,508 / 16,593
Roll angle to dNf (°)	[ζdNf,e/l]	23,183 / 23,321
Roll angle at dFf (°)	[ζdFf,e/l]	24,748 / 24,951
Diameter of single contact point B (mm)	[d-B]	89,225 ( 89,252 / 89,187 )
Diameter of single contact point D (mm)	[d-D]	89,869 ( 89,827 / 89,869 )
Addendum contact ratio	[ε]	0,357 ( 0,397 / 0,338 )

**General influence factors**

		----- Gear 1 ----- Gear 2 --
Nominal circum. force at pitch circle (N)	[F]	2417,4
Axial force (N)	[Fa]	0,0
Radial force (N)	[Fr]	879,9
Normal force (N)	[Fnorm]	2572,5
Nominal circumferential force per mm (N/mm)	[w]	163,34
Only as information: Forces at operating pitch circle:		
Nominal circumferential force (N)	[Ftw]	2454,0
Axial force (N)	[Faw]	0,0
Radial force (N)	[Frw]	771,8
Circumferential speed reference circle (m/s)	[v]	8,40
Circumferential speed operating pitch circle (m/s)	[v(dw)]	8,27
Running-in value (μm)	[yp]	0,5
Running-in value (μm)	[yf]	0,5
Correction factor	[CM]	0,800
Gear blank factor	[CR]	1,000
Basic rack factor	[CBS]	0,975
Material coefficient	[E/Est]	1,000
Singular tooth stiffness (N/mm/μm)	[c]	15,698
Meshing stiffness (N/mm/μm)	[cvα]	23,561
Meshing stiffness (N/mm/μm)	[cvβ]	20,027
Reduced mass (kg/mm)	[mRed]	0,00157
Resonance speed (min-1)	[nE 1]	50859
Resonance ratio (-)	[N]	0,137
Subcritical range		
Running-in value (μm)	[yα]	0,5
Bearing distance l of pinion shaft (mm)	[l]	30,400
Distance s of pinion shaft (mm)	[s]	3,040
Outside diameter of pinion shaft (mm)	[dsh]	15,200

7/15

Load in accordance with Figure 13, ISO 6336-1:2006 0.a), 1.b), 2.c), 3.d), 4.e)	[-]	4
Coefficient K' according to Figure 13, ISO 6336-1:2006 Without stiffening	[K]	-1,00
Tooth trace deviation (active) (μm)	[FBγ]	3,22
from deformation of shaft (μm)	[fsh*B1]	1,29
fsh (μm) = 1,29 , B1=1,00 , fHβ5 (μm) = 5,50		
Tooth without tooth trace modification		
Position of contact pattern: favorable		
from production tolerances (μm)	[fmc*B2]	10,26
B2= 1,00		
Tooth trace deviation, theoretical (μm)	[FBx]	3,79
Running-in value (μm)	[yβ]	0,57
Dynamic factor	[Kv]	1,068
Face load factor - flank	[KHβ]	1,123
- Tooth root	[KFβ]	1,103
- Scuffing	[KBβ]	1,123
Transverse load factor - flank	[KHα]	1,000
- Tooth root	[KFα]	1,000
- Scuffing	[KBα]	1,000

**Tooth root load capacity**

Calculation of Tooth form coefficients according method: B		
Internal toothing:		Calculation of pF and sFn according to ISO 6336-3:2007-04-01
Internal toothing:		Calculation of YF, YS with pinion type cutter, z0= 29, x0= 0,000, paP0*=
0,380		
		----- Gear 1 ----- Gear 2 --
Calculated with generating profile shift coefficient	[xE,e]	0,4198 -0,1200
Tooth form factor	[YF]	1,13 1,16
Stress correction factor	[YS]	2,29 2,20
Load application angle (°)	[αFen]	22,56 19,36
Load application diameter (mm)	[da,]	24,070 -89,225
Bending moment arm (mm)	[hF]	0,92 1,46
Tooth thickness at root (mm)	[sFn]	2,19 2,75
Tooth root radius (mm)	[ρF]	0,44 0,50
Bending moment arm (-)	[hF/mm]	0,921 1,464
Tooth thickness at root (-)	[sFn/mm]	2,191 2,753
Tooth root radius (-)	[ρF/mm]	0,440 0,496
Calculation cross section diameter (mm)	[dcr,]	21,672 -92,607
Tangents on calculation cross section (°)	[σcr,]	30,000 60,000
Notch parameter	[q]	2,490 2,774
Helix angle factor	[Yβ]	1,000
Deep tooth factor	[YDT]	1,000
Gear rim thickness (mm)	[sr]	3,13 3,48
Gear rim factor	[Yβ]	1,00 1,00
Effective facewidth (mm)	[bEFF]	15,20 14,80
Nominal stress at tooth root (N/mm²)	[σF0]	412,91 418,31
Tooth root stress (N/mm²)	[σF]	728,37 740,68

8/15

Permissible bending stress at root of Test-gear			
Notch sensitivity factor	[YdreIT]	1,000	1,003
Surface factor	[YRreIT]	0,957	0,957
Size factor, tooth root	[YX]	1,000	1,000
Finite life factor	[YNT]	0,906	0,931
$Y_{c} = Y_{dreIT} \cdot Y_{RreIT} \cdot Y_{X} \cdot Y_{NT}$		0,867	0,893
Alternating bending factor, mean stress influence coefficient			
Technology factor	[YM]	1,000	1,000
Coefficient for surface factor like for shot peening; The standard gives no applicable information about this...	[YT]	1,100	1,100
Stress correction factor	[Yst]		2,00
$Y_{st} \cdot \sigma_{Flim}$ (N/mm <sup>2</sup> )	[oFE]	860,00	860,00
Permissible tooth root stress $\sigma_{FG/SFmin}$ (N/mm <sup>2</sup> )	[oFP]	683,12	703,90
Limit strength tooth root (N/mm <sup>2</sup> )	[oFG]	819,74	844,67
Required safety	[SFmin]	1,20	1,20

Flank safety

		----- Gear 1 -----	Gear 2 --
Zone factor	[ZH]		2,684
Elasticity factor ( $\sigma$ -N/mm <sup>2</sup> )	[ZE]		189,812
Contact ratio factor	[Zc]		0,882
Helix angle factor	[ZB]		1,000
Effective facewidth (mm)	[bEFF]		14,80
Nominal contact stress (N/mm <sup>2</sup> )	[oH0]		1032,60
Contact stress at operating pitch circle (N/mm <sup>2</sup> )	[oHw]		1385,03
Single tooth contact factor	[ZB,ZD]	1,00	1,00
Contact stress (N/mm <sup>2</sup> )	[oHB, oHD]	1385,03	1385,03
Lubrication factor for NL	[ZL]	1,020	1,020
Speed factor for NL	[ZV]	0,995	0,995
Roughness factor for NL	[ZR]	0,943	0,943
Material hardening factor for NL	[ZW]	1,000	1,000
Finite life factor	[ZNT]	0,937	0,977
Limited pitting is permitted:	[ZL-ZV-ZR-ZNT]		0,897 0,935
No			
Size factor (flank)	[ZX]	1,000	1,000
Permissible contact stress, $\sigma_{HG}/SHmin$ (N/mm <sup>2</sup> )	[oHP]	1495,03	1558,92
Pitting stress limit (N/mm <sup>2</sup> )	[oHG]	1345,53	1403,03
Required safety	[SHmin]	0,90	0,90

Micropitting according to

ISO/TS 6336-22:2018

Calculation has not been carried out. Lubricant: Load stage micropitting test not known

Scuffing load capacity

Calculation method according to	ISO/TS 6336-20/21:2017	
Helical load factor for scuffing	[KBV]	1,000
Lubrication coefficient for lubrication type	[XS]	1,000
Scuffing test and load stage	[FZGes] FZG - Test A / 8,3 / 90 (ISO 14835 - 1)	12

9/15

Multiple meshing factor	[Xmp]	1,000
Relative structural factor, scuffing	[XWreIT]	1,000
Thermal contact factor (N/mm/s, 5/K)	[BM]	13,780 13,780
Relevant tip relief ( $\mu$ m)	[Ca]	2,00 2,00
Optimal tip relief ( $\mu$ m)	[Ceff]	15,61
Ca taken as optimal in the calculation (0=no, 1=yes)		0 0
Effective facewidth (mm)	[bEFF]	14,800
Applicable circumferential force/facewidth (N/mm)	[wBl]	293,856
$KBy = 1,000 \cdot wBl \cdot KBy = 293,856$		
Angle factor	[XaB]	0,939
$\epsilon_1: 1,311, \epsilon_2: 0,357$		

Flash temperature-criteria		
Lubricant factor	[XL]	0,830
Tooth mass temperature ( $^{\circ}$ C)	[oMi]	77,29
$\theta Mi = \theta oil + XS \cdot 0,47 \cdot Xmp \cdot \theta flm$		
Average flash temperature ( $^{\circ}$ C)	[oFlm]	15,51
Scuffing temperature ( $^{\circ}$ C)	[oS]	348,80
$\Gamma$ coordinates (point of highest temperature)	[Gamma]	0,553
[Gamma]= -0,310 [GammaE]= 1,139		
Highest contact temp. ( $^{\circ}$ C)	[oB]	105,10
Flash factor ( $^{\circ}$ K <sup>0.4</sup> N <sup>-0.4</sup> ·75 <sup>0.5</sup> s <sup>0.5</sup> m <sup>-0.5</sup> mm)	[XM]	50,058
Approach factor	[XJ]	1,000
Load sharing factor	[XT]	1,000
Dynamic viscosity (mPa*s)	[etaM]	41,90 (70.0 $^{\circ}$ C)
Coefficient of friction	[mu]	0,064

Integral temperature-criteria		
Lubricant factor	[XL]	1,000
Tooth mass temperature ( $^{\circ}$ C)	[oMiC]	77,40
$\theta MC = \theta oil + XS \cdot 0,70 \cdot \theta flaint$		
Mean flash temperature ( $^{\circ}$ C)	[oFlaint]	10,57
Integral scuffing temperature ( $^{\circ}$ C)	[oSint]	360,78
Flash factor ( $^{\circ}$ K <sup>0.4</sup> N <sup>-0.4</sup> ·75 <sup>0.5</sup> s <sup>0.5</sup> m <sup>-0.5</sup> mm)	[XM]	50,058
Running-in factor, well run in	[XE]	1,000
Contact ratio factor	[Xc]	0,262
Dynamic viscosity (mPa*s)	[etaOil]	41,90 (70.0 $^{\circ}$ C)
Mean coefficient of friction	[mu]	0,083
Geometry factor	[XBE]	0,157
Meshing factor	[XQ]	1,000
Tip relief factor	[XCa]	1,295
Integral tooth flank temperature ( $^{\circ}$ C)	[oInt]	93,25

Measurements for tooth thickness

		----- Gear 1 -----	Gear 2 --
Tooth thickness tolerance		DIN 3967 cd25	DIN 3967 cd25
Tooth thickness allowance (normal section) (mm)	[As,e/I]	-0,054 / -0,084	-0,070 / -0,110
Number of teeth spanned	[k]	4,000	11,000
For internal toothing: k = measurement gap number			
Base tangent length (no backlash) (mm)	[Wk]	10,993	32,274
Base tangent length with allowance (mm)	[Wk,e/I]	10,942 / 10,914	32,340 / 32,378
(mm)	[DeltaWk,e/I]	-0,051 / -0,079	-0,066 / -0,103
Diameter of measuring circle (mm)	[dMvWk,m]	24,218	90,551
Theoretical diameter of ball/pin (mm)	[DM]	1,947	1,663
Effective diameter of ball/pin (mm)	[DMeff]	2,000	1,750

10/15

Radial single-ball measurement backlash free (mm)	[MRk]	13,500	43,735
Radial single-ball measurement (mm)	[MRk,e/I]	13,450 / 13,421	43,895 / 43,837
Diameter of measuring circle (mm)	[dMMr,m]	23,944	90,069
Diameter measurement over two balls without clearance (mm)	[MdK]	26,943	87,470
Diameter two ball measure (mm)	[MdK,e/I]	26,841 / 26,784	87,790 / 87,675
Diameter measurement over pins without clearance (mm)	[MdR]	26,943	87,470
Measurement over pins according to DIN 3960 (mm)	[MdR,e/I]	26,841 / 26,784	87,790 / 87,675
Measurement over 3 pins, axial, according to AGMA 2002 (mm)			
[dk3A,e/I]	26,841 / 26,784	87,790 / 87,675	
Dimensions over 3 pins without clearance (mm)	[Md3R]	26,884	-0,000
Measurement over 3 pins with allowance (mm)	[Md3R,e/I]	26,783 / 26,727	-0,000 / -0,000

Chordal tooth thickness (no backlash) (mm)	[sc]	1,928	1,553
Normal chordal tooth thickness with allowance (mm)	[sc,e/I]	1,876 / 1,846	1,483 / 1,443
Reference chordal height from da,m (mm)	[ha]	1,559	0,978
Tooth thickness, arc (mm)	[sn]	1,930	1,553
(mm)	[sn,e/I]	1,876 / 1,846	1,483 / 1,443

Backlash free center distance (mm)	[aControl,e/I]	33,189 / 33,291	
Backlash free center distance, allowances (mm)	[ita]	0,189 / 0,291	
dNI,i with aControl (mm)	[dNd0,i]	21,781	91,995
Reserve (dNF0,i-dF,e)/2 (mm)	[cF0,i]	-0,145	0,064
Tip clearance (mm)	[c0,i(aControl)]	0,055	0,045
Center distance allowances (mm)	[Aa,e/I]	-0,013 / 0,013	
Circumferential backlash from Aa (mm)	[tw_Aa,e/I]	0,008 / -0,008	
Radial backlash (mm)	[rwe/I]	0,304 / 0,176	
Circumferential backlash (transverse section) (mm)	[tw,e/I]	0,199 / 0,114	
Normal backlash (mm)	[jn,e/I]	0,191 / 0,108	
Torsional angle on input with output fixed:			
Total torsional angle ( $^{\circ}$ )	[iTSys]	1,0063/0,5780	

Toothing tolerances

		----- Gear 1 -----	Gear 2 --
According to ISO 1328-1:1995, ISO 1328-2:1997			
Accuracy grade	[Q]	6	6
Single pitch deviation ( $\mu$ m)	[fpkT]	7,00	7,50
Base circle pitch deviation ( $\mu$ m)	[fpbT]	6,60	7,00
Sector pitch deviation over k/8 pitches ( $\mu$ m)	[Fpk/8T]	9,50	15,00
Profile form deviation ( $\mu$ m)	[ffoT]	5,50	6,50
Profile slope deviation ( $\mu$ m)	[ffoT]	4,60	5,50
Total profile deviation ( $\mu$ m)	[FoT]	7,50	8,50
Helix form deviation ( $\mu$ m)	[ffBT]	7,00	7,50
Helix slope deviation ( $\mu$ m)	[ffBT]	7,00	7,50
Total helix deviation ( $\mu$ m)	[FBT]	10,00	11,00
Total cumulative pitch deviation ( $\mu$ m)	[FPT]	20,00	26,00
Runout ( $\mu$ m)	[FRT]	16,00	21,00
Single flank composite, total ( $\mu$ m)	[FisT]	34,00	41,00
Single flank composite, tooth-to-tooth ( $\mu$ m)	[flsT]	14,00	15,00
Radial composite, total ( $\mu$ m)	[FidT]	21,00	26,00
Radial composite, tooth-to-tooth ( $\mu$ m)	[fidT]	5,00	5,00
FidT (F <sub>r</sub> ), fidT (F <sub>r</sub> ) according to ISO 1328:1997 calculated with the geometric mean values for mn and d			
Axis alignment tolerances (recommendation acc. to ISO TR 10064-3:1996, Quality)			
6			
Maximum value for deviation error of axis ( $\mu$ m)	[FzB]	11,30	(FzB= 11,00 )
Maximum value for inclination error of axes ( $\mu$ m)	[FzS]	22,59	

11/15

Modifying and defining the tooth form

<b>Profile and tooth trace modifications for gear 1</b>		
<b>Symmetric (both flanks)</b>		
- flankline crowning		
Cb = 10,000 $\mu$ m		
rcrown=288mm		

Data for the tooth form calculation :  
Data not available.  
Please run the calculation in the "Tooth form" tab and open the main report again.

Supplementary data

Maximal possible center distance (eps_a=1,0)	[aMAX]	32,463
Mass (g)	[m]	31,77 164,41
Total mass (g)	[mGes]	196,18
Moment of inertia for system, relative to the input: calculation without consideration of the exact tooth shape		
Single gears, (da+df)/2...di (kg*m <sup>2</sup> )	[J]	3,137e-06 0,0003723
System (da+df)/2...di (kg*m <sup>2</sup> )	[J]	2,745e-05
Torsional stiffness at driving gear with fixed driven gear:		
Torsional stiffness (MNm/rad)	[cr]	0,035
Torsion when subjected to nominal torque ( $^{\circ}$ )	[ocr]	0,045
Mean coefficient of friction (as defined in Niemann)	[mu]	0,093
Wear sliding coef. by Niemann	[zetaW]	0,609
Loss factor	[HV]	0,120
Gear power loss (KW)	[PVZ]	0,225
Meshing efficiency (%)	[eta]	98,890
Sound pressure level according to Masuda, without contact analysis	[dB(A)]	68,4

Service life, damage

Calculation with load spectrum		
Required safety for tooth root	[SFmin]	1,20
Required safety for tooth flank	[SHmin]	0,90
Service life (calculated with required safeties):		
System service life (h)	[Hatt]	1394
Tooth root service life (h)	[HFatt]	1394 2886
Tooth flank service life (h)	[HHatt]	8,25e+04 3,228e+05

Damage calculated on the basis of the required service life	[H] (1000,0 h)			
No.	F1%	F2%	H1%	H2%
1	0,0000	0,0000	0,0000	0,0000
2	0,0000	0,0000	0,0000	0,0000
3	71,7363	34,6503	1,2122	0,3098
4	0,0000	0,0000	0,0000	0,0000

12/15

Σ 71,7363 34,6503 1,2122 0,3098

Damage calculated on basis of system service life [Hatt] (1394,0 h)

No.	F1%	F2%	H1%	H2%
1	0,0000	0,0000	0,0000	0,0000
2	0,0000	0,0000	0,0000	0,0000
3	100,0000	48,3023	1,6897	0,4318
4	0,0000	0,0000	0,0000	0,0000

Σ 100,0000 48,3023 1,6897 0,4318

Damage calculated on basis of individual service life HFatt & HHatt

(h)	HFatt1	HFatt2	HHatt1	HHatt2
	1394		2886	
				8,25e+04
				3,228e+05
No.	F1%	F2%	H1%	H2%
1	0,00	0,00	0,00	0,00
2	0,00	0,00	0,00	0,00
3	100,00	100,00	100,00	100,00
4	0,00	0,00	0,00	0,00

Most critical duty cycle elements for Scoring (SB, Sint), Tooth Flank Fracture (SFF), hardened layer (SEHT) and Micropitting (Slam)  
 SB: 3  
 Sint: 4

**Application factor calculated according to ISO 6336-6, Annex A.3**

(The slope of the S-N curve (Woehler lines) in the range of endurance limit according to ISO 6336-6, Table A.1 is used.)

Gear		p	Teq		KA
1	Tooth root	8,738	27,8	KA,F	1 1,000
1	Tooth flank	6,611	27,8	KA,H	1 1,000
2	Tooth root	8,738	108,8	KA,F	2 1,000
2	Tooth flank	6,611	89,5	KA,H	2 0,823

Application factor, ISO 6336-6 A.3 [KAmax] 1,000  
 [KA,Fmax / KA,Hmax] 1,000 / 1,000

Note: If an application factor is entered, the indicated values for KA come with 1,500 zu multiplizieren!

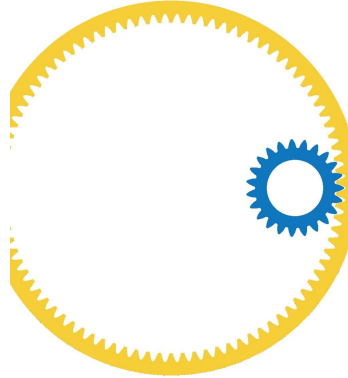
**Classification according to F.E.M., Edition 1,001, 1998**

Spectrum factor	[km]	0,432
Spectrum class	[L]	3
Application class, predefined service life	[T]	3
Machine class, predefined service life	[M]	4
Application class, achievable service life	[T]	3
Machine class, achievable service life	[M]	4

**Remarks:**

- Specifications with [e/l] imply: Maximum [e] and minimum value [l] for Taking all tolerances into account
- Specifications with [m] imply: Mean value within tolerance
- For the backlash tolerance, the center distance tolerances and the tooth thickness allowance are taken into account.
- The maximum and minimum clearance according to the largest or smallest allowances are defined..
- The calculation is performed for the operating pitch circle.

- Details of calculation method:  
 cy according to Method B  
 Kv according to Method B  
 KHβ and KFβ according to Method C  
 fma according to Equation 64, fsh according to 57/58, Fβx according to 52/53/54  
 KHα, KFα according to Method B
- The logarithmically interpolated value taken from the values for the fatigue strength and the static strength, based on the number of load cycles, is used for coefficients ZL, ZV, ZR, ZW, ZX, YdreT, YRrelT and YX..



**Tolerance field for tooth form calculation**

- Diameter: Mean value, Tooth thickness: Mean value  
 da1 = 26,0375 mm, df1 = 21,2984 mm, As1 = -0,0690 mm  
 da2 = 88,0301 mm, df2 = 92,7949 mm, As2 = -0,0900 mm

Figure: Tooth system

D

KISSsoft calculation report 42CrMo4

**Important hint: At least one warning has occurred during the calculation:**

1-> Calculation for load spectra:  
 The application factor should be set to 1,0!

2-> Load spectrum with negative torque:  
 In the transition from + to - torque the tooth is submitted to alternating bending stress.  
 This transition should be considered with an additional duty cycle element with an alternating bending factor (mean stress influence factor, Y<sub>M</sub>).  
 Consult the manual for more information.  
 (Element no. 4)

Load spectrum with negative load bins:  
 The working flank changes from right flank to left flank or vice versa.  
 These bins can be neglected when calculating the damage.  
 See the corresponding inputs in 'Details' of tab 'Rating'.

**Calculation of a spur-toothed cylindrical gear pair**

Drawing or article number:  
 Gear 1: 0,000,0  
 Gear 2: 0,000,0

**Load spectrum**

Own Input  
 Number of bins in the load spectrum: 4  
 Reference gear: Gear 1  
 Application factor, K<sub>A</sub>: 1,50

Bin No.	Frequency [%]	Power [kW]	Speed [1/min]	Torque [Nm]	Coefficients							
					K <sub>v</sub>	K <sub>α</sub>	K <sub>Fβ</sub>	K <sub>Hα</sub>	K <sub>Hβ</sub>	Y <sub>M1</sub>	Y <sub>M2</sub>	
1	45,0000	7,1862	4183,8	16,4020	1,056	1,251	1,208	1,017	1,000	1,000	1,000	
2	18,0000	9,3176	5927,1	15,0120	1,084	1,271	1,224	1,030	1,000	1,000	1,000	
3	28,0000	9,1349	3137,8	27,8000	1,030	1,130	1,108	1,000	1,000	1,000	1,000	
4	9,0000	-8,5259	4183,8	-19,4600	1,050	1,204	1,170	1,000	1,000	1,000	1,000	

Numbers of load cycles			
Bin No.	Frequency	Load cycles, gear 1	Load cycles, gear 2
		[ ]	[ ]

[%]			
1	45,0000	112962600	28868220
2	18,0000	64012140	16358658
3	28,0000	52715880	13471836
4	9,0000	22592520	5773644
SUM	00,0000	252283140	64472358

Notice:  
 - Tooth flank with load spectrum: Consider all negative load spectrum bins as positive  
 - Tooth root with load spectrum: Consider all negative load spectrum bins as positive

S-N curve (Woehler line) in the long life domain according: according to standard

Notice:  
 Calculation-method according to:  
 - ISO 6336-6 / DIN3990-6  
 During the calculation all the load factors (ISO 6336/DIN 3990: K<sub>v</sub>, K<sub>Hβ</sub>, K<sub>Fβ</sub>, AGMA 2001: K<sub>v</sub>, K<sub>m</sub>, ...) for each load spectrum bin are calculated separately.

Notice:  
 Calculation with methods ISO 6336 and AGMA 2001 results in a reduction of resistance in the domain of fatigue resistance (from circa 10<sup>7</sup> to 10<sup>8</sup> cycles).  
 The lifetime calculation takes this into account (also with the S-N curve (Woehler Curve) of the Miner type).

**Results**

**Calculation for load spectra:**  
**The application factor should be set to 1,0!**

Safeties, calculated with load spectrum:  
 Root safety: 1,039 1,055  
 Flank safety: 0,838 0,934

Safeties against scuffing/micropitting/EHT/TFE are indicated for the most critical element of the load spectrum:  
 Safety against scuffing (integral temperature): 3,976  
 Safety against scuffing (flash temperature): 10,382

Analysis of critical elements in load spectrum: See section 10

**Only as information: Calculation with reference power**

Calculation method	ISO 6336:2006 (replaced)
	----- Gear 1 ----- Gear 2 --
Power (kW)	[P] 20,300
Speed (1/min)	[n] 6973,0 1782,0
Torque (Nm)	[T] 27,8 108,8
Application factor	[K <sub>A</sub> ] 1,50
Required service life (h)	[H] 1000,00
Gear driving (+) / driven (-)	+ -
Working flank gear 1:	Right flank

Gear 1 direction of rotation: Counterclockwise

**Tooth geometry and material**

Geometry calculation according to	ISO 21771:2007
	----- Gear 1 ----- Gear 2 --
Center distance (mm)	[a] 33,000
Center distance tolerance	ISO 286:2010 Measure js7
Normal module (mm)	[m] 1,0000
Normal pressure angle (°)	[α <sub>n</sub> ] 20,0000
Helix angle at reference circle (°)	[β] 0,0000
Number of teeth	[z] 23 -90
Facewidth (mm)	[b] 15,20 14,80
Hand of gear	Spur gear
Accuracy grade	[Q-ISO 1328:1995] 6 6
Inner diameter (mm)	[d] 15,00
External diameter (mm)	[d <sub>e</sub> ] 99,80
Inner diameter of gear rim (mm)	[d <sub>bi</sub> ] 0,00
Outer diameter of gear rim (mm)	[d <sub>be</sub> ] 0,00

Material  
 Gear 1  
 42 CrMo 4 (2), Through hardened steel, flame/ind. hardened  
 ISO 6336-5 Figure 11/12 (MQ) Flank & root hardened

Gear 2  
 42 CrMo 4 (2), Through hardened steel, flame/ind. hardened  
 ISO 6336-5 Figure 11/12 (MQ) Flank & root hardened

Surface hardness	----- Gear 1 ----- Gear 2 --
	HRC 56 HRC 56
Material treatment according to ISO 6336:2006 Normal, life factors ZNT and YNT >=0,85	
Fatigue strength, tooth root stress (N/mm <sup>2</sup> )	[σ <sub>Flim</sub> ] 370,00 370,00
Fatigue strength for Hertzian pressure (N/mm <sup>2</sup> )	[σ <sub>Hlim</sub> ] 1220,00 1220,00
Tensile strength (N/mm <sup>2</sup> )	[σ <sub>B</sub> ] 1100,00 1100,00
Yield point (N/mm <sup>2</sup> )	[σ <sub>S</sub> ] 900,00 900,00
Young's modulus (N/mm <sup>2</sup> )	[E] 206000 206000
Poisson's ratio	[ν] 0,300 0,300
Roughness average value DS, flank (μm)	[RA <sub>H</sub> ] 0,60 0,60
Roughness average value DS, root (μm)	[RA <sub>F</sub> ] 3,00 3,00
Mean roughness height, Rz, flank (μm)	[RZ <sub>H</sub> ] 4,80 4,80
Mean roughness height, Rz, root (μm)	[RZ <sub>F</sub> ] 20,00 20,00

Reference profile	1,25 / 0,38 / 1,0 ISO 53:1998 Profil A
Dedendum coefficient	[h <sub>fP</sub> <sup>*</sup> ] 1,250
Root radius factor	[ρ <sub>fP</sub> <sup>*</sup> ] 0,380 (ρ <sub>fPmax</sub> <sup>*</sup> = 0,472)
Addendum coefficient	[ha <sub>fP</sub> <sup>*</sup> ] 1,000
Tip radius factor	[ρa <sub>fP</sub> <sup>*</sup> ] 0,000
Protuberance height coefficient	[h <sub>prP</sub> <sup>*</sup> ] 0,000
Protuberance angle	[α <sub>prP</sub> <sup>*</sup> ] 0,000
Tip form height coefficient	[h <sub>FaP</sub> <sup>*</sup> ] 0,000
Ramp angle	[α <sub>kP</sub> <sup>*</sup> ] 0,000
	not topping

Reference profile	2:	1,25 / 0,38 / 1,0 ISO 53:1998 Profil A
Dedendum coefficient	[h <sub>fP</sub> <sup>*</sup> ] 1,250	
Root radius factor	[ρ <sub>fP</sub> <sup>*</sup> ] 0,380	(ρ <sub>fPmax</sub> <sup>*</sup> = 0,472)
Addendum coefficient	[ha <sub>fP</sub> <sup>*</sup> ] 1,000	
Tip radius factor	[ρa <sub>fP</sub> <sup>*</sup> ] 0,000	
Protuberance height coefficient	[h <sub>prP</sub> <sup>*</sup> ] 0,000	
Protuberance angle	[α <sub>prP</sub> <sup>*</sup> ] 0,000	
Tip form height coefficient	[h <sub>FaP</sub> <sup>*</sup> ] 0,000	
Ramp angle	[α <sub>kP</sub> <sup>*</sup> ] 0,000	
		not topping

Information on final machining		
Dedendum reference profile	[h <sub>fP</sub> <sup>*</sup> ] 1,250	1,250
Tooth root radius Refer. profile	[ρ <sub>fP</sub> <sup>*</sup> ] 0,380	0,380
Addendum Reference profile	[ha <sub>fP</sub> <sup>*</sup> ] 1,000	1,000
Protuberance height coefficient	[h <sub>prP</sub> <sup>*</sup> ] 0,000	0,000
Protuberance angle (°)	[α <sub>prP</sub> <sup>*</sup> ] 0,000	0,000
Tip form height coefficient	[h <sub>FaP</sub> <sup>*</sup> ] 0,000	0,000
Ramp angle (°)	[α <sub>kP</sub> <sup>*</sup> ] 0,000	0,000
Type of profile modification:	none (only running-in)	
Tip relief by running in (μm)	[Ca L/R] 3,4 / 3,4	3,4 / 3,4
Lubrication type	Oil bath lubrication	
Type of oil	ISO-VG 220	
Lubricant base	Mineral-oil base	
Oil nominal kinematic viscosity at 40°C (mm <sup>2</sup> /s)	[ν <sub>40</sub> ] 220,00	
Oil nominal kinematic viscosity at 100°C (mm <sup>2</sup> /s)	[ν <sub>100</sub> ] 17,50	
Specific density at 15°C (kg/dm <sup>3</sup> )	[ρ] 0,895	
Oil temperature (°C)	[T <sub>S</sub> ] 70,000	

Gear pair	
Overall transmission ratio	[i <sub>tot</sub> ] 3,913
Gear ratio	[u] -3,913
Transverse module (mm)	[m <sub>t</sub> ] 1,000
Transverse pressure angle (°)	[α <sub>t</sub> ] 20,000
Working pressure angle (°)	[α <sub>w</sub> <sup>*</sup> ] 17,459
	[α <sub>w<sub>t</sub>,e<sub>l</sub>l</sub> <sup>*</sup> ] 17,390 / 17,528
Working pressure angle at normal section (°)	[α <sub>wn</sub> <sup>*</sup> ] 17,459
Helix angle at operating pitch circle (°)	[β <sub>w</sub> ] 0,000
Base helix angle (°)	[β <sub>b</sub> ] 0,000
Reference center distance (mm)	[a <sub>d</sub> ] 33,500
Pitch on reference circle (mm)	[p <sub>t</sub> ] 3,142
Base pitch (mm)	[p <sub>bt</sub> ] 2,952
Transverse pitch on contact-path (mm)	[p <sub>et</sub> ] 2,952
Sum of profile shift coefficients	[Σx <sub>i</sub> ] 0,4702
Transverse contact ratio	[ε <sub>α</sub> ] 1,668
Transverse contact ratio with allowances	[ε <sub>α,e<sub>m</sub>/l</sub> ] 1,703 / 1,675 / 1,647
Overlap ratio	[ε <sub>β</sub> ] 0,000

Total contact ratio	[ev]	1,668
Total contact ratio with allowances	[ev,e/m/l]	1,703 / 1,675 / 1,647
Length of path of contact (mm)	[ga, e/l]	4,924 / 5,029 / 4,863
Length T1-A (mm)	[T1A]	2,345 / 2,241 / 2,387
Length T1-B (mm)	[T1B]	4,317 / 4,317 / 4,298
Length T1-C (mm)	[T1C]	3,399 / 3,413 / 3,384
Length T1-D (mm)	[T1D]	5,298 / 5,193 / 5,339
Length T1-E (mm)	[T1E]	7,269 / 7,269 / 7,251
Length T2-A (mm)	[T2A]	12,246 / 12,183 / 12,246
Length T2-B (mm)	[T2B]	14,218 / 14,260 / 14,158
Length T2-C (mm)	[T2C]	13,300 / 13,356 / 13,244
Length T2-D (mm)	[T2D]	15,199 / 15,135 / 15,199
Length T2-E (mm)	[T2E]	17,170 / 17,212 / 17,110

Length T1-T2 (mm)	[T1T2]	9,901 / 9,943 / 9,859
Minimal length of contact line (mm)	[Lmin]	14,800

**Gear 1**

Profile shift coefficient	[x]	0,4940
Tooth thickness, arc, in module	[sn*]	1,9304
Tip alteration (mm)	[k*mm]	0,030
Reference diameter (mm)	[d]	23,000
Base diameter (mm)	[db]	21,613
Tip diameter (mm)	[da]	26,048
(mm)	[da,e/l]	26,048 / 26,027
Tip diameter allowances (mm)	[Ada,e/l]	0,000 / -0,021
Tip form diameter (mm)	[dFa]	26,048
(mm)	[dFa,e/l]	26,048 / 26,027
Root diameter (mm)	[df]	21,488
Generating Profile shift coefficient	[xE,e/l]	0,4198 / 0,3786
Generated root diameter with xE (mm)	[dF,e/l]	21,340 / 21,257
Root form diameter (mm)	[dFf]	22,163
(mm)	[dFf,e/l]	22,071 / 22,024

Internal toothing: Calculation dFf with pinion type cutter (z0=	25	, x0=0,000 )
Involute length (mm)	[l_dFa_l_dFf]	2,166
Addendum, m <sub>a</sub> (h <sub>a</sub> *+x*k) (mm)	[ha]	1,524
(mm)	[ha,e/l]	1,524 / 1,514
Dedendum (mm)	[hf=mn*(hF*-x)]	0,756
(mm)	[hf,e/l]	0,830 / 0,871
Tooth height (mm)	[h]	2,280
Virtual gear no. of teeth	[zn]	23,000
Normal tooth thickness at tip circle (mm)	[san]	0,477
(mm)	[san,e/l]	0,429 / 0,382
Normal tooth thickness at tip form circle (mm)	[sFan]	0,477
(mm)	[sFan,e/l]	0,429 / 0,382
Normal space width at root circle (mm)	[efn]	0,000
(mm)	[efn,e/l]	0,000 / 0,000

**Gear 2**

Profile shift coefficient	[x]	-0,0238
---------------------------	-----	---------

5/15

Tooth thickness, arc, in module	[sn*]	1,5535
Tip alteration (mm)	[k*mm]	0,000
Reference diameter (mm)	[d]	90,000
Base diameter (mm)	[db]	84,572
Tip diameter (mm)	[da]	88,048
(mm)	[da,e/l]	88,048 / 88,013
Tip diameter allowances (mm)	[Ada,e/l]	0,000 / -0,035
Tip form diameter (mm)	[dFa]	88,048
(mm)	[dFa,e/l]	88,048 / 88,013
Root diameter (mm)	[df]	92,548
Generating Profile shift coefficient	[xE,e/l]	-0,1200 / -0,1749
Generated root diameter with xE (mm)	[dF,e/l]	92,850 / 92,740
Root form diameter (mm)	[dFf]	91,910
(mm)	[dFf,e/l]	92,244 / 92,124
Internal toothing: Calculation dFf with pinion type cutter (z0=	29	, x0=0,000 )
Involute length (mm)	[l_dFa_l_dFf]	2,055
Addendum, m <sub>a</sub> (h <sub>a</sub> *+x*k) (mm)	[ha]	0,976
(mm)	[ha,e/l]	0,994 / 0,976
Dedendum (mm)	[hf=mn*(hF*-x)]	1,274
(mm)	[hf,e/l]	1,370 / 1,425
Tooth height (mm)	[h]	2,250
Virtual gear no. of teeth	[zn]	90,000
Normal tooth thickness at tip circle (mm)	[san]	0,887
(mm)	[san,e/l]	0,818 / 0,768
Normal tooth thickness at tip form circle (mm)	[sFan]	0,887
(mm)	[sFan,e/l]	0,818 / 0,768
Normal space width at root circle (mm)	[efn]	0,586
(mm)	[efn,e/l]	0,574 / 0,566

**Gear specific pair data Gear pair 1, Gear 1**

Operating pitch diameter (mm)	[dw]	22,657
(mm)	[dw,e/l]	22,648 / 22,665
Active tip diameter (mm)	[dNa]	26,048
(mm)	[dNa,e/l]	26,048 / 26,027
Theoretical tip clearance (mm)	[c]	0,250
Effective tip clearance (mm)	[c,e/l]	0,424 / 0,333
Active root diameter (mm)	[dNf]	22,116
(mm)	[dNf,e/l]	22,134 / 22,073
Reserve (dNf-dFf)/2 (mm)	[cF,e/l]	0,055 / 0,001
Max. sliding velocity at tip (m/s)	[vga]	2,104
Specific sliding at the tip	[ζa]	0,396
Specific sliding at the root	[ζf]	-0,334
Mean specific sliding	[ζm]	0,365
Sliding factor on tip	[Kga]	0,254
Sliding factor on root	[Kgf]	-0,069
Roll angle at dFa (°)	[ζdFa,e/l]	38,543 / 38,443
Roll angle to dNa (°)	[ζdNa,e/l]	38,543 / 38,443
Roll angle to dNf (°)	[ζdNf,e/l]	12,657 / 11,881
Roll angle at dFf (°)	[ζdFf,e/l]	11,861 / 11,222
Diameter of single contact point B (mm)	[d-B]	23,274 ( 23,274 / 23,260 )
Diameter of single contact point D (mm)	[d-D]	24,070 ( 23,979 / 24,107 )
Addendum contact ratio	[ε]	1,311 ( 1,306 / 1,310 )

6/15

**Gear specific pair data Gear pair 1, Gear 2**

Operating pitch diameter (mm)	[dw]	88,657
(mm)	[dw,e/l]	88,690 / 88,623
Active tip diameter (mm)	[dNa]	88,048
(mm)	[dNa,e/l]	88,048 / 88,013
Theoretical tip clearance (mm)	[c]	0,280
Effective tip clearance (mm)	[c,e/l]	0,408 / 0,324
Active root diameter (mm)	[dNf]	91,279
(mm)	[dNf,e/l]	91,310 / 91,233
Reserve (dNf-dFf)/2 (mm)	[cF,e/l]	0,505 / 0,407
Max. sliding velocity at tip (m/s)	[vga]	0,573
Specific sliding at the tip	[ζa]	0,251
Specific sliding at the root	[ζf]	-0,657
Mean specific sliding	[ζm]	0,365
Sliding factor on tip	[Kga]	0,069
Sliding factor on root	[Kgf]	-0,254
Roll angle at dFa (°)	[ζdFa,e/l]	16,508 / 16,593
Roll angle to dNa (°)	[ζdNa,e/l]	16,508 / 16,593
Roll angle to dNf (°)	[ζdNf,e/l]	23,183 / 23,321
Roll angle at dFf (°)	[ζdFf,e/l]	24,748 / 24,951
Diameter of single contact point B (mm)	[d-B]	89,225 ( 89,252 / 89,187 )
Diameter of single contact point D (mm)	[d-D]	89,869 ( 89,827 / 89,869 )
Addendum contact ratio	[ε]	0,357 ( 0,397 / 0,338 )

**General influence factors**

		----- Gear 1 ----- Gear 2 --
Nominal circum. force at pitch circle (N)	[F]	2417,4
Axial force (N)	[Fa]	0,0
Radial force (N)	[Fr]	879,9
Normal force (N)	[Fnorm]	2572,5
Nominal circumferential force per mm (N/mm)	[w]	163,34
Only as information: Forces at operating pitch circle:		
Nominal circumferential force (N)	[Ftw]	2454,0
Axial force (N)	[Faw]	0,0
Radial force (N)	[Frw]	771,8
Circumferential speed reference circle (m/s)	[v]	8,40
Circumferential speed operating pitch circle (m/s)	[v(dw)]	8,27
Running-in value (μm)	[yp]	0,5
Running-in value (μm)	[yf]	0,5
Correction factor	[CM]	0,800
Gear blank factor	[CR]	1,000
Basic rack factor	[CBS]	0,975
Material coefficient	[E/Est]	1,000
Singular tooth stiffness (N/mm/μm)	[c]	15,698
Meshing stiffness (N/mm/μm)	[cvα]	23,561
Meshing stiffness (N/mm/μm)	[cvβ]	20,027
Reduced mass (kg/mm)	[mRed]	0,00157
Resonance speed (min-1)	[nE 1]	50859
Resonance ratio (-)	[N]	0,137
Subcritical range		
Running-in value (μm)	[yα]	0,5
Bearing distance l of pinion shaft (mm)	[l]	30,400
Distance s of pinion shaft (mm)	[s]	3,040
Outside diameter of pinion shaft (mm)	[dsh]	15,200

7/15

Load in accordance with Figure 13, ISO 6336-1:2006	0.a), 1.b), 2.c), 3.d), 4.e)	[ ]	4
Coefficient K' according to Figure 13, ISO 6336-1:2006	Without stiffening	[K]	-1,00
Tooth trace deviation (active) (μm)	from deformation of shaft (μm)	[Fβy]	3,22
ish (μm) = 1,29 , B1=1,00 , fhβ5 (μm) = 5,50		[fsh*B1]	1,29
Tooth without tooth trace modification			
Position of contact pattern:	favorable		
from production tolerances (μm)	B2= 1,00	[fmc*B2]	10,26
Tooth trace deviation, theoretical (μm)		[Fβx]	3,79
Running-in value (μm)		[yβ]	0,57
Dynamic factor		[Kv]	1,068
Face load factor - flank		[KHβ]	1,123
- Tooth root		[KFβ]	1,103
- Scuffing		[KBβ]	1,123
Transverse load factor - flank		[KHα]	1,000
- Tooth root		[KFα]	1,000
- Scuffing		[KBα]	1,000

**Tooth root load capacity**

Calculation of Tooth form coefficients according method: B		
Internal toothing:	Calculation of pF and sFn according to ISO 6336-3:2007-04-01	
Internal toothing:	Calculation of YF, YS with pinion type cutter, z0=	
0,380	29	, x0= 0,000 , paP0*=
	----- Gear 1 ----- Gear 2 --	
Calculated with generating profile shift coefficient	[xE,e]	0,4198 -0,1200
Tooth form factor	[YF]	1,13 1,16
Stress correction factor	[YS]	2,29 2,20
Load application angle (°)	[αFen]	22,56 19,36
Load application diameter (mm)	[da, ]	24,070 -89,225
Bending moment arm (mm)	[hF]	0,92 1,46
Tooth thickness at root (mm)	[sFn]	2,19 2,75
Tooth root radius (mm)	[ρF]	0,44 0,50
Bending moment arm (-)	[hF/mm]	0,921 1,464
Tooth thickness at root (-)	[sFn/mm]	2,191 2,753
Tooth root radius (-)	[ρF/mm]	0,440 0,496
Calculation cross section diameter (mm)	[dgr, ]	21,672 -92,607
Tangents on calculation cross section (°)	[σgr, ]	30,000 60,000
Notch parameter	[q]	2,490 2,774
Helix angle factor	[Yβ]	1,000
Deep tooth factor	[YDT]	1,000
Gear rim thickness (mm)	[sr]	3,13 3,48
Gear rim factor	[YB]	1,00 1,00
Effective facewidth (mm)	[bEFF]	15,20 14,80
Nominal stress at tooth root (N/mm²)	[σF0]	412,91 419,31
Tooth root stress (N/mm²)	[σF]	729,37 740,68

8/15

Permissible bending stress at root of Test-gear			
Notch sensitivity factor	[YdreIT]	1,000	1,003
Surface factor	[YRreIT]	0,957	0,957
Size factor, tooth root	[YX]	1,000	1,000
Finite life factor	[YNT]	0,906	0,931
$Y_{\sigma} = Y_{dreIT} \cdot Y_{RreIT} \cdot Y_X \cdot Y_{NT}$		0,867	0,893
Alternating bending factor, mean stress influence coefficient			
Technology factor	[YM]	1,000	1,000
Coefficient for surface factor like for shot peening; The standard gives no applicable information about this...	[YT]	1,100	1,100
Stress correction factor	[Yst]	2,00	
Yst*oFlim (N/mm <sup>2</sup> )	[oFE]	740,00	740,00
Permissible tooth root stress oFG/SFmin (N/mm <sup>2</sup> )	[oFP]	587,80	605,68
Limit strength tooth root (N/mm <sup>2</sup> )	[oFG]	705,36	726,81
Required safety	[SFmin]	1,20	1,20

**Flank safety**

		----- Gear 1 -----	----- Gear 2 --
Zone factor	[ZH]		2,684
Elasticity factor (N/mm <sup>2</sup> )	[ZE]		189,812
Contact ratio factor	[Zc]		0,882
Helix angle factor	[ZB]		1,000
Effective facewidth (mm)	[beff]		14,80
Nominal contact stress (N/mm <sup>2</sup> )	[oH0]		1032,60
Contact stress at operating pitch circle (N/mm <sup>2</sup> )	[oHw]		1385,03
Single tooth contact factor	[ZB,ZD]	1,00	1,00
Contact stress (N/mm <sup>2</sup> )	[oHB, oHD]	1385,03	1385,03
Lubrication factor for NL	[ZL]	1,020	1,020
Speed factor for NL	[ZV]	0,995	0,995
Roughness factor for NL	[ZR]	0,943	0,943
Material hardening factor for NL	[ZW]	1,000	1,000
Finite life factor	[ZNT]	0,937	0,977
	[ZL*ZV*ZR*ZNT]	0,897	0,935
Limited pitting is permitted:		No	
Size factor (flank)	[ZX]	1,000	1,000
Permissible contact stress, oHG/SHmin (N/mm <sup>2</sup> )	[oHP]	1215,96	1267,93
Pitting stress limit (N/mm <sup>2</sup> )	[oHG]	1094,36	1141,13
Required safety	[SHmin]	0,90	0,90

**Micropitting according to**

ISO/TS 6336-22:2018

Calculation has not been carried out. Lubricant: Load stage micropitting test not known

**Scuffing load capacity**

Calculation method according to		ISO/TS 6336-20/21:2017
Helical load factor for scuffing	[KBv]	1,000
Lubrication coefficient for lubrication type	[XS]	1,000
Scuffing test and load stage	[FZGtest]	FZG - Test A / 8,3 / 90 (ISO 14835 - 1) 12

9/15

Multiple meshing factor	[Xmp]	1,000
Relative structural factor, scuffing	[XWreIT]	1,000
Thermal contact factor (N/mm/s,5/K)	[BM]	13,780 13,780
Relevant tip relief (µm)	[Ca]	3,40 3,40
Optimal tip relief (µm)	[Ceff]	15,61
Ca taken as optimal in the calculation (0=no, 1=yes)		0 0
Effective facewidth (mm)	[beff]	14,800
Applicable circumferential force/facewidth (N/mm)	[wBl]	293,856
KBγ = 1,000 , wBl*KBy = 293,856		
Angle factor	[Xaβ]	0,939
ε1: 1,311 , ε2: 0,357		

Flash temperature-criteria		
Lubricant factor	[XL]	0,830
Tooth mass temperature (°C)	[θMi]	77,29
θMi = θoil + XS*0,47*Xmp*θflm		
Average flash temperature (°C)	[θflm]	15,51
Scuffing temperature (°C)	[θS]	348,80
Γ coordinates (point of highest temperature)	[Γ]	0,553
[Γ,A]= -0,310 [Γ,E]= 1,139		
Highest contact temp. (°C)	[θB]	105,10
Flash factor (K <sup>0,4</sup> N <sup>-0,4</sup> 75 <sup>0,4</sup> s <sup>0,4</sup> m <sup>-0,4</sup> .5 <sup>0,4</sup> mm)	[XM]	50,058
Approach factor	[XJ]	1,000
Load sharing factor	[XT]	1,000
Dynamic viscosity (mPa*s)	[ηM]	41,90 ( 70,0 °C)
Coefficient of friction	[μ-]	0,064

Integral temperature-criteria		
Lubricant factor	[XL]	1,000
Tooth mass temperature (°C)	[θMC]	76,73
θMC = θoil + XS*0,70*θflmt		
Mean flash temperature (°C)	[θflmt]	9,62
Integral scuffing temperature (°C)	[θSint]	360,78
Flash factor (K <sup>0,4</sup> N <sup>-0,4</sup> 75 <sup>0,4</sup> s <sup>0,4</sup> m <sup>-0,4</sup> .5 <sup>0,4</sup> mm)	[XM]	50,058
Running-in factor, well run in	[XE]	1,000
Contact ratio factor	[Xc]	0,262
Dynamic viscosity (mPa*s)	[ηOl]	41,90 ( 70,0 °C)
Mean coefficient of friction	[μ-]	0,083
Geometry factor	[XBE]	0,157
Meshing factor	[XQ]	1,000
Tip relief factor	[XCa]	1,423
Integral tooth flank temperature (°C)	[θint]	91,16

**Measurements for tooth thickness**

		----- Gear 1 -----	----- Gear 2 --
Tooth thickness tolerance		DIN 3967 cd25	DIN 3967 cd25
Tooth thickness allowance (normal section) (mm)	[As,eI]	-0,054 /-0,084	-0,070 /-0,110
Number of teeth spanned	[k]	4,000	11,000
For internal toothing: k = measurement gap number			
Base tangent length (no backlash) (mm)	[Wk]	10,993	32,274
Base tangent length with allowance (mm)	[Wk,eI]	10,942 / 10,914	32,340 / 32,378
(mm)	[ΔWk,eI]	-0,051 / -0,079	-0,066 / -0,103
Diameter of measuring circle (mm)	[dMvWk,m]	24,218	90,551
Theoretical diameter of ball/pin (mm)	[DM]	1,947	1,663
Effective diameter of ball/pin (mm)	[DMeff]	2,000	1,750

10/15

Radial single-ball measurement backlash free (mm)	[MRk]	13,500	43,735
Radial single-ball measurement (mm)	[MRk,eI]	13,450 / 13,421	43,895 / 43,837
Diameter of measuring circle (mm)	[dMMr,m]	23,944	90,069
Diametral measurement over two balls without clearance (mm)	[MdK]	26,943	87,470
Diametral two ball measure (mm)	[MdK,eI]	26,841 / 26,784	87,790 / 87,675
Diametral measurement over pins without clearance (mm)	[MdR]	26,943	87,470
Measurement over pins according to DIN 3960 (mm)	[MdR,eI]	26,841 / 26,784	87,790 / 87,675
Measurement over 3 pins, axial, according to AGMA 2002 (mm)			
	[dk3A,eI]	26,841 / 26,784	87,790 / 87,675
Dimensions over 3 pins without clearance (mm)	[Md3R]	26,884	-0,000
Measurement over 3 pins with allowance (mm)	[Md3R,eI]	26,783 / 26,727	-0,000 / -0,000

Chordal tooth thickness (no backlash) (mm)	[sc]	1,928	1,553
Normal chordal tooth thickness with allowance (mm)	[sca,eI]	1,876 / 1,846	1,483 / 1,443
Reference chordal height from da,m (mm)	[ha]	1,559	0,978
Tooth thickness, arc (mm)	[sn]	1,930	1,553
(mm)	[sna,eI]	1,876 / 1,846	1,483 / 1,443

Backlash free center distance (mm)	[aControl,eI]	33,189 / 33,291
Backlash free center distance, allowances (mm)	[ita]	0,189 / 0,291
dNI,i with aControl (mm)	[dNf0,i]	21,781
Reserve (dNf0,i-dFLe)2 (mm)	[cF0,i]	-0,145
Tip clearance (mm)	[c0,i(aControl)]	0,055
Center distance allowances (mm)	[Aa,eI]	-0,013 / 0,013

Circumferential backlash from Aa (mm)	[tw_Aa,eI]	0,008 / -0,008
Radial backlash (mm)	[rwa,eI]	0,304 / 0,176
Circumferential backlash (transverse section) (mm)	[twa,eI]	0,199 / 0,114
Normal backlash (mm)	[na,eI]	0,191 / 0,108
Torsional angle on input with output fixed:		
Total torsional angle (°)	[tSys]	1,0063/0,5780

**Toothing tolerances**

According to ISO 1328-1:1995, ISO 1328-2:1997		----- Gear 1 -----	----- Gear 2 --
Accuracy grade	[Q]	6	6
Single pitch deviation (µm)	[fPt]	7,00	7,50
Base circle pitch deviation (µm)	[fPbT]	6,60	7,00
Sector pitch deviation over k/8 pitches (µm)	[Fpk/8T]	9,50	15,00
Profile form deviation (µm)	[ffoT]	5,50	6,50
Profile slope deviation (µm)	[fHcT]	4,60	5,50
Total profile deviation (µm)	[FoT]	7,50	8,50
Helix form deviation (µm)	[fPβT]	7,00	7,50
Helix slope deviation (µm)	[fHβT]	7,00	7,50
Total helix deviation (µm)	[FβT]	10,00	11,00
Total cumulative pitch deviation (µm)	[FpT]	20,00	26,00
Runout (µm)	[FrT]	16,00	21,00
Single flank composite, total (µm)	[FisT]	34,00	41,00
Single flank composite, tooth-to-tooth (µm)	[fisT]	14,00	15,00
Radial composite, total (µm)	[FidT]	21,00	26,00
Radial composite, tooth-to-tooth (µm)	[fidT]	5,00	5,00
FidT (F <sub>r</sub> ), fidT (F <sub>i</sub> ) according to ISO 1328:1997 calculated with the geometric mean values for mn and d			

Axis alignment tolerances (recommendation acc. to ISO TR 10064-3:1996, Quality)

Maximum value for deviation error of axis (µm)	[Fβ]	11,30	(Fβ= 11,00 )
Maximum value for inclination error of axes (µm)	[Fβ]	22,59	

11/15

**Modifying and defining the tooth form**

**Profile and tooth trace modifications for gear 1**

**Symmetric (both flanks)**  
 - flankline crowning  
 Cb = 10,000 µm  
 rcrown=288mm

Data for the tooth form calculation :

**Calculation of Gear 1**  
 Tooth form, Gear 1, Step 1: Automatic (final machining)  
 haP<sup>0</sup>= 1,120, hP<sup>0</sup>= 1,250, pP<sup>0</sup>= 0,380

**Calculation of Gear 2**  
 Tooth form, Gear 2, Step 1: Automatic (final machining)  
 z0= 29, x0=0,0000, da0= 31,505 mm, a0= -30,645 mm  
 haP<sup>0</sup>= 1,253, paP<sup>0</sup>= 0,380, hP<sup>0</sup>= 1,130, pP<sup>0</sup>= 0,000

**Supplementary data**

Maximal possible center distance (eps_a=1,0)	[aMAX]	32,463
Mass (g)	[m]	31,77 164,41
Total mass (g)	[mGes]	196,18
Moment of inertia for system, relative to the input: calculation without consideration of the exact tooth shape		
Single gears, (da+df)2...di (kg*m <sup>2</sup> )	[J]	3,137e-06 0,0003723
System (da+df)2...di (kg*m <sup>2</sup> )	[J]	2,745e-05
Torsional stiffness at driving gear with fixed driven gear:		
Torsional stiffness (MNm/rad)	[cr]	0,035
Torsion when subjected to nominal torque (°)	[δcr]	0,045
Mean coefficient of friction (as defined in Niemann)	[μ-]	0,093
Wear sliding coef. by Niemann	[ζw]	0,609
Loss factor	[HV]	0,120
Gear power loss (KW)	[PVZ]	0,225
Meshing efficiency (%)	[ηz]	98,890
Sound pressure level according to Masuda, without contact analysis	[dB(A)]	68,4

**Service life, damage**

Calculation with load spectrum		
Required safety for tooth root	[SFmin]	1,20
Required safety for tooth flank	[SHmin]	0,90

Service life (calculated with required safeties):		
System service life (h)	[Hatt]	30,081

Tooth root service life (h)	[HFatt]	30,08 104,1
-----------------------------	---------	-------------

12/15

Tooth flank service life (h) [HHatt] 407 1593

Damage calculated on the basis of the required service life [H] (1000,0 h)

No.	F1%	F2%	H1%	H2%
1	0,0000	0,0000	3,3589	0,8584
2	0,0000	0,0000	0,8209	0,2098
3	3324,4061	961,0388	237,4690	60,6865
4	0,0000	0,0000	4,0615	1,0380
Σ	3324,4061	961,0388	245,7104	62,7926

Damage calculated on basis of system service life [Hatt] (30,1 h)

No.	F1%	F2%	H1%	H2%
1	0,0000	0,0000	0,1010	0,0258
2	0,0000	0,0000	0,0247	0,0063
3	100,0000	28,9086	7,1432	1,8255
4	0,0000	0,0000	0,1222	0,0312
Σ	100,0000	28,9086	7,3911	1,8888

Damage calculated on basis of individual service life HFatt & HHatt

(h)	HFatt1	HFatt2	HHatt1	HHatt2
30,08	104,1	407	1593	
No.	F1%	F2%	H1%	H2%
1	0,00	0,00	1,37	1,37
2	0,00	0,00	0,33	0,33
3	100,00	100,00	96,65	96,65
4	0,00	0,00	1,65	1,65
Σ	100,00	100,00	100,00	100,00

Most critical duty cycle elements for Scoring (SB, Sint), Tooth Flank Fracture (SFF), hardened layer (SEHT) and Micropitting (Slam)  
 SB: 3  
 Slnt: 4

**Application factor calculated according to ISO 6336-6, Annex A.3**

(The slope of the S-N curve (Woehler lines) in the range of endurance limit according to ISO 6336-6, Table A.1 is used.)

Gear		p	Teq		KA
1	Tooth root	8,738	27,8	KA,F	1 / 1,000
1	Tooth flank	6,611	27,8	KA,H	1 / 1,000
2	Tooth root	8,738	108,8	KA,F	2 / 1,000
2	Tooth flank	6,611	89,5	KA,H	2 / 0,823

Application factor, ISO 6336-6 A.3 [KAmax] 1,000  
 [KA,Fmax / KA,Hmax] 1,000 / 1,000

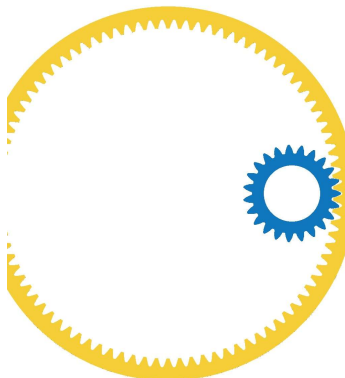
Note: If an application factor is entered, the indicated values for KA come with 1,500 zu multiplizieren!

**Classification according to F.E.M., Edition 1,001, 1998**

Spectrum factor	[km]	0,432
Spectrum class	[L]	3
Application class, predefined service life	[T]	3
Machine class, predefined service life	[M]	4
Application class, achievable service life	[T]	0
Machine class, achievable service life	[M]	1

**Remarks:**

- Specifications with [L,e] imply: Maximum [e] and minimum value [l] for Taking all tolerances into account
- Specifications with [m] imply: Mean value within tolerance
- For the backlash tolerance, the center distance tolerances and the tooth thickness allowance are taken into account.
- The maximum and minimum clearance according to the largest or smallest allowances are defined..
- The calculation is performed for the operating pitch circle.
- Details of calculation method: cy according to Method B Kv according to Method B KHβ and KFβ according to Method C lmg according to Equation 64, lsh according to 57/58, Fβx according to 52/53/54 KHα, KFα according to Method B
- The logarithmically interpolated value taken from the values for the fatigue strength and the static strength, based on the number of load cycles, is used for coefficients ZL, ZV, ZR, ZW, ZX, YdrelT, YRrelT and YX..



**Tolerance field for tooth form calculation**

- Diameter: Mean value, Tooth thickness: Mean value
- da1 = 26,0375 mm, df1 = 21,2984 mm, As1 = -0,0690 mm
- da2 = 88,0301 mm, df2 = 92,7949 mm, As2 = -0,0900 mm

Figure: Tooth system



E

KISSsoft calculation report: Planet 16MnCr5, Ring  
42CrMo4

**Important hint: At least one warning has occurred during the calculation:**

1-> Calculation for load spectra:  
 The application factor should be set to 1,0!

2-> Load spectrum with negative torque:  
 In the transition from + to - torque the tooth is submitted to alternating bending stress.  
 This transition should be considered with an additional duty cycle element with an alternating bending factor (mean stress influence factor, Y<sub>M</sub>).  
 Consult the manual for more information.  
 (Element no. 4)

Load spectrum with negative load bins:  
 The working flank changes from right flank to left flank or vice versa.  
 These bins can be neglected when calculating the damage.  
 See the corresponding inputs in 'Details' of tab 'Rating'.

**Calculation of a spur-toothed cylindrical gear pair**

Drawing or article number:  
 Gear 1: 0,000,0  
 Gear 2: 0,000,0

**Load spectrum**

Own Input  
 Number of bins in the load spectrum: 4  
 Reference gear: Gear 1  
 Application factor, K<sub>A</sub>: 1,50

Bin No.	Frequency [%]	Power [kW]	Speed [1/min]	Torque [Nm]	Coefficients							
					K <sub>v</sub>	K <sub>β</sub>	K <sub>Fβ</sub>	K <sub>βa</sub>	K <sub>γ</sub>	Y <sub>M1</sub>	Y <sub>M2</sub>	
1	45,0000	7,1862	4183,8	16,4020	1,056	1,251	1,208	1,017	1,000	1,000	1,000	
2	18,0000	9,3176	5927,1	15,0120	1,084	1,271	1,224	1,030	1,000	1,000	1,000	
3	28,0000	9,1349	3137,8	27,8000	1,030	1,130	1,108	1,000	1,000	1,000	1,000	
4	9,0000	-8,5259	4183,8	-19,4600	1,050	1,204	1,170	1,000	1,000	1,000	1,000	

Numbers of load cycles			
Bin No.	Frequency	Load cycles, gear 1	Load cycles, gear 2
	[1]	[1]	[1]

[%]			
1	45,0000	112962600	28868220
2	18,0000	64012140	16358658
3	28,0000	52715880	13471836
4	9,0000	22592520	5773644
SUM	00,0000	252283140	64472358

Notice:  
 - Tooth flank with load spectrum: Consider all negative load spectrum bins as positive  
 - Tooth root with load spectrum: Consider all negative load spectrum bins as positive

S-N curve (Woehler line) in the long life domain according: according to standard

Notice:  
 Calculation-method according to:  
 - ISO 6336-6 / DIN3990-6  
 During the calculation all the load factors (ISO 6336/DIN 3990: K<sub>v</sub>, K<sub>Hβ</sub>, K<sub>Fβ</sub>, AGMA 2001: K<sub>v</sub>, K<sub>m</sub>, ...) for each load spectrum bin are calculated separately.

Notice:  
 Calculation with methods ISO 6336 and AGMA 2001 results in a reduction of resistance in the domain of fatigue resistance (from circa 10<sup>7</sup> to 10<sup>8</sup> cycles).  
 The lifetime calculation takes this into account (also with the S-N curve (Woehler Curve) of the Miner type).

**Results**

**Calculation for load spectra:**  
**The application factor should be set to 1,0!**

Safeties, calculated with load spectrum:  
 Root safety: 1,208 1,055  
 Flank safety: 1,030 0,934

Safeties against scuffing/micropitting/EHT/TFE are indicated for the most critical element of the load spectrum:  
 Safety against scuffing (integral temperature): 3,859  
 Safety against scuffing (flash temperature): 10,382

Analysis of critical elements in load spectrum: See section 10

**Only as information: Calculation with reference power**

Calculation method	ISO 6336:2006 (replaced)
	----- Gear 1 ----- Gear 2 --
Power (kW)	[P] 20,300
Speed (1/min)	[n] 6973,0 1782,0
Torque (Nm)	[T] 27,8 108,8
Application factor	[K <sub>A</sub> ] 1,50
Required service life (h)	[H] 1000,00
Gear driving (+) / driven (-)	+ -
Working flank gear 1:	Right flank

Gear 1 direction of rotation: Counterclockwise

**Tooth geometry and material**

Geometry calculation according to	ISO 21771:2007
	----- Gear 1 ----- Gear 2 --
Center distance (mm)	[a] 33,000
Center distance tolerance	ISO 286:2010 Measure js7
Normal module (mm)	[m] 1,0000
Normal pressure angle (°)	[αn] 20,0000
Helix angle at reference circle (°)	[β] 0,0000
Number of teeth	[z] 23 -90
Facewidth (mm)	[b] 15,20 14,80
Hand of gear	Spur gear
Accuracy grade	[Q-ISO 1328:1995] 6 6
Inner diameter (mm)	[d] 15,00
External diameter (mm)	[d <sub>e</sub> ] 99,80
Inner diameter of gear rim (mm)	[d <sub>bi</sub> ] 0,00
Outer diameter of gear rim (mm)	[d <sub>be</sub> ] 0,00

**Material**

Gear 1  
 16 MnCr 5 (1), Case-carburized steel, case-hardened  
 ISO 6336-5 Figure 9/10 (MQ), Core hardness >=25HRC Jominy J=12mm<HRC28

Gear 2  
 42 CrMo 4 (2), Through hardened steel, flame/ind. hardened  
 ISO 6336-5 Figure 11/12 (MQ) Flank & root hardened

	----- Gear 1 ----- Gear 2 --
Surface hardness	HRC 59 HRC 56
Material treatment according to ISO 6336:2006 Normal, life factors ZNT and YNT >=0,85	
Fatigue strength, tooth root stress (N/mm <sup>2</sup> )	[σ <sub>Flim</sub> ] 430,00 370,00
Fatigue strength for Hertzian pressure (N/mm <sup>2</sup> )	[σ <sub>Hlim</sub> ] 1500,00 1220,00
Tensile strength (N/mm <sup>2</sup> )	[σ <sub>B</sub> ] 1000,00 1100,00
Yield point (N/mm <sup>2</sup> )	[σ <sub>S</sub> ] 695,00 900,00
Young's modulus (N/mm <sup>2</sup> )	[E] 206000 206000
Poisson's ratio	[ν] 0,300 0,300
Roughness average value DS, flank (μm)	[RA <sub>H</sub> ] 0,60 0,60
Roughness average value DS, root (μm)	[RA <sub>F</sub> ] 3,00 3,00
Mean roughness height, Rz, flank (μm)	[RZ <sub>H</sub> ] 4,80 4,80
Mean roughness height, Rz, root (μm)	[RZ <sub>F</sub> ] 20,00 20,00

**Gear reference profile**

Reference profile	1,25 / 0,38 / 1,0 ISO 53:1998 Profil A
Dedendum coefficient	[h <sub>F</sub> P <sup>*</sup> ] 1,250
Root radius factor	[ρ <sub>F</sub> P <sup>*</sup> ] 0,380 (p <sub>F</sub> P <sub>max</sub> <sup>*</sup> = 0,472)
Addendum coefficient	[ha <sub>F</sub> P <sup>*</sup> ] 1,000
Tip radius factor	[ρa <sub>F</sub> P <sup>*</sup> ] 0,000
Protuberance height coefficient	[h <sub>pr</sub> P <sup>*</sup> ] 0,000
Protuberance angle	[α <sub>pr</sub> P <sup>*</sup> ] 0,000
Tip form height coefficient	[h <sub>Fa</sub> P <sup>*</sup> ] 0,000
Ramp angle	[α <sub>K</sub> P <sup>*</sup> ] 0,000
	not topping

**Gear reference profile**

Reference profile	1,25 / 0,38 / 1,0 ISO 53:1998 Profil A
Dedendum coefficient	[h <sub>F</sub> P <sup>*</sup> ] 1,250
Root radius factor	[ρ <sub>F</sub> P <sup>*</sup> ] 0,380 (p <sub>F</sub> P <sub>max</sub> <sup>*</sup> = 0,472)
Addendum coefficient	[ha <sub>F</sub> P <sup>*</sup> ] 1,000
Tip radius factor	[ρa <sub>F</sub> P <sup>*</sup> ] 0,000
Protuberance height coefficient	[h <sub>pr</sub> P <sup>*</sup> ] 0,000
Protuberance angle	[α <sub>pr</sub> P <sup>*</sup> ] 0,000
Tip form height coefficient	[h <sub>Fa</sub> P <sup>*</sup> ] 0,000
Ramp angle	[α <sub>K</sub> P <sup>*</sup> ] 0,000
	not topping

**Information on final machining**

Dedendum reference profile	[h <sub>F</sub> P <sup>*</sup> ] 1,250 1,250
Tooth root radius Refer. profile	[ρ <sub>F</sub> P <sup>*</sup> ] 0,380 0,380
Addendum Reference profile	[ha <sub>F</sub> P <sup>*</sup> ] 1,000 1,000
Protuberance height coefficient	[h <sub>pr</sub> P <sup>*</sup> ] 0,000 0,000
Protuberance angle (°)	[α <sub>pr</sub> P <sup>*</sup> ] 0,000 0,000
Tip form height coefficient	[h <sub>Fa</sub> P <sup>*</sup> ] 0,000 0,000
Ramp angle (°)	[α <sub>K</sub> P <sup>*</sup> ] 0,000 0,000
Type of profile modification:	none (only running-in)
Tip relief by running in (μm)	[Ca L/R] 2,0 / 2,0 3,4 / 3,4
Lubrication type	Oil bath lubrication
Type of oil	ISO-VG 220
Lubricant base	Mineral-oil base
Oil nominal kinematic viscosity at 40°C (mm <sup>2</sup> /s)	[ν <sub>40</sub> ] 220,00
Oil nominal kinematic viscosity at 100°C (mm <sup>2</sup> /s)	[ν <sub>100</sub> ] 17,50
Specific density at 15°C (kg/dm <sup>3</sup> )	[ρ] 0,895
Oil temperature (°C)	[T <sub>S</sub> ] 70,000

**Gear pair**

Overall transmission ratio	[i <sub>tot</sub> ] 3,913
Gear ratio	[i] -3,913
Transverse module (mm)	[m <sub>t</sub> ] 1,000
Transverse pressure angle (°)	[α <sub>t</sub> ] 20,000
Working pressure angle (°)	[α <sub>w</sub> t] 17,459
	[α <sub>w</sub> t,e/i] 17,390 / 17,528
Working pressure angle at normal section (°)	[α <sub>wn</sub> ] 17,459
Helix angle at operating pitch circle (°)	[β <sub>w</sub> ] 0,000
Base helix angle (°)	[β <sub>b</sub> ] 0,000
Reference center distance (mm)	[a <sub>d</sub> ] 33,500
Pitch on reference circle (mm)	[p <sub>t</sub> ] 3,142
Base pitch (mm)	[p <sub>bt</sub> ] 2,952
Transverse pitch on contact-path (mm)	[p <sub>et</sub> ] 2,952
Sum of profile shift coefficients	[Σx <sub>i</sub> ] 0,4702
Transverse contact ratio	[ε <sub>α</sub> ] 1,668
Transverse contact ratio with allowances	[ε <sub>α,e/m/i</sub> ] 1,703 / 1,675 / 1,647
Overlap ratio	[ε <sub>β</sub> ] 0,000

Total contact ratio	[ev]	1,668
Total contact ratio with allowances	[ev,e/m/l]	1,703 / 1,675 / 1,647
Length of path of contact (mm)	[ga, e/l]	4,924 / 5,029 / 4,863
Length T1-A (mm)	[T1A]	2,345 / 2,241 / 2,387
Length T1-B (mm)	[T1B]	4,317 / 4,317 / 4,298
Length T1-C (mm)	[T1C]	3,399 / 3,413 / 3,384
Length T1-D (mm)	[T1D]	5,298 / 5,193 / 5,339
Length T1-E (mm)	[T1E]	7,269 / 7,269 / 7,251
Length T2-A (mm)	[T2A]	12,246 / 12,183 / 12,246
Length T2-B (mm)	[T2B]	14,218 / 14,260 / 14,158
Length T2-C (mm)	[T2C]	13,300 / 13,356 / 13,244
Length T2-D (mm)	[T2D]	15,199 / 15,135 / 15,199
Length T2-E (mm)	[T2E]	17,170 / 17,212 / 17,110

Length T1-T2 (mm)	[T1T2]	9,901 / 9,943 / 9,859
Minimal length of contact line (mm)	[Lmin]	14,800

**Gear 1**

Profile shift coefficient	[x]	0,4940
Tooth thickness, arc, in module	[sn*]	1,9304
Tip alteration (mm)	[k*mm]	0,030
Reference diameter (mm)	[d]	23,000
Base diameter (mm)	[db]	21,613
Tip diameter (mm)	[da]	26,048
(mm)	[da,e/l]	26,048 / 26,027
Tip diameter allowances (mm)	[Ada,e/l]	0,000 / -0,021
Tip form diameter (mm)	[dFa]	26,048
(mm)	[dFa,e/l]	26,048 / 26,027
Root diameter (mm)	[df]	21,488
Generating Profile shift coefficient	[xE,e/l]	0,4198 / 0,3786
Generated root diameter with xE (mm)	[dfe,l]	21,340 / 21,257
Root form diameter (mm)	[dFf]	22,163
(mm)	[dFf,e/l]	22,071 / 22,024

Internal toothing: Calculation dFf with pinion type cutter (z0= 25 , x0=0,000 )	[dFf]	22,071 / 22,024
Involute length (mm)	[l_dFa_l_dFf]	2,166
Addendum, m <sub>a</sub> (h <sub>a</sub> *+x*k) (mm)	[ha]	1,524
(mm)	[ha,e/l]	1,524 / 1,514
Dedendum (mm)	[hf=mn*(hF*-x)]	0,756
(mm)	[hf,e/l]	0,830 / 0,871
Tooth height (mm)	[h]	2,280
Virtual gear no. of teeth	[zn]	23,000
Normal tooth thickness at tip circle (mm)	[san]	0,477
(mm)	[san,e/l]	0,429 / 0,382
Normal tooth thickness at tip form circle (mm)	[sFan]	0,477
(mm)	[sFan,e/l]	0,429 / 0,382
Normal space width at root circle (mm)	[efn]	0,000
(mm)	[efn,e/l]	0,000 / 0,000

**Gear 2**

Profile shift coefficient	[x]	-0,0238
---------------------------	-----	---------

5/15

Tooth thickness, arc, in module	[sn*]	1,5535
Tip alteration (mm)	[k*mm]	0,000
Reference diameter (mm)	[d]	90,000
Base diameter (mm)	[db]	84,572
Tip diameter (mm)	[da]	88,048
(mm)	[da,e/l]	88,048 / 88,013
Tip diameter allowances (mm)	[Ada,e/l]	0,000 / -0,035
Tip form diameter (mm)	[dFa]	88,048
(mm)	[dFa,e/l]	88,048 / 88,013
Root diameter (mm)	[df]	92,548
Generating Profile shift coefficient	[xE,e/l]	-0,1200 / -0,1749
Generated root diameter with xE (mm)	[dfe,l]	92,850 / 92,740
Root form diameter (mm)	[dFf]	91,910
(mm)	[dFf,e/l]	92,244 / 92,124
Internal toothing: Calculation dFf with pinion type cutter (z0= 29 , x0=0,000 )	[dFf]	92,244 / 92,124
Involute length (mm)	[l_dFa_l_dFf]	2,055
Addendum, m <sub>a</sub> (h <sub>a</sub> *+x*k) (mm)	[ha]	0,976
(mm)	[ha,e/l]	0,994 / 0,976
Dedendum (mm)	[hf=mn*(hF*-x)]	1,274
(mm)	[hf,e/l]	1,370 / 1,425
Tooth height (mm)	[h]	2,250
Virtual gear no. of teeth	[zn]	90,000
Normal tooth thickness at tip circle (mm)	[san]	0,887
(mm)	[san,e/l]	0,818 / 0,768
Normal tooth thickness at tip form circle (mm)	[sFan]	0,887
(mm)	[sFan,e/l]	0,818 / 0,768
Normal space width at root circle (mm)	[efn]	0,586
(mm)	[efn,e/l]	0,574 / 0,566

**Gear specific pair data Gear pair 1, Gear 1**

Operating pitch diameter (mm)	[dw]	22,657
(mm)	[dwe,e/l]	22,648 / 22,665
Active tip diameter (mm)	[dNa]	26,048
(mm)	[dNa,e/l]	26,048 / 26,027
Theoretical tip clearance (mm)	[c]	0,250
Effective tip clearance (mm)	[c,e/l]	0,424 / 0,333
Active root diameter (mm)	[dNf]	22,116
(mm)	[dNf,e/l]	22,134 / 22,073
Reserve (dNf-dFf)/2 (mm)	[cFe,l]	0,055 / 0,001
Max. sliding velocity at tip (m/s)	[vga]	2,104
Specific sliding at the tip	[ζa]	0,396
Specific sliding at the root	[ζf]	-0,334
Mean specific sliding	[ζm]	0,365
Sliding factor on tip	[Kga]	0,254
Sliding factor on root	[Kgf]	-0,069
Roll angle at dFa (°)	[ζdFa,e/l]	38,543 / 38,443
Roll angle to dNa (°)	[ζdNa,e/l]	38,543 / 38,443
Roll angle to dNf (°)	[ζdNf,e/l]	12,657 / 11,881
Roll angle at dFf (°)	[ζdFf,e/l]	11,861 / 11,222
Diameter of single contact point B (mm)	[d-B]	23,274 ( 23,274 / 23,260 )
Diameter of single contact point D (mm)	[d-D]	24,070 ( 23,979 / 24,107 )
Addendum contact ratio	[ε]	1,311 ( 1,306 / 1,310 )

6/15

**Gear specific pair data Gear pair 1, Gear 2**

Operating pitch diameter (mm)	[dw]	88,657
(mm)	[dwe,e/l]	88,690 / 88,623
Active tip diameter (mm)	[dNa]	88,048
(mm)	[dNa,e/l]	88,048 / 88,013
Theoretical tip clearance (mm)	[c]	0,280
Effective tip clearance (mm)	[c,e/l]	0,408 / 0,324
Active root diameter (mm)	[dNf]	91,279
(mm)	[dNf,e/l]	91,310 / 91,233
Reserve (dNf-dFf)/2 (mm)	[cFe,l]	0,505 / 0,407
Max. sliding velocity at tip (m/s)	[vga]	0,573
Specific sliding at the tip	[ζa]	0,251
Specific sliding at the root	[ζf]	-0,657
Mean specific sliding	[ζm]	0,365
Sliding factor on tip	[Kga]	0,069
Sliding factor on root	[Kgf]	-0,254
Roll angle at dFa (°)	[ζdFa,e/l]	16,508 / 16,593
Roll angle to dNa (°)	[ζdNa,e/l]	16,508 / 16,593
Roll angle to dNf (°)	[ζdNf,e/l]	23,183 / 23,321
Roll angle at dFf (°)	[ζdFf,e/l]	24,748 / 24,951
Diameter of single contact point B (mm)	[d-B]	89,225 ( 89,252 / 89,187 )
Diameter of single contact point D (mm)	[d-D]	89,869 ( 89,827 / 89,869 )
Addendum contact ratio	[ε]	0,357 ( 0,397 / 0,338 )

**General influence factors**

		----- Gear 1 ----- Gear 2 --
Nominal circum. force at pitch circle (N)	[F]	2417,4
Axial force (N)	[Fa]	0,0
Radial force (N)	[Fr]	879,9
Normal force (N)	[Fnorm]	2572,5
Nominal circumferential force per mm (N/mm)	[w]	163,34
Only as information: Forces at operating pitch circle:		
Nominal circumferential force (N)	[Ftw]	2454,0
Axial force (N)	[Faw]	0,0
Radial force (N)	[Frw]	771,8
Circumferential speed reference circle (m/s)	[v]	8,40
Circumferential speed operating pitch circle (m/s)	[v(dw)]	8,27
Running-in value (μm)	[yp]	0,5
Running-in value (μm)	[yf]	0,5
Correction factor	[CM]	0,800
Gear blank factor	[CR]	1,000
Basic rack factor	[CBS]	0,975
Material coefficient	[E/Est]	1,000
Singular tooth stiffness (N/mm/μm)	[c]	15,698
Meshing stiffness (N/mm/μm)	[cvα]	23,561
Meshing stiffness (N/mm/μm)	[cvβ]	20,027
Reduced mass (kg/mm)	[mRed]	0,00157
Resonance speed (min-1)	[nE 1]	50859
Resonance ratio (-)	[N]	0,137
Subcritical range		
Running-in value (μm)	[yα]	0,5
Bearing distance l of pinion shaft (mm)	[l]	30,400
Distance s of pinion shaft (mm)	[s]	3,040
Outside diameter of pinion shaft (mm)	[dsh]	15,200

7/15

Load in accordance with Figure 13, ISO 6336-1:2006 0.a), 1.b), 2.c), 3.d), 4.e)	[ ]	4
Coefficient K' according to Figure 13, ISO 6336-1:2006 Without stiffening	[K]	-1,00
Tooth trace deviation (active) (μm)	[Fβy]	3,22
from deformation of shaft (μm)	[fsh*B1]	1,29
fsh (μm) = 1,29 , B1=1,00 , fHβ5 (μm) = 5,50		
Tooth without tooth trace modification		
Position of contact pattern: favorable		
from production tolerances (μm)	[fmc*B2]	10,26
B2= 1,00		
Tooth trace deviation, theoretical (μm)	[Fβx]	3,79
Running-in value (μm)	[yβ]	0,57
Dynamic factor	[Kv]	1,068
Face load factor - flank	[KHβ]	1,123
- Tooth root	[KFβ]	1,103
- Scuffing	[KBβ]	1,123
Transverse load factor - flank	[KHα]	1,000
- Tooth root	[KFα]	1,000
- Scuffing	[KBα]	1,000

**Tooth root load capacity**

Calculation of Tooth form coefficients according method: B		Calculation of pF and sFn according to ISO 6336-3:2007-04-01
Internal toothing:		Calculation of YF, YS with pinion type cutter, z0= 29 , x0= 0,000 , paP0*=
0,380		----- Gear 1 ----- Gear 2 --
Calculated with generating profile shift coefficient	[xE,e]	0,4198 -0,1200
Tooth form factor	[YF]	1,13 1,16
Stress correction factor	[YS]	2,29 2,20
Load application angle (°)	[αFen]	22,56 19,36
Load application diameter (mm)	[da,]	24,070 -89,225
Bending moment arm (mm)	[hF]	0,92 1,46
Tooth thickness at root (mm)	[sFn]	2,19 2,75
Tooth root radius (mm)	[ρF]	0,44 0,50
Bending moment arm (-)	[hF/mm]	0,921 1,464
Tooth thickness at root (-)	[sFn/mm]	2,191 2,753
Tooth root radius (-)	[ρF/mm]	0,440 0,496
Calculation cross section diameter (mm)	[dcr,]	21,672 -92,607
Tangents on calculation cross section (°)	[σcr,]	30,000 60,000
Notch parameter	[q]	2,490 2,774
Helix angle factor	[Yβ]	1,000
Deep tooth factor	[YDT]	1,000
Gear rim thickness (mm)	[sr]	3,13 3,48
Gear rim factor	[YB]	1,00 1,00
Effective facewidth (mm)	[bEFF]	15,20 14,80
Nominal stress at tooth root (N/mm²)	[σF0]	412,91 418,31
Tooth root stress (N/mm²)	[σF]	728,37 740,68

8/15

Permissible bending stress at root of Test-gear			
Notch sensitivity factor	[YdreIT]	1,000	1,003
Surface factor	[YRreIT]	0,957	0,957
Size factor, tooth root	[YX]	1,000	1,000
Finite life factor	[YNT]	0,906	0,931
$Y_{c} = Y_{dreIT} \cdot Y_{RreIT} \cdot Y_{X} \cdot Y_{NT}$		0,867	0,893
Alternating bending factor, mean stress influence coefficient			
Technology factor	[YM]	1,000	1,000
	[YT]	1,100	1,100
Coefficient for surface factor like for shot peening; The standard gives no applicable information about this...			
Stress correction factor	[Yst]	2,00	
Yst*oFlim (N/mm <sup>2</sup> )	[oFE]	860,00	740,00
Permissible tooth root stress $\sigma_{FG}/SF_{min}$ (N/mm <sup>2</sup> )	[oFP]	683,12	605,68
Limit strength tooth root (N/mm <sup>2</sup> )	[oFG]	819,74	726,81
Required safety	[SFmin]	1,20	1,20

Flank safety

		----- Gear 1 -----	----- Gear 2 -----
Zone factor	[ZH]		2,684
Elasticity factor ( $\sqrt{N/mm^2}$ )	[ZE]		189,812
Contact ratio factor	[Zc]		0,882
Helix angle factor	[ZB]		1,000
Effective facewidth (mm)	[beff]		14,80
Nominal contact stress (N/mm <sup>2</sup> )	[oH0]		1032,60
Contact stress at operating pitch circle (N/mm <sup>2</sup> )	[oHw]		1385,03
Single tooth contact factor	[ZB,ZD]	1,00	1,00
Contact stress (N/mm <sup>2</sup> )	[oHB, oHD]	1385,03	1385,03
Lubrication factor for NL	[ZL]	1,020	1,020
Speed factor for NL	[ZV]	0,995	0,995
Roughness factor for NL	[ZR]	0,943	0,943
Material hardening factor for NL	[ZW]	1,000	1,000
Finite life factor	[ZNT]	0,937	0,977
	[ZL*ZV*ZR*ZNT]	0,897	0,935
Limited pitting is permitted:	No		
Size factor (flank)	[ZX]	1,000	1,000
Permissible contact stress, $\sigma_{HG}/SH_{min}$ (N/mm <sup>2</sup> )	[oHP]	1495,03	1267,93
Pitting stress limit (N/mm <sup>2</sup> )	[oHG]	1345,53	1141,13
Required safety	[SHmin]	0,90	0,90

Micropitting according to

ISO/TS 6336-22:2018

Calculation has not been carried out, lubricant: Load stage micropitting test not known

Scuffing load capacity

Calculation method according to	ISO/TS 6336-20/21:2017	
Helical load factor for scuffing	[KBv]	1,000
Lubrication coefficient for lubrication type	[XS]	1,000
Scuffing test and load stage	[FZGes] FZG - Test A / 8,3 / 90 (ISO 14835 - 1)	12

9/15

Multiple meshing factor	[Xmp]	1,000
Relative structural factor, scuffing	[XWreIT]	1,000
Thermal contact factor (N/mm/s, 5/K)	[BM]	13,780
Relevant tip relief ( $\mu m$ )	[Ca]	2,00
Optimal tip relief ( $\mu m$ )	[Ceff]	15,61
Ca taken as optimal in the calculation (0=no, 1=yes)		0
Effective facewidth (mm)	[beff]	14,800
Applicable circumferential force/facewidth (N/mm)	[wBt]	293,856
KB <sub>y</sub> = 1,000 , wBt*KB <sub>y</sub> = 293,856		
Angle factor	[Xaβ]	0,939
ε1: 1,311 , ε2: 0,357		

Flash temperature-criteria		
Lubricant factor	[XL]	0,830
Tooth mass temperature (°C)	[θMi]	77,29
$\theta_{Mi} = \theta_{oil} + X_{S^0,47} \cdot X_{mp} \cdot \theta_{flm}$		
Average flash temperature (°C)	[θflm]	15,51
Scuffing temperature (°C)	[θS]	348,80
Γ coordinates (point of highest temperature)	[Γ]	0,553
[Γ,A]= -0,310 [Γ,E]= 1,139		
Highest contact temp. (°C)	[θB]	105,10
Flash factor ( $^{\circ}K^{\circ}N^{\circ}.75^{\circ}s^{\circ}.5^{\circ}m^{\circ}.5^{\circ}mm$ )	[XM]	50,058
Approach factor	[XJ]	1,000
Load sharing factor	[XT]	1,000
Dynamic viscosity (mPa*s)	[ηM]	41,90
Coefficient of friction	[μ-]	( 70,0 °C) 0,064

Integral temperature-criteria		
Lubricant factor	[XL]	1,000
Tooth mass temperature (°C)	[θMC]	77,40
$\theta_{MC} = \theta_{oil} + X_{S^0,70} \cdot \theta_{flint}$		
Mean flash temperature (°C)	[θflint]	10,57
Integral scuffing temperature (°C)	[θSint]	360,78
Flash factor ( $^{\circ}K^{\circ}N^{\circ}.75^{\circ}s^{\circ}.5^{\circ}m^{\circ}.5^{\circ}mm$ )	[XM]	50,058
Running-in factor, well run in	[XE]	1,000
Contact ratio factor	[Xc]	0,262
Dynamic viscosity (mPa*s)	[ηOil]	41,90
Mean coefficient of friction	[μ-]	( 70,0 °C) 0,083
Geometry factor	[XBE]	0,157
Meshing factor	[XQ]	1,000
Tip relief factor	[XCa]	1,295
Integral tooth flank temperature (°C)	[θint]	93,25

Measurements for tooth thickness

		----- Gear 1 -----	----- Gear 2 -----
Tooth thickness tolerance		DIN 3967 cd25	DIN 3967 cd25
Tooth thickness allowance (normal section) (mm)	[As,e/I]	-0,054 / -0,084	-0,070 / -0,110
Number of teeth spanned	[k]	4,000	11,000
For internal toothing: k = measurement gap number			
Base tangent length (no backlash) (mm)	[Wk]	10,993	32,274
Base tangent length with allowance (mm)	[Wk,e/I]	10,942 / 10,914	32,340 / 32,378
(mm)	[ΔWk,e/I]	-0,051 / -0,079	-0,066 / -0,103
Diameter of measuring circle (mm)	[dM <sub>Wk,m</sub> ]	24,218	90,551
Theoretical diameter of ball/pin (mm)	[DM]	1,947	1,663
Effective diameter of ball/pin (mm)	[DMeff]	2,000	1,750

10/15

Radial single-ball measurement backlash free (mm)	[MRk]	13,500	43,735
Radial single-ball measurement (mm)	[MRk,e/I]	13,450 / 13,421	43,895 / 43,837
Diameter of measuring circle (mm)	[dMMr,m]	23,944	90,069
Diameter measurement over two balls without clearance (mm)	[MdK]	26,943	87,470
Diameter two ball measure (mm)	[MdK,e/I]	26,841 / 26,784	87,790 / 87,675
Diameter measurement over pins without clearance (mm)	[MdR]	26,943	87,470
Measurement over pins according to DIN 3960 (mm)	[MdR,e/I]	26,841 / 26,784	87,790 / 87,675
Measurement over 3 pins, axial, according to AGMA 2002 (mm)			
	[dk3A,e/I]	26,841 / 26,784	87,790 / 87,675
Dimensions over 3 pins without clearance (mm)	[Md3R]	26,884	-0,000
Measurement over 3 pins with allowance (mm)	[Md3R,e/I]	26,783 / 26,727	-0,000 / -0,000

Chordal tooth thickness (no backlash) (mm)	[sc]	1,928	1,553
Normal chordal tooth thickness with allowance (mm)	[sc,e/I]	1,876 / 1,846	1,483 / 1,443
Reference chordal height from da,m (mm)	[ha]	1,559	0,978
Tooth thickness, arc (mm)	[sn]	1,930	1,553
(mm)	[sn,e/I]	1,876 / 1,846	1,483 / 1,443

Backlash free center distance (mm)	[aControl,e/I]	33,189 / 33,291
Backlash free center distance, allowances (mm)	[ita]	0,189 / 0,291
dNI,i with aControl (mm)	[dNf0,i]	21,781
Reserve (dNI,i-dFf,e)/2 (mm)	[cF0,i]	-0,145
Tip clearance (mm)	[c0,i(aControl)]	0,055
Center distance allowances (mm)	[Aa,e/I]	-0,013 / 0,013
Circumferential backlash from Aa (mm)	[Iw_Aa,e/I]	0,008 / -0,008
Radial backlash (mm)	[Irw,e/I]	0,304 / 0,176
Circumferential backlash (transverse section) (mm)	[Iw,e/I]	0,199 / 0,114
Normal backlash (mm)	[In,e/I]	0,191 / 0,108
Torsional angle on input with output fixed:		
Total torsional angle (°)	[I <sub>t</sub> Sys]	1,0063/0,5780

Toothing tolerances

		----- Gear 1 -----	----- Gear 2 -----
According to ISO 1328-1:1995, ISO 1328-2:1997			
Accuracy grade	[Q]	6	6
Single pitch deviation ( $\mu m$ )	[fpkT]	7,00	7,50
Base circle pitch deviation ( $\mu m$ )	[fpbT]	6,60	7,00
Sector pitch deviation over k/8 pitches ( $\mu m$ )	[Fpk/8T]	9,50	15,00
Profile form deviation ( $\mu m$ )	[ffoT]	5,50	6,50
Profile slope deviation ( $\mu m$ )	[ffoT]	4,60	5,50
Total profile deviation ( $\mu m$ )	[FoT]	7,50	8,50
Helix form deviation ( $\mu m$ )	[ffBT]	7,00	7,50
Helix slope deviation ( $\mu m$ )	[ffBT]	7,00	7,50
Total helix deviation ( $\mu m$ )	[FBT]	10,00	11,00
Total cumulative pitch deviation ( $\mu m$ )	[FPt]	20,00	26,00
Runout ( $\mu m$ )	[FRt]	16,00	21,00
Single flank composite, total ( $\mu m$ )	[FisT]	34,00	41,00
Single flank composite, tooth-to-tooth ( $\mu m$ )	[fisT]	14,00	15,00
Radial composite, total ( $\mu m$ )	[FidT]	21,00	26,00
Radial composite, tooth-to-tooth ( $\mu m$ )	[fidT]	5,00	5,00
FidT (F <sub>r</sub> ), fidT (F <sub>r</sub> ) according to ISO 1328:1997 calculated with the geometric mean values for mn and d			
Axis alignment tolerances (recommendation acc. to ISO TR 10064-3:1996, Quality)			
		6	
Maximum value for deviation error of axis ( $\mu m$ )	[Fβ]	11,30	(Fβ= 11,00 )
Maximum value for inclination error of axes ( $\mu m$ )	[Fβ]	22,59	

11/15

Modifying and defining the tooth form

Profile and tooth trace modifications for gear 1

Symmetric (both flanks)

- flankline crowning
- Cb = 10,000 μm
- rcrown=288mm

Data for the tooth form calculation :

Data not available.

Please run the calculation in the "Tooth form" tab and open the main report again.

Supplementary data

Maximal possible center distance (eps_a=1,0)	[aMAX]	32,463
Mass (g)	[m]	31,77
Total mass (g)	[mGes]	196,18
Moment of inertia for system, relative to the input: calculation without consideration of the exact tooth shape		
Single gears, (da+df)/2...di (kg*m <sup>2</sup> )	[J]	3,137e-06
System (da+df)/2...di (kg*m <sup>2</sup> )	[J]	2,745e-05
Torsional stiffness at driving gear with fixed driven gear:		
Torsional stiffness (MNm/rad)	[cr]	0,035
Torsion when subjected to nominal torque (°)	[δcr]	0,045
Mean coefficient of friction (as defined in Niemann)	[μ-]	0,093
Wear sliding coef. by Niemann	[ζw]	0,609
Loss factor	[HV]	0,120
Gear power loss (KW)	[PVZ]	0,225
Meshing efficiency (%)	[ηz]	98,890
Sound pressure level according to Masuda, without contact analysis	[dB(A)]	68,4

Service life, damage

Calculation with load spectrum		
Required safety for tooth root	[SFmin]	1,20
Required safety for tooth flank	[SHmin]	0,90
Service life (calculated with required safeties):		
System service life (h)	[Hatt]	104
Tooth root service life (h)	[HFatt]	1394
Tooth flank service life (h)	[HHatt]	8,25e+04
		1593

Damage calculated on the basis of the required service life	[H] (1000,0 h)			
No.	F1%	F2%	H1%	H2%
1	0,0000	0,0000	0,0000	0,8584
2	0,0000	0,0000	0,0000	0,2098
3	71,7363	961,0388	1,2122	60,6865
4	0,0000	0,0000	0,0000	1,0380

12/15

Σ 71,7363 961,0388 1,2122 62,7926

Damage calculated on basis of system service life [Hatt] (104,1 h)

No.	F1%	F2%	H1%	H2%
1	0,0000	0,0000	0,0000	0,0893
2	0,0000	0,0000	0,0000	0,0218
3	7,4645	100,0000	0,1261	6,3147
4	0,0000	0,0000	0,0000	0,1080
Σ	7,4645	100,0000	0,1261	6,5338

Damage calculated on basis of individual service life HFatt & HHatt

(h)	HFatt1	HFatt2	HHatt1	HHatt2
1394			104,1	8,25e+04
1593				
No.	F1%	F2%	H1%	H2%
1	0,00	0,00	0,00	1,37
2	0,00	0,00	0,00	0,33
3	100,00	100,00	100,00	96,65
4	0,00	0,00	0,00	1,65
Σ	100,00	100,00	100,00	100,00

Most critical duty cycle elements for Scoring (SB, Sint), Tooth Flank Fracture (SFF), hardened layer (SEHT) and Micropitting (Slam)  
 SB: 3  
 Sint: 4

**Application factor calculated according to ISO 6336-6, Annex A.3**

(The slope of the S-N curve (Woehler lines) in the range of endurance limit according to ISO 6336-6, Table A.1 is used.)

Gear		p	Teq		KA
1	Tooth root	8,738	27,8	KA,F	1 1,000
1	Tooth flank	6,611	27,8	KA,H	1 1,000
2	Tooth root	8,738	108,8	KA,F	2 1,000
2	Tooth flank	6,611	89,5	KA,H	2 0,823

Application factor, ISO 6336-6 A.3 [KAmax] 1,000  
 [KA,Fmax / KA,Hmax] 1,000 / 1,000

Note: If an application factor is entered, the indicated values for KA come with 1,500 zu multiplizieren!

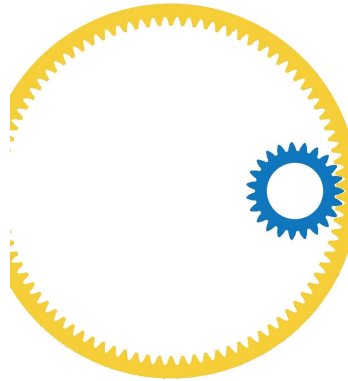
**Classification according to F.E.M., Edition 1,001, 1998**

Spectrum factor	[km]	0,432
Spectrum class	[L]	3
Application class, predefined service life	[T]	3
Machine class, predefined service life	[M]	4
Application class, achievable service life	[T]	0
Machine class, achievable service life	[M]	1

**Remarks:**

- Specifications with [e/l] imply: Maximum [e] and minimum value [l] for Taking all tolerances into account
  - Specifications with [m] imply: Mean value within tolerance
  - For the backlash tolerance, the center distance tolerances and the tooth thickness allowance are taken into account.
- The maximum and minimum clearance according to the largest or smallest allowances are defined.  
 The calculation is performed for the operating pitch circle.

- Details of calculation method:  
 cy according to Method B  
 Kv according to Method B  
 KHβ and KFβ according to Method C  
 fma according to Equation 64, fsh according to 57/58, Fβx according to 52/53/54  
 KHα, KFα according to Method B
- The logarithmically interpolated value taken from the values for the fatigue strength and the static strength, based on the number of load cycles, is used for coefficients ZL, ZV, ZR, ZW, ZX, YdreT, YRrelT and YX..



**Tolerance field for tooth form calculation**

- Diameter: Mean value, Tooth thickness: Mean value  
 da1 = 26,0375 mm, df1 = 21,2984 mm, As1 = -0,0690 mm  
 da2 = 88,0301 mm, df2 = 92,7949 mm, As2 = -0,0900 mm

Figure: Tooth system

F

KISSsoft calculation report 42CrMo4 Equivalent  
Lifespan

**Important hint: At least one warning has occurred during the calculation:**

1-> Calculation for load spectra:  
 The application factor should be set to 1,0!

2-> Load spectrum with negative torque:  
 In the transition from + to - torque the tooth is submitted to alternating bending stress.  
 This transition should be considered with an additional duty cycle element with an alternating bending factor (mean stress influence factor, YM).  
 Consult the manual for more information.  
 (Element no. 4)

Load spectrum with negative load bins:  
 The working flank changes from right flank to left flank or vice versa.  
 These bins can be neglected when calculating the damage.  
 See the corresponding inputs in 'Details' of tab 'Rating'.

**Calculation of a spur-toothed cylindrical gear pair**

Drawing or article number:  
 Gear 1: 0,000,0  
 Gear 2: 0,000,0

**Load spectrum**

Own Input  
 Number of bins in the load spectrum: 4  
 Reference gear: Gear 1  
 Application factor, KA: 1,50

Bin No.	Frequency [%]	Power [kW]	Speed [1/min]	Torque [Nm]	Coefficients							
					$K_v$	$K_{\beta}$	$K_{F\beta}$	$K_{H\beta}$	$K_y$	$Y_{M1}$	$Y_{M2}$	
1	45,0000	7,1862	4183,8	16,4020	1,064	1,311	1,265	1,058	1,000	1,000	1,000	
2	18,0000	9,3176	5927,1	15,0120	1,096	1,333	1,284	1,071	1,000	1,000	1,000	
3	28,0000	9,1349	3137,8	27,8000	1,034	1,165	1,142	1,000	1,000	1,000	1,000	
4	9,0000	-8,5259	4183,8	-19,4600	1,057	1,254	1,218	1,023	1,000	1,000	1,000	

Numbers of load cycles			
Bin No.	Frequency	Load cycles, gear 1	Load cycles, gear 2
	[1]	[1]	[1]

[%]			
1	45,0000	112962600	28868220
2	18,0000	64012140	16358658
3	28,0000	52715880	13471836
4	9,0000	22592520	5773644
SUM	00,0000	252283140	64472358

Notice:  
 - Tooth flank with load spectrum: Consider all negative load spectrum bins as positive  
 - Tooth root with load spectrum: Consider all negative load spectrum bins as positive

S-N curve (Woehler line) in the long life domain according: according to standard

Notice:  
 Calculation-method according to:  
 - ISO 6336-6 / DIN3990-6  
 During the calculation all the load factors (ISO 6336/DIN 3990: Kv, KH $\beta$ , KF $\beta$ ; AGMA 2001: Kv, Km, ...) for each load spectrum bin are calculated separately.

Notice:  
 Calculation with methods ISO 6336 and AGMA 2001 results in a reduction of resistance in the domain of fatigue resistance (from circa 10<sup>7</sup> to 10<sup>8</sup> cycles).  
 The lifetime calculation takes this into account (also with the S-N curve (Woehler Curve) of the Miner type).

**Results**

**Calculation for load spectra:**  
**The application factor should be set to 1,0!**

Safeties, calculated with load spectrum:		
Root safety	1,217	1,241
Flank safety	0,908	1,007
Wear safety factor	932,836	3646,812

Safeties against scuffing/micropitting/EHT/TFE are indicated for the most critical element of the load spectrum:  
 Safety against scuffing (integral temperature) 4,131  
 Safety against scuffing (flash temperature) 12,106

Analysis of critical elements in load spectrum: See section 10

**Only as information: Calculation with reference power**

Calculation method	ISO 6336:2006 (replaced)	
	----- Gear 1 -----	----- Gear 2 -----
Power (kW)	[P]	20,300
Speed (1/min)	[n]	6973,0 1782,0
Torque (Nm)	[T]	27,8 108,8
Application factor	[KA]	1,50
Required service life (h)	[H]	1000,0
Gear driving (+) / driven (-)		+ -

Working flank gear 1: Right flank  
 Gear 1 direction of rotation: Counterclockwise

not topping

**Tooth geometry and material**

Geometry calculation according to

ISO 21771:2007

	----- Gear 1 -----	----- Gear 2 -----
Center distance (mm)	[a]	33,000
Center distance tolerance	ISO 286:2010 Measure js7	
Normal module (mm)	[m]	1,0000
Normal pressure angle (°)	[ $\alpha_n$ ]	20,0000
Helix angle at reference circle (°)	[ $\beta$ ]	0,0000
Number of teeth	[z]	23 -90
Facewidth (mm)	[b]	18,40 18,00
Hand of gear	Spur gear	
Accuracy grade	[Q-ISO 1328:1995]	6 6
Inner diameter (mm)	[d]	15,00
External diameter (mm)	[d <sub>e</sub> ]	99,80
Inner diameter of gear rim (mm)	[d <sub>bi</sub> ]	0,00
Outer diameter of gear rim (mm)	[d <sub>be</sub> ]	0,00

**Material**

Gear 1  
 42 CrMo 4 (2), Through hardened steel, flame/ind. hardened  
 ISO 6336-5 Figure 11/12 (MQ) Flank & root hardened

Gear 2  
 42 CrMo 4 (2), Through hardened steel, flame/ind. hardened  
 ISO 6336-5 Figure 11/12 (MQ) Flank & root hardened

	----- Gear 1 -----	----- Gear 2 -----
Surface hardness	HRC 56	HRC 56
Material treatment according to ISO 6336:2006 Normal, life factors ZNT and YNT >=0,85		
Fatigue strength, tooth root stress (N/mm <sup>2</sup> )	[ $\sigma_{Flim}$ ]	370,00 370,00
Fatigue strength for Hertzian pressure (N/mm <sup>2</sup> )	[ $\sigma_{Hlim}$ ]	1220,00 1220,00
Tensile strength (N/mm <sup>2</sup> )	[ $\sigma_B$ ]	1100,00 1100,00
Yield point (N/mm <sup>2</sup> )	[ $\sigma_S$ ]	900,00 900,00
Young's modulus (N/mm <sup>2</sup> )	[E]	206000 206000
Poisson's ratio	[ $\nu$ ]	0,300 0,300
Roughness average value DS, flank (µm)	[RAH]	0,60 0,60
Roughness average value DS, root (µm)	[RAF]	3,00 3,00
Mean roughness height, Rz, flank (µm)	[RZH]	4,80 4,80
Mean roughness height, Rz, root (µm)	[RZF]	20,00 20,00

Gear reference profile 1:

Reference profile	1,25 / 0,38 / 1,0 ISO 53:1998 Profil A
Dedendum coefficient	[hP*] 1,250
Root radius factor	[rP*] 0,380 (pFPmax= 0,472)
Addendum coefficient	[haP*] 1,000
Tip radius factor	[paP*] 0,000
Protuberance height coefficient	[hprP*] 0,000
Protuberance angle	[ $\alpha prP$ ] 0,000
Tip form height coefficient	[hFaP*] 0,000
Ramp angle	[ $\alpha KP$ ] 0,000

Gear reference profile 2:

Reference profile	1,25 / 0,38 / 1,0 ISO 53:1998 Profil A
Dedendum coefficient	[hP*] 1,250
Root radius factor	[rP*] 0,380 (pFPmax= 0,472)
Addendum coefficient	[haP*] 1,000
Tip radius factor	[paP*] 0,000
Protuberance height coefficient	[hprP*] 0,000
Protuberance angle	[ $\alpha prP$ ] 0,000
Tip form height coefficient	[hFaP*] 0,000
Ramp angle	[ $\alpha KP$ ] 0,000

**Information on final machining**

Dedendum reference profile	[hP*] 1,250	1,250
Tooth root radius Refer. profile	[rP*] 0,380	0,380
Addendum Reference profile	[haP*] 1,000	1,000
Protuberance height coefficient	[hprP*] 0,000	0,000
Protuberance angle (°)	[ $\alpha prP$ ] 0,000	0,000
Tip form height coefficient	[hFaP*] 0,000	0,000
Ramp angle (°)	[ $\alpha KP$ ] 0,000	0,000

Type of profile modification: none (only running-in)  
 Tip relief by running in (µm) [Ca L/R] 3,4 / 3,4 3,4 / 3,4

**Lubrication type**

Type of oil	ISO-VG 220
Lubricant base	Mineral-oil base
Oil nominal kinematic viscosity at 40°C (mm <sup>2</sup> /s)	[ $\nu_{40}$ ] 220,00
Oil nominal kinematic viscosity at 100°C (mm <sup>2</sup> /s)	[ $\nu_{100}$ ] 17,50
Specific density at 15°C (kg/dm <sup>3</sup> )	[ $\rho$ ] 0,895
Oil temperature (°C)	[TS] 70,000

**Gear pair**

Overall transmission ratio	[itot] 3,913
Gear ratio	[u] -3,913
Transverse module (mm)	[m <sub>t</sub> ] 1,000
Transverse pressure angle (°)	[ $\alpha_t$ ] 20,000
Working pressure angle (°)	[ $\alpha_w$ ] 17,459
	[ $\alpha_{wt,e/l}$ ] 17,390 / 17,528
Working pressure angle at normal section (°)	[ $\alpha_{wn}$ ] 17,459
Helix angle at operating pitch circle (°)	[ $\beta_w$ ] 0,000
Base helix angle (°)	[ $\beta_b$ ] 0,000
Reference center distance (mm)	[ $a_d$ ] 33,500
Pitch on reference circle (mm)	[p <sub>t</sub> ] 3,142
Base pitch (mm)	[p <sub>b</sub> ] 2,952
Transverse pitch on contact-path (mm)	[p <sub>e</sub> ] 2,952
Sum of profile shift coefficients	[ $\Sigma x$ ] 0,4702
Transverse contact ratio	[ $\epsilon_{\alpha}$ ] 1,668
Transverse contact ratio with allowances	[ $\epsilon_{\alpha,e/m/l}$ ] 1,703 / 1,675 / 1,647

Overlap ratio	[εβ]	0,000
Total contact ratio	[εv]	1,668
Total contact ratio with allowances	[εv,e/mv]	1,703 / 1,675 / 1,647
Length of path of contact (mm)	[ga, e/i]	4,924 ( 5,029 / 4,863 )
Length T1-A (mm)	[T1A]	2,345 ( 2,241 / 2,387 )
Length T1-B (mm)	[T1B]	4,317 ( 4,317 / 4,298 )
Length T1-C (mm)	[T1C]	3,399 ( 3,413 / 3,384 )
Length T1-D (mm)	[T1D]	5,298 ( 5,193 / 5,339 )
Length T1-E (mm)	[T1E]	7,269 ( 7,269 / 7,251 )
Length T2-A (mm)	[T2A]	12,246 ( 12,183 / 12,246 )
Length T2-B (mm)	[T2B]	14,218 ( 14,260 / 14,158 )
Length T2-C (mm)	[T2C]	13,300 ( 13,356 / 13,244 )
Length T2-D (mm)	[T2D]	15,199 ( 15,135 / 15,199 )
Length T2-E (mm)	[T2E]	17,170 ( 17,212 / 17,110 )
Length T1-T2 (mm)	[T1T2]	9,901 ( 9,943 / 9,859 )
Minimal length of contact line (mm)	[Lmin]	18,000

**Gear 1**

Profile shift coefficient	[x]	0,4940
Tooth thickness, arc, in module	[sn*]	1,9304
Tip alteration (mm)	[k*mm]	0,030
Reference diameter (mm)	[d]	23,000
Base diameter (mm)	[db]	21,613
Tip diameter (mm)	[da]	26,048
(mm)	[da,e/i]	26,048 / 26,027
Tip diameter allowances (mm)	[Ada,e/i]	0,000 / -0,021
Tip form diameter (mm)	[dFa]	26,048
(mm)	[dFa,e/i]	26,048 / 26,027
Root diameter (mm)	[dF]	21,488
Generating Profile shift coefficient	[xE,e/i]	0,4198 / 0,3786
Generated root diameter with xE (mm)	[dF,e/i]	21,340 / 21,257
Root form diameter (mm)	[dFf]	22,163
(mm)	[dFf,e/i]	22,071 / 22,024
Internal toothing: Calculation dFF with pinion type cutter (z0=	25	, x0=0,000 )
Involute length (mm)	[l_dFa-l_dFF]	2,166
Addendum, m <sub>a</sub> (h <sub>a</sub> *+x+k) (mm)	[ha]	1,524
(mm)	[ha,e/i]	1,524 / 1,514
Dedendum (mm)	[hf=mn*(hF*-x)]	0,756
(mm)	[hf,e/i]	0,830 / 0,871
Tooth height (mm)	[h]	2,280
Virtual gear no. of teeth	[zn]	23,000
Normal tooth thickness at tip circle (mm)	[san]	0,477
(mm)	[san,e/i]	0,429 / 0,382
Normal tooth thickness at tip form circle (mm)	[sFan]	0,477
(mm)	[sFan,e/i]	0,429 / 0,382
Normal space width at root circle (mm)	[efn]	0,000
(mm)	[efn,e/i]	0,000 / 0,000

**Gear 2**

5/15

Profile shift coefficient	[x]	-0,0238
Tooth thickness, arc, in module	[sn*]	1,5535
Tip alteration (mm)	[k*mm]	0,000
Reference diameter (mm)	[d]	90,000
Base diameter (mm)	[db]	84,572
Tip diameter (mm)	[da]	88,048
(mm)	[da,e/i]	88,048 / 88,013
Tip diameter allowances (mm)	[Ada,e/i]	0,000 / -0,035
Tip form diameter (mm)	[dFa]	88,048
(mm)	[dFa,e/i]	88,048 / 88,013
Root diameter (mm)	[dF]	92,548
Generating Profile shift coefficient	[xE,e/i]	-0,1200 / -0,1749
Generated root diameter with xE (mm)	[dF,e/i]	92,850 / 92,740
Root form diameter (mm)	[dFf]	91,910
(mm)	[dFf,e/i]	92,244 / 92,124
Internal toothing: Calculation dFi with pinion type cutter (z0=	29	, x0=0,000 )
Involute length (mm)	[l_dFa-l_dFi]	2,055
Addendum, m <sub>a</sub> (h <sub>a</sub> *+x+k) (mm)	[ha]	0,976
(mm)	[ha,e/i]	0,994 / 0,976
Dedendum (mm)	[hf=mn*(hF*-x)]	1,274
(mm)	[hf,e/i]	1,370 / 1,425
Tooth height (mm)	[h]	2,250
Virtual gear no. of teeth	[zn]	90,000
Normal tooth thickness at tip circle (mm)	[san]	0,887
(mm)	[san,e/i]	0,818 / 0,768
Normal tooth thickness at tip form circle (mm)	[sFan]	0,887
(mm)	[sFan,e/i]	0,818 / 0,768
Normal space width at root circle (mm)	[efn]	0,586
(mm)	[efn,e/i]	0,574 / 0,566

**Gear specific pair data Gear pair 1, Gear 1**

Operating pitch diameter (mm)	[dw]	22,657
(mm)	[dw,e/i]	22,648 / 22,665
Active tip diameter (mm)	[dNa]	26,048
(mm)	[dNa,e/i]	26,048 / 26,027
Theoretical tip clearance (mm)	[c]	0,250
Effective tip clearance (mm)	[c,e/i]	0,424 / 0,333
Active root diameter (mm)	[dNf]	22,116
(mm)	[dNf,e/i]	22,134 / 22,073
Reserve (dNf-dFf)/2 (mm)	[cF,e/i]	0,055 / 0,001
Max. sliding velocity at tip (m/s)	[vga]	2,104
Specific sliding at the tip	[ζa]	0,396
Specific sliding at the root	[ζf]	-0,334
Mean specific sliding	[ζm]	0,365
Sliding factor on tip	[Kga]	0,254
Sliding factor on root	[Kgf]	-0,069
Roll angle at dFa (°)	[ζdFa,e/i]	38,543 / 38,443
Roll angle to dNa (°)	[ζdNa,e/i]	38,543 / 38,443
Roll angle to dNf (°)	[ζdNf,e/i]	12,657 / 11,881
Roll angle at dFi (°)	[ζdFi,e/i]	11,861 / 11,222
Diameter of single contact point B (mm)	[d-B]	23,274 ( 23,274 / 23,260 )
Diameter of single contact point D (mm)	[d-D]	24,070 ( 23,979 / 24,107 )
Addendum contact ratio	[ε]	1,311 ( 1,306 / 1,310 )

6/15

**Gear specific pair data Gear pair 1, Gear 2**

Operating pitch diameter (mm)	[dw]	88,657
(mm)	[dw,e/i]	88,690 / 88,623
Active tip diameter (mm)	[dNa]	88,048
(mm)	[dNa,e/i]	88,048 / 88,013
Theoretical tip clearance (mm)	[c]	0,280
Effective tip clearance (mm)	[c,e/i]	0,408 / 0,324
Active root diameter (mm)	[dNf]	91,279
(mm)	[dNf,e/i]	91,310 / 91,233
Reserve (dNf-dFf)/2 (mm)	[cF,e/i]	0,505 / 0,407
Max. sliding velocity at tip (m/s)	[vga]	0,573
Specific sliding at the tip	[ζa]	0,251
Specific sliding at the root	[ζf]	-0,657
Mean specific sliding	[ζm]	0,365
Sliding factor on tip	[Kga]	0,069
Sliding factor on root	[Kgf]	-0,254
Roll angle at dFa (°)	[ζdFa,e/i]	16,508 / 16,593
Roll angle to dNa (°)	[ζdNa,e/i]	16,508 / 16,593
Roll angle to dNf (°)	[ζdNf,e/i]	23,183 / 23,321
Roll angle at dFi (°)	[ζdFi,e/i]	24,748 / 24,951
Diameter of single contact point B (mm)	[d-B]	89,225 ( 89,252 / 89,187 )
Diameter of single contact point D (mm)	[d-D]	89,869 ( 89,827 / 89,869 )
Addendum contact ratio	[ε]	0,357 ( 0,397 / 0,338 )

**General influence factors**

Nominal circum. force at pitch circle (N)	[F]	2417,4
Axial force (N)	[Fa]	0,0
Radial force (N)	[Fr]	879,9
Normal force (N)	[Fnorm]	2572,5
Nominal circumferential force per mm (N/mm)	[w]	134,30
Only as information: Forces at operating pitch circle:		
Nominal circumferential force (N)	[Ftw]	2454,0
Axial force (N)	[Faw]	0,0
Radial force (N)	[Frw]	771,8
Circumferential speed reference circle (m/s)	[v]	8,40
Circumferential speed operating pitch circle (m/s)	[v(dw)]	8,27
Running-in value (µm)	[yp]	0,5
Running-in value (µm)	[yf]	0,5
Correction factor	[CM]	0,800
Gear blank factor	[CR]	1,000
Basic rack factor	[CBS]	0,975
Material coefficient	[E/Est]	1,000
Singular tooth stiffness (N/mm/µm)	[c]	15,698
Meshing stiffness (N/mm/µm)	[cvc]	23,561
Meshing stiffness (N/mm/µm)	[cvβ]	20,027
Reduced mass (kg/mm)	[mRed]	0,00157
Resonance speed (min-1)	[nE1]	50859
Resonance ratio (-)	[N]	0,137
Subcritical range		
Running-in value (µm)	[yc]	0,5
Bearing distance l of pinion shaft (mm)	[l]	36,800
Distance s of pinion shaft (mm)	[s]	3,680

7/15

Outside diameter of pinion shaft (mm)	[dsh]	18,400
Load in accordance with Figure 13, ISO 6336-1:2006 (0.a), 1.b), 2.c), 3.d), 4.e)	[-]	4
Coefficient K' according to Figure 13, ISO 6336-1:2006	[K]	-1,00
Without stiffening		
Tooth trace deviation (active) (µm)	[Fβy]	3,38
from deformation of shaft (µm)	[fsh*β1]	1,14
fsh (µm) = 1,14 , B1=1,00 , fHβ5 (µm) = 5,50		
Tooth without tooth trace modification		
Position of contact pattern: favorable		
from production tolerances (µm)	[fma*β2]	10,26
B2= 1,00		
Tooth trace deviation, theoretical (µm)	[Fβx]	3,98
Running-in value (µm)	[yβ]	0,60
Dynamic factor	[Kv]	1,076
Face load factor - flank	[KHβ]	1,156
- Tooth root	[KFβ]	1,135
- Scuffing	[KBβ]	1,156
Transverse load factor - flank	[KHα]	1,000
- Tooth root	[KFα]	1,000
- Scuffing	[KBα]	1,000

**Tooth root load capacity**

Calculation of Tooth form coefficients according method: B		
Internal toothing:		Calculation of pF and sFn according to ISO 6336-3:2007-04-01
Internal toothing:		Calculation of YF, YS with pinion type cutter, z0= 29 , x0= 0,000 , paP0*=
0,380		
Calculated with generating profile shift coefficient		----- Gear 1 ----- Gear 2 -----
Tooth form factor	[xFe]	0,4198 -0,1200
Stress correction factor	[YF]	1,13 1,16
Load application angle (°)	[YS]	2,29 2,20
Load application diameter (mm)	[σFn]	22,56 19,36
Bending moment arm (mm)	[da]	24,070 -89,225
Tooth thickness at root (mm)	[hF]	0,92 1,46
Tooth root radius (mm)	[sFn]	2,19 2,75
Bending moment arm (-)	[pF]	0,44 0,50
Tooth thickness at root (-)	[hF/mm]	0,921 1,464
Tooth root radius (-)	[sFn/mm]	2,191 2,753
Calculation cross section diameter (mm)	[pF/mm]	0,440 0,496
Tangents on calculation cross section (°)	[d <sub>gr</sub> ]	21,672 -92,607
Notch parameter	[σ <sub>gr</sub> ]	30,000 60,000
	[qa]	2,490 2,774
Helix angle factor	[Yβ]	1,000
Deep tooth factor	[YDT]	1,000
Gear rim thickness (mm)	[sr]	3,13 3,48
Gear rim factor	[YB]	1,00 1,00
Effective facewidth (mm)	[beff]	18,40 18,00
Nominal stress at tooth root (N/mm²)	[σF0]	341,10 344,76
Tooth root stress (N/mm²)	[σF]	624,34 631,05

8/15



Permissible bending stress at root of Test-gear			
Notch sensitivity factor	[YdreIT]	1,000	1,003
Surface factor	[YRreIT]	0,957	0,957
Size factor, tooth root	[YX]	1,000	1,000
Finite life factor	[YNT]	0,906	0,931
$Y_{c} = Y_{dent} \cdot Y_{root} \cdot Y_{s} \cdot Y_{nt}$		0,867	0,893
Alternating bending factor, mean stress influence coefficient	[YM]	1,000	1,000
Technology factor	[YT]	1,100	1,100
Coefficient for surface factor like for shot peening; The standard gives no applicable information about this...			
Stress correction factor	[Yst]	2,00	
$Y_{st} \cdot \sigma_{Flim}$ (N/mm <sup>2</sup> )	[oFE]	740,00	740,00
Permissible tooth root stress $\sigma_{FG}/SF_{min}$ (N/mm <sup>2</sup> )	[oFP]	587,80	605,68
Limit strength tooth root (N/mm <sup>2</sup> )	[oFG]	705,36	726,81
Required safety	[SFmin]	1,20	1,20

**Flank safety**

		----- Gear 1 -----	Gear 2 --
Zone factor	[ZH]	2,684	
Elasticity factor ( $\sqrt{N/mm^2}$ )	[ZE]	189,812	
Contact ratio factor	[Zc]	0,882	
Helix angle factor	[Zb]	1,000	
Effective facewidth (mm)	[b <sub>eff</sub> ]	18,00	
Nominal contact stress (N/mm <sup>2</sup> )	[oH0]	936,33	
Contact stress at operating pitch circle (N/mm <sup>2</sup> )	[oHW]	1278,82	
Single tooth contact factor	[ZB,ZD]	1,00	1,00
Contact stress (N/mm <sup>2</sup> )	[oHB, oHD]	1278,82	1278,82
Lubrication factor for NL	[ZL]	1,020	1,020
Speed factor for NL	[ZV]	0,995	0,995
Roughness factor for NL	[ZR]	0,943	0,943
Material hardening factor for NL	[ZW]	1,000	1,000
Finite life factor	[ZNT]	0,937	0,977
Limited pitting is permitted:	No		
Size factor (flank)	[ZX]	1,000	1,000
Permissible contact stress, $\sigma_{HG}/SH_{min}$ (N/mm <sup>2</sup> )	[oHP]	1215,96	1267,93
Pitting stress limit (N/mm <sup>2</sup> )	[oHG]	1094,36	1141,13
Required safety	[SHmin]	0,90	0,90

**Wear**

Wear does not usually occur with oil lubrication and circumferential speeds over 1 m/s.  
The limit for using the calculation method has been exceeded.

Line load at reference diameter (N/mm)	[w]	134,30
Line load at reference diameter (N/mm) 250.52	[K <sub>a</sub> K <sub>s</sub> K <sub>r</sub> K <sub>β</sub> K <sub>H</sub> K <sub>Hc</sub> w]	
Loss factor	[H <sub>c</sub> ]	0,120
Length of active flank (mm)	[ln]	2,18 1,71
Wear factor (mm <sup>3</sup> /Nm/10 <sup>6</sup> )	[k <sub>w</sub> ]	2,89451e-05 2,26421e-05
Normal tooth thickness on reference circle (dNa=dNf)/2 (mm)	[s <sub>n</sub> ]	1,48 1,48

9/15

Maximum permissible wear (%)	[W <sub>lim</sub> ]	15,00
Permissible wear on flank (mm)	[δ <sub>wlim</sub> ]	0,22 0,22
Wear removal (mm)	[δ <sub>w</sub> ]	0,0005 0,0001
Wear removal (mg)	[=FL*b*z*ro*δWn]	3,7 2,9
Required safety	[S <sub>wmin</sub> ]	1,10

Calculation of local wear with speeds and load distribution according to method A:  
Calculation has not been carried out, contact analysis under load is required..

**Micropitting according to**

ISO/TS 6336-22:2018

Calculation has not been carried out, lubricant: Load stage micropitting test not known

**Scuffing load capacity**

Calculation method according to	ISO/TS 6336-20/21:2017	
Helical load factor for scuffing	[Kβv]	1,000
Lubrication coefficient for lubrication type	[XS]	1,000
Scuffing test and load stage	[FZGtest] FZG - Test A / 8,3 / 90 (ISO 14635 - 1)	12
Multiple meshing factor	[Xmp]	1,000
Relative structural factor, scuffing	[XWreIT]	1,000
Thermal contact factor (N/mm <sup>2</sup> /s <sup>0.5</sup> /K)	[BM]	13,780 13,780
Relevant tip relief (μm)	[Ca]	3,40 3,40
Optimal tip relief (μm)	[Ceff]	12,83
Ca taken as optimal in the calculation (0=no, 1=yes)		0 0
Effective facewidth (mm)	[b <sub>eff</sub> ]	18,000
Applicable circumferential force/facewidth (N/mm)	[wBt]	250,518
Kβy = 1,000 , wBt*Kβy = 250,518		
Angle factor	[Xαβ]	0,939
ε1: 1.311 , ε2: 0.357		
Flash temperature-criteria		
Lubricant factor	[XL]	0,830
Tooth mass temperature (°C)	[θM]	76,27
θMi = θoil + XS*0,47*Xmp*θflm		
Average flash temperature (°C)	[θflm]	13,33
Scuffing temperature (°C)	[θS]	348,80
Γ coordinates (point of highest temperature)	[Γ]	0,553
[Γ <sub>r</sub> A]= -0,310 [Γ <sub>r</sub> E]= 1,139		
Highest contact temp. (°C)	[θB]	100,16
Flash factor (°K <sup>2</sup> N <sup>-1</sup> .75*s <sup>0.5</sup> m <sup>-1</sup> .5mm)	[XM]	50,058
Approach factor	[XJ]	1,000
Load sharing factor	[XT]	1,000
Dynamic viscosity (mPa*s)	[ηM]	41,90 ( 70,0 °C)
Coefficient of friction	[μ <sub>n</sub> ]	0,062
Integral temperature-criteria		
Lubricant factor	[XL]	1,000
Tooth mass temperature (°C)	[θMC]	75,53
θMC = θoil + XS*0,70*θflaint		
Mean flash temperature (°C)	[θflaint]	7,89
Integral scuffing temperature (°C)	[θSint]	360,78
Flash factor (°K <sup>2</sup> N <sup>-1</sup> .75*s <sup>0.5</sup> m <sup>-1</sup> .5mm)	[XM]	50,058

10/15

Running-in factor, well run in	[XE]	1,000
Contact ratio factor	[Xe]	0,262
Dynamic viscosity (mPa*s)	[ηOil]	41,90 ( 70,0 °C)
Mean coefficient of friction	[μ <sub>n</sub> ]	0,080
Geometry factor	[XBE]	0,157
Meshing factor	[XQ]	1,000
Tip relief factor	[XCa]	1,490
Integral tooth flank temperature (°C)	[θint]	87,37

**Measurements for tooth thickness**

		----- Gear 1 -----	Gear 2 --
Tooth thickness tolerance		DIN 3967 cd25	DIN 3967 cd25
Tooth thickness allowance (normal section) (mm)	[As,eI]	-0,054 /-0,084	-0,070 /-0,110
Number of teeth spanned	[k]	4,000	11,000
For internal toothing: k = measurement gap number			
Base tangent length (no backlash) (mm)	[Wk]	10,993	32,274
Base tangent length with allowance (mm)	[Wk,eI]	10,942 / 10,914	32,340 / 32,378
(mm)	[ΔWk,eI]	-0,051 / -0,079	-0,066 / -0,103
Diameter of measuring circle (mm)	[dM/Wk,m]	24,218	90,551
Theoretical diameter of ball/pin (mm)	[DM]	1,947	1,663
Effective diameter of ball/pin (mm)	[DM,eI]	2,000	1,750
Radial single-ball measurement backlash free (mm)	[MRk]	13,500	43,735
Radial single-ball measurement (mm)	[MRk,eI]	13,450 / 13,421	43,895 / 43,837
Diameter of measuring circle (mm)	[dMMr,m]	23,944	90,069
Diametral measurement over two balls without clearance (mm)	[MdK]	26,943	87,470
Diametral two ball measure (mm)	[MdK,eI]	26,841 / 26,784	87,790 / 87,675
Diametral measurement over pins without clearance (mm)	[MdR]	26,943	87,470
Measurement over pins according to DIN 3960 (mm)	[MdR,eI]	26,841 / 26,784	87,790 / 87,675
Measurement over 3 pins, axial, according to AGMA 2002 (mm)			
	[dk3A,eI]	26,841 / 26,784	87,790 / 87,675
Dimensions over 3 pins without clearance (mm)	[Md3R]	26,884	-0,000
Measurement over 3 pins with allowance (mm)	[Md3R,eI]	26,783 / 26,727	-0,000 / -0,000
Chordal tooth thickness (no backlash) (mm)	[sc]	1,928	1,553
Normal chordal tooth thickness with allowance (mm)	[sc,eI]	1,876 / 1,846	1,483 / 1,443
Reference chordal height from da,m (mm)	[ha]	1,559	0,978
Tooth thickness, arc (mm)	[sn]	1,930	1,553
(mm)	[sn,eI]	1,876 / 1,846	1,483 / 1,443
Backlash free center distance (mm)	[aControl,eI]	33,189 / 33,291	
Backlash free center distance, allowances (mm)	[ita]	0,189 / 0,291	
dNi with aControl (mm)	[dNi0,j]	21,781	91,995
Reserve (dNi0,-dFi,eI)/2 (mm)	[cF0,j]	-0,145	0,064
Tip clearance (mm)	[c0,i(aControl)]	0,055	0,045
Center distance allowances (mm)	[Aa,eI]	-0,013 / 0,013	
Circumferential backlash from Aa (mm)	[Itw_Aa,eI]	0,008 / -0,008	
Radial backlash (mm)	[Itw,eI]	0,304 / 0,176	
Circumferential backlash (transverse section) (mm)	[Itw,eI]	0,199 / 0,114	
Normal backlash (mm)	[Itw,eI]	0,191 / 0,108	
Torsional angle on input with output fixed:			
Total torsional angle (°)	[ItSvs]	1,0063/0,5780	

**Toothing tolerances**

11/15

		----- Gear 1 -----	Gear 2 --
According to ISO 1328-1:1995, ISO 1328-2:1997			
Accuracy grade	[Q]	6	6
Single pitch deviation (μm)	[fpt]	7,00	7,50
Base circle pitch deviation (μm)	[fpbT]	6,60	7,00
Sector pitch deviation over k/8 pitches (μm)	[Fpk/8T]	9,50	15,00
Profile form deviation (μm)	[ffgT]	5,50	6,50
Profile slope deviation (μm)	[ffsT]	4,60	5,50
Total profile deviation (μm)	[FpT]	7,50	8,50
Helix form deviation (μm)	[ffBT]	7,00	7,50
Helix slope deviation (μm)	[ffBT]	7,00	7,50
Total helix deviation (μm)	[FBT]	10,00	11,00
Total cumulative pitch deviation (μm)	[FpT]	20,00	26,00
Runout (μm)	[FRt]	16,00	21,00
Single flank composite, total (μm)	[FisT]	34,00	41,00
Single flank composite, tooth-to-tooth (μm)	[fisT]	14,00	15,00
Radial composite, total (μm)	[FidT]	21,00	26,00
Radial composite, tooth-to-tooth (μm)	[fidT]	5,00	5,00
FidT (F <sub>T</sub> ), fidT (f <sub>T</sub> ) according to ISO 1328:1997 calculated with the geometric mean values for mn and d			

Axis alignment tolerances (recommendation acc. to ISO TR 10064-3:1996, Quality 6)

Maximum value for deviation error of axis (μm)	[fzβ]	11,24 (Fβ= 11,00 )
Maximum value for inclination error of axes (μm)	[fzδ]	22,49

**Modifying and defining the tooth form**

**Profile and tooth trace modifications for gear 1**

**Symmetric (both flanks)**

- flankline crowning  
Cb = 10,000 μm  
rcrown=4232mm

Data for the tooth form calculation :

**Calculation of Gear 1**

Tooth form, Gear 1, Step 1: Automatic (final machining)  
haP<sup>0</sup>= 1,120, hP<sup>0</sup>= 1,250, pP<sup>0</sup>= 0,380

**Calculation of Gear 2**

Tooth form, Gear 2, Step 1: Automatic (final machining)  
z0= 29, x0=0,0000, da0= 31,505 mm, a0= -30,645 mm  
haP0<sup>0</sup>= 1,253, paP0<sup>0</sup>= 0,380, hP0<sup>0</sup>= 1,130, pP0<sup>0</sup>= 0,000

**Supplementary data**

Maximal possible center distance (eps_a=1,0)	[aMAX]	32,463
Mass (g)	[m]	38,46 199,96
Total mass (g)	[mGes]	238,42

Moment of inertia for system, relative to the input:  
calculation without consideration of the exact tooth shape

12/15

Single gears, (da+df)/2...di (kg/m³)	[J]	3,798e-06	0,0004527
System (da+df)/2...di (kg/m³)	[J]	3,337e-05	
Torsional stiffness at driving gear with fixed driven gear:			
Torsional stiffness (MNm/rad)	[cr]	0,043	
Torsion when subjected to nominal torque (°)	[δcr]	0,037	
Mean coefficient of friction (as defined in Niemann)	[μ <sub>n</sub> ]	0,090	
Wear sliding coef, by Niemann	[δw]	0,609	
Loss factor	[HV]	0,120	
Gear power loss (KW)	[PVZ]	0,219	
Meshing efficiency (%)	[ηz]	98,922	
Sound pressure level according to Masuda, without contact analysis	[dB(A)]	68,6	

**Service life, damage**

Calculation with load spectrum			
Required safety for tooth root	[SFmin]	1,20	
Required safety for tooth flank	[SHmin]	0,90	
Required safety for wear	[SWmin]	1,10	

Service life (calculated with required safeties):			
System service life (h)	[Hatt]	1358	

Tooth root service life (h)	[HFatt]	2019	5282
Tooth flank service life (h)	[HHatt]	1358	5312
Wear service life (h)	[HWatt]	8,48e+05	1e+06

Damage calculated on the basis of the required service life [H] (1000,0 h)						
No.	F1%	F2%	H1%	H2%	W1%	W2%
1	0,0000	0,0000	0,0000	0,0000	0,0488	0,0125
2	0,0000	0,0000	0,0000	0,0000	0,0269	0,0069
3	49,5333	18,9323	73,1386	18,6910	0,0316	0,0081
4	0,0000	0,0000	0,5201	0,1329	0,0107	0,0027
Σ	49,5333	18,9323	73,6587	18,8239	0,1179	0,0302

Damage calculated on basis of system service life [Hatt] (1357,6 h)						
No.	F1%	F2%	H1%	H2%	W1%	W2%
1	0,0000	0,0000	0,0000	0,0000	0,0663	0,0170
2	0,0000	0,0000	0,0000	0,0000	0,0365	0,0093
3	67,2470	25,7027	99,2939	25,3751	0,0428	0,0110
4	0,0000	0,0000	0,7061	0,1805	0,0145	0,0037
Σ	67,2470	25,7027	100,0000	25,5556	0,1601	0,0410

Damage calculated on basis of individual service life HFatt & HHatt & HWatt						
(h)	HFatt1	HFatt2	HHatt1	HHatt2	HWatt1	HWatt2
	2019	5282	1358	5312	8,48e+05	1e+06
No.	F1%	F2%	H1%	H2%	W1%	W2%
1	0,00	0,00	0,00	0,00	41,41	41,41
2	0,00	0,00	0,00	0,00	22,79	22,79
3	100,00	100,00	99,29	99,29	26,76	26,76
4	0,00	0,00	0,71	0,71	9,04	9,04
Σ	100,00	100,00	100,00	100,00	100,00	100,00

Most critical duty cycle elements for Scoring (SB, Sint), Tooth Flank Fracture (SFF), hardened layer (SEHT) and Micropitting (Slam)

SB: 3  
Sint: 4

**Application factor calculated according to ISO 6336-6, Annex A.3**

(The slope of the S-N curve (Woehler lines) in the range of endurance limit according to ISO 6336-6, Table A.1 is used.)

Gear		p	Teq		KA
1	Tooth root	8,738	27,8	KA,F	1 1,000
1	Tooth flank	6,611	27,8	KA,H	1 1,000
2	Tooth root	8,738	108,8	KA,F	2 1,000
2	Tooth flank	6,611	89,5	KA,H	2 0,823

Application factor, ISO 6336-6 A.3 [KAm<sub>ax</sub>] 1,000

[KA,Fmax / KA,Hmax] 1,000 / 1,000

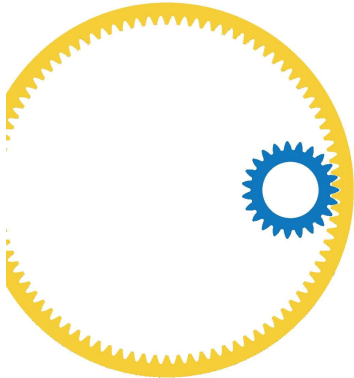
Note: If an application factor is entered, the indicated values for KA come with 1,500 zu multiplizieren!

**Classification according to F.E.M., Edition 1.001, 1998**

Spectrum factor	[km]	0,432
Spectrum class	[L]	3
Application class, predefined service life	[T]	3
Machine class, predefined service life	[M]	4
Application class, achievable service life	[T]	3
Machine class, achievable service life	[M]	4

**Remarks:**

- Specifications with [e/l] imply: Maximum [e] and minimum value [l] for Taking all tolerances into account
- Specifications with [m] imply: Mean value within tolerance
- For the backlash tolerance, the center distance tolerances and the tooth thickness allowance are taken into account.
- The maximum and minimum clearance according to the largest or smallest allowances are defined..
- The calculation is performed for the operating pitch circle.
- Details of calculation method:
  - cy according to Method B
  - Kv according to Method B
  - KHβ and KFβ according to Method C
  - fmg according to Equation 64, fsh according to 57/58, Fβx according to 52/53/54
  - KHα, KFα according to Method B
- The logarithmically interpolated value taken from the values for the fatigue strength and the static strength, based on the number of load cycles, is used for coefficients ZL, ZV, ZR, ZW, ZX, YdrelT, YRrelT and YX..



Tolerance field for tooth form calculation  
 - Diameter: Mean value, Tooth thickness: Mean value  
 da1 = 26,0375 mm, d1 = 21,2984 mm, As1 = -0,0690 mm  
 da2 = 88,0301 mm, d2 = 92,7949 mm, As2 = -0,0900 mm

Figure: Tooth system

# G

Technical Information Sheet Trudisk

**TRUMPF**



# TruDisk

Technical data

**TruDisk 4002****TruDisk 4006****TruDisk 5000**

PROTECTION CLASS	IP54	IP54	IP54
AMBIENT TEMPERATURE	10 °C - 50 °C	10 °C - 50 °C	10 °C - 50 °C

**TruDisk 5001****TruDisk 5002****TruDisk 5006****LASER PARAMETERS**

LASER POWER ON THE WORKPIECE	5000 W	5000 W	5000 W
TYPICAL POWER CONSTANCY AT RATED POWER	± 1 % with active power regulation	± 1 % with active power regulation	± 1 % with active power regulation
CONTINUOUSLY ADJUSTABLE POWER RANGE	120 W - 5000 W with active power regulation	120 W - 5000 W with active power regulation	120 W - 5000 W with active power regulation
BEAM QUALITY AT THE INPUT COUPLING IN THE LLK	4 mm ■ mrad	8 mm ■ mrad	25 mm ■ mrad
NUMERICAL APERTURE ON THE OUTPUT COUPLING AFTER LLK	0.1	0.1	0.1
WAVELENGTH	1030 nm	1030 nm	1030 nm
MINIMUM LASER LIGHT CABLE DIAMETER	100 µm	200 µm	600 µm
TYP. LEISTUNGSKONSTANZ BEI NENNLEISTUNG ÜBER 8 STD. BEI KONSTANTER UMGEBUNGSTEMPERATUR			
MAX. LEISTUNGSKONSTANZ BEI NENNLEISTUNG ÜBER 8 STD. BEI KONSTANTER UMGEBUNGSTEMPERATUR			
TYPICAL POWER CONSTANCY AT RATED POWER OVER 8 HOURS AT CONSTANT AMBIENT TEMPERATURE			

**STRUCTURAL DESIGN**

WIDTH	1175 mm	1175 mm	1175 mm
HEIGHT	1430 mm	1430 mm	1430 mm
DEPTH	725 mm	725 mm	725 mm
MAXIMUM NUMBER OF LASER LIGHT CABLES	2	2	2
MAXIMUM NUMBER OF LASER LIGHT CABLES FOR EXTENDED DEVICE SIZE	4	4	4

**INSTALLATION**

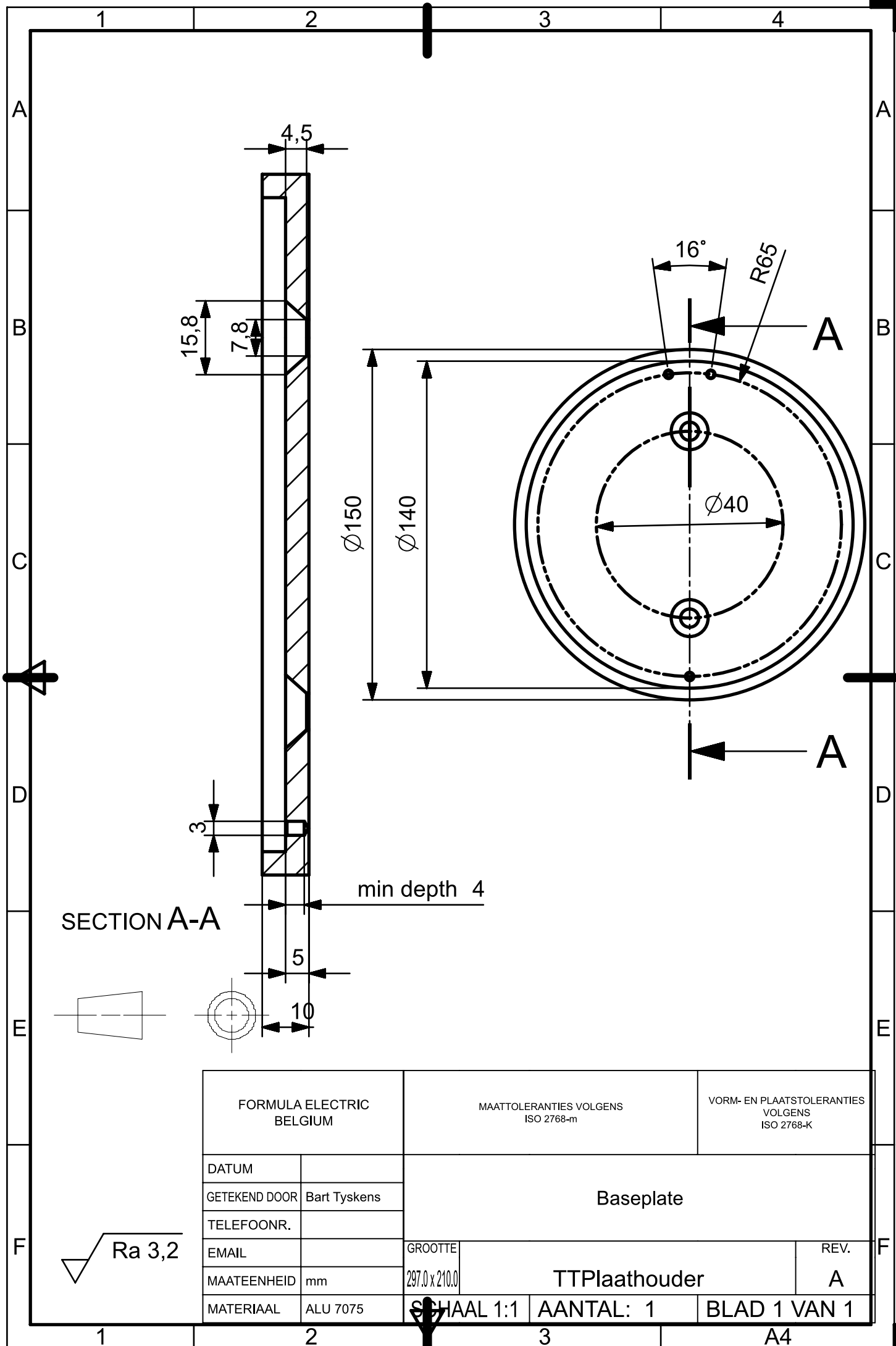
PROTECTION CLASS	IP54	IP54	IP54
AMBIENT TEMPERATURE	10 °C - 50 °C	10 °C - 50 °C	10 °C - 50 °C

**TruDisk 6000****TruDisk 6001****TruDisk 6001 P****LASER PARAMETERS**

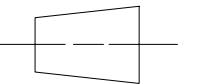
LASER POWER ON THE WORKPIECE	6000 W	6000 W	6000 W
TYPICAL POWER CONSTANCY AT RATED POWER	-	± 1 % with active power regulation	-



## Technical Drawings Laser Hardening Setup



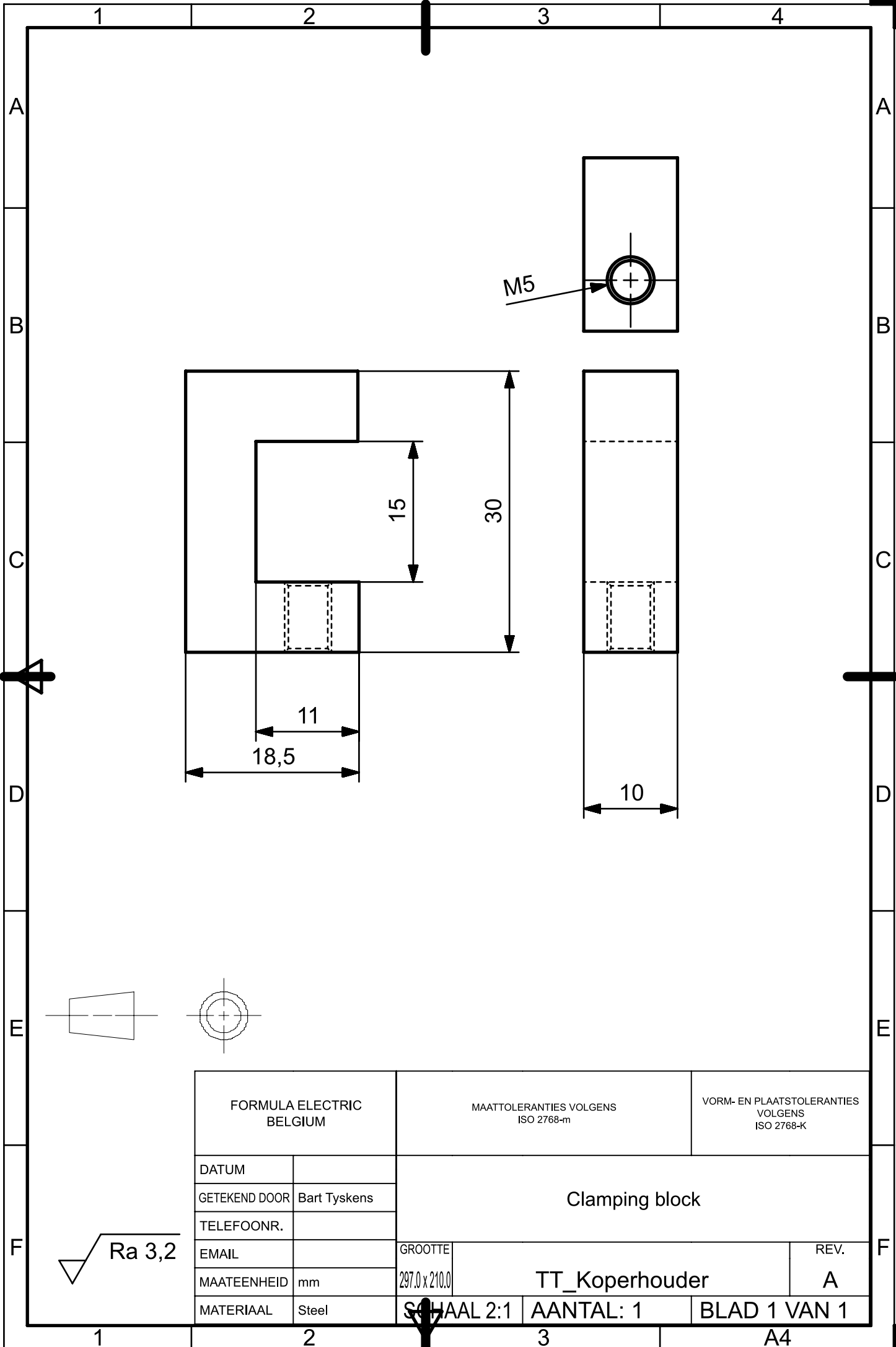
SECTION A-A



Ra 3,2

FORMULA ELECTRIC BELGIUM		MAATTOLERANTIES VOLGENS ISO 2768-m		VORM- EN PLAATSTOLERANTIES VOLGENS ISO 2768-K	
DATUM		Baseplate			
GETEKEND DOOR	Bart Tyskens				
TELEFOONNR.		GROOTTE		REV.	
EMAIL		297,0 x 210,0		TTPlaathouder	
MAATEENHEID	mm	SCHAAL 1:1		AANTAL: 1	
MATERIAAL	ALU 7075			BLAD 1 VAN 1	

A4

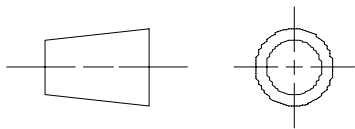
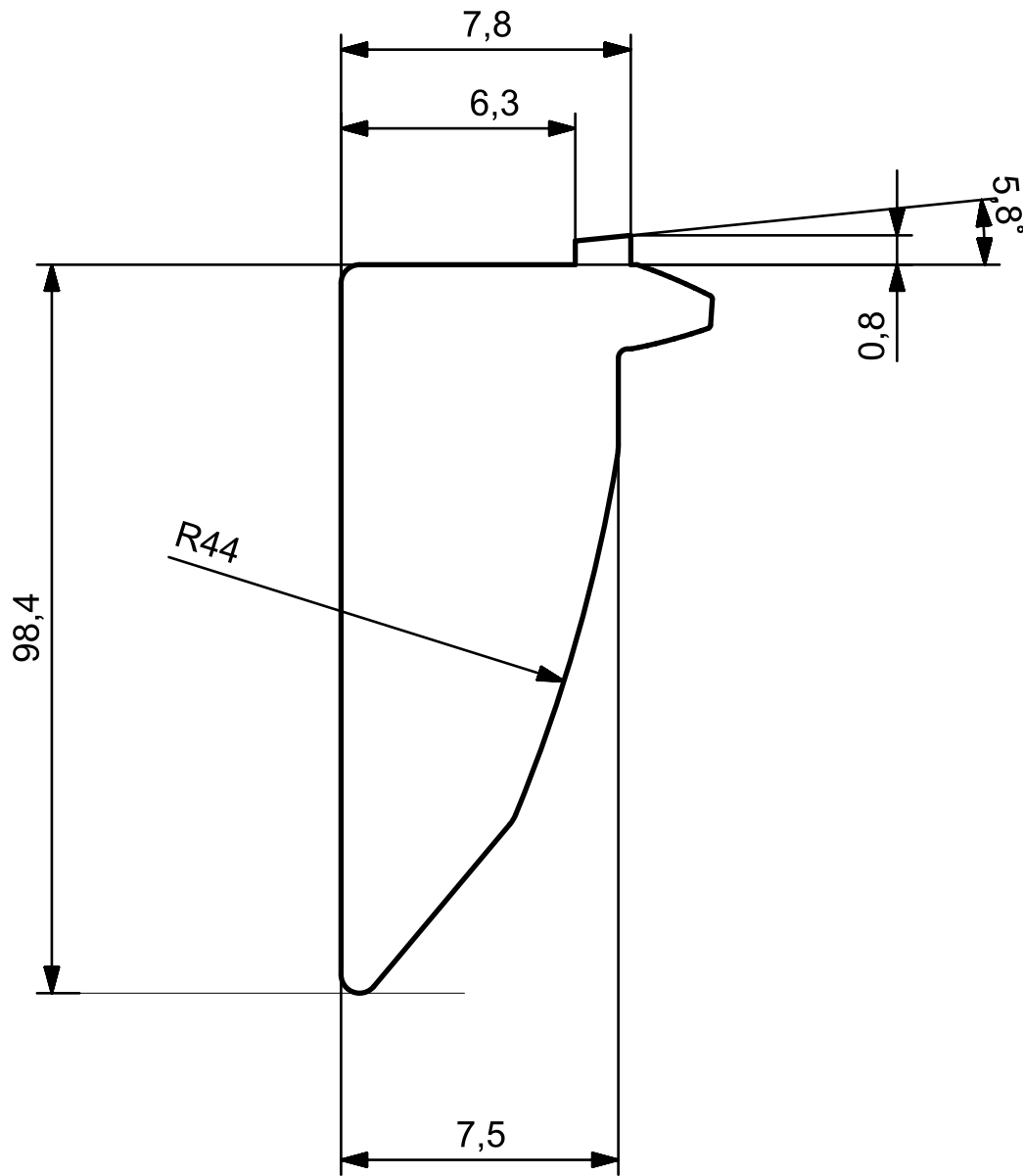


FORMULA ELECTRIC BELGIUM		MAATTOLERANTIES VOLGENS ISO 2768-m		VORM- EN PLAATSTOLERANTIES VOLGENS ISO 2768-K	
DATUM		Clamping block			
GETEKEND DOOR	Bart Tyskens				
TELEFOONR.		GROOTTE		REV.	
EMAIL		297.0 x 210.0		TT_Koperhouder	
MAATEENHEID	mm	SCHAAL 2:1		A	
MATERIAAL	Steel	AANTAL: 1		BLAD 1 VAN 1	

Ra 3,2



For tooth profile, see appended .dxf-file



Ra 3,2

FORMULA ELECTRIC BELGIUM		MAATTOLERANTIES VOLGENS ISO 2768-m		VORM- EN PLAATSTOLERANTIES VOLGENS ISO 2768-K	
DATUM		Cooling block			
GETEKEND DOOR	Bart Tyskens				
TELEFOONR.		TT_Koelblok			
EMAIL					
MAATEENHEID	mm	GROOTTE	AANTAL: 2		REV. A
MATERIAAL	ALU 7075	SCHAAL 5:1	BLAD 1 VAN 1		

1

2

3

A4

1 2 3 4

A

A

15

8

B

B

8

C

C

A

A

M6 full depth

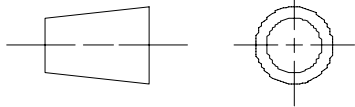
5

M 5

D

D

SECTION A-A



E

E

FORMULA ELECTRIC  
BELGIUM

MAATTOLERANTIES VOLGENS  
ISO 2768-m

VORM- EN PLAATSTOLERANTIES  
VOLGENS  
ISO 2768-K

DATUM

GETEKEND DOOR Ward Lenaerts

TELEFOONR.

EMAIL

MAATEENHEID mm

MATERIAAL Steel

GROOTTE

297,0 x 210,0

REV.

A

Gear clamp

TT\_aanspanningsblok

SCHAAL 5:1

AANTAL: 1

BLAD 1 VAN 1

Ra 3,2

F

F

1

2

3

A4

1 2 3 4

A

A

B

B

C

C

D

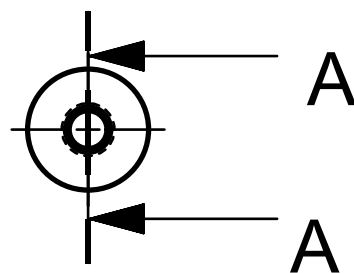
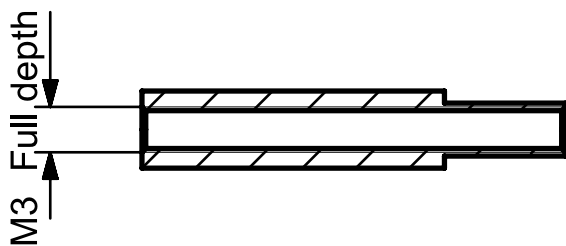
D

E

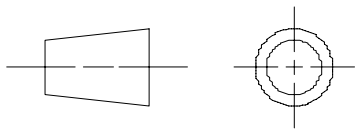
E

F

F



SECTION A-A



Ø6 h6

Ø8 g6

FORMULA ELECTRIC  
BELGIUM

MAATTOLERANTIES VOLGENS  
ISO 2768-m

VORM- EN PLAATSTOLERANTIES  
VOLGENS  
ISO 2768-K

DATUM  
GETEKEND DOOR Ward Lenaerts

Gear clamping pin

TELEFOONR.

EMAIL

GROOTTE

REV.

MAATEENHEID mm

297.0 x 210.0

TT\_Steunas

A

MATERIAAL ALU 7075

SCHAAL 2:1

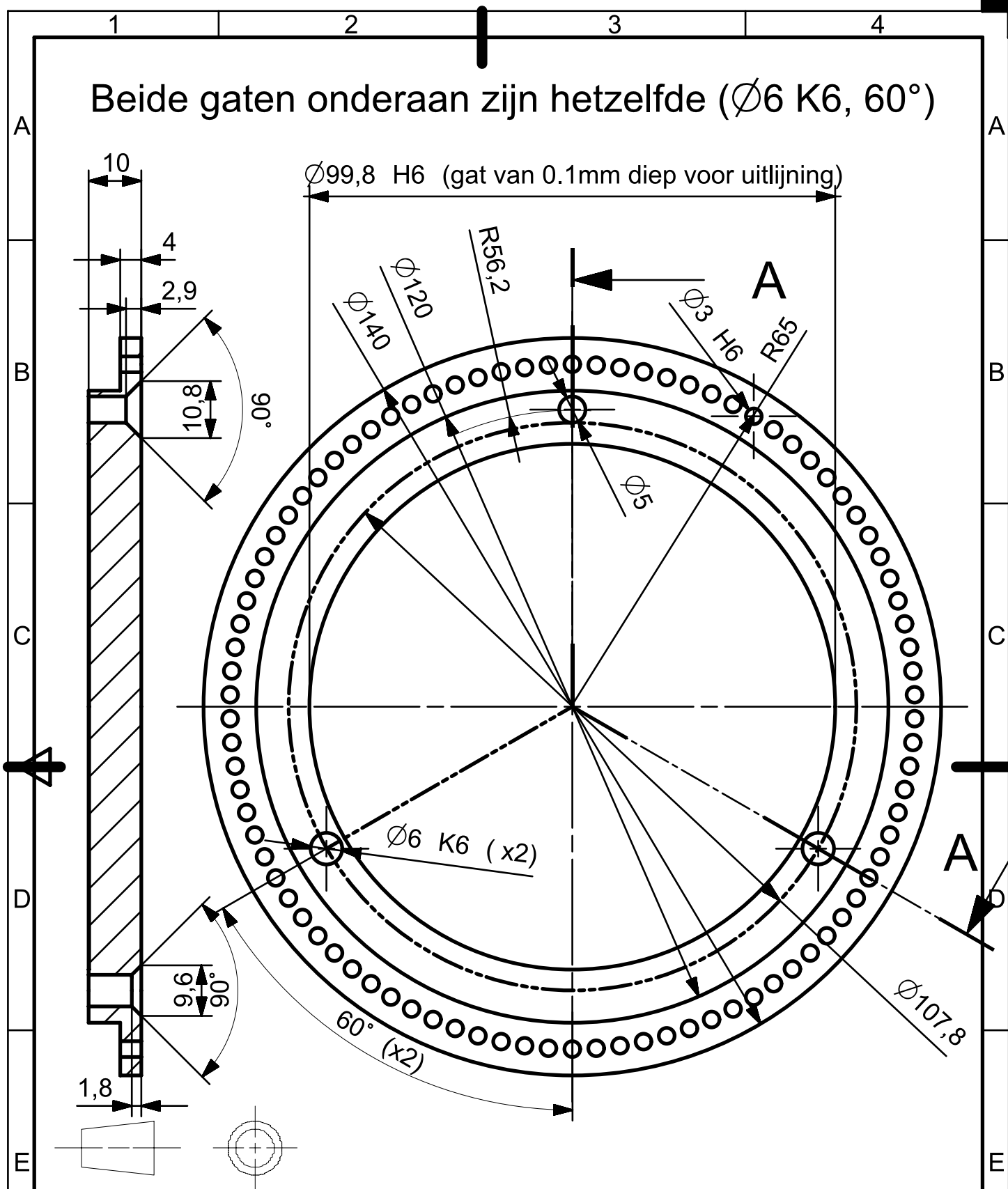
AANTAL: 2

BLAD 1 VAN 1

Ra 3,2

1 2 3 A4

Beide gaten onderaan zijn hetzelfde ( $\varnothing 6$  K6,  $60^\circ$ )



SECTION A-A

Ra 3,2

FORMULA ELECTRIC BELGIUM		MAATTOLERANTIES VOLGENS ISO 2768-m		VORM- EN PLAATSTOLERANTIES VOLGENS ISO 2768-K	
DATUM		Turntable			
GETEKEND DOOR	Ward Lenaerts				
TELEFOONR.		TT_Opspanplaat 2.0			
EMAIL					
MAATEENHEID	mm	GROOTTE	297.0 x 210.0	REV.	A
MATERIAAL	ALU 7075	SCHAAL 1:1	AANTAL: 1	BLAD 1 VAN 1	

A4



## Calculation of the required tilt angle ( $\theta$ )

The objective is to find the intersection point between two ellipses that represent the imaginary circle connecting the tooth tops at the 2 sides of the ring gear, when the ring gear is tilted.

$$(R_{top})^2 \cdot y^2 + (R_{top} \cdot \cos(\theta))^2 \cdot x^2 = 1$$

Being the equation that represents the ellipses. With  $R_{top}$  the radius of the tooth tops.  $\theta$  the needed tilt angle.  $x$  and  $y$ , the respective coordinates.

$$y_1 = \sqrt{\left(1 - \frac{x^2}{R_{top}^2}\right) \cdot (R_{top})^2 \cdot (\cos(\theta))^2}$$

$y_1$  being the y-coordinate of the upper half of ellipse 1.

$$y_2 = -\left(\sqrt{\left(1 - \frac{x^2}{R_{top}^2}\right) \cdot (R_{top})^2 \cdot (\cos(\theta))^2}\right) + b$$

$y_2$  being the y-coordinate of the lower half of ellipse 2.  $b$ , the width of the ring gear. To be more accurate the width of the gear,  $b$ , should be multiplied by the sine of the tilt angle, but as we will see the needed tilt angle will be very close to  $90^\circ$ . Because we want to find an intersection between the two ellipses we have to make the equations of the two ellipses equal to each other. From this we find :

$$\theta = \arccos\left(\frac{\left(\frac{b}{2}\right)^2}{R_{top}^2 - x^2}\right)$$

# J

Matlab script : Model concept 1 (see subsection  
4.4.2)

## Table of Contents

Generating point cloud .....	1
Influence of diffuse reflection .....	3
Influence of diffuse reflection 2.0 .....	3
How much power is initially absorbed and how reflected power is absorbed .....	4
Influence of the tangent angle of the tooth profile on the intensity profile .....	5
Normalizing the arrays .....	6
Influence of changing absorptivity depending on the incident angle .....	9
Influence of temperature .....	11
Plotting final graph .....	11
2D Simplification .....	12
3D Simplification .....	13

## Generating point cloud

```
% The objective of this section is to generate a point cloud in which
the
% X-coordinates have a equal distance compared to each other. The
original
% points file ('points3.txt') was created by storing the points of the
% spline that approximate the tooth profile of the ring gear.

clear;
clc;

[Y,X]=textread('points3.txt');
Arr=[X,Y];

k=1;

for x=X(1):0.05:X(length(X))

    P1=[x,0,0];
    P2=[x,1,0];

    dmin=1000;

    for i=2:length(X)-1

        P=[X(i),Y(i),0];
        P3=[X(i-1),Y(i-1),0];
        P4=[X(i+1),Y(i+1),0];

        a=P1-P2;
        b=P-P2;
        b2=P3-P2;
        b3=P4-P2;

        d=norm(cross(a,b))/norm(a);
        d2=norm(cross(a,b2))/norm(a);
```

1

```
d3=norm(cross(a,b3))/norm(a);

    if d<dmin

        dmin=d;
        P_least=P;

        if d2<d3

            P_least2=P3;
            dmin2=d2;

        else

            P_least2=P4;
            dmin2=d3;

        end

    end

end

Ynew=(dmin./(dmin+dmin2)).*(P_least2(2)-
P_least(2))+P_least(2);

Arr_new(k,1)=X;
Arr_new(k,2)=Ynew;

k=k+1;

end

% For every point the tangent angle is determined and saved in the
array.

for i=2:length(Arr_new)-1

    th1=atan2(Arr_new(i+1,2)-Arr_new(i,2) , Arr_new(i+1,1)-
Arr_new(i,1));
    th2=atan2(Arr_new(i,2)-Arr_new(i-1,2) , Arr_new(i,1)-
Arr_new(i-1,1));

    th=(th1+th2)/2;

    Arr_new(i,3)=th;

end

Arr_new(1,3)=Arr_new(2,3);
Arr_new(length(Arr_new),3)=Arr_new(length(Arr_new)-1,3);
```

2

## Influence of diffuse reflection

```
cos_tot=0;
cos_arr=[];

k=1;

D_beam=5; % Diameter of the used input beam
F=(D_beam./2)/sqrt(2);
G=F;

for i=length(Arr_new):-1:length(Arr_new)./2

    cos_tot=0;

    for j=1:1:length(Arr_new)./2-1

        A=exp(-((Arr_new(j,1))./F).^2); % Gaussian input intensity
        profile

        y1=Arr_new(i,2);
        y2=Arr_new(j,2);
        x1=Arr_new(i,1);
        x2=Arr_new(j,1);
        alfa=atan2(y1-y2,x1-x2); % alfa is the angle between a certain
        point on the tooth flank and the tooth top of the adjacent flank

        th_tot=(Arr_new(j,3)+pi./2)-alfa;
        cos_tot=cos_tot+A.*cos(th_tot); % We assume that the intensity
        of the diffuse reflected power changes with a cosine relation
        depending on the reflected angle

    end

    cos_arr(k)=cos_tot;
    k=k+1;

end
```

## Influence of diffuse reflection 2.0

```
% This section tackles the influence of power being reflected under
% different angles in the plane of the ring gear. Some of the
reflected power
% might not hit the adjacent tooth flank.

sum=0;

for i=1:1:length(Arr_new)./2-1

    cos_tot=0;
```

3

```
th_tot_max=-1;

for j=length(Arr_new):-1:length(Arr_new)./2

    y1=Arr_new(i,2);
    y2=Arr_new(j,2);
    x1=Arr_new(i,1);
    x2=Arr_new(j,1);
    alfa=atan2(y2-y1,x2-x1);
    th_tot=-((Arr_new(i,3)+pi./2)-alfa);

    if th_tot>th_tot_max

        th_tot_max=th_tot;

    end

end

sum=sum+(sin(th_tot_max)+1)./2); %Sum of the integrals

end

ratio=sum/i % 'Ratio' represents the amount of power that is reflected
and
% hits the adjacent tooth flank in comparison with the total reflected
power.

ratio =

    0.5539
```

## How much power is initially absorbed and how reflected power is absorbed.

```
Pin=1000; % Used for reference
A=0.7; % Estimated absorption coefficient
Pinit=Pin.*A; % Initially absorbed power
Prefl=Pin.*(1-A); % Initially reflected power

cos_arr=cos_arr./max(cos_arr);

k=0;
Ltot=0;
Arr_new;

for i=1:length(Arr_new)/2-1
```

4

```

for j=length(Arr_new):-1:length(Arr_new)

    X1=Arr_new(i,1);
    Y1=Arr_new(i,2);

    X2=Arr_new(j,1);
    Y2=Arr_new(j,2);

    L=((X1-X2).^2+(Y1-Y2).^2).^0.5;

    k=k+1;

    Ltot=Ltot+L;

end

end

L_avg=Ltot/k; % L_avg is the average length from a point on the left
tooth flank until the right tooth flank

th=atan2(D_beam./2,L_avg);
procent=(sin(th)+sin(th))./2; % We suppose that only this amount of
reflected power will effectively have an influence
% on the intensity profile

Pin=A.*Prefl.*ratio.*procent; % The useful reflected power is
multiplied with the absorptivity because
% only a certain amount of the reflected power that hits the
adjacent
% tooth will be absorbed. In theory a part of the reflected power
will
% also be reflected by the adjacent tooth but we will neglect this
power.

```

## Influence of the tangent angle of the tooth profile on the intensity profile

```

Arr_neww=[];

for i=1:length(Arr_new)

    A=exp(-((Arr_new(i,1))./F).^2);

    Arr_neww(i,1)=A.*cos(Arr_new(i,3)); % The intensity amplitude is
multiplied with the cosine of the tangent angle
    Arr_neww(i,2)=1./(cos(Arr_new(i,3))); % The length is divided by
the cosine of the tangent angle.

end

```

5

```

% The total power will ofcourse stays the same!

```

```

Arr_newww=[0];

for j=2:length(Arr_newww)

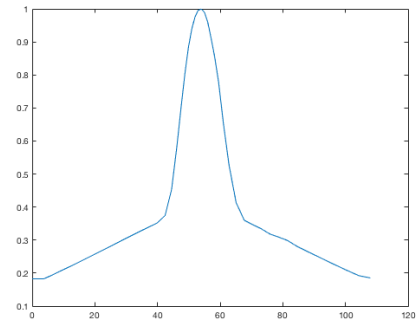
    Arr_newww(j,1)=Arr_newww(j-1,1)+Arr_neww(j,2);
    Arr_newww(j,2)=Arr_neww(j,1);

end

Arr_newww(1,2)=Arr_neww(2,2);

figure(1)
plot(Arr_newww(:,1),Arr_newww(:,2))

```



## Normalizing the arrays

```

d_tot=0;

for i=1:length(Arr_new)-1

    X1=Arr_new(i,1);
    X2=Arr_new(i+1,1);

    Y1=Arr_new(i,2);

```

6

```

    Y2=Arr_new(i+1,2);

    d=((Y2-Y1).^2+(X2-X1).^2).^0.5;

    d_tot=d_tot+d; %d_tot is the circumference from one tooth top
until the other

end

norm_factor=Arr_newww(length(Arr_newww),1)./d_tot;

for i=1:length(Arr_newww)

    Arr_newww(i,1)=Arr_newww(i,1)./norm_factor; % Normalizing

end

cos_arr_new=[];
ltot=0;

for i=1:length(cos_arr)

    l=1./(cos(Arr_new(i,3)));
    ltot=ltot+l;

    cos_arr_new(i,1)=ltot;
    cos_arr_new(i,2)=cos_arr(i); % cos_arr_new represents the new
'projected' intensity profile

end

max=cos_arr_new(length(cos_arr_new));

for i=1:length(cos_arr_new)

    cos_arr_new(i,1)=cos_arr_new(i,1)./max;

end

max=Arr_newww(length(Arr_newww),1);

for i=1:length(Arr_newww)

    Arr_newww(i,1)=Arr_newww(i,1)./max.*2;

end

int1=0;

for i=1:length(Arr_newww)-1

    Y2=Arr_newww(i+1,2);
    Y1=Arr_newww(i,2);

```

7

```

    X2=Arr_newww(i+1,1);
    X1=Arr_newww(i,1);

    int1=int1+((Y2+Y1)./2).*(X2-X1);

end

int1_final=int1./2;
int2=0;

for i=1:length(cos_arr_new)-1

    Y2=cos_arr_new(i+1,2);
    Y1=cos_arr_new(i,2);

    X2=cos_arr_new(i+1,1);
    X1=cos_arr_new(i,1);

    int2=int2+((Y2+Y1)./2).*(X2-X1);

end

for i=1:length(Arr_newww)

    Arr_newww(i,2)=Arr_newww(i,2)./int1_final; % Normalising

end

for i=1:length(cos_arr_new)

    cos_arr_new(i,2)=cos_arr_new(i,2)./int2; % Normalising

end

final_cos_arr=[cos_arr_new(:,1),Pin.*cos_arr_new(:,2)];
final_arr_new=[Arr_newww(1:24,1),Pin.*Arr_newww(1:24,2)];

sum_arr=[];

for i=1:length(final_cos_arr)

    sum_arr(i,1)=final_arr_new(i,1);
    sum_arr(i,2)=final_cos_arr(i,2)+final_arr_new(i,2);

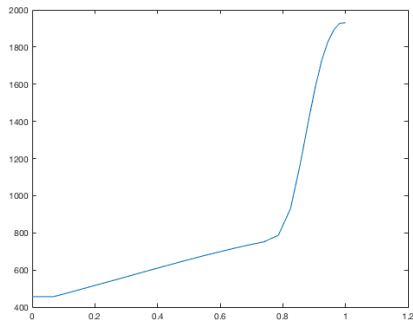
end

figure(2)
plot(sum_arr(:,1),sum_arr(:,2))
hold on

```

8





## Influence of changing absorptivity depending on the incident angle

```
Abs_0=0.4; % Absorption (%) for 0° (based on literature)
Abs_75=0.5; % Absorption (%) for 75° (based on literature)

th=75.*pi./180;

C=Abs_0; %abs @0°
B=(Abs_75-Abs_0)./(th.^2);

th=0:0.01:75.*pi./180;

Abs=B.*th.^2+C; % Quadratic relation between absorptivity and incident
angle based on literature (which is only correct if the angle stays
below the brewster angle

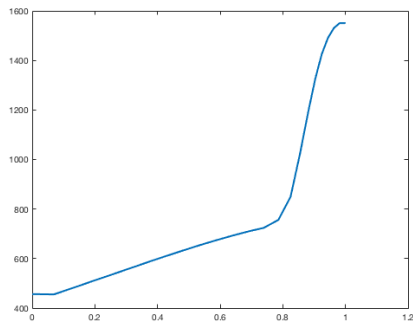
TH=[];

% The coming section is used because the tangent angle of tooth
surface can
% be split up into two linear sections
```

9

```
for i=1:length(sum_arr)
    xx=sum_arr(i,1);
    if xx<=0.78591
        TH(i)=(xx./0.78591).*0.15-1.31;
    else
        TH(i)=(xx-1)./(0.78591-1).*(-1.16);
    end
end
ABS=(B.*TH.^2+C)./(Abs_75);
final_arr_neww=[];
for i=1:length(final_arr_neww)
    final_arr_neww(i,2)=final_arr_neww(i,2).*ABS(i);
    final_arr_neww(i,1)=final_arr_neww(i,1);
end
for i=1:length(final_cos_arr)
    sum_arr(i,1)=final_arr_neww(i,1);
    sum_arr(i,2)=final_cos_arr(i,2)+final_arr_neww(i,2);
end
figure(3)
plot(sum_arr(:,1),sum_arr(:,2),'Linewidth',2)
sum_arr=[];
for i=1:length(sum_arr)
    sum_arr(i,1)=sum_arr(i,1).*d_tot./2;
    sum_arr(i,2)=sum_arr(i,2);
end
```

10



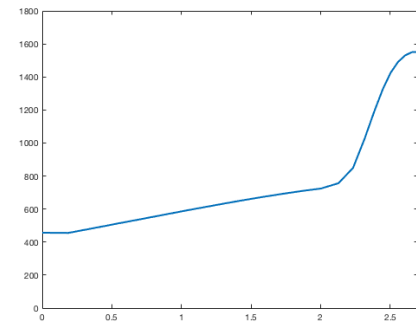
## Influence of temperature

```
% This is accounted in Ansys itself, as can be read in the thesis
itself.
```

## Plotting final graph

```
figure(4)
plot(sum_arr(:,1),sum_arr(:,2),'Linewidth',2)
axis([0 2.7 0 1800])
```

11



## 2D Simplification

```
x=-d_tot./2:0.01:d_tot./2;
d_tot./2;
A1=550;
z1=A1;

R_beam=0.47;
F2=R_beam./sqrt(2);
A2=830;
z2=A2.*exp(-(x./F2).^2);

A3=180;
a=sqrt(A)./(d_tot./2);
a=6.6;
z3=-(a.*x).^2+A3;

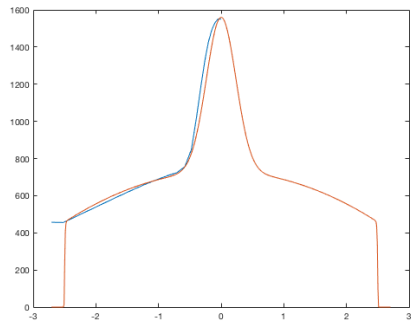
F3=d_tot./2;
F3=2.5;
n=400;
z4=exp(-(x./F3).^n);
```

12

```

ztot=(z1+z2+z3).*z4;
figure(5)
plot(sum_arr(:,1)-d_tot./2,sum_arr(:,2),'Linewidth',1)
hold on
plot(x,ztot)
% This graph represents the actual distribution. The advantage of this
% is
% that it is easy to implement into Ansys.

```



### 3D Simplification

```

[x,y]=meshgrid(-3:0.02:3);
dbeam=D_beam;
G=(dbeam./2)./sqrt(2);
Z=(A1+A2.*exp(-(x./F2).^2)+A3-(a.*x).^2).*exp(-(y./G).^2).*exp(-(x./
F3).^n);
figure(6)
view(0,0)
mesh(x,y,Z/1550)
xlabel('X (mm)','FontSize',16)
ylabel('Y (mm)','FontSize',16)

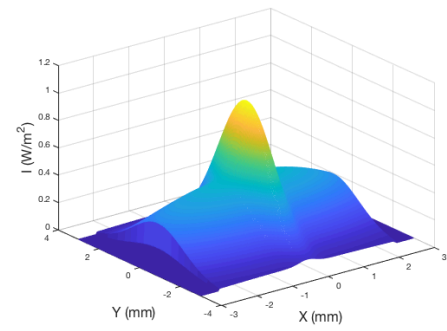
```

13

```

zlabel('I (W/m^2)','FontSize',16)

```



Published with MATLAB® R2019a

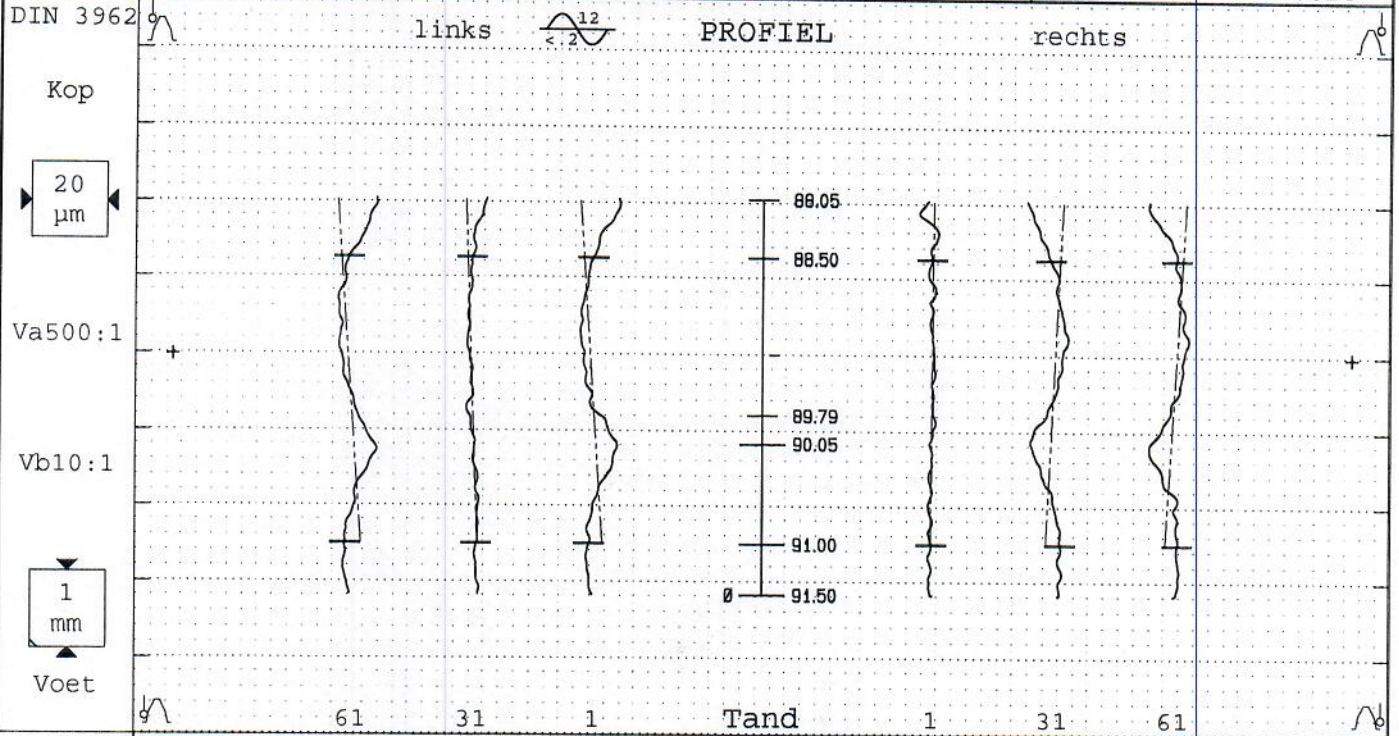
14

K

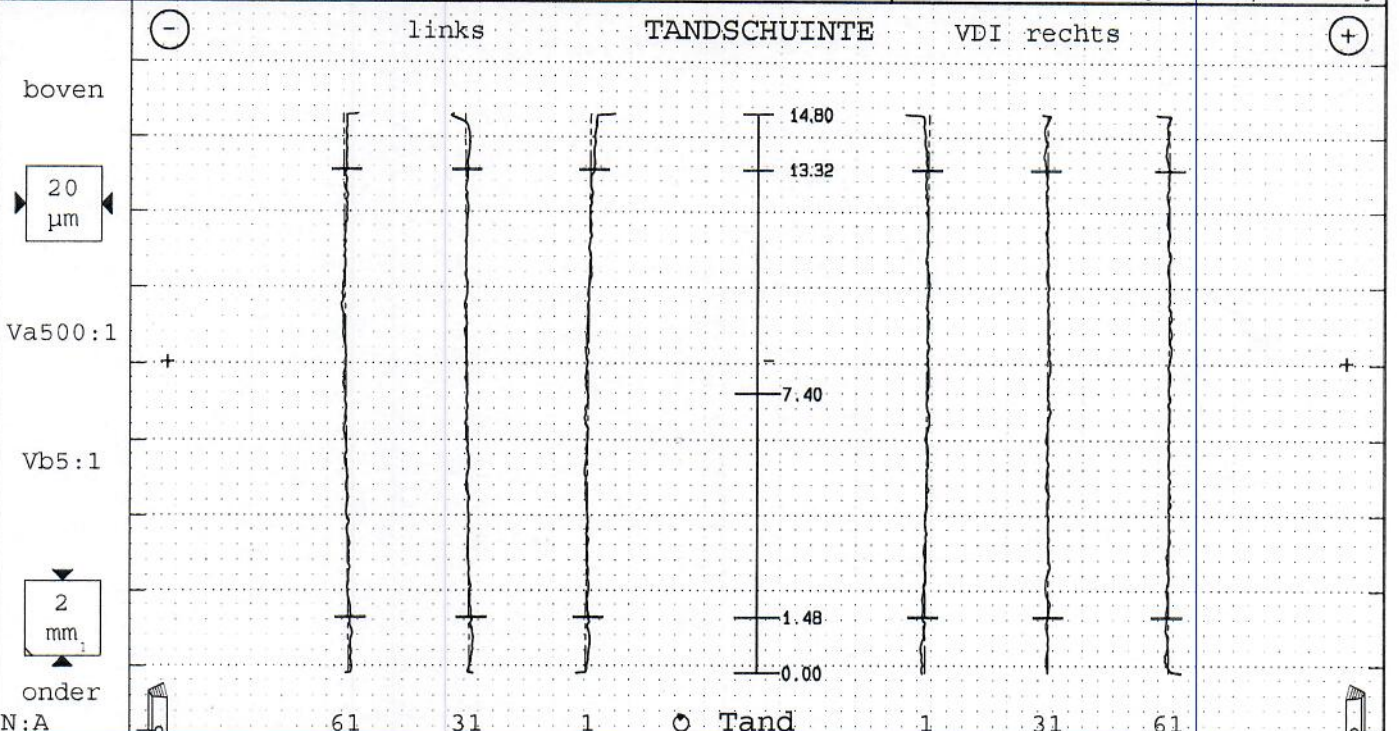
Measurement report ring gear wire EDM

# Profiel/Tandschuinite Vertanding

Prog.Nr.: GST0426c12 4.15.0 0 P 40	Kontroleur: Anke	Datum: 11.03.2021 09:04
Benaming: Ringwiel	Tandenaantal z -90	Tandbreedte b 14.8mm
Tekeningnr.: Ringwiel Z=90	Module m 1mm	Prof.meetber. La 3.76mm
Ordernr/volgnr.:	Ingrijphoek 20°	Tandsch.meetber. L&S 11.84mm
Klant/mach.: Formula Electric B	Tandsch.hoek βo 0°	St.-uitw. LNF (M)1 16.8mm
Meetplaats: P40 B7001	Grondcirkel-ø db 84.5723mm	Taster ø ' -14 (#14) 1mm
Toestand : Eindproduct	Tandsch.hoek βb 0°	Pr.versch.F. x - .024



	Meetwaard [µm] Kwaliteit			toel. Waard Kwal			Meetwaard [µm] Kwaliteit			
fHam	4.4	6	V 2.6				2.8	4	V 4.0	
fHa	5.3	7	2.7	5.1	±5	6	0.4	3.6	4	6
Fa	10.4	7	3.5	9.9	8	6	2.0	10.1	10	6
ffa	10.0	8	2.9	9.5	6	6	2.2	9.3	8	9
V/K-ø [mm]	92.543 [92.373/92.428]						87.994 [88.013/88.048]			



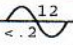
	Meetwaard [µm] Kwaliteit			toel. Waard Kwal			Meetwaard [µm] Kwaliteit			
fHβm	L 0.5	1	V 2.2				R 0.1	1	V 1.0	
fHβ	L 1.3	1	L 1.1	R 0.9	±8	6	R 0.7	1	L 0.3	R 0.0
Fβ	2.7	2	2.0	2.6	9	6	1.8	1	1.4	1.5
ffβ	2.0	2	1.3	1.9	5.5	6	1.6	2	1.6	1.5





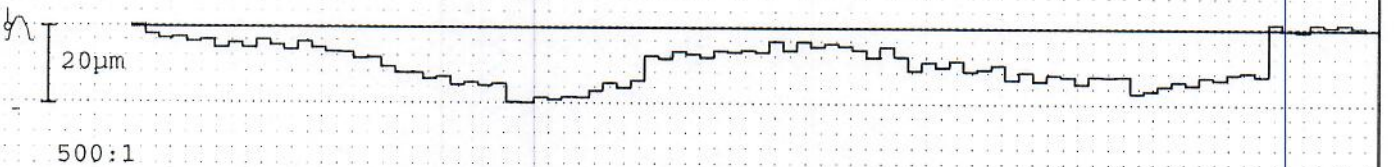
# Steek Vertanding

Prog.Nr.: GST0426c12 4.15.0 0 P 40	Kontroleur: Anke	Datum: 11.03.2021 09:04
Benaming: Ringwiel	Tandenaantal z -90	Ingrijphoek 20°
Tekeningnr.: Ringwiel Z=90	Module m 1mm	Tandsch.hoek $\beta_0$ 0°
Ordernr/volgnr.:	Meetplaats: P40 B7001	
Klant/mach.: Formula Electric B	Toestand: Eindproduct	

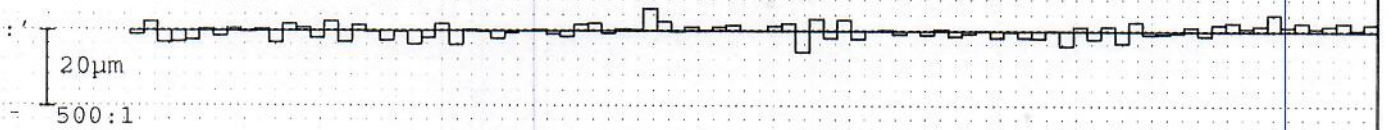
DIN 3962  **Individuele Afwijking Steek fp linker flank**



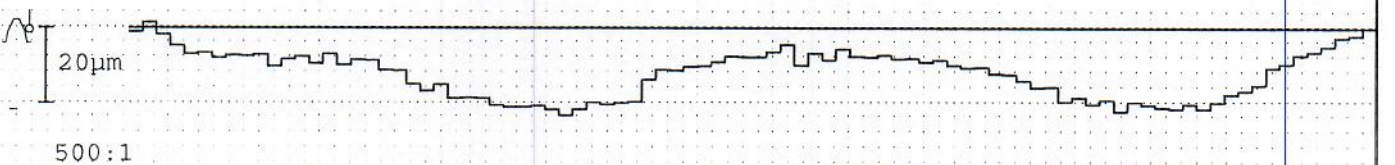
**Totale Afwijking Steek Fp linker flank**



**Individuele Afwijking Steek fp rechter flank**

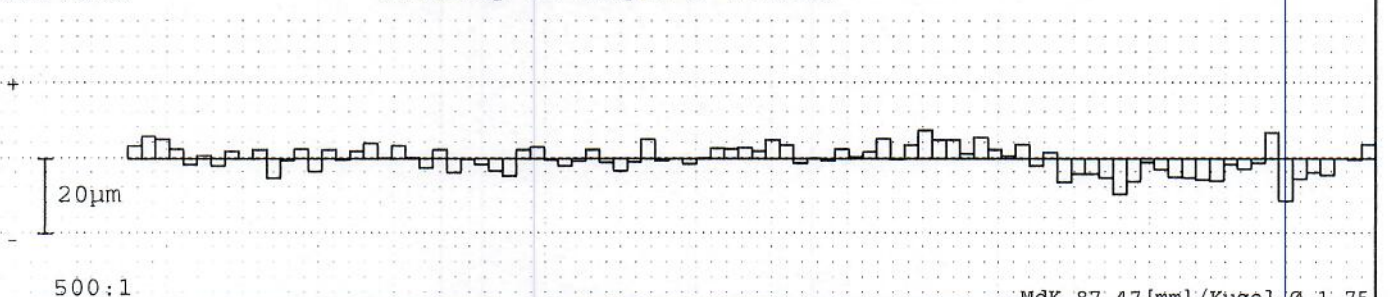


**Totale Afwijking Steek Fp rechter flank**



Teilungsmekreis: 89.793 z=7.4mm		linker flank				rechter flank			
		Meetwaard	Kwal.	toel.Waard	Kwal.	Meetwaard	Kwal.	toel.Waard	Kwal.
gr. Individuele Afwijking	fp max	13.7	8	7.0	6	6.0	6	7.0	6
Sprong	fu max	15.5	8	9.0	6	8.9	6	9.0	6
Variatie	Rp	18.4				11.6			
Totale Afwijking	Fp	21.2	6	25.0	6	24.8	6	25.0	6
Segment Afwijking	Fpz/8	16.5	7	16.0	6	19.9	7	16.0	6

DIN 3962 **Rondloop Fr (Kogel- $\emptyset$  = 1.75mm)**



MdK 87.47 [mm]/Kugel- $\emptyset$  1.75

Rondheids Afwijking	Fr	18.8	7	16.0	6	toel. Waard	87.79	87.675
Tanddikte Variatie	Rs	15.6	8	10.0	6	Meetwaard	87.679	87.655





Benaming <b>0</b>	Tekeningnummer <b>Ringwiel Z=90</b>	Revisienummer <b>0</b>	Productienummer <b>0</b>
Klant <b>0</b>	Extern ordernummer <b>0</b>	Productnummer <b>0 1</b>	Opmerking <b>0 Onbehandeld</b>
Controleur <b>0</b>	Datum <b>04-05-2021</b>	Tijd <b>12:14</b>	Aantal pagina's <b>1</b>

FCFVLAK1		MM	▱ 0.05		STANDAARD		ISO 1101
Element	NOM	+TOL	-TOL	METG	AFW	BUITOL	
VLK_A	0.000	0.050		0.003	0.003	0.000	
FCFRONDH1		MM	○ 0.03		STANDAARD		ISO 1101
Element	NOM	+TOL	-TOL	METG	AFW	BUITOL	
KOPCIRKEL	0.000	0.030		0.020	0.020	0.000	
#	MM	LOC1 - KOPCIRKEL					
AS	NOM	+TOL	-TOL	METG	AFW	BUITOL	
D	88.000	0.050	-0.050	87.987	-0.013	0.000	
FCFVLAK2		MM	▱ 0.05		STANDAARD		ISO 1101
Element	NOM	+TOL	-TOL	METG	AFW	BUITOL	
VLK_B	0.000	0.050		0.001	0.001	0.000	

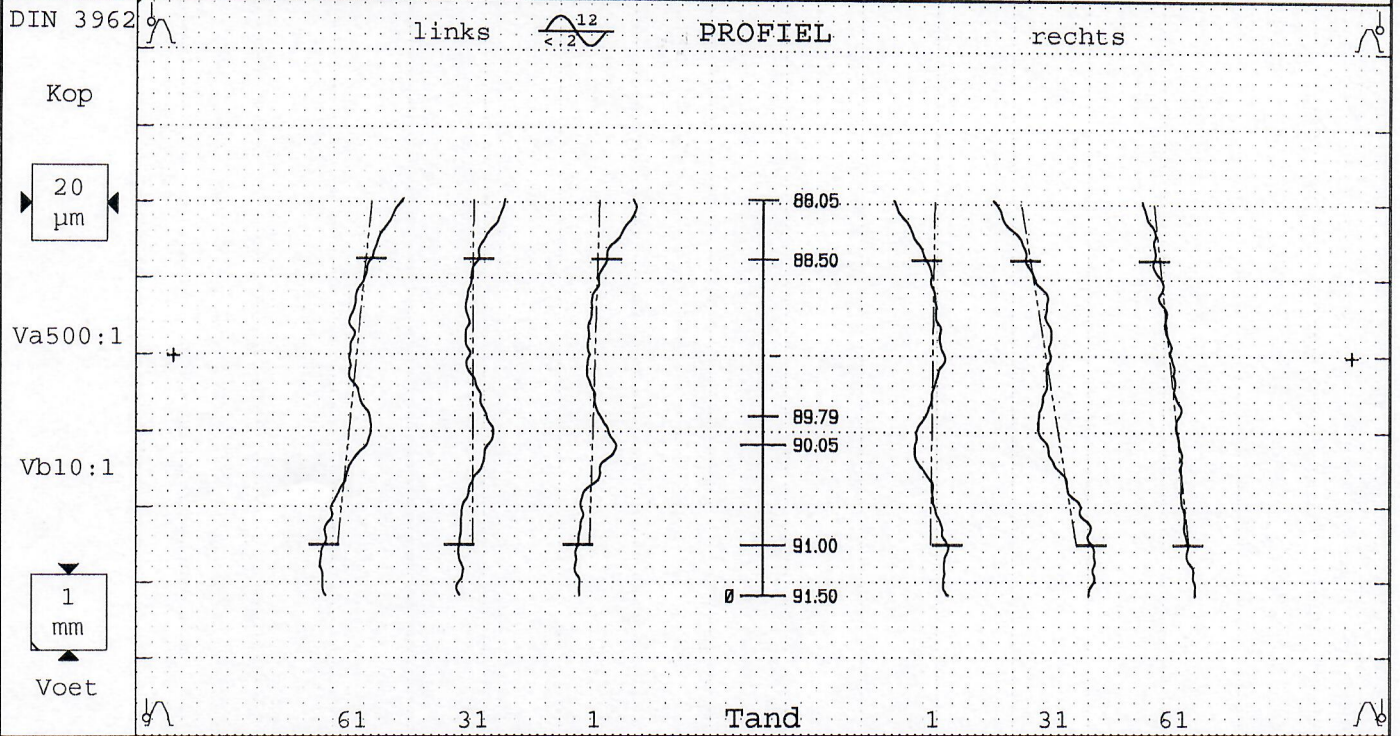
L

Measurement report carburized ring gear

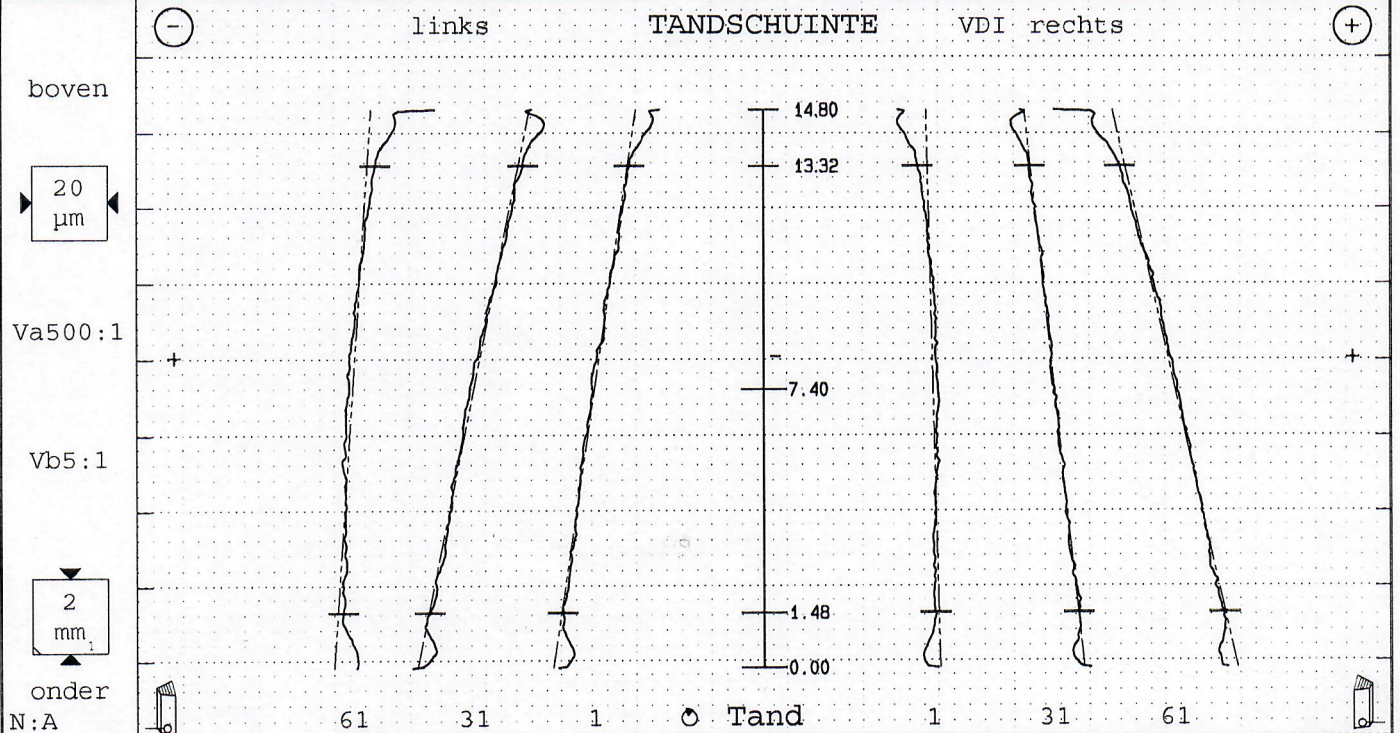


# Profiel/Tandschuinste Vertanding

Prog.Nr.: GST0426c12 4.15.0 0 P 40	Kontroleur: Anke	Datum: 04.05.2021 11:57
Benaming: Ringwiel	Tandenaantal z -90	Tandbreedte b 14.8mm
Tekeningnr.: Ringwiel Z=90	Module m 1mm	Prof.meetber. La 3.76mm
Ordernr./volgnr.: Nr.3 gecementeerd	Ingrijphoek 20°	Tandsch.meetber. Lß 11.84mm
Klant/mach.: Formula Electric B	Tandsch.hoek $\alpha_o$ 0°	St.-uitw. LNF(M1)1 16.8mm
Meetplaats: P40 B7001	Grondcirkel- $\emptyset$ db 84.5723mm	Taster $\emptyset$ ' -14 (#14) 1mm
Toestand: Eindproduct	Tandsch.hoek $\beta_b$ 0°	Pr.versch.F. x -.024



	Meetwaard [µm] Kwaliteit				toel. Waard Kwal				Meetwaard [µm] Kwaliteit				
fH <sub>am</sub>	-3.2	5	V 7.3		±5	6	±5	6	-6.4	7	V 13.1		
fH <sub>a</sub>	-7.4	8	-0.1	-2.1	±5	6	±5	6	0.8	-12.3	9	-7.7	
F <sub>a</sub>	12.4	8	9.0	10.1	8	6	8	6	8.8	17.6	9	9.3	
f <sub>fa</sub>	9.6	8	8.9	9.4	6	6	6	6	9.1	9.8	8	3.7	
V/K- $\emptyset$ [mm]	92.394	[92.373/92.428]								87.891	[88.013/88.048]		

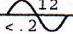


	Meetwaard [µm] Kwaliteit				toel. Waard Kwal				Meetwaard [µm] Kwaliteit			
fH <sub>ßm</sub>	R16.4	9	V 15.9		±8	6	±8	6	L14.0	8	V 23.5	
fH <sub>ß</sub>	R 7.9	R23.8	9	R17.6	±8	6	±8	6	L 2.9	L12.6	L26.4	10
F <sub>ß</sub>	8.9	24.9	9	17.8	9	6	9	6	5.7	13.6	27.6	9
f <sub>fß</sub>	3.8	2.5	2.3		5.5	6	5.5	6	4.2	1.6	2.8	

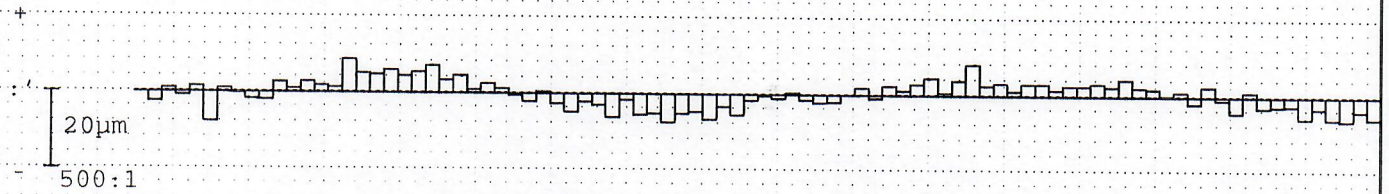


# Steek Vertanding

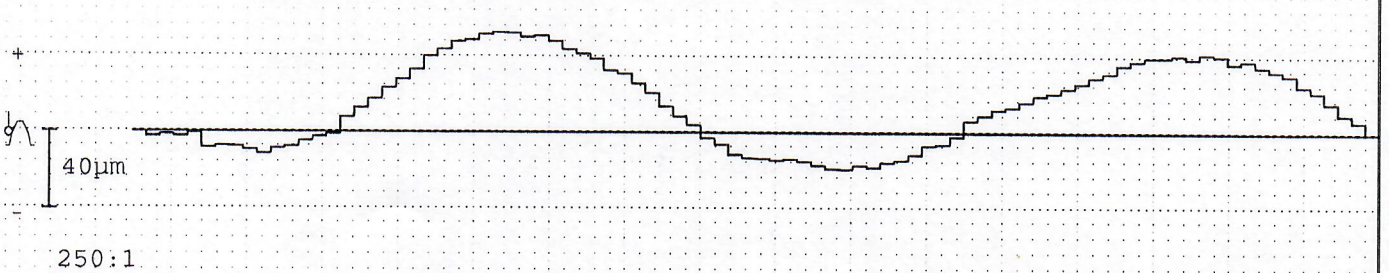
Prog.Nr.: GST0426c12 4.15.0 0 P 40	Kontroleur: Anke	Datum: 04.05.2021 11:57
Benaming: Ringwiel	Tandenaantal z -90	Ingrijphoek 20°
Tekeningnr.: Ringwiel Z=90	Module m 1mm	Tandsch.hoek $\beta_0$ 0°
Ordernr./volgnr.: Nr.3 gecementeerd	Meetplaats: P40 B7001	
Klant/mach.: Formula Electric B	Toestand: Eindproduct	

DIN 3962 

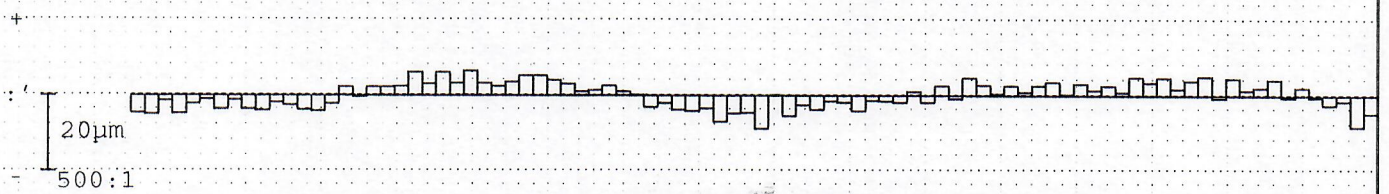
## Individuele Afwijking Steek fp linker flank



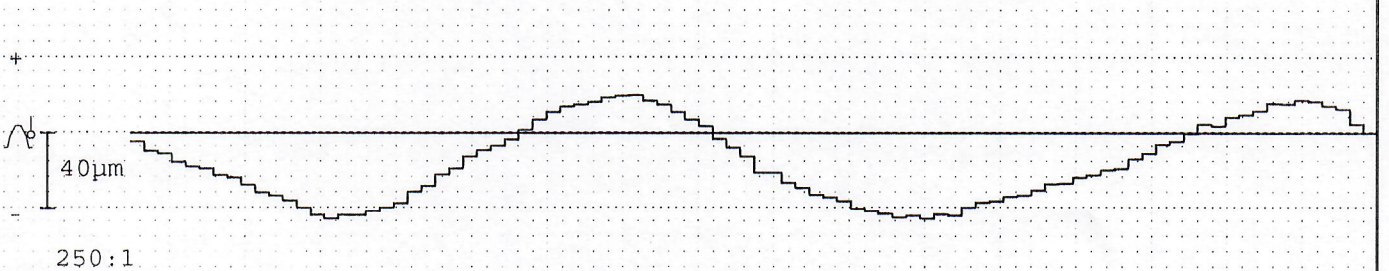
## Totale Afwijking Steek Fp linker flank



## Individuele Afwijking Steek fp rechter flank



## Totale Afwijking Steek Fp rechter flank

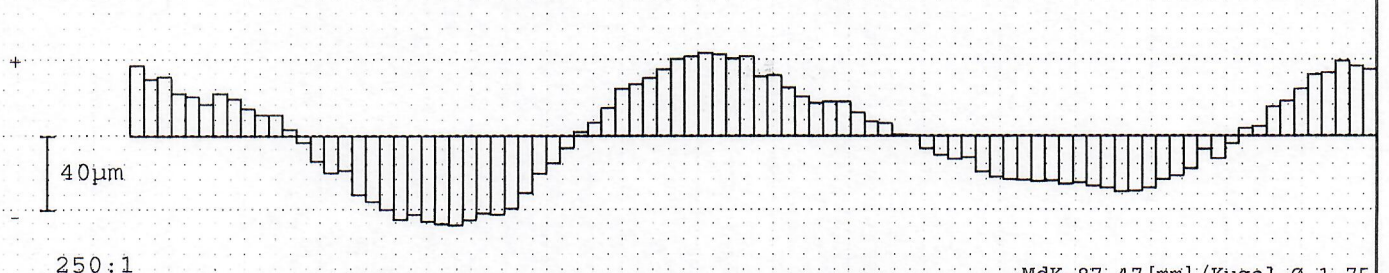


Teilungsmesskreis: 89.793 z=7.4mm

		linker flank				rechter flank			
		Meetwaard	Kwal.	toel.Waard	Kwal.	Meetwaard	Kwal.	toel.Waard	Kwal.
gr. Individuele Afwijking	fp max	8.6	7	7.0	6	8.8	7	7.0	6
Sprong	fu max	9.3	7	9.0	6	8.8	6	9.0	6
Variatie	Rp	16.2				15.3			
Totale Afwijking	Fp	71.8	10	25.0	6	66.0	10	25.0	6
Segment Afwijking	Fpz/s	53.0	10	16.0	6	48.5	10	16.0	6

DIN 3962

## Rondloop Fr (Kogel-Ø = 1.75mm)



		Mdk 87.47 [mm]/Kugel-Ø 1.75	
		toel.Waard	Meetwaard
Rondheids Afwijking	Fr	87.79	87.675
Tanddikte Variatie	Rs	87.618	87.462





Benaming <b>0</b>	Tekeningnummer <b>Ringwiel Z=90</b>	Revisienummer <b>0</b>	Productienummer <b>0</b>
Klant <b>0</b>	Extern ordernummer <b>0</b>	Productnummer <b>0 3</b>	Opmerking <b>0 Gecementeerd.</b>
Controleur <b>0</b>	Datum <b>04-05-2021</b>	Tijd <b>13:28</b>	Aantal pagina's <b>1</b>

FCFVLAK1		MM	▧ 0.05		STANDAARD	ISO 1101
Element	NOM	+TOL	-TOL	METG	AFW	BITOL
VLK_A	0.000	0.050		0.032	0.032	0.000
FCFRONDH1		MM	○ 0.03		STANDAARD	ISO 1101
Element	NOM	+TOL	-TOL	METG	AFW	BITOL
KOPCIRKEL	0.000	0.030		0.102	0.102	0.072
#	MM	LOC1 - KOPCIRKEL				
AS	NOM	+TOL	-TOL	METG	AFW	BITOL
D	88.000	0.150	-0.150	87.893	-0.107	0.000
FCFVLAK2		MM	▧ 0.05		STANDAARD	ISO 1101
Element	NOM	+TOL	-TOL	METG	AFW	BITOL
VLK_B	0.000	0.050		0.026	0.026	0.000



## Measurement report laser hardened ring gear





Benaming <b>0</b>	Tekeningnummer <b>test</b>	Revisienummer <b>0</b>	Productienummer <b>0</b>
Klant <b>0</b>	Extern ordernummer <b>0</b>	Productnummer <b>0</b>	Opmerking <b>0</b>
Controleur <b>0</b>	Datum <b>18-05-2021</b>	Tijd <b>15:02</b>	Aantal pagina's <b>1</b>

FCVLAK1		MM	▱ 0.05		STANDAARD	ISO 1101
Element	NOM	+TOL	-TOL	METG	AFW	BITOL
VLK1	0.000	0.050		0.059	0.059	0.009
⊕	MM	LOC1 - KOPCIRKEL				
AS	NOM	+TOL	-TOL	METG	AFW	BITOL
D	88.000	0.050	-0.050	87.934	-0.066	0.016
FCFRONDH1		MM	○ 0.03		STANDAARD	ISO 1101
Element	NOM	+TOL	-TOL	METG	AFW	BITOL
KOPCIRKEL	0.000	0.030		0.107	0.107	0.077
FCVLAK2		MM	▱ 0.05		STANDAARD	ISO 1101
Element	NOM	+TOL	-TOL	METG	AFW	BITOL
VLK2	0.000	0.050		0.055	0.055	0.005

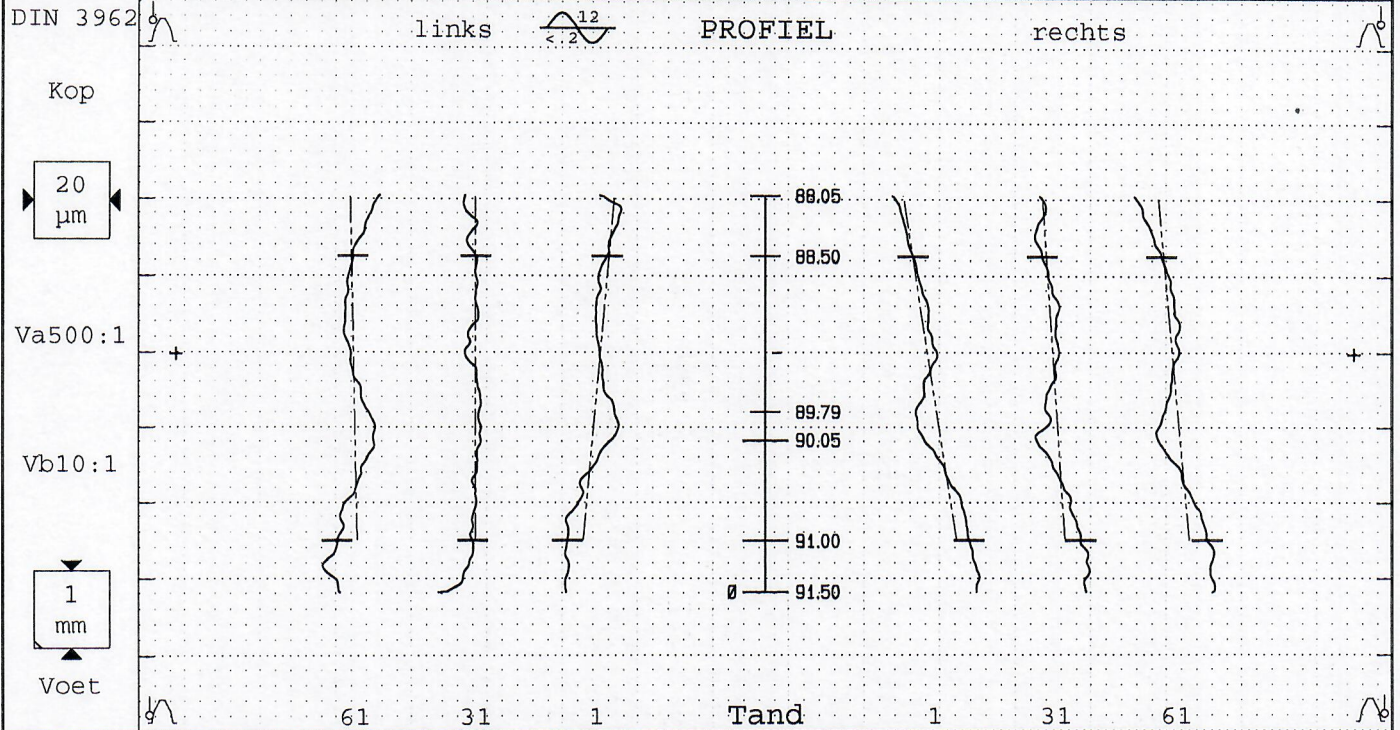
A

B

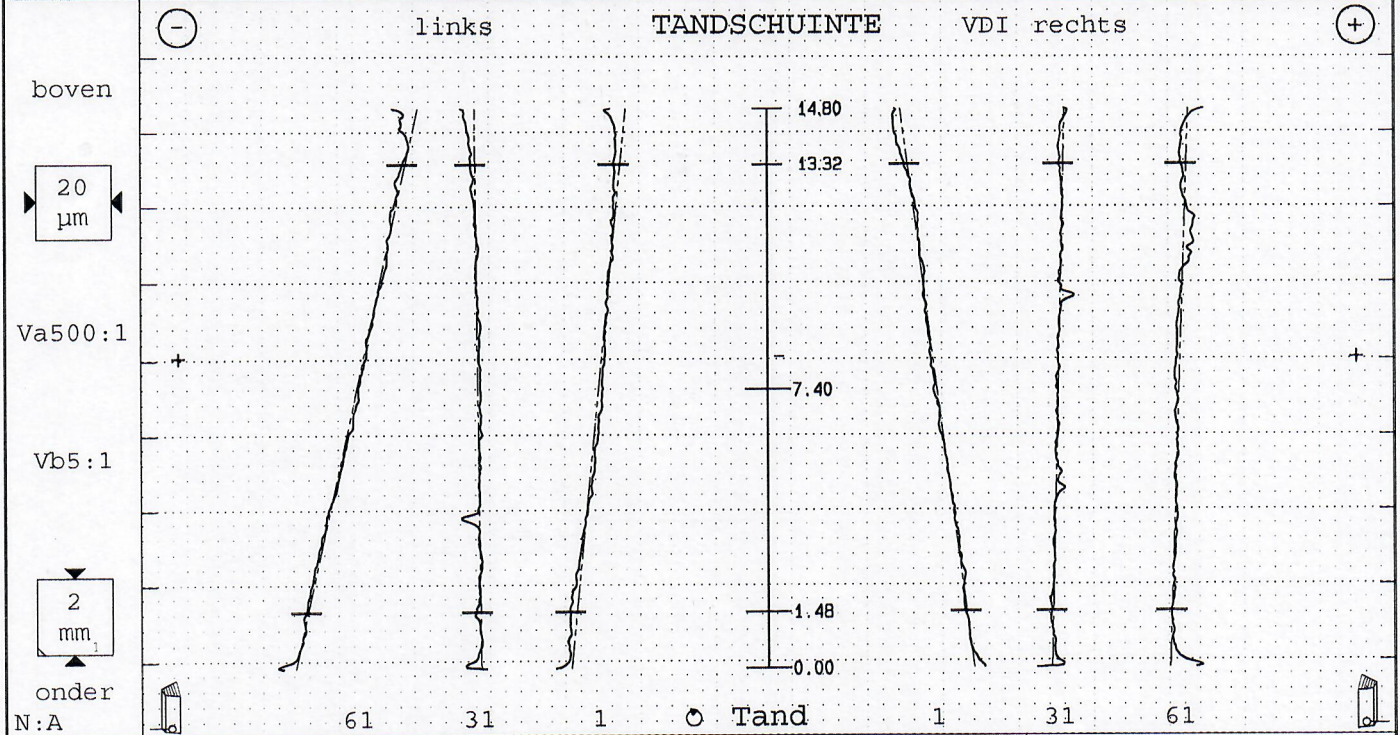


# Profiel/Tandschuinite Vertanding

Prog.Nr.: GST0426c12 4.15.0 0 P 40	Kontroleur: Anke	Datum: 18.05.2021 14:41
Benaming: Ringwiel	Tandenaantal z -90	Tandbreedte b 14.8mm
Tekeningnr.: Ringwiel Z=90	Module m 1mm	Prof.meetber. La 3.76mm
Ordernr/volgnr.:	Ingrijphoek 20°	Tandsch.meetber. L&S 11.84mm
Klant/mach.: Formula Electric B	Tandsch.hoek $\beta_o$ 0°	St.-uitw. LNF(M1)1 16.8mm
Meetplaats: P40 B7001	Grondcirkel- $\emptyset$ db 84.5723mm	Taster $\emptyset$ '-14(#14)1mm
Toestand: Eindproduct	Tandsch.hoek $\beta_b$ 0°	Pr.versch.F. x - .024



	Meetwaard [ $\mu$ m] Kwaliteit			toel.Waard Kwal			Meetwaard [ $\mu$ m] Kwaliteit					
fH <sub>am</sub>	-1.7	3	V 8.4				-7.8	8	V 6.6			
fH <sub>a</sub>	1.6	0.0	-6.8	7	$\pm 5$	6	$\pm 5$	6	-11.6	9	-5.0	-6.8
F <sub>a</sub>	10.0	4.4	14.0	8	8	6	8	6	14.8	8	12.1	13.5
ffa	10.7	4.4	11.7	8	6	6	6	6	9.0	10.3	10.9	8
V/K- $\emptyset$ [mm]	92.372 [92.373/92.428]						87.876 [88.013/88.048]					



	Meetwaard [ $\mu$ m] Kwaliteit			toel.Waard Kwal			Meetwaard [ $\mu$ m] Kwaliteit					
fH <sub>βm</sub>	R12.2	8	V 27.2				L 2.8	3	V 19.4			
fH <sub>β</sub>	R26.0	10	L 1.2	R11.7	$\pm 8$	6	$\pm 8$	6	L15.4	8	R 3.0	R 4.0
F <sub>β</sub>	25.7	9	5.5	12.3	9	6	9	6	16.0	8	6.7	6.4
ff <sub>β</sub>	2.9	5.8	7	3.4	5.5	6	5.5	6	2.1	5.0	6	4.2

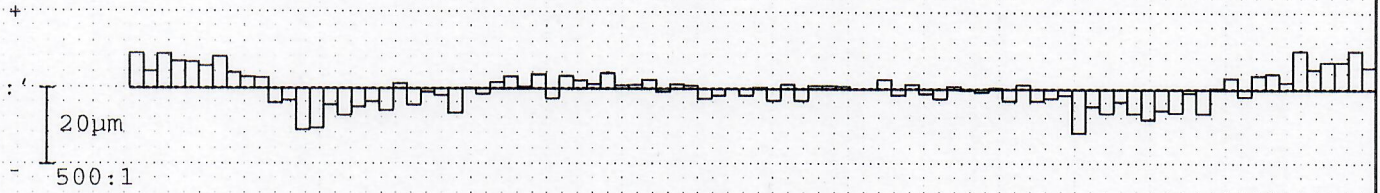


# Steek Vertanding

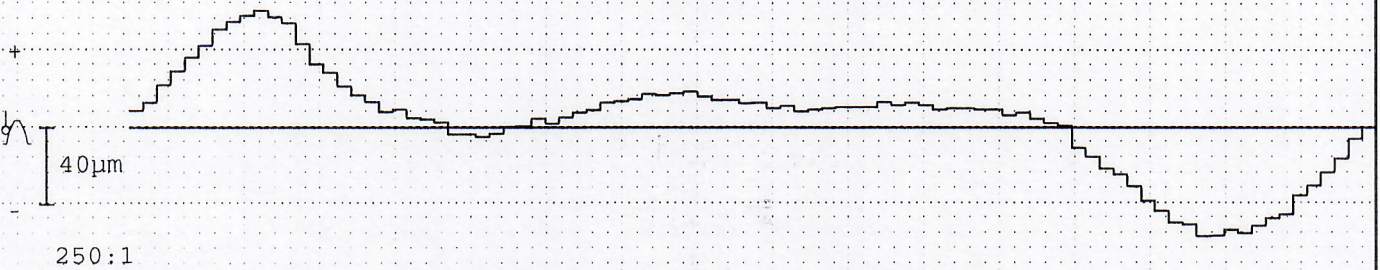
Prog.Nr.: GST0426c12 4.15.0 0 P 40	Kontroleur: Anke	Datum: 18.05.2021 14:41
Benaming: Ringwiel	Tandenaantal z -90	Ingrijphoek 20°
Tekeningnr.: Ringwiel Z=90	Module m 1mm	Tandsch.hoek $\delta_0$ 0°
Ordernr/volgnr.:	Meetplaats: P40 B7001	
Klant/mach.: Formula Electric B	Toestand: Eindproduct	

DIN 3962

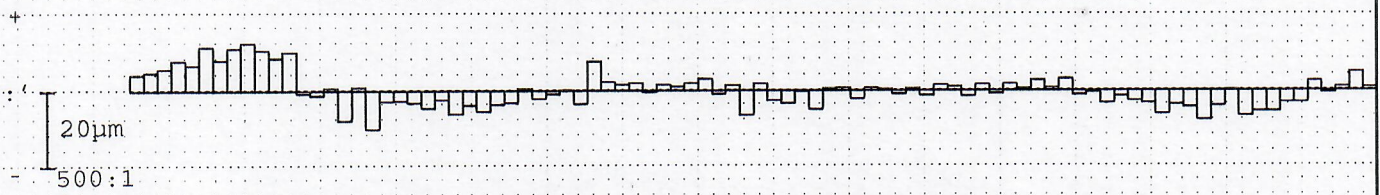
## Individuele Afwijking Steek fp linker flank



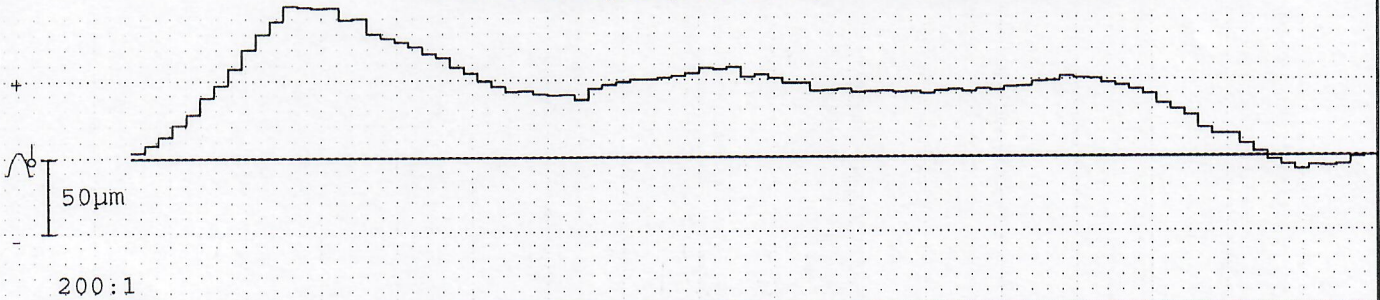
## Totale Afwijking Steek Fp linker flank



## Individuele Afwijking Steek fp rechter flank



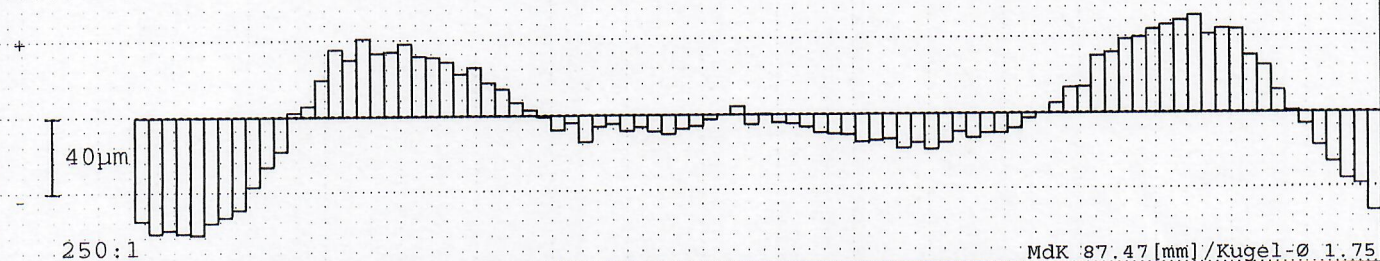
## Totale Afwijking Steek Fp rechter flank



		linker flank				rechter flank			
		Meetwaarde	Kwal.	toel.Waarde	Kwal.	Meetwaarde	Kwal.	toel.Waarde	Kwal.
gr. Individuele Afwijking	fp max	11.5	8	7.0	6	12.3	8	7.0	6
Sprong	fu max	10.1	7	9.0	6	11.1	7	9.0	6
Variatie	Rp	21.7				22.5			
Totale Afwijking	Fp	118	11	25.0	6	109	10	25.0	6
Segment Afwijking	Fpz/8	82.3	11	16.0	6	95.8	11	16.0	6

DIN 3962

## Rondloop Fr (Kogel-Ø =1.75mm)



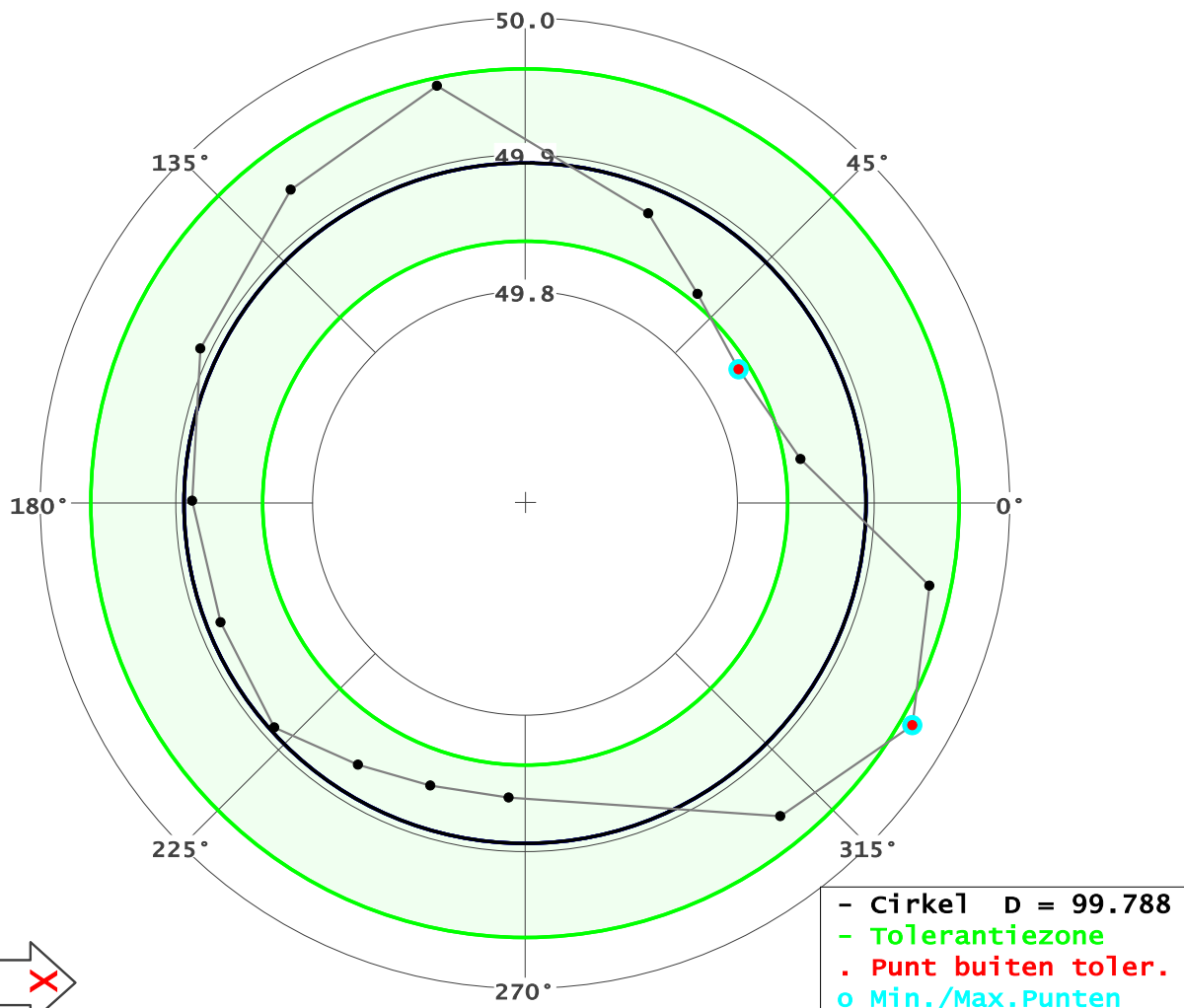
MdK 87.47 [mm] / Kugel-Ø 1.75

Rondheids Afwijking	Fr	114	12	16.0	6	toel.Waarde	87.79	87.675
Tanddikte Variatie	Rø	89.4	12	10.0	6	Meetwaarde	87.644	87.517

N

Roundness measurement laser hardened ring gear

Gebruikersnaam	Admin	Datum en tijd	11/05/2021 10:48
Stuknummer tekening		Omschrijving tekening	
Datum tekening		Operator	
MeetMachine		Opmerking	



[mm] | Vergroting: 183

Tolerantiezone	0.126	Boventol.	0.069
		Ondertol.	-0.057
X	0.001	Aantal punten	16
Y	-0.011	Min./Max.Punte	12 / 15
Z	0.000	Std.dev * 4	0.187
Actueel Radius	49.894	Rondheid	0.143
Min. afst.	-0.066	Max. afst.	0.077
X	42.236	X	43.343
Y	26.438	Y	-24.870
Radius	49.828	Radius	49.971
Phi	32.045	Phi	330.153



FACULTEIT INDUSTRIËLE INGENIEURSWETENSCHAPPEN  
CAMPUS GROEPT LEUVEN  
Andreas Vesaliusstraat 13  
3000 LEUVEN, België  
tel. + 32 16 30 10 30  
iiw.groept@kuleuven.be  
[www.iw.kuleuven.be](http://www.iw.kuleuven.be)

